Engineering Doctoral Thesis

Multi-Directional Quantitative Schlieren 3D-CT Measurements Technique for Combustion and Supersonic Flows

(燃焼ならびに超音速流動のための多方向
定量シュリーレン3D-CT計測技術)

Supervisor
Prof. Dr. YOJIRO "ISHINO"

Nagoya Institute of Technology
Graduate School of Engineering (Doctoral Program)
Department of Electrical and Mechanical Engineering

By
AHMAD ZAID "NAZARI"

March 2021

Engineering Doctoral Thesis

Multi-Directional Quantitative Schlieren 3D-CT Measurements Technique for Combustion and Supersonic Flows

(燃焼ならびに超音速流動のための多方向
定量シュリーレン3D-CT計測技術)

Supervisor
Prof. Dr. YOJIRO "ISHINO"

Nagoya Institute of Technology
Graduate School of Engineering (Doctoral Program)
Department of Electrical and Mechanical Engineering

Date of Enrollment: April 2017

By
Student ID No. 29513007
AHMAD ZAID "NAZARI"

Date of Graduation: March 2021

ACKNOWLEDGMENTS

In the Name of God, the Most Gracious and the Most Merciful

First of all and foremost, I am thankful to God the creator of the universe, the true lord of the worlds, for everything, and for giving us lifetime, health, patience and capability to complete this work.

Special appreciation goes to my supervisor Prof. Dr. Yojiro ISHINO for his advising, support, way of thinking about research, constructive comments, and suggestions throughout the experimental and thesis works from beginning to end which have contributed to the success of this research. I would also like to thank Assoc. Prof. Yu SAIKI for his kind support, and Mr. Yuta ISHIKO and all other students of this laboratory for their heartfelt support in the daily research activities.

I would like to thank the Ph.D. defense committee members, Professor Masato TAGAWA and Professor Masahiro FURUTANI of Nagoya Institute of Technology and Professor Yoshiaki MIYAZATO of the University of Kitakyushu for their time, interest and kind supports. I thank our colleagues from the University of Kitakyushu who provided the micro nozzles that greatly assisted the research.

My special gratefulness goes to the Government of Japan, particularly the Japanese Ministry of Education, Culture, Sports, Science and Technology (MEXT) for the scholarship granted me to pursue the study program. This research work was partly supported by the Japan Society for the Promotion of Science (JSPS) Grants-in-Aid for Scientific Research (C)16K06118.


Jasmine (lilac) Flower

Finally, I would like to thank everyone, my relatives, friends, university and governmental offices staffs ..., who was part of my success and as well as my apology that I could not mention personally one by one, and all of them are under my eye and have a place in my good prayers.

Last but not least, and most importantly, I would like to express my deepest gratitude and appreciation to my beloved family, for their love, patience, understanding, support, encouragement, and prayers throughout my study program and in daily life the ups and downs.

Ahmad Zaid NAZARI

March 2021, Nagoya, Japan

ABSTRACT

" You Think, You (Human) Are a Small Creature, While the Whole Universe Is Summed Up (ABSTRACTED) Inside You. " (***Ali ibn Abi Talib***)

In the previous works, a three-dimensional computerized tomography (3D-CT) non-scanning technique using a delicate 20-directional quantitative schlieren optical system is employed and developed. By using 3D-CT technique, measurement of the instantaneous density distributions of several types of flames in laminar and turbulent flows have been successfully obtained.

In the present work, the results of the conducted research to extend and improve the above method are summarized and reported in chapters 2 to 5.

In **CHAPTER 1**, the necessary information regarding the research method and the experimental apparatus setup is described.

In **CHAPTER 2**, two new techniques (1) and (2) are introduced for image processing.

(1) A novel technique "multi-path integration" method is proposed for noise reduction in projections images of CT.

(2) A new technique "inverse process" method is employed which enables us to obtain vertical schlieren brightness gradient from horizontal experimental data without the necessity of a new optical system and can be used for obtaining any optional directions of schlieren brightness gradient.

In **CHAPTER 3**, the findings of the complex three-dimensional structure of the supersonic microjets from axisymmetric convergent-divergent (Laval) micro nozzles with circular and square outlet shapes are reported. First, from the multi-directional schlieren images, from the symmetry and diagonal views of square microjets for the first shock-cells, two different patterns of shock waves are observed, and the shock-cell spacing L_s and supersonic core length L_c for all nozzle pressure ratios are investigated and reported. Next, from the measurement results by three-dimensional CT measurement, the three-dimensional structures of square microjets are more clearly observed with two types "upright" and "diagonal" of "cross-shaped" of cross-sectional structures. In addition, gradual changes in the cross-sectional structure in the flow direction, which is called the "axis-switching" phenomenon are clearly observed.

In **CHAPTER 4**, by using the mentioned method, measurement of three-dimensional (3D) density distributions of the initial flame kernels induced by spark-ignition of three types of fuel jets from direct injection nozzle has been conducted. The 3D data of initial flame kernel after ignition is of importance to further understanding of the complicated ignition process of the gasoline direct injection (GDI) engine.

In **CHAPTER 5**, experimental and analytical studies have been conducted to obtain the information needed for a deep understanding of the relation between "equivalence ratio" and "refractive index" in the flow fields. A "universal relationship" between a refractive index of a premixed gas of fuel and air and its equivalence ratio has been discovered in this study. Using this relationship, it is possible to measure the equivalence ratio of all the premixed gas from its refractive index only with a unique coefficient, except for the premixed gas of light fuels. The uniqueness of the relation coefficient enables us to obtain the local equivalent ratio distributions of even multi-fuel premixed gas from its refractive index CT measured. This method can be applied to develop gas alarm systems that can be used without knowing the fuel type.

In **CHAPTER 6**, the conclusions are given.

NOMENCLATURE

" In Science, Each New Point of View Calls Forth a Revolution in NOMENCLATURE. "

(*Friedrich Engels*)

A : Cross section area [m^2]

AFR : Air fuel ratio [-]

a_0 : Transparent width of light source image on schlieren stop location when no knife-edge is present (and without any disturbance in the test section) [m]

a_n : Transparent width of light source image on schlieren stop location when knife-edge is present (and without any disturbance in the test section) [m]

B : Brightness of schlieren image [-]

B_0 : Brightness of schlieren image when no knife-edge is present (and without any disturbance in the test section) [-]

B_{nf} : Brightness of schlieren image in no-flame (no disturbance) condition in the test section [-]

B_{nj} : Brightness of schlieren image in no-jet (no disturbance) condition in the test section [-]

b : Nozzle width [m]; rectangular nozzle

b_j : Fully expanded jet width [m]; rectangular nozzle

c : Speed of light in vacuum [m/s]

$C_{i,k,p}$: Overlapped passage area in reconstruction matrix [-]

D : Nozzle exit diameter [m]

D_j : Fully expanded jet diameter [m]

Dt : Density thickness of deviation density [$(kg/m^3)(m)$]; derived value

Dt' : Density thickness [$(kg/m^3)(m)$]; derived value

Dt^* : Density thickness of deviation density [$(kg/m^3)(m)$]; actual value

$DNPR$: Design nozzle pressure ratio ($=P_o/P_e$) [-]

f : Focal length of convergent lens in schlieren system [m]

h : Nozzle height [m]; rectangular nozzle

h_j : Fully expanded jet height [m]; rectangular nozzle

JPR : Jet pressure ratio ($=P_e/P_b$) [-]

K : Gladstone-Dale constant of air [m^3/kg]

L_c : Supersonic core length [m]

L_s : Shock-cell spacing (length) [m]

M_d : Nozzle design Mach number [-]

M_j : Fully expanded jet Mach number [-]

n : Refractive index [-]; derived value

n^* : Refractive index [-]; actual value

n_a^* : Refractive index of ambient gas of air [-]; actual value

n_m : Modified refractive index [-]; derived value, ($n_m = \Delta n_m + n_{ma}^*$)

n_m^* : Modified refractive index [-]; actual value

n_{ma}^* : Modified refractive index of ambient gas of air [-]; actual value

NPR : Nozzle pressure ratio ($=P_o/P_b$) [-]

O_{plm} : Modified optical path length [m]; derived value

O_{plm}^* : Modified optical path length [m]; actual value

P_o : Plenum (absolute, stagnation) pressure [MPa]

P_b : Back pressure [MPa]

P_e : Exit pressure [MPa]

P_G : Gauge pressure [MPa]

R : Radius of reconstruction area [m]

Re : Reynolds number [-]

T : Temperature [K]

T_b : Ambient temperature [K]

v : Velocity [m/s]

x, y, z : Cartesian coordinates system of reconstruction volume [m]

X, Y : Inclined coordinates by angle θ [m]

$y_{i,k}$: Projection data value in CT-reconstruction system

Greek symbols

γ : Specific heat ratio of air [-]

ΔB : Deviation brightness on schlieren image [-]

Δa : The resulting displacement at the schlieren stop location corresponding to deflection of the light beam [m]

Δn_m : Deviation modified refractive index [-]; derived value, ($\Delta n_m = n_m - n_{ma}^*$)

Δn_m^* : Deviation modified refractive index [-]; actual value, ($\Delta n_m^* = n_m^* - n_{ma}^*$)

Δs : Transparent width of light source image on schlieren stop location [m]

$\Delta\rho$: Deviation density [kg/m^3]; derived value

$\Delta\rho^*$: Deviation density [kg/m^3]; actual value, (Supersonic jet: $\Delta\rho^* = \rho^* - \rho_a^*$, Flame: $\Delta\rho^* = \rho_a^* - \rho^*$)

δ : Boundary layer thickness of supersonic jet [m]

θ : Angle of observation, Angle of incidence [° (degree)]

λ^m_j : CT-reconstructed value in one pixel in reconstruction matrix

ρ : Density [kg/m^3]; derived value, (Supersonic jet: $\rho = \Delta\rho + \rho_a^*$, Flame: $\rho = \rho_a^* - \Delta\rho$)

ρ^* : Density [kg/m^3]; actual value

ρ_a^* : Ambient density of air [kg/m^3]; actual value

ρ_{ref} : Reference density [kg/m^3]

φ : Equivalence ratio [-], Elevation angle [° (degree)]

Subscripts

a, b : Ambient value

e : Nozzle exit

i : Pixel position number in projection data

j :Fully expanded jet condition, Pixel position number in reconstruction matrix

k : Number of directional projection data

m : Modified value of refractive index

n : No disturbance condition in the test section

o : Plenum chamber value (stagnation condition)

p : Overlapped pixel in the passing beam path

Superscripts

m : Iteration number in CT-reconstruction system

Table of Contents

1

CHAPTER 1

Background

Experimental Method and Apparatus Setup

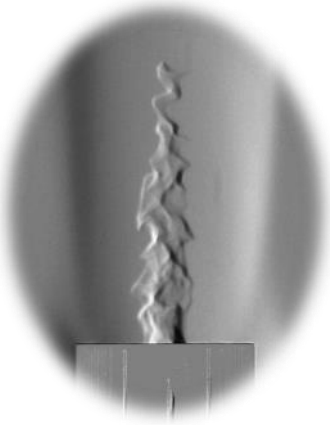

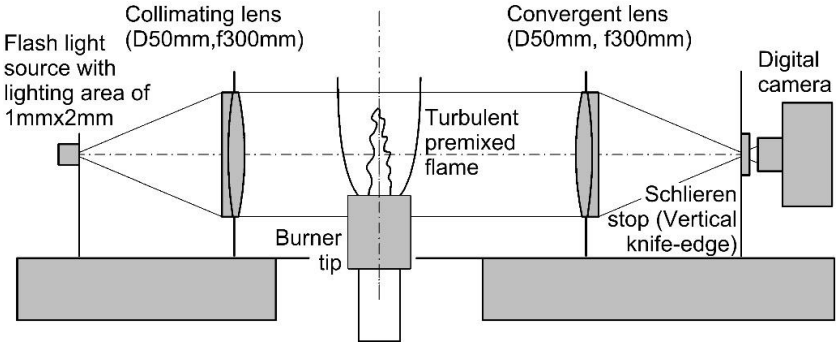

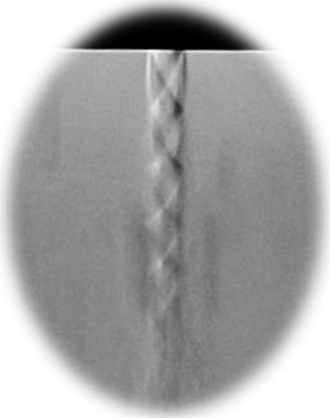

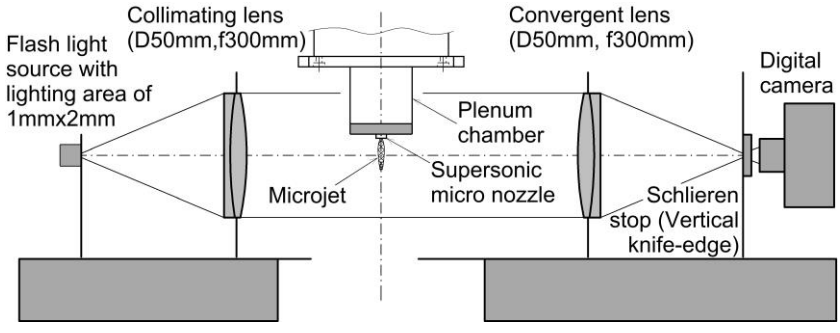

CHAPTER 1
BACKGROUND: METHOD AND APPARATUS SETUP

1.1. Schlieren Imaging and Flow Visualization

Visual observation and investigation of a fluid flow provide useful and comprehensive insight into the flow field under inspection and can derive quantitative data from observed flow patterns. Mostly fluids are transparent and therefore invisible, but there are some good techniques that can visualize the flowing fluids with non-uniform density. Schlieren technique is very sensitive to density change and can visualize invisible flows (the optical inhomogeneities) in transparent media like air, water, and glass. It has been widely implemented in fluids and combustion. In combustion, having information for the flame development and the mixture formation of fuel and air is very useful for deep understanding and analysis of the ignition systems. In fluid dynamics, schlieren imaging and technique is a common tool, with this technique, air flows, shock wave, compression and expansion fans in supersonic jet flows can be depicted very detailed for uses in aero-dynamical studies and can visualize invisible flow [1]. Recently, this technique is reviewed in [2] and is shown that schlieren photography has been developed from a qualitative visualization method into a quantitative measurement method. Also, this method for flow visualization does not require the introduction of additives into the flow field [3] and is capable of providing useful qualitative and quantitative schlieren system information on the variations in fluid density, temperature, and static pressure.

1.2. The Previous Works

In the daily activities of today's world, human's attention and desire to use available energy and resources in the best manner. Therefore, accurate and deep knowledge of existing phenomena is necessary. In the Department of Mechanical Engineering of the Nagoya Institute of Technology under the Energy Field an innovative schlieren 3D-CT technique made and developed. Using this method to investigate and understand complex flow structures and phenomena which are impossible to study analytically and the experimental results can be served as validation data for numerical simulations.

In previous studies [4][5][6][7][8][9][10], by employing and developing a non-scanning three-dimensional computerized tomography (3D-CT) technique using a delicate multi(20)-directional quantitative schlieren optical system with a flashlight source, the following measurements have been successfully obtained:

(a) Measurement of a local burning velocity of a turbulent premixed flame [4],

(b) Measurement of light-emission distributions of premixed flames [5],

(c) Measurement of instantaneous 3D density distributions of high-speed premixed turbulent flames [6][7][8],

(d) Measurement of 3D density distributions of a steady non-axisymmetric premixed flame [7] and

(e) Measurement of instantaneous 3D density distributions of spark-ignited premixed spherical flame kernels in laminar and turbulent flows [9][10].

1.3. The Present Works

The present study is performed for a 3D (three-dimensional) measurements of instantaneous density distributions of non-uniform density field of a fluid phenomenon by CT (computerized tomography) method (3D-CT non-scanning technique), using the multi(20)-directional quantitative schlieren optical system.

In the present study, the Intel FORTRAN program is used to implement CT-reconstruction and process the different data obtained by the schlieren optical system.

The current work is categorized into the four main sections;

I. Introducing two new techniques (chapter 2), (1) a new "inverse process" technique to obtain vertical schlieren brightness gradient from horizontal experimental data and (2) a novel "multi-path integration" technique for image-noise reduction [11][12][13]. The mentioned techniques are reported in a journal and international conferences and they were very interesting and welcomed and received medal and two best paper awards from the American Society of Thermal and Fluids Engineers (ASTFE)[1] and the Visualization Society of Japan (VSJ)[2].

II. Investigation of perfectly and imperfectly expanded circular and square supersonic microjets (chapter 3) [14].

III. Measurements of density distributions of spark-ignited flame kernels in propane/air-fuel jets issuing from the direct injection nozzle (chapter 4) [15].

IV. Measurements of instantaneous "modified refractive index" of a dual-fuel premixed gas flow of two jets and introducing a "universal relationship" between a "refractive index" of a premixed

[1] https://www.nitech.ac.jp/honor/2019/best-research-paper-awardwo2019.html

[2] https://www.vsj.jp/vsjinfo/recognition/recognition30.html

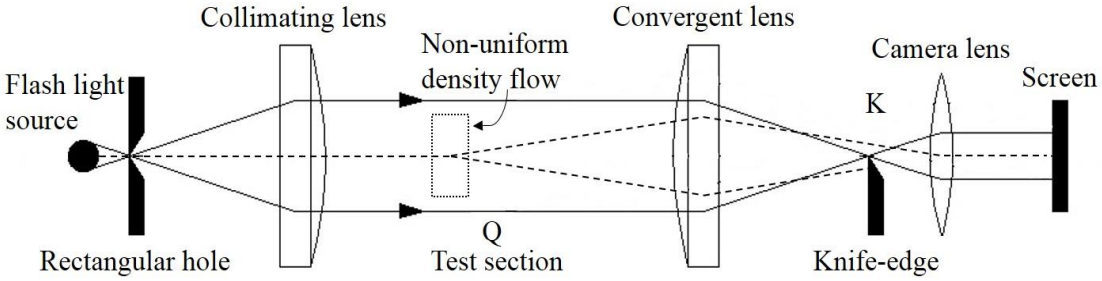

Fig. 1.1 Schematic diagram of the quantitative schlieren optical system.

gas of fuel and air and its "equivalence ratio" (chapter 5) [16].

Schlieren photography visualizes the pressure (category (II), chapter 3) and temperature (category (III), chapter 4) gradients. In other words, the schlieren method is sensitive to changes in the refractive index of the medium (category (IV), chapter 5), while caused by thermal or pressure gradients.

1.4. The Basic Principle of Schlieren Optical System

"Schlieren" is originally from the German word "Schliere" which means "streak" in the English language. "Schliere" denotes optical inhomogeneity in a transparent medium that causes an irregular light deflection. The conventional schlieren technique, for the first time in German physicist August Toepler's book (1864) is discussed in detail and became widely known. This method uses only a single beam of light, which finds applications for visualizing the flow in combustion problems and high-speed flows involving shocks where the gradients in the refractive index are large.

A schematic diagram of the schlieren imaging technique in one direction is shown in Fig. 1.1. Light from the light source passes the hole. The first (collimating) lens produces a parallel beam that passes through the test section Q because the hole is placed at the focal point of the first lens. The second (convergent) lens forms an image at the focal point K where the knife-edge is located. However, density gradients arising in the test section lead to beam deflection shown by dashed lines in Fig. 1.1.

A key element in the schlieren arrangement is the knife-edge. It is an opaque sheet with a sharp edge made from a simple razor blade. If the deflected light moves downwards, it is blocked by the knife-edge and the screen is darkened. The screen is suitably illuminated if the deflected light moves up. Accordingly, the knife-edge serves as a cut-off filter for intensity.

An appropriate term that characterizes this process is called contrast (equation (1.1)), measured as the ratio of change in light intensity (brightness) at a point (ΔB) and the initial light intensity (brightness) at that location (B). The initial light intensity (brightness) expresses light intensity without any disturbance in the test section. Therefore, the knife-edge can control contrast in light intensity. The change, in contrast, depends on the initial blockage and hence the initial intensity distribution on the screen. If the initial light beam (undeflected, since no disturbance in the test section) is completely cut-off by the knife-edge, the screen would be dark. Any subsequent beam deflection would illuminate the screen, thus

producing a significant increase in contrast.

$$contrast = \frac{\Delta B}{B}. \tag{1.1}$$

For quantitative schlieren photography, the light beam cut-off 50% by the knife-edge. The cut-off amount determines by using a photodiode. In a schlieren measurement, beam displacement normal to the knife-edge will translate into an intensity variation on the screen. Displacements that are blocked by the knife-edge sheet are not recorded. Similarly, displacements parallel to the knife-edge will also not change the intensity distribution. Knife-edge orientation will reveal directional density gradients.

1.5. Relation Between Refractive Index and Density [1]

In optics, the refractive index *n* defined by the following equation:

$$n = \frac{c}{v}. \tag{1.2}$$

It is a dimensionless number for a material that defines how much light is deflected and how light propagates through that medium, where *c* is the speed of light in vacuum (approximately 300,000 kilometers per second) and *v* is the velocity of light in the medium. Light travels in a vacuum at an approximate speed of *v* = 300,000 km/s, with a refractive index of *n* = 1.0, but decreases to *v* = 225,000 km/s in water (refractive index *n* = 1.3) and in glass to *v* = 200,000 km/s (refractive index *n* = 1.5).

The relation between density and refractive index was proposed as a means of examining gasses (Gladstone, Dale (1864)). This relation is shown in the following equation:

$$n - 1 = K\rho. \tag{1.3}$$

n: refractive index

K: Gladstone-Dale constant [m^3/kg]

(In the present measurement for air, $K = 2.2587\times10^{-4}$ m^3/kg)

ρ: density [kg/m^3]

Therefore, equation (1.3) gives,

$$\frac{\partial n}{\partial x} = K\frac{\partial \rho}{\partial x}. \tag{1.4}$$

1.6. Angle of Refraction

In the schlieren system, obtaining an image is due to the deflection of the light beam in a variable refractive index field towards regions that have a higher refractive index. In order to retrieve quantitative information from a schlieren image, one has to determine the angle of refraction of the light beam ($\Delta\theta$) emerging from the test section into the surrounding air.

If the light beam moves from a medium with refractive index n to one with refractive index $n + \Delta n$, with an incidence angle of θ and a refraction angle $\theta + \Delta\theta$ which is depicted in Fig. 1.2. Variation $\Delta\theta$ of the angle of refraction is determined as follows. By using Snell's law,

$$\frac{n+\Delta n}{n} = \frac{\sin\theta}{\sin(\theta+\Delta\theta)}. \tag{1.5}$$

Then from the theorem of trigonometric function,

$$\frac{n+\Delta n}{n} = \frac{\sin\theta}{\sin\theta\cos\Delta\theta + \cos\theta\sin\Delta\theta}. \tag{1.6}$$

Since $\Delta\theta$ is very small, then $cos\Delta\theta = 1$ and $sin\Delta\theta = \Delta\theta$,

$$1+\frac{\Delta n}{n} = \frac{1}{1+\Delta\theta\dfrac{\cos\theta}{\sin\theta}}. \tag{1.7}$$

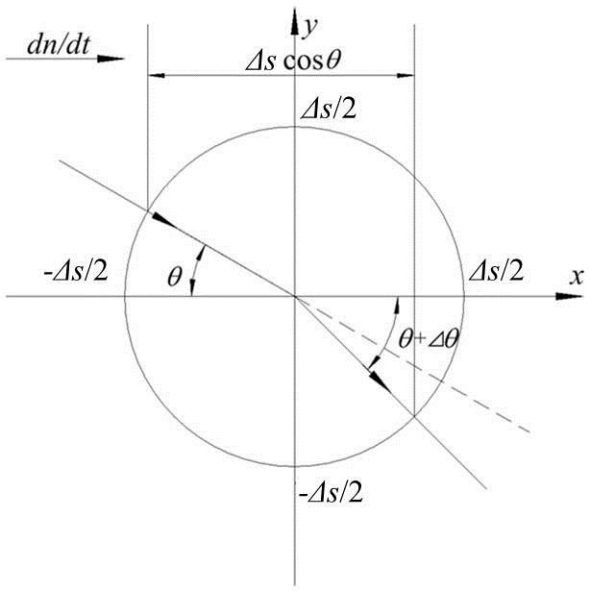

Fig. 1.2 Schematic diagram of refraction of light beam.

Therefore, equation (1.7) gives,

$$1+\Delta\theta\frac{\cos\theta}{\sin\theta}+\frac{\Delta n}{n}+\frac{\Delta n}{n}\Delta\theta\frac{\cos\theta}{\sin\theta}=1. \tag{1.8}$$

For small values of $\Delta\theta$ and Δn, the last term in the left-hand side of the equation (1.8) is approximated zero,

$$\Delta\theta\frac{\cos\theta}{\sin\theta}+\frac{\Delta n}{n}=0. \tag{1.9}$$

Then, equation (1.9) gives

$$\Delta\theta=-(\frac{\sin\theta}{\cos\theta})\frac{\Delta n}{n}. \tag{1.10}$$

From Fig. 1.2, for small value of $\Delta\theta$, it is straightforward to derive the following equations (1.11) to (1.13),

$$\frac{\Delta n}{\Delta x}=\frac{dn}{dx}, \tag{1.11}$$

$$\Delta x=\Delta s\cos\theta, \tag{1.12}$$

and

$$\Delta n=\frac{dn}{dx}\Delta s\cos\theta. \tag{1.13}$$

Finally by combining the equation (1.10) and equation (1.13), it can be found the equation for the variation $\Delta\theta$ of the angle of refraction,

$$\Delta\theta=-\frac{1}{n}\left(\frac{dn}{dx}\right)\Delta s\sin\theta. \tag{1.14}$$

When deforming the traveling direction of the light beam in the $\vec{s}$ direction, then the angle of refraction can be expressed as,

$$\Delta\theta = -\frac{1}{n}\left(\frac{\overrightarrow{\Delta s}}{\left|\overrightarrow{\Delta s}\right|}\times\frac{\frac{\overrightarrow{dn}}{dx}}{\left|\frac{\overrightarrow{dn}}{dx}\right|}\right)\left|\overrightarrow{\Delta s}\right|\left|\frac{\overrightarrow{dn}}{dx}\right|. \tag{1.15}$$

Further, the refraction angle when passing through the refractive index medium is not uniform,

$$\Delta\theta = \int \frac{1}{n}\left(\frac{\partial n}{\partial x}\right)ds, \tag{1.16}$$

Since for air $n \cong 1 \rightarrow \frac{1}{n} \cong 1$, then,

$$\Delta\theta = \int\left(\frac{\partial n}{\partial x}\right)ds. \tag{1.17}$$

By combining the above equation (1.17) with equation (1.4), then the angle of refraction can be expressed as,

$$\Delta\theta = K\int\left(\frac{\partial \rho}{\partial x}\right)ds. \tag{1.18}$$

1.7. Quantitative Schlieren System [1][17]

Using a point light source or a slit light source is necessary for the quantitative schlieren system. Consider the system shown in Fig. 1.1. A light source with dimensions $a_s \times b_s$ is kept at the focus of the first (collimating) lens and provides a parallel beam of light that passes the test section.

The dashed lines show the path of the light beam in the presence of disturbances in the test section. The second (convergent) lens, kept at the focus of the knife-edge collects the light beam and passes onto the screen located at the focus of the test section.

If no disturbance is present, the light beam at the focus of second lens would be ideal as shown in Fig. 1.3, with dimensions $a_0 \times b_0$. These are related to the initial dimensions by the following equation,

$$\frac{a_0}{a_s} = \frac{b_0}{b_s} = \frac{f_2}{f_1}. \tag{1.19}$$

Where, f_1 and f_2 are the focal lengths of first and second lens, respectively.

In a schlieren system, the knife-edge kept at the focal length of the second lens is first adjusted, when

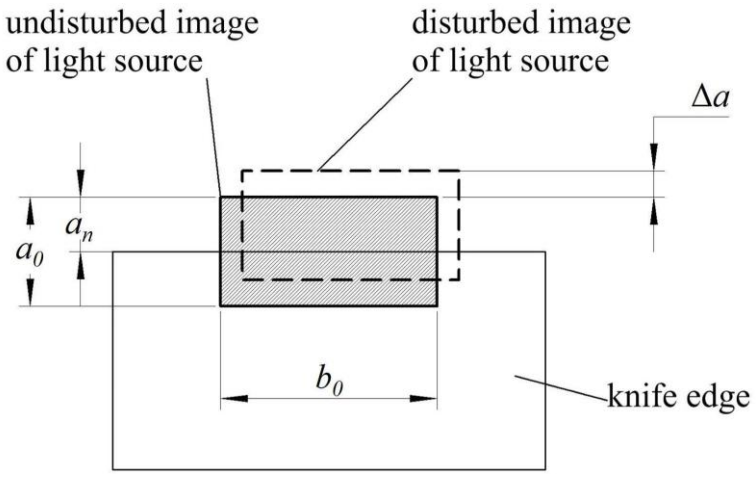

Fig. 1.3 Shift of light source image in the plane of the knife-edge.

no disturbance in the test section is present, to cut off all but an amount corresponding to the dimension a_n of the light beam. Let a_0 be the original size of the light beam, in other words, a_0 and a_n are transparent widths of the light source image on schlieren stop location without and with knife-edge respectively (and without any disturbance in the test section). If the knife-edge is properly positioned, the illumination at the screen uniformly changes depending upon its direction of the movement. Let B_0 be the illumination (brightness) at the screen when no knife-edge is present. The illumination B_n with the knife-edge inserted in the focal plane of the second lens but without any disturbance in the test section will be given by:

$$\frac{B_0}{B_n} = \frac{a_0}{a_n} \Rightarrow B_n = \frac{a_n}{a_0} B_0 \,. \tag{1.20}$$

Let Δa be the deflection of the light beam (resulting displacement) in the vertical direction above the knife-edge corresponding to the angular deflection ($\Delta\theta$) of the beam after the test section experiences a change in the refractive index. Then from Fig. 1.3, Δa can be expressed,

$$\Delta a = f \cdot \tan \Delta\theta \,, \tag{1.21}$$

since $\Delta\theta$ is very small, then $tan\ \Delta\theta = \Delta\theta$, and

$$\Delta a = f \cdot \Delta\theta \,. \tag{1.22}$$

Where, f is the focal length of the second lens. Let B be the final illumination (brightness) on the screen after the light beam has deflected upwards by an amount Δa due to the inhomogeneous distribution of refractive index gradients in the test section. Hence,

$$\frac{B}{B_0} = \frac{a_n + \Delta a}{a_0}. \tag{1.23}$$

The change in the light intensity (deviation brightness) on the screen (on schlieren image) ΔB is given by,

$$\Delta B = B - B_n. \tag{1.24}$$

The relative illumination intensity or contrast can be expressed as,

$$contrast = \frac{\Delta B}{B_0} = \frac{B - B_n}{B_0} = \frac{\Delta a}{a_0}. \tag{1.25}$$

By using equation (1.22), then,

$$contrast = \frac{\Delta B}{B_0} = \frac{f \cdot \Delta\theta}{a_0}. \tag{1.26}$$

Equation (1.26) shows that the contrast in a schlieren system is directly proportional to the focal length of the second lens. Larger the focal length, greater will be the sensitivity of the system. Combining equation (1.18) and equation (1.26), then,

$$\frac{\Delta B}{B_0} = \frac{f}{a_0} K \int \left(\frac{\partial \rho}{\partial x} \right) ds, \tag{1.27}$$

If the knife-edge is rotated by 90º, the deflection angle on *y*-axis will be measured, then,

$$\frac{\Delta B}{B_0} = \frac{f}{a_0} K \int \left(\frac{\partial \rho}{\partial y} \right) ds. \tag{1.28}$$

This equation shows that changes of the relative illumination intensity or contrast in the Toepler's schlieren technique records the average gradient of density or refractive index over the path of the light beam in the directional perpendicular to the knife-edge.

Note, in the present study the light source shape, is a rectangular order to ensure quantitative properties, the light source image is moved by refraction requires a large enough not away from the knife-edge.

1.8. 20-Directional Quantitative Schlieren Method [4]-[16]

In the present study, in the schlieren 3D-CT system, the 3D-CT process requires 2D distributions (images) of the "density thickness" $Dt'(X(\theta))$, called "projections", which is defined by the line-of-sight-integration of density deviation from ambient gas density. Here the procedure for obtaining the density thickness distribution $Dt'(X(\theta))$ from a schlieren image, is explained as follows.

Density, deviation density and deviation density thickness with an asterisk sign (*) express the actual values and without this sign represent derived values from the CT-reconstruction process.

Figure 1.4 indicates the conversion process of image data and formation of projection image (density thickness) in the proposed schlieren 3D-CT system. Some used expressions in this section and Fig. 1.4 are summarized in Table 1.1. Figure 1.4(a) depicts density distribution $\rho^*(x, y)$ of target flow having an

Table 1.1 The used expressions in Fig. 1.4.

a_0	transparent width of light source image on schlieren stop location when no knife-edge is present (and without any disturbance in the test section)
a_n	transparent width of light source image on schlieren stop location when knife-edge is present (and without any disturbance in the test section)
f	the focal length of convergent lens (second lens)
K	Gladstone-Dale constant for air ($K = 2.2587 \times 10^{-4}$ m^3/kg)
b_0	transparent height of light source image on schlieren stop location
B_0	brightness of schlieren image when no knife-edge is present (and without any disturbance in the test section)
$B(X)$	brightness of schlieren image
$B_{nf}(X)$	brightness of schlieren image in no-flame condition (without any disturbance in the test section)
$\Delta B(X)$	deviation brightness in schlieren image
ρ	density (kg/m^3); derived value, ($\rho = \rho_a^* - \Delta\rho$)
ρ^*	density (kg/m^3); actual value
ρ_a^*	density of ambient air (kg/m^3); actual value
$\Delta\rho$	deviation density (kg/m^3); derived value
$\Delta\rho^*$	deviation density (kg/m^3); actual value, ($\Delta\rho^* = \rho_a^* - \rho^*$)
Dt	density thickness of deviation density [(kg/m^3)(m)]; derived value
Dt'	density thickness [(kg/m^3)(m)]; derived value
Dt^*	density thickness of deviation density [(kg/m^3)(m)]; actual value

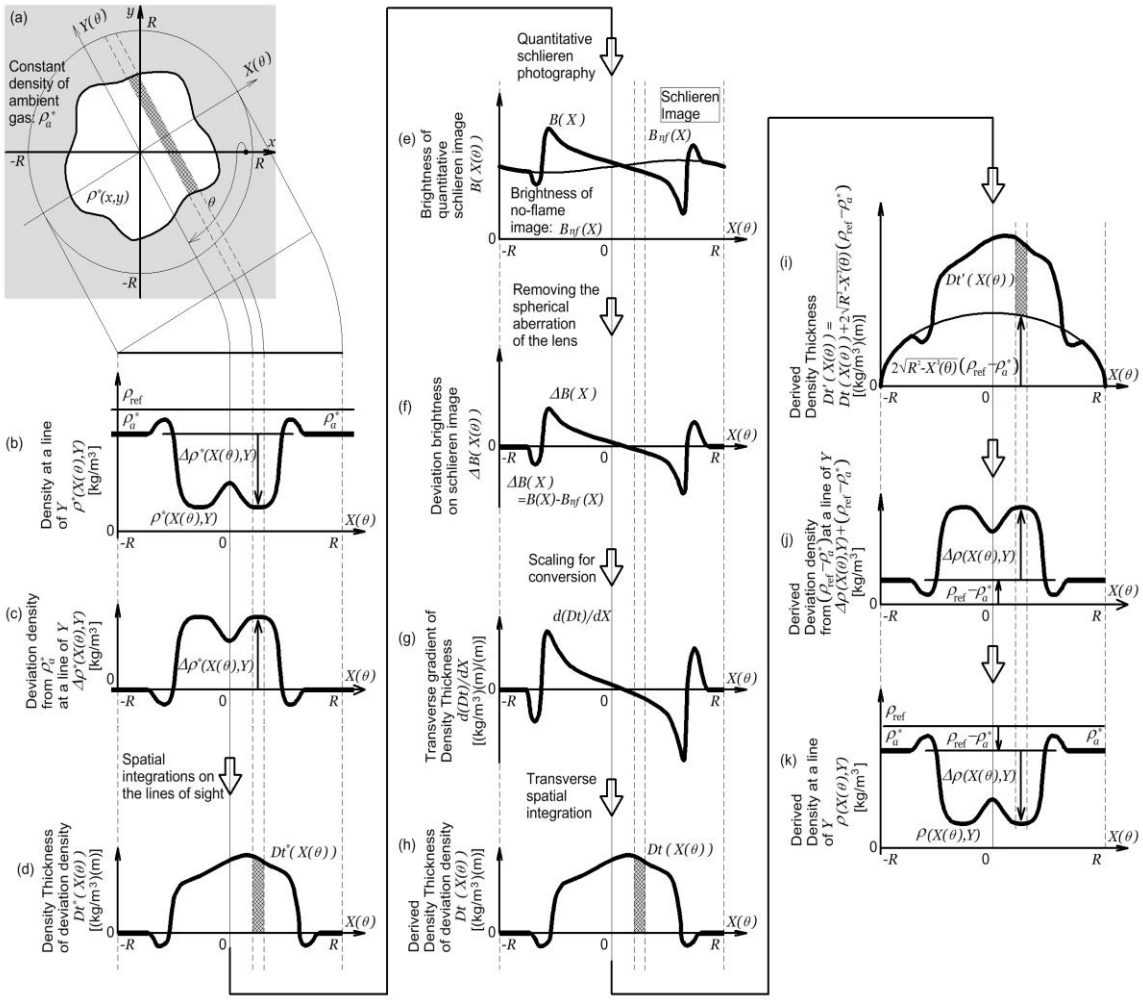

Fig. 1.4 Processes of formation of schlieren brightness and conversion to projections of *Dt'* [4]-[16].

ambient gas (air) region of constant density ρ_a* on peripheral of the observed range of radius R. This configuration is consistent with the characteristics of stand-alone flames.

Figure 1.4(b)-(k) shows observations in the direction of θ from the *x*-axis. The inclined coordinates are denoted by $X(\theta)$ and $Y(\theta)$ as indicated in Fig. 1.4(a). Fig. 1.4(c) gives the deviation density on the line of *Y*,

$$\Delta\rho^*(X(\theta),Y) = \rho_a^* - \rho^*(X(\theta),Y)\,. \tag{1.29}$$

Where ρ_a* is the density of ambient gas (air) and ρ*$(X(\theta),Y)$ is the density of the gas. Because of the lower density of burnt gas, deviation density has a non-negative value in all regions. The deviation density $\Delta\rho$*$(X(\theta),Y)$ is spatially-integrated automatically along the line of sight in schlieren observation, resulting in deviation density thickness Dt*$(X(\theta))$ of Fig. 1.4(d).

In practice for obtaining density thickness (Fig. 1.4(i)), the image processing activity starts from Fig. 1.4(e) by obtaining two sets of images, "with target" and "without target" (without any disturbance in the

test section) with a horizontal brightness gradient in the *x*-direction. Two sets of images present by schlieren observation as $B(X)$ and $B_{nf}(X)$ (brightness of schlieren image in no-flame condition). Brightness of schlieren image $B(X)$ is given as X-directional gradient value of deviation density thickness $Dt^*(X(\theta))$ shifted by brightness of schlieren image in no-flame condition $B_{nf}(X)$, indicated in Fig. 1.4(e).

To obtain the density thickness $Dt'(X(\theta))$ from $B(X)$ and $B_{nf}(X)$, both are processed in the following manners of Fig. 1.4(f)-(h). As indicated in Fig. 1.4(f), deviation brightness in schlieren image $\Delta B(X)$

$$\Delta B(X) = B(X) - B_{nf}(X), \tag{1.30}$$

is scaled to $d(Dt)/dX$ (Fig. 1.4(g)) by next expression

$$\frac{d(Dt)}{dX} = -\frac{a_0}{f \cdot K}\left(\frac{\Delta B(X)}{B_0(X)}\right). \tag{1.31}$$

Where K is Gladstone-Dale constant for air ($K = 2.2587 \times 10^{-4}$ m^3/kg), a_0 is transparent width of the light source image on schlieren stop location and f is the focal length of the convergent lens (second lens). B_0 is the illumination (brightness) at the screen when no knife-edge is present (and without any disturbance in the test section).

Deviation density thickness $Dt(X(\theta))$ is, therefore, reproduced by transverse-integration of $d(Dt)/dX$ from schlieren images, as shown in Fig. 1.4(h).

In addition, deviation density thickness $Dt(X(\theta))$ can be expressed as follows.

$$Dt(X(\theta)) = \int_{-\infty}^{+\infty} \rho(x,s)ds, \tag{1.32}$$

and

$$Dt(X(\theta)) = \int_{-\infty}^{+\infty}\int_{0}^{x} \frac{d\rho(x,s)}{dx}dxds. \tag{1.33}$$

By combining the equation (1.27) and equation (1.33), deviation density thickness can be expressed as follows.

$$Dt(X(\theta)) = \int_{0}^{x} \frac{a_0}{f \cdot K}\frac{\Delta B(X)}{B_0(X)}dx. \tag{1.34}$$

Accordingly, by using this equation, the deviation density thickness $Dt(X(\theta))$ from schlieren image

brightness is calculable. Finally, the "density thickness" $Dt'(X(\theta))$ is obtained by adding the thickness of $(\rho_{ref} - \rho_a^*)$ to the deviation density thickness $Dt(X(\theta))$ on peripheral of the observed range of radius R (Fig. 1.4(i)), as expressed by,

$$Dt'(X(\theta)) = Dt(X(\theta)) + 2(R^2 - X^2(\theta))^{1/2}(\rho_{ref} - \rho_a^*) . \tag{1.35}$$

If, $\rho_{ref} = \rho_a^*$, accordingly, $Dt'(X(\theta)) = Dt(X(\theta))$.

Because in CT-reconstruction calculation, a non-negative value of detection value is recommended, "deviation density" is used instead of "density". As shown in Fig. 1.4(j), using the non-deviation treatment for projections of CT by employing reference density, guarantee which the CT-reconstructed deviation density $(\Delta\rho(X(\theta),Y)+(\rho_{ref} - \rho_a^*))$ is non-negative and CT-reconstruction is possible, this fact is very important for supersonic flows (see chapter 3, Fig. 3.1 and Fig. 3.24, ρ lower than the ambient ρ_a^*).

1.9. 3D-CT (Three-Dimensional Computerized Tomography) Method [4]-[16]

In this investigation, the CT procedure is carried out in each horizontal plane of the z-axis for the reconstruction of deviation density distribution $\Delta\rho(x, y)$ (Fig. 1.4(j)) from linear data set of density thickness $Dt'(X(\theta))$ called "projections", of numerous directions (θ) which is shown in Fig. 1.5. This reconstructed deviation density distribution $\Delta\rho(x, y)$ is converted to 2D density distribution $(\rho(x, y) = \rho_{ref} - [\Delta\rho(X(\theta),Y) + (\rho_{ref} - \rho_a^*)])$ as follows, and ρ_{ref}, in which one step (Fig. 1.4(i)) was added, and this step is again subtracted and removed (Fig. 1.4(k)).

$$\rho(x, y) = \rho_a^* - \Delta\rho(x, y) . \tag{1.36}$$

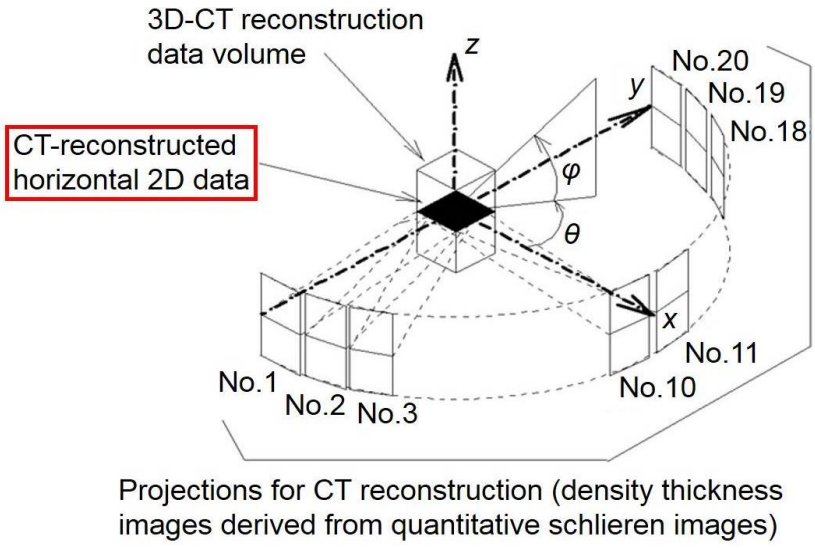

Fig. 1.5 3D-CT (Three-dimensional computerized tomography) non-scanning conceptual diagram.

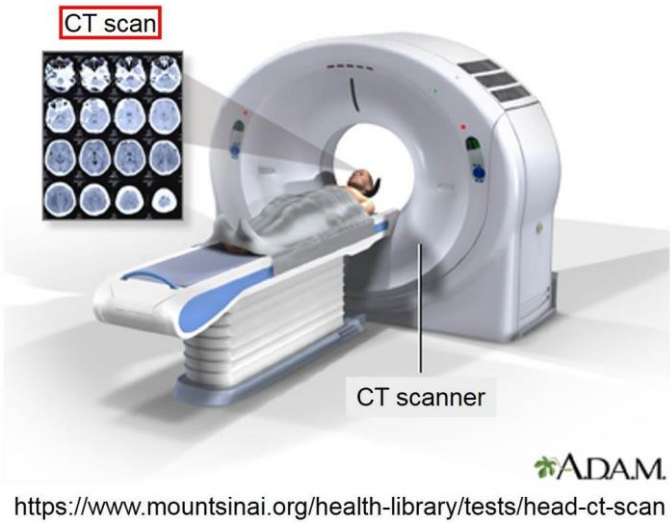

Fig. 1.6 CT-scanner.

The reconstruction was performed cross-section by cross-section and then the cross-sections were stacked to form a three-dimensional density distribution (Fig. 1.5). Therefore, the 2D distributions $\rho(x, y)$ is accumulated in layers to form the 3D-CT distribution $\rho(x, y, z)$.

Generally, CT (computerized tomography) is performed in 2 steps. First data acquisition (record of projections) performs and next image reconstruction from projections. In most cases, one of two types of methods (algorithms) is used in reconstructing images, analytical and iterative algorithms [18]. An algorithm is a step-by-step mathematical procedure to be followed in calculations by a computer.

In this study, the distributed back-projection (DBP) method is used as the CT-reconstruction method. This reconstruction method has been subjected to development as a distribution type of BP (back-projection) method using iterative operation, and it carries out the same processing as the ML-EM method. Therefore, first, describe the ML-EM method referred to as the principle of distributed back-projection method used in this study.

From a technological point of view, this experimental method (CT non-scanning, Fig. 1.5) has a similarity with CT-scanner uses in medical engineering for medical diagnostics (Fig. 1.6). CT-scan combines a series of X-ray images obtained from different angles to produce cross-sectional (tomographic) images of specific areas of a scanned object (human body). In the schlieren 3D-CT (three-dimensional computerized tomography) measurement technique employs schlieren photography (instead of X-ray images) from 20-direction to reconstruct 3D-density distributions data (cross-sectional density distributions) of a target flow.

1.10. ML-EM Method

In the present study, the maximum likelihood-expectation maximization (ML-EM) method [5]-[16] is employed for CT-reconstruction. This reconstruction method is a kind of iterative reconstruction methods. The iterative reconstruction has recently become be attractive as an alternative to conventional filtered

back-projection (FBP) algorithm [19], because of its quantitative capability. ML-EM method is the combination of two following methods.

- The maximum likelihood (ML) method: is an estimation method for the parameters of a statistical model, given observations.
- The expectation-maximization (EM) method: is an iterative method to find (local) maximum likelihood (ML) or maximum a posteriori (MAP) estimates of parameters in statistical models, where the model depends on unobserved latent variables.

The maximum likelihood (ML) estimation method used by maximizing a likelihood function, to estimate the parameters of a probability distribution, so under the assumed model, the observed data is most probable.

First, explain the principle of the ML method. We set λ for the reconstructed value in one pixel (CT value in this study), x for the actually measured brightness value, C for the measurement probability. Here, the measurement probability refers to the probability that the photon emitted from the pixel is measured by the measuring instrument. For example, when, there is an object that absorbs the photon (attenuates the brightness value) between the measured target pixel and the measuring instrument, this probability changes.

Here, assuming that the number of measurements is i times, the maximum likelihood estimation (ML) of λ_{ML} is simply expressed by the following equation (1.37).

$$\lambda_{ML} = \frac{\sum_{i=1}^{n} x_i}{\sum_{i=1}^{n} C_i} . \tag{1.37}$$

However, since brightness exists also in the pixels around the measured pixel, the brightness value detected by the measuring device is obtained by adding the brightness of the peripheral pixels, and the brightness of the measured pixel cannot be measured directly. Therefore, consider the model as shown in Fig. 1.7 and perform maximum likelihood estimation by MAP (maximum a posteriori) estimation.

The MAP estimation is a maximum a posteriori probability estimation, which is a method for estimating the parameters we want to estimate based on a prior numerical value and can be said to be an expansion of ML estimation. In other words, ML is a special case of maximum a posteriori estimation (MAP) that assumes a uniform prior distribution of the parameters.

Here, y_{ij} is the brightness detected (measured projection data) by the j-th detector (pixel) of the detector group i. Thus, y_{11} is considered to be the sum of λ_1 λ_4 λ_7 (when the detection probability is 1).

In this way, x_{ij} is set as the brightness value detected by the j-th detector of the detector group i only by λ_j. When MAP is estimated for x_{ij} in consideration of detection probability, can be expressed by the following equation (1.38).

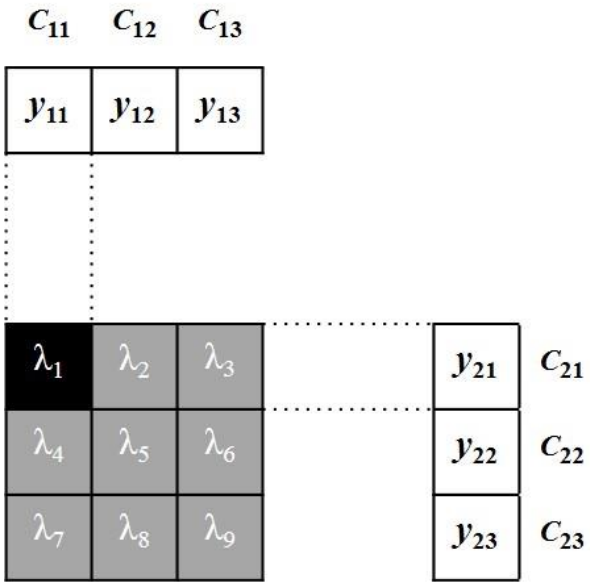

Fig. 1.7 MAP estimation.

$$x_{ij} = \frac{y_i C_{ij} \lambda_j}{\sum_{p=1}^{m} C_{ip} \lambda_p}. \tag{1.38}$$

Therefore, the numerical value of the pixel to be found from the last two equations ((1.37) and (1.38)) is obtained by the ML method as follows.

$$\lambda_j = \frac{1}{\sum_{i=1}^{n} C_{ij}} \sum_{i=1}^{n} \frac{y_i C_{ij} \lambda_j}{\sum_{p=1}^{m} C_{ip} \lambda_p}. \tag{1.39}$$

However, since λ_j also exists on the right-hand side in this formula, the calculation is performed with the initial estimated value as the initial value. It is also necessary to combine successive calculations in which the next estimated value is set as an initial value and calculation is continued.

The expectation-maximization (EM) algorithm is a method for performing maximum likelihood (ML) estimation in the presence of latent variables. The EM (expectation-maximization) method is a procedure of performing sequential calculations until the expected value becomes maximized. In other words, using the obtained and detected probabilities, compare the estimated value of y_{ij} with the actually measured y_{ij}, and terminate the calculation when the difference becomes minimum (until convergence) or when the specified number of calculations is reached.

Therefore, in ML-EM reconstruction, for improvement of reconstruction image λ_j, the iteration is progressed by equation (1.39) and it is suitable to rewrite the equation (1.39) as follows.

$$\lambda_j^{m+1} = \frac{1}{\sum_{i=1}^{n} C_{ij}} \sum_{i=1}^{n} \frac{y_i C_{ij} \lambda_j^m}{\sum_{p=1}^{P} C_{ip} \lambda_p^m} . \tag{1.40}$$

Where, m is the iteration number, $\lambda^m{}_j$ is the pixel value of the reconstructed image at the pixel j for m-th iteration, y_i the measured projection data at i-th pixel, and C_{ij} the detection probability which represents as the overlapped area between i-th ray and pixel j.

This algorithm converges to the maximum likelihood estimate of a probability distribution function from the observed data [20]. All projection data y_i is distributed along the projection beam at the back-projection process. It is, therefore, recommended that this CT method should be referred to as the "DBP (distributed back-projection) method" after the conventional "FBP (filtered back-projection) method".

In the present study, the conventional back-projection image is progressed by twenty ML-EM iterative steps. The emission light is assumed to be a parallel beam for simplification of calculation.

1.11. Distributed Back-Projection (DBP) Method

The most commonly used methods in CT for parallel beam projection data are the filtered back-projection (FBP) methods and the simplest algorithm for reconstruction is the summation method or the back-projection method [19].

The back-projection method is a method of returning the projection data in each projection direction and taking the sum thereof. Therefore, there arises a problem that radial artifacts are tending to be generated by the back-projection beam. Also, if you have a large numerical value in part of the projected area, artifacts due to that value tend to occur. For this reason, a filtered back-projection (FBP) method is widely employed to reduce these artifacts by using a filter. In other words, can remove blurring by applying a convolution filter. However, it is difficult to reduce artifacts unless the filter is properly selected, and also the reduction of radial artifacts is difficult.

Therefore, in this study, by extending the BP (back-projection) method as a distributed back-projection (DBP) method by iterative calculation, this distributed back-projection method is used. It is possible to process equivalent to the ML-EM method with the passing volume of the back-projection beam as the detected probability.

In the distributed back-projection method, the calculation is based on the back-projection beam, and it is easy to deal with refraction and reflection of beam and extension to three-dimensional CT-reconstruction. The suitability of the distributed back-projection method is that one projection data value can be appropriately distributed and arranged in the beam path direction with respect to all reconstruction pixels through which the back-projection beam passes.

To explain the operation of the distributed back-projection method, consider the (m + 1)-th iteration in the two-dimensional reconstruction system as shown in Fig. 1.8. Assume that the reconstructed CT value

distribution λ^m_j is given to each reconstruction matrix (j = 1, 2, 3… J), as a result of iteration m times.

Let us consider the distribution of the data value $y_{i,k}$ of the i-th pixel of the k-th direction projection data. The product of the passage area $C_{i,k,p}$ and the reconstructed CT value $\lambda^m{}_{j\,i,k,p}$ is calculated for all the reconstruction pixels ($j_{i,k,p}$ is the address of the p-th $P_{i,k}$ pixel which the beam passing through it from the i-th pixel of the k-th direction projection data) through which the back-projection beam from the pixel passes, and the projection data value $y_{i,k}$ is distributed at a proportional quantity to it.

The distribution amount is expressed by the following equation (1.41),

$$\Delta\lambda^{m+1}_{j_{i,k,p}} = y_{i,k}\left(\frac{C_{i,k,p}\lambda^m_{j_{i,k,p}}}{\sum_{p=1}^{P_{i,k}}\left(C_{i,k,p}\lambda^m_{j_{i,k,p}}\right)}\right). \qquad (1.41)$$

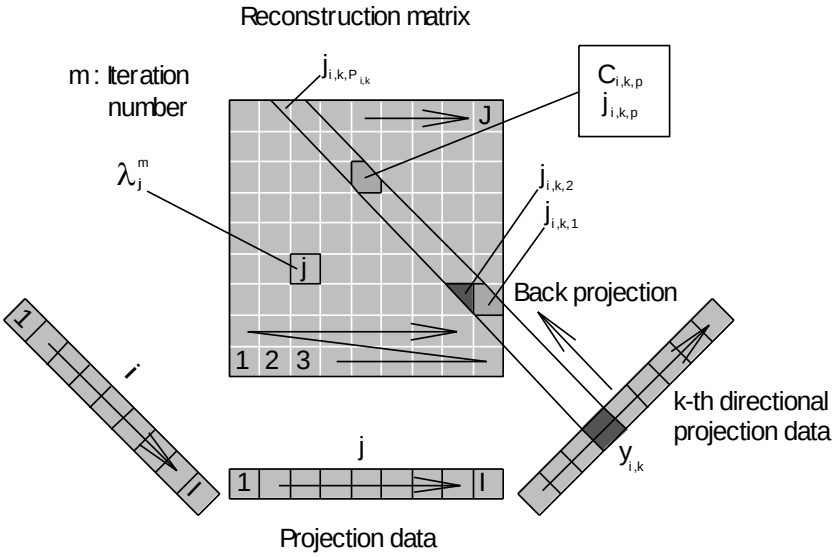

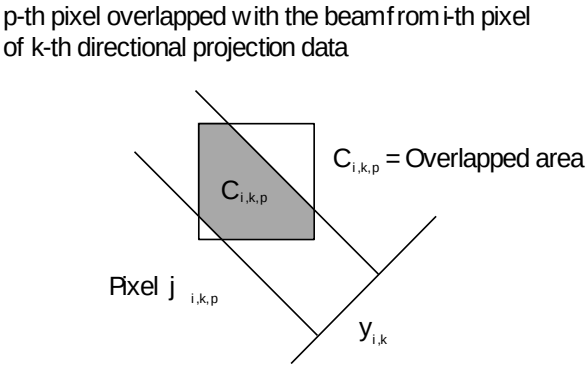

Fig. 1.8 Notation and coordinate system for ML-EM (distributed back-projection) method.

By performing this distribution for all the back-projection beams (k = 1, 2, 3… K, i = 1, 2, 3… I), the reconstructed CT distribution λ_j^{m+1} (j = 1, 2, 3… J) after m iterations is completed. Distribution accuracy improves by iterative operation. Distribution arrangement of projection values in the beam direction which could not be achieved by the BP method and FBP method is achieved by introducing the effect of the projection value in the other direction through the previous reconstructed CT distribution value. The distributed back-projection method is a processing system of the back-projection system, so refraction and reflection of the beam can be taken into consideration and it can be applied to the analysis of engine combustion process in cylindrical glass, etc. For the same reason, the extension to three-dimensional CT-reconstruction does not cause any problem in principle. Also, unlike the BP method and the FBP method, it is notable that radial artifacts do not occur, and the reconstructed value is quantitative. The numerical simulation of a circular "phantom (virtual) image" as a flame front shape is employed to test the ML-EM algorithm, for the different number of projection directions. The proper reconstruction can be obtained in the case of 20 directions and more [7].

1.12. Projection and Back-Projection Types

In 3D-CT measurement, first, the target flow is photographed or measured from multiple directions. The obtained data for each direction called "projection". The CT-reconstruction result is obtained by the

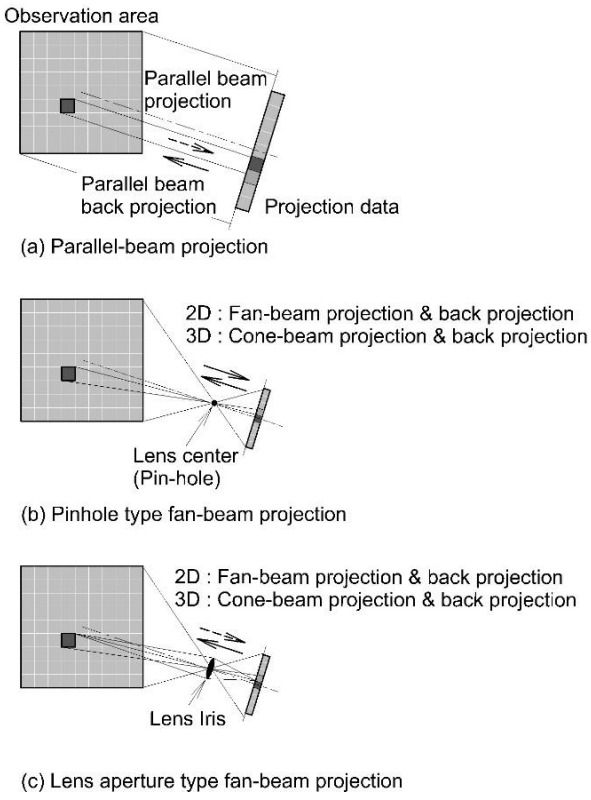

Fig. 1.9 Explanatory drawing of projection and back-projection type (horizontal cross-section).

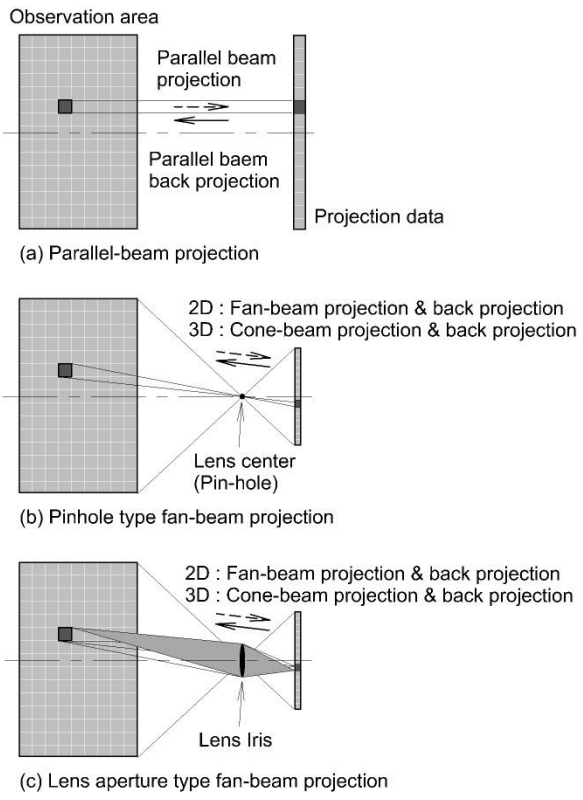

Fig. 1.10 Explanatory drawing of projection and back-projection type (vertical cross-section).

"back-projection" process from the obtained "projections" data to the reconstruction matrix. There are three main methods for such projection and back-projection process, which called parallel-beam, fan-beam, and cone-beam type. Figures 1.9 and 1.10 show the explanatory views of the horizontal and vertical cross-sections of these three methods.

Figure 1.9(a) shows the projection beams are parallel (parallel-beam type), in the case of obtaining horizontal cross-section by CT-reconstruction. This type can be set for the transparent CT method. Figures 1.9(b) and (c) show the two types (fan-beam and cone-beam type) required for complex analysis of the radial CT method. It is called a fan-beam type because the beams spread in a fan shape. However, when the projection beams are managed in three dimensions, it is called a cone-beam type.

Consider the aperture area of the lens, therefore, ray tracing is required for the total luminous flux passing through the lens aperture as shown in Fig. 1.9(c), but in this study, a pinhole lens approximation as shown in Fig. 1.9(b) is used for simplification.

Figure 1.10(a) shows the projection beams are parallel (parallel-beam type), in the case of obtaining vertical cross-section by CT-reconstruction. As shown in Fig. 1.10(a), for projection within a vertical cross-section, the information of each height cross-section becomes independent. Therefore, by applying "two-dimensional stacked three-dimensional CT analysis", first, the "two-dimensional (2D) distributions" (horizontal cross-sections) are accumulated in layers to form the three-dimensional (3D) CT-reconstruction distributions, and then the vertical cross-sections can be applied. On the other hand, since the radial CT method uses a lens as shown in Fig. 1.10(b) and Fig. 1.10(c), it is necessary to perform "complete three-dimensional CT analysis" to treat the beam as a cone-beam in this method. However, if the lens is installed far enough or if a telecentric optical system is used, the same treatment as in Fig. 1.10(a) can be performed, but in either case, the amount of light is significantly reduced.

1.13. Area Calculation for CT-Reconstruction Matrix

In 3D-CT measurement, the reconstruction results are obtained by back-projecting all the projections data from multiple directions to the reconstruction area. The projections data can be obtained by the analysis of the target flow images from multiple directions photography system. In order to properly distribute the back-projection beam, the volume in the beam path direction of the entire reconstruction area through which the beam passes is calculated, and the projection data value is distributed by the ratio of the volume and the reconstruction CT value of the voxel. Therefore, it is necessary to obtain the volume accurately in order to perform distribution back-projection with higher accuracy. However, since it can be treated as a reconstruction in a parallel-beam in the imaging of the 20-direction schlieren optical system, the reconstruction performed by applying "two-dimensional stacked three-dimensional CT analysis", as described in the previous section.

However, if the area passed by all the parallel-beams be calculated for the reconstructed area, the calculation load becomes large and the calculation time becomes long in the CT-reconstruction process. Therefore, in order to reduce the calculation load, the characteristics of the experimental equipment are

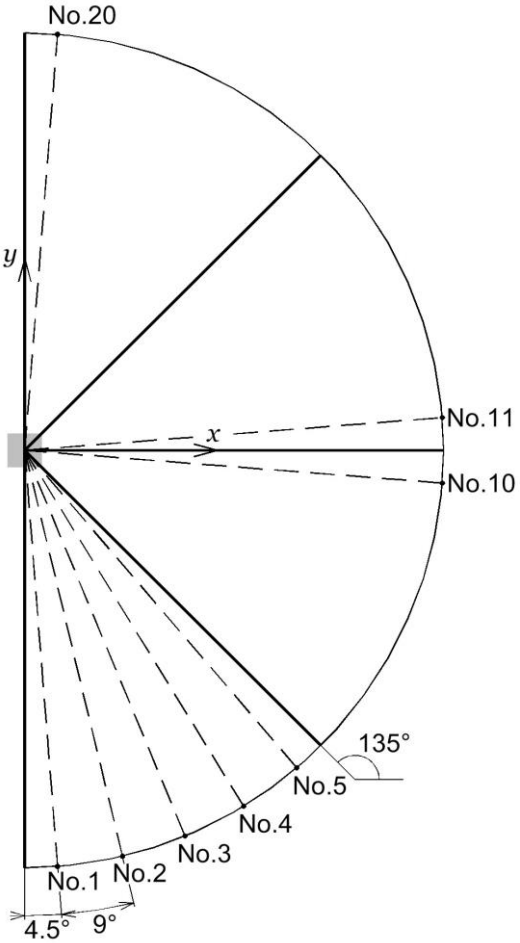

Fig. 1.11 Lens position symmetry and reconstruction area.

utilized and proportionality is employed for the symmetrical areas.

In the quantitative schlieren 3D-CT reconstruction system images obtained from 20 directions, and as shown in Fig. 1.11, the back-projection beam can be set for the central reconstruction target area. Normally, it is necessary to find the area through which the entire beam passes for the voxels in the reconstructed region for all lenses, but the symmetry between lenses is utilized. In this case, the calculation for lens No.1 to No.5 is sufficient, because lens No.1 and lens No.20 have symmetry with respect to the *x*-axis. In addition, since the reconstruction target area is square, lens No.1 and lens No.10 have symmetry with respect to the area through which the back-projections beams pass with respect to

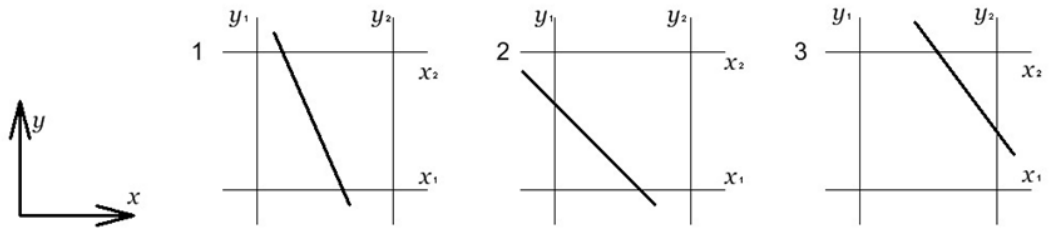

Fig. 1.12 Relationship between the back-projection beam and horizontal reconstruction area.

the intermediate axis as shown in Fig. 1.11. Also, since lens No.10 and lens No.11 have symmetry with respect to the *x*-axis, it can be said that lens No.11 has symmetry with lens No.1.

In other words, lens No.(11 – *n*), No.(10 + *n*), and No.(21 – *n*) have a positional relationship with respect to the reconstruction area compared to any *n* lens among the lenses No.1 to No.5 (*n* = 1, 2, ..., 5). In addition, the area through which the back-projection-beam passes is also equal. Therefore, it can be said that if the area is calculated for lens No.1 to the lens. No.5, it can be applied to the passing area of other lenses. The beam from lens No.1 to lens No.5 in this study is 94.5° to 130.5° with respect to the *x*-axis as shown in Fig. 1.11.

The back-projection beam from the pixels in the projection data that passes through the cells in the reconstruction area makes boundaries for the cells in the reconstruction area. This boundary line can be classified for each cell as shown in Fig. 1.12, depending on how the beam passes. In the classification here is present which side of the cell forms the boundary, and the angle of the boundary line is not specified.

Similarly, considering the incident angle of the back-projection beam, the positional relationship between the cell boundary and the cell, and the polygon formed from the cell boundary can be patterned as shown in Fig. 1.13. The first digits in the numbers of the patterns are corresponding to the left border of the back-projection beam that divides the pixels, and the second digits in the numbers are corresponding to the border on the right, based on the classification of Fig. 1.12. From the positional relationship shown in Fig. 1.11 and the relationship between the pixel size in the projection data and the voxel size of the reconstruction area, in addition to this, there is no other patterns exist as shown in Fig. 1.13 in this study. These polygons can be divided into rectangles and right triangles as shown in Fig. 1.14, and the area is calculated using these divisions for simplification of calculation.

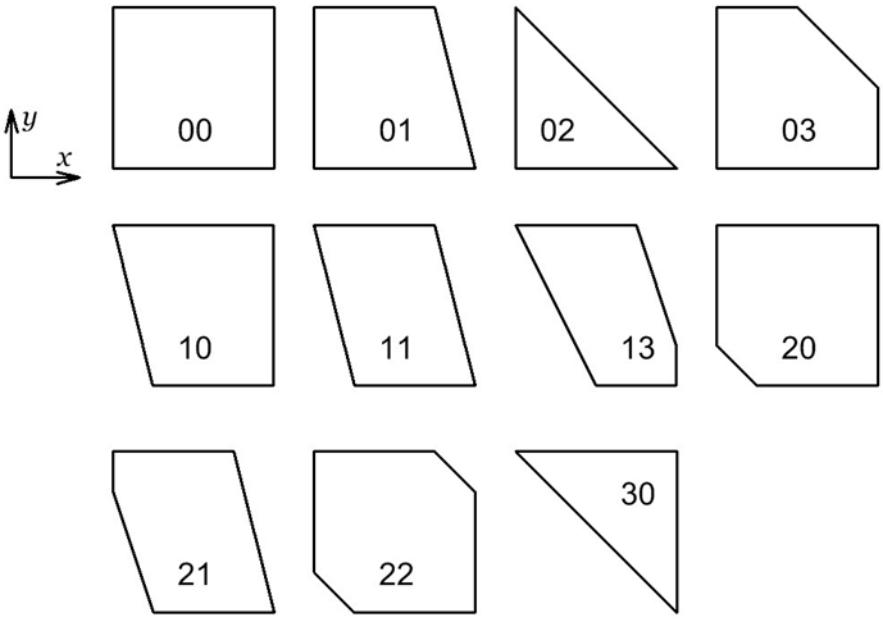

Fig. 1.13 Horizontal cross-section polygonal pattern formed in the reconstruction area.

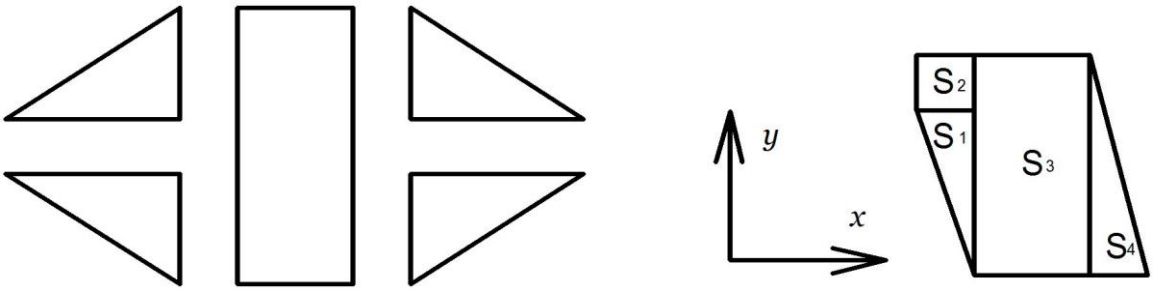

(a) (b)

Fig. 1.14 Polygon triangulation, (a) Dividing elements pattern, (b) Example of polygon division.

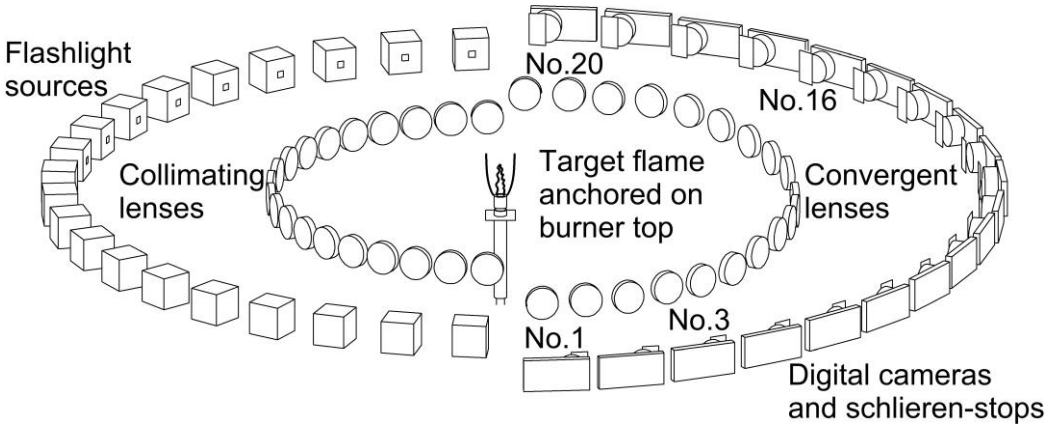

Fig. 1.15 Schematic of 20-directional schlieren photography.

1.14. Multi(20)-Directional Quantitative Schlieren Photography

The multi-directional schlieren optical system shown in Fig. 1.15 is designed as a combining system for the quantitative schlieren method described previously and the 3D-CT (three-dimensional computerized tomography) method.

Fig. 1.15 to Fig. 1.17 illustrates the concept of a 20-directional schlieren camera. In the camera system, the target flame/non-uniform density field is observed from 180° direction using numerous schlieren optical systems simultaneously from θ = –85.5° to +85.5° at an interval of 9°. The target flow/non-uniform density field places as the center for the first lens and the second lens which are located around the target flow. Then, the schlieren stops of vertical knife-edges and the flashlights are installed in a position equal to the focal length of the lens in the circumferential direction. The photographing cameras are installed behind the knife-edges.

As shown in Fig. 1.16, the center of the target flow nozzle exit has been selected as an origin of *xyz*-coordinate system. The *z*-axis is set vertically upward and the *x*-axis and the *y*-axis are orthogonal to

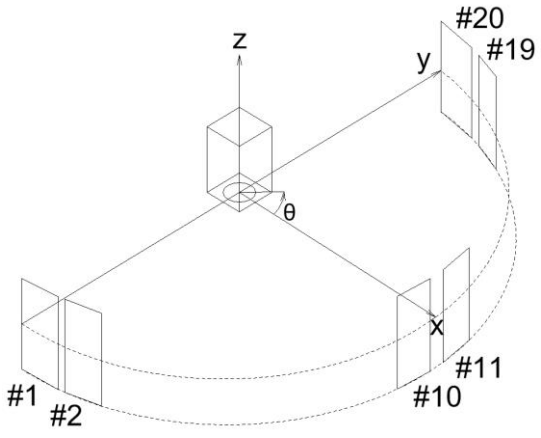

Fig. 1.16 Coordinate system of 20-directional schlieren photography.

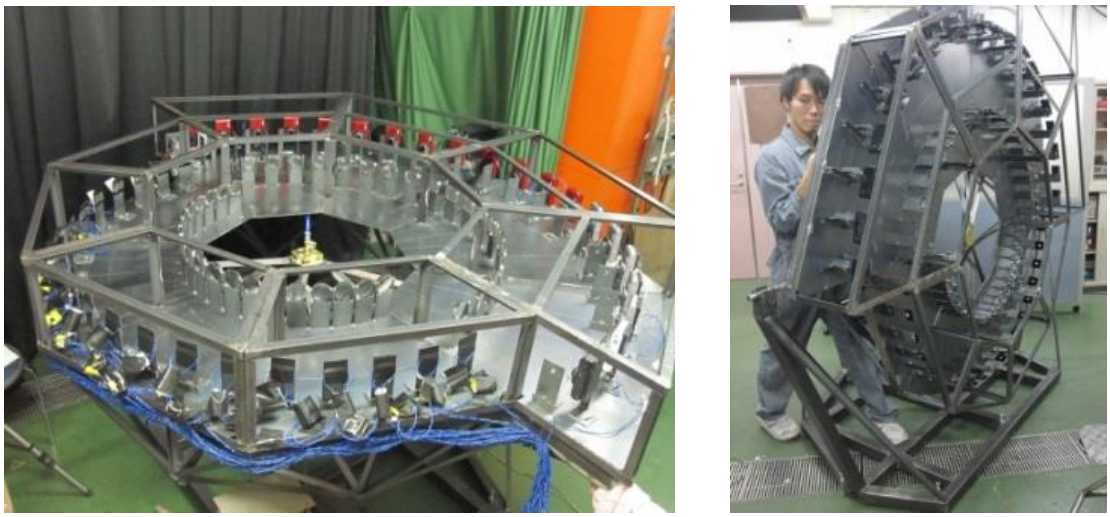

(a) Horizontal position (b) Vertical position

Fig. 1.17 The 20-directional schlieren camera system.

each other in the horizontal plane. The *x*-axis is located between camera No.10 (θ = −4.5°) and camera No.11 (θ = +4.5°). Here angle θ is defined as the horizontal angle from *x*-axis, and counterclockwise as viewed from the top is positive. Twenty camera systems capture the multi-directional views in the 20 angle positions from θ = −85.5 to 85.5 degree at interval of 9 degree (Camera No. 1: θ = −85.5°, No. 2: θ = −76.5°, No. 9: θ = −13.5°, No. 10: θ = −4.5°, No. 11: θ = +4.5°, No. 12: θ = +13.5°, No. 19: θ = +76.5°, No.20: θ = +85.5°).

In order to measure the instantaneous density distribution by multi-directional quantitative schlieren 3D-CT method, a multi-schlieren optical system was actually fabricated. The mentioned system is shown in Fig. 1.17. According to the angle of the target flow, this system can freely set the horizontal angle as well as the vertical angle as shown in Fig. 1.17(a) and Fig. 1.17(b) respectively. In the present study, the camera position is set to the horizontal position and is located in ambient air of the density ρ_a* = 1.2

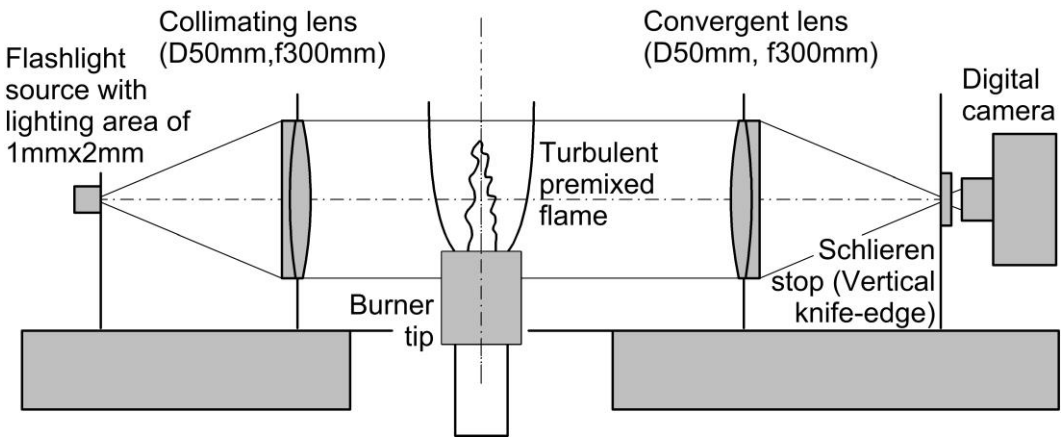

Fig. 1.18 Single unit of quantitative schlieren optical system of the multi-directional schlieren camera.

kg/m^3. The maximum length of the camera system from side to side is about 215 cm. Fig. 1.18 depicts the single unit of quantitative schlieren system in the multi-directional schlieren camera. The center of the flashlights, lenses, knife-edges, and cameras are located 10 cm above the holding surface and 115 cm above ground level. The position of the cameras, knife-edges, and flashlights are adjustable in the 20 camera system. The details of each part are described in the following subsections.

1.15. Flashlight

The light unit has a flashlight source of a uniform luminance rectangular area. Both the uniformity of the luminosity and the definite shape are essential for a quantitative schlieren observation. Just ahead and attached to the light source, a rectangular slit is installed which controls the size of the lighting area. As shown in Fig. 1.19 the rectangular slit is made from a simple razor blade attached to an opaque plate. The opaque plate restricts the light just to the rectangular slit. The specifications of the flashlight used in the multi-directional schlieren optical system are shown below.

Flashlight specifications

Type:	Xenon flash lamp
Condenser capacity:	3.3 μF
Luminance time:	35 μs
Charging time:	30 seconds
Light source shape and size (slit):	Rectangular, 1 mm (width) × 2 mm (height)
Distance to lens:	30 cm

The luminance time of the flashlight is very short and fast, so it is suitable for such phenomena to take place fast like unsteady flows (for example turbulent flames) and supersonic flows. In addition, the flashlight has different emission time and emission intensity (radiance) depending on the condenser

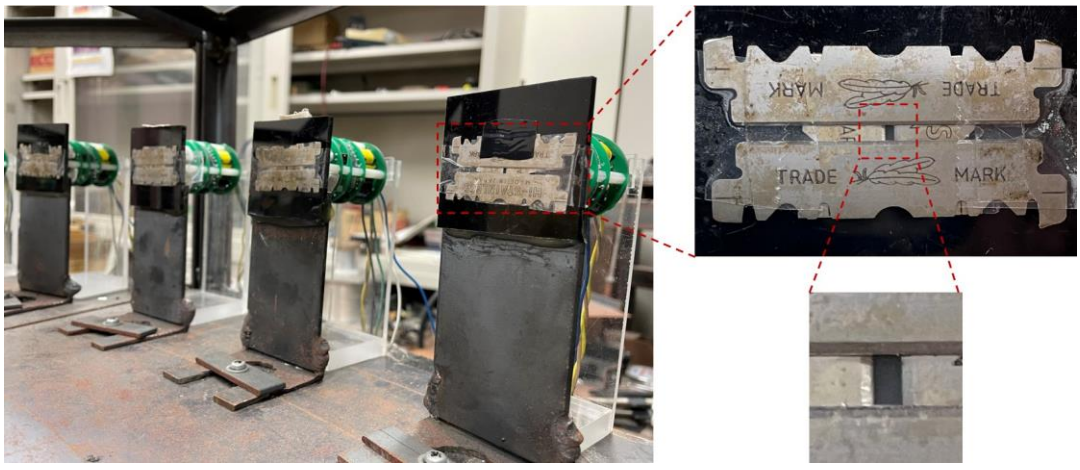

Fig. 1.19 Rectangular slit made from a simple razor blade for the flashlight unit.

capacity and charging time. Therefore, in order to have the light emission time and the light emission intensity (radiance) uniform, the light emission is made with a constant charging time, as well as the batteries should have sufficient charge which use in the switch box. Accordingly, the procedure for quantitative schlieren photography is briefly shown.

Step 1: Discharge the flash lamp and wait 30 seconds.

Step 2: Perform shooting (photographing).

1.16. The First and Second Lens

The same lens is used for the first (collimating) lens and the second (convergent) lens. The lens specifications are shown below. (distance: first lens to center = 37 cm, second lens to center = 57 cm)

Lens specifications

Type:	Plano convex achromatic lens
Focal length:	300 mm
Lens diameter:	50 mm

1.17. The Schlieren Stop (Knife-Edge)

Some deflected rays of light based on the density gradient do not pass through the focal point but is stopped by the schlieren stop (refer to section 1.4). The vertical knife-edge is used as a schlieren stop. The knife-edge orientation will reveal directional density gradients (Fig. 2.3 and Fig. 2.5). In our schlieren optical system the vertical knife-edge located from left to right as shown in Fig. 1.20. First, the knife-edge must adjust to find the right position to place it between camera and lens. Therefore, the knife-edge should be carefully moving back and forward to ensured it positioned at the focus of the second lens, by comparing the results on the camera screen.

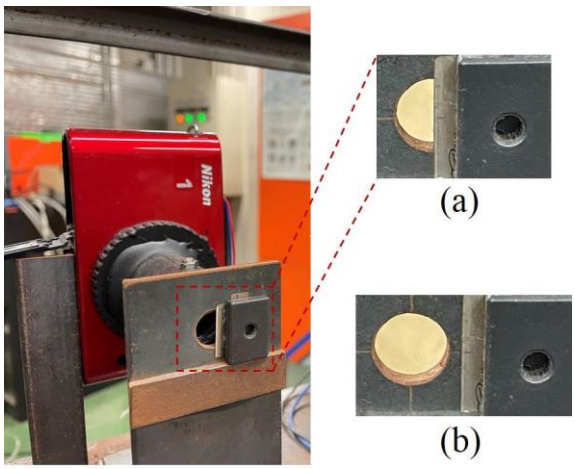

Fig. 1.20 Schlieren stop (vertical knife-edge) made from a simple razor blade, (a) with, (b) without, positioning to cut-off the light beam.

Schlieren stop specifications

Type:	Simple razor blade
Orientation:	Vertical from left to right
Light blocking width:	0.5 mm (the light beam cut-off 50% (refer to section 1.23, Weber ratio) that percentage determines by a photodiode, light source width = 1 mm)
Distance to lens:	30 cm

1.18. Digital Camera

Fig. 1.21(a) shows the camera which is installed in the 20-directional schlieren photography system. The digital camera is used for measurement after remodeling a commercially available digital mirrorless single-lens camera. For remodeling the camera, the original lens replaced with the lens shown in Fig. 1.21(a) left and Fig. 1.22. Also, the light quantity is adjusted by using a neutral-density (ND) filter[3] (Fuji 1.5, exposure adjustment multiple 3.16) (Fig. 1.21(b)). The camera specification after remodeling is shown below.

Camera specifications

Model:	NIKON 1 J1
Focal length:	30 mm
Image sensor type:	CMOS
Shutter speed:	33 ms (=1/30 s)

In the present study, a stepped neutral-density filter is used for calibrating the cameras. The image of

(a) (b)

Fig. 1.21 (a) Digital mirrorless single-eye camera (modified camera (left), commercial camera (right)), (b) Neutral-density (ND) filter.

[3] In photography and optics, a neutral-density filter, or ND filter, is a filter that reduces or modifies the intensity of all wavelengths, or colors, of light equally, giving no changes in hue of color rendition. (Wikipedia)

grayscale divided into 20 levels (stepped neutral-density filter) is obtained without the knife-edge, and the tone correction is performed for each camera, and the individual difference of each camera is corrected.

1.19. 5 Groups-6 Sheets Focusing Lenses

Fig. 1.22 shows the 5 groups-6 sheets focusing lenses that are attached to the camera in Fig. 1.21. The lens specifications are shown below.

Lens specifications

Lens composition:	5 groups-6 sheets
Focal length:	30 mm
Front diameter:	10 mm

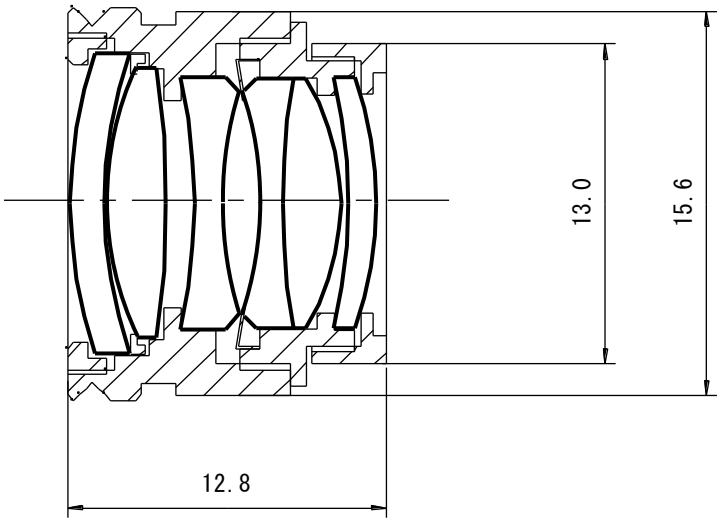

Fig. 1.22 Camera lens outline.

1.20. Corresponding Circuit

In order to simultaneously capture schlieren images from target non-uniform density flow by multiple directions using 20 cameras, it is necessary to adjust the flashlights timing of the multi-directional schlieren optical system altogether and also adjusting the shooting timing of the flashlights and the cameras altogether.

Therefore, in this experiment, a synchronous circuit of flashlights and cameras is made. The synchronous circuit is shown in Fig. 1.23.

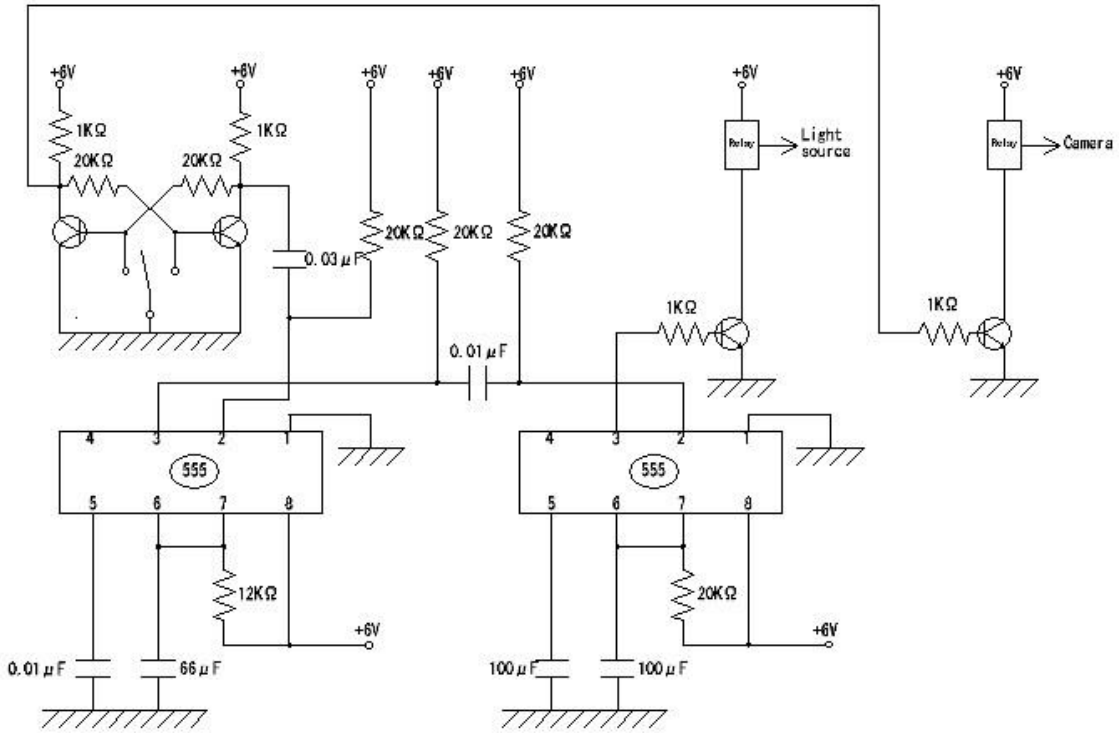

Fig. 1.23 Synchronous circuit.

1.21. High-Speed Camera

For pre-investigation and for time series observation of the target flow, high-speed schlieren movies with a high-speed camera are performed simultaneously with the 20-direction schlieren photographing apparatus. This high-speed digital camera system captures high-resolution images and movies for playback and analysis and has the capability of slow-motion playback.

The specifications of the high-speed camera used for high-speed schlieren photography are shown below.

High-speed camera specifications

Model:	Photron made FASTCAM-512 PCI 2K
Frame rate at full pixel resolution:	2000 frames per second (fps)

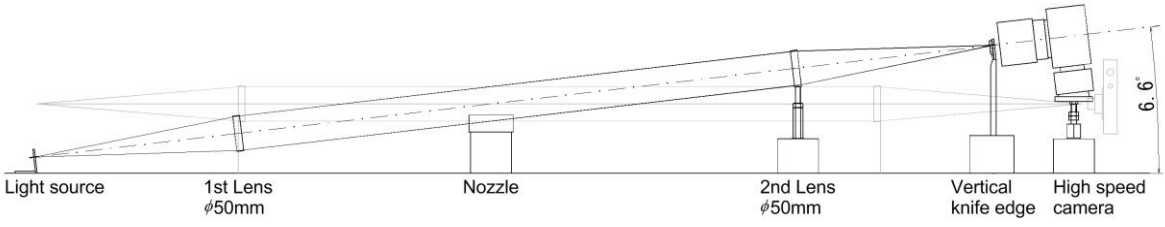

Fig. 1.24 Schematic diagram of high-speed schlieren optical system.

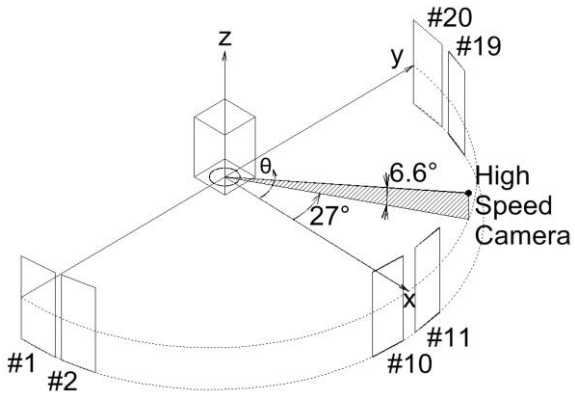

Fig. 1.25 High-speed camera installation position.

Frame rate at reduced pixel resolution:	32000 frames per second (fps)
Image sensor type:	CMOS
Shutter speed:	16.7 ms to 4 μs
Full element resolution:	512×512 Pixel
Monochrome tone density:	10-bits (1,024 steps)
Color tone density:	32-bits

The high-speed camera obtains the single directional schlieren movies using additional schlieren optics (two achromatic lenses, a continuous light source and a schlieren stop shown in Fig. 1.24), which installed in the direction of $\theta = 27°$ (between cameras No. 13 and No. 14) in elevation angle $\varphi = 6.6°$. The position of the high-speed camera is shown in Fig. 1.25. For photographing, a Nikon single-lens reflex (focal length 50 mm, F value 1.4) is attached to a high-speed camera, and a white LED pinhole type light source with a diameter of 0.75 mm is used.

1.22. 3D Modeling and 3D Printing

In order to get a deeper understanding of the three-dimensional shape of the flame obtained by the 3D-CT reconstruction, we performed three-dimensional modeling and printing with a 3D printer. First, 3D modeling is performed by converting the 3D-CT reconstructed density data to STL (Stereo Lithography) file (ASCII format) by using Intel FORTRAN program. Next, in order to satisfactorily express the features of the flames and supersonic micro-jets shape, "Mesh Lab" is used for confirmation of the obtained STL file and three-dimensional stereoscopic display. Finally, for 3D printing, make an executable file (x3g file) for the MakerBot 3D printer "Replicator 2X" shown in Fig. 1.26, using the "Maker Ware Software" that comes with the 3D printer. Also, can convert STL file to OBJ file format for 3D printing using Meshmixer software. This makes it possible to actually observe the flame shape with the hand and not only to look at the 3D model on the computer screen. The 3D printers used for this three-dimensional printing are shown in Fig. 1.26, and the specifications of the 3D printers are listed

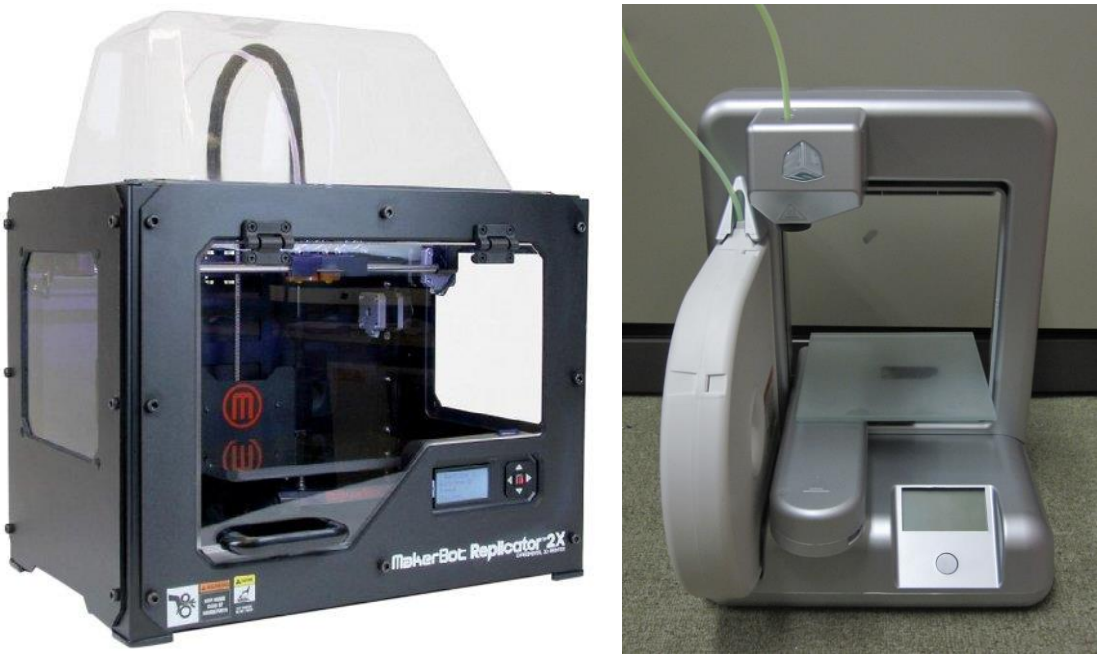

(a) "MakerBot Replicator 2X" (b) "Cubify Cube"

Fig. 1.26 3D printers

below.

"MakerBot Replicator 2X" 3D printer specifications

Printable size:	246 (l) × 152 (h) × 155 (w) mm
Minimum stacking pitch (resolution):	0.1 mm
Print jets:	0.4 mm × 2 jets
Corresponding material:	PLA, ABS resin

"Cubify Cube" 3D printer specifications

Printable size:	152.5 (l) × 152.5 (h) × 152.5 (w) mm
Minimum stacking pitch (resolution):	0.2 mm
Print jets:	0.4 mm × 1 jet
Corresponding material:	PLA, ABS resin

1.23. Digital Image and Humans Visual System Basic Concepts [21]

In the present study, one of the key factors is digital image processing. In digital image processing, the digital image(s) process by a suitable algorithm using a digital computer. This section is provided an introduction to some basic concepts of the digital image.

"Digital images" are a matrix with a rectangular array of numbers (elements), which numbers called "pixels" (picture elements). The $m \times n$ matrix has m rows and n columns. The digital image dimensions

($x \times y$) are equal to the columns and rows of the corresponding matrix ($x \times y = n \times m$). In other words, the digital image is equivalent to a two-dimensional (2D) function, $f(x, y)$, where x and y are two-dimensional coordinates. The value of function f at any point presents the intensity or gray level of the image at that point.

An image can be monochromatic (colorless) or chromatic (color). In digital imaging, the light beams (or other waves) change attenuation as they pass through or reflect off objects, and contain the information that form the image. The colorless light is called "monochromatic (or achromatic) light". The intensity range of monochromatic light changes from black to grays and finally to white. The term "gray level" is generally equivalent to monochromatic "intensity". The term "grayscale" expresses the range of measured values of monochromatic light from black to white which the term grayscale images are mostly used for monochromatic images.

The basic components of "chromatic (color) light" such as the light seen by the eye, by the film and by the photo sensor in a digital camera, are red, green and blue (RGB). The resulting "image" is a series of numbers from 0 to 255 representing the intensity of red, green and blue light at each point on the sensor. Add the maximum amount of each of these three and the color white (R = 255, G = 255, B = 255) is formed and take away all three and the color black (R = 0, G = 0, B = 0) is formed. By adding different amounts of each of these three, all other colors are formed.

"Brightness" is usually used to describe the quality of the light source. Brightness is the light intensity that the human visual system can be perceived it and it is impossible to measure practically. It can be defined, the intensity (gray level) for a monochrome image at any coordinates (x, y) by,

$$L = f(x, y)\,. \tag{1.42}$$

The smallest discernible change in intensity level is represented by "intensity resolution". The number of intensity levels is an integer power of 2 (8 bits, 16bits, …), for example, 8 bits of intensity resolution has 2^8 = 256 levels (0 to 255). The "gray (or intensity) scale", is expressed within a given interval [L_{min}, L_{max}], where L_{min} = 0 (or 0%) (total absence, black) and L_{max} = 255 (or 100%) (total presence, white). All values in between indicate the gray amount from black to white.

In the 3D-CT quantitative schlieren measurement technique, the digital cameras present 8-bit color depth JPEG images this equates to (2^8)^3=16,777,216 total potential RGB color values. As the bit-depth rating increases, the number of colors and tonal values increases exponentially as listed in Table 1.2, resulting in smoother brightness. By increasing bit-depth from 1-bit to 8-bit per color, the improvements easy to see as shown in Fig. 1.27, but it is difficult or impossible to notice between 10-bit, 11-bit, and 12-bit due to the limitations of the human eye [22]. All JPEG images convert to the portable gray map (PGM) format. The portable gray map (PGM) format contains 256 monochrome grayscale values that represent different shades of gray from black (0) to white (255).

"Spatial resolution" is a term that expresses the number of dots (pixels) per unit distance that made a digital image, and have application in the printing and publishing industry. For better quality, print

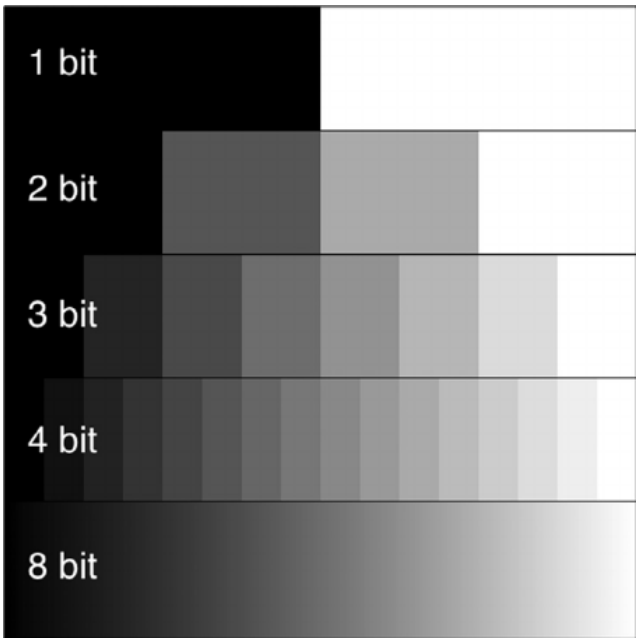

Fig. 1.27 Bit-depth.

resolution in photography should be not less than 300 "dots per inch (dpi)". We are used 300 to 600 dpi (ppi[4]) in our calculation and image processing system (e.g. voxel size: 0.04 mm in each direction, 25.4mm ÷ 0.04mm/pixel ≈ 600 ppi).

Table 1.2 Bit-depths converted to potential gray tones and colors.

Bits per color	Monochrome grayscale values	Potential RGB color values
1-bit	$2^1 = 2$	$(2^1)^3 = 8$
2-bit	$2^2 = 4$	$(2^2)^3 = 64$
3-bit	$2^3 = 8$	$(2^3)^3 = 512$
4-bit	$2^4 = 16$	$(2^4)^3 = 4096$
6-bit	$2^6 = 64$	$(2^6)^3 = 262144$
8-bit	$2^8 = 256$	$(2^8)^3 = 16.77$ Million
10-bit	$2^{10} = 1024$	$(2^{10})^3 = 1.07$ Billion
11-bit	$2^{11} = 2048$	$(2^{11})^3 = 8.59$ Billion
12-bit	$2^{12} = 4096$	$(2^{12})^3 = 68.72$ Billion

The "Weber ratio" is defined as the quantity $\Delta B_c/B_0$ (see equation (1.1)), where ΔB_c is the change of illumination discriminable 50% of the time with background illumination B_0, in other words, the light

[4] Pixels per inch

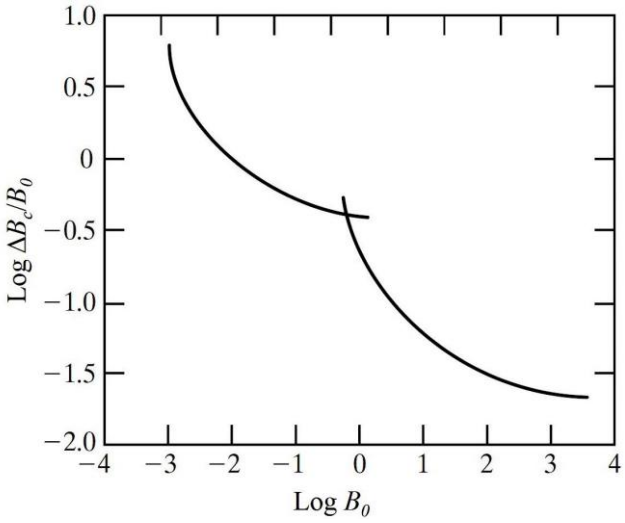

Fig. 1.28 Typical Weber ratio as a function of intensity [21].

beam cut-off 50% by the knife-edge (refer to section 1.4). A small value of the Weber ratio represents "good" brightness discrimination, since a small percentage change in intensity is discriminable, and vice versa. Fig. 1.28 [21] depicts the typical Weber ratio as a function of intensity. As shown in Fig. 1.28 when the Weber ratio is large the related brightness discrimination is poor, and as background illumination increases (the Weber ratio decreases), it improves significantly.

The human eye consists of two types of photoreceptor cells which have functional roles in image-forming. These cells called rods and cones, with about 120 million rod cells, and 6 million cone cells [23]. The density of rods and cones is shown in Fig. 1.29 for a cross-section of the right eye [21].

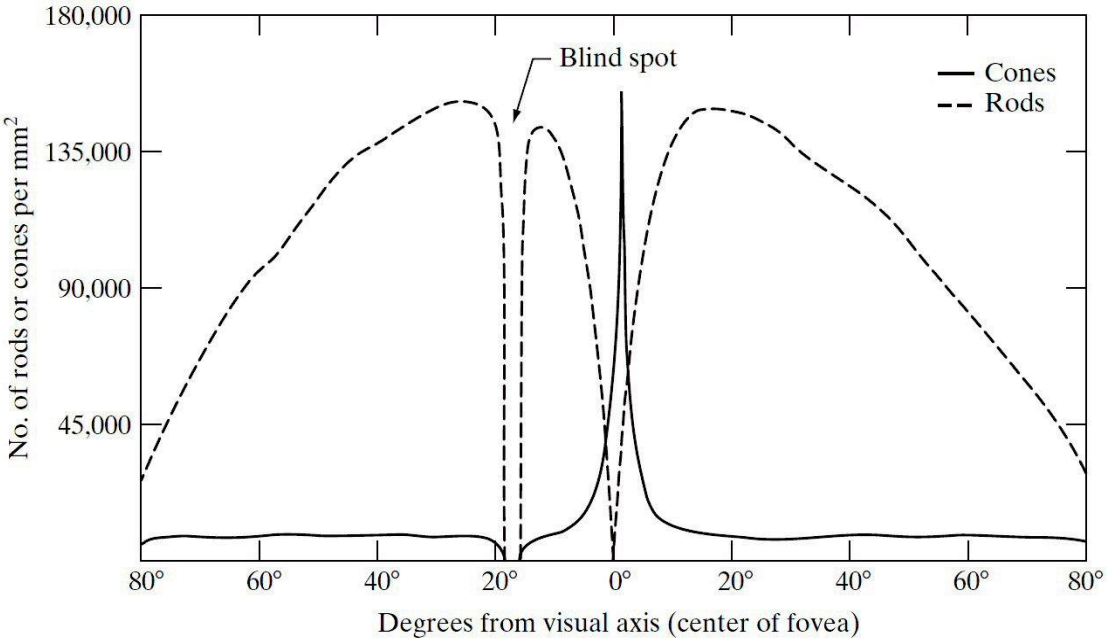

Fig. 1.29 Distribution of rods and cones in the retina [21].

Rod cells better than cone cells can function in lower light, night vision and monochrome color vision, that is why colors are not obvious in dim light, and cone cells have more role in color vision [23]. Rods are very sensitive and can be stimulated by a single photon [24]. Cones produce a signal by sufficiently brighter light (a larger number of photons). There are three different types of cone cells in humans based on response to light of different wavelengths [23]. As shown in Fig. 1.28, the curve has two branches. These branches have reflected in the function of the rods and cones. The low levels and high levels of illumination vision are carried out by the rods and the cones, respectively [21].

1.24. Summary of the Images Processing in the Schlieren 3D-CT Technique

A brief overview of images preparing for 3D-CT reconstruction is given in this section. In each experiment for all 20 cameras, as listed in Table 1.3, the different images must be obtained in order to perform an accurate 3D-CT reconstruction of the target flow.

Table 1.3 Detail of images in each experiment.

No.	Cases	Number of images	Related Figure	Related Equations	Related Nomenclature
1	Rod image	1	Fig. 1.30		
2	Grayscale images	16	Fig. 1.31		
3	Target flow images	1, 2, …	Fig. 1.32(2)	Eq. (1.24), Eq. (1.30)	B
4	Knife-edge images (without target)	16	Fig. 1.32(3)	Eq. (1.24), Eq. (1.30)	B_n, B_{nf}, B_{nj}
5	No knife-edge images (without target)	16	Fig. 1.32(4)	Eq. (1.26), Eq. (1.31)	B_0

Images processing steps are as follow:

1. All obtained images are transformed from JPEG format to PGM (portable gray map) format since we want to work with grayscale.
2. For cases with 16 number images (cases No.2, No.4 and No.5), an average is obtained, since it is necessary to work just with one image for each direction.
3. The first objective is to set a reference system for adjustment and alignment of all images since images for all 20 directions will be used simultaneously in the CT-reconstruction. Therefore, from all 20 directions, images of a circular cross-section rod (Fig. 1.30(a), cases No.1) obtain, which all details (dimensions and sizes) are known. First, the rod images rotate, align, and resize (Fig. 1.30(b)) based on the actual rod size, and the information obtained from rod alignment are used to align and adjust all other images.
4. The image of grayscale (Fig. 1.31, case No.2,) divided into 20 levels (stepped neutral-density filter) is obtained without the knife-edge, and the tone correction is performed for each camera, and the individual difference of each camera is corrected.

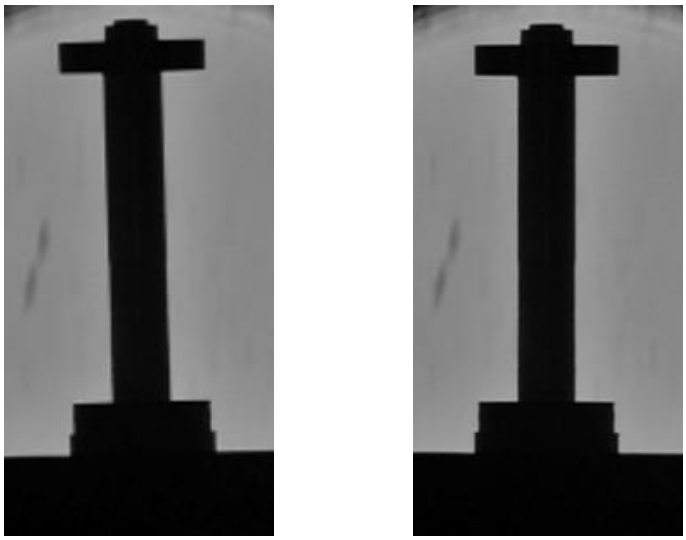

(a) Before alignment (b) After alignment

Fig. 1.30 Rod image as a reference system for adjustment and alignment of all images.

5. In the previous work, the target high-speed turbulent burner flames are investigated and reported [6], and the sample results for only camera number 10 are depicted in Fig. 1.32. Two sets of images present by schlieren observation, "with target $B(X)$" (Fig. 1.32(2), case No.3) and "without target B_{nf} (X)" (Fig. 1.32(3), case No.4, without any disturbance in the test section). As described in section 1.8, these two sets using "no knife-edge" data (Fig. 1.32(4), case No.5) are processed to obtain projection images (density thickness Dt, Fig. 1.32(6)).

6. Using the density thickness images (Fig. 1.32(6)) as projections for CT-reconstruction, 3D instantaneous density distributions of the target flow field can be obtained.

7. 3D modeling is performed by converting the 3D-CT reconstructed density data to STL (Stereo Lithography) file (Fig. 1.32(7)). 3D model of CT-reconstructed result expresses the instantaneous 3D flame shape. This 3D solid model is 3D-printed (Fig. 1.32(8)) for a threshold density level of 0.7 kg/m^3. Observing the flame shape and touching with the hand is more valuable than only

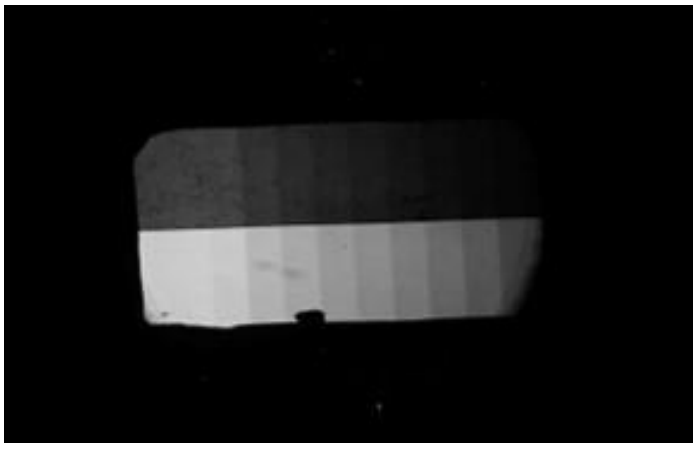

Fig. 1.31 Grayscale (stepped neutral-density filter) image.

looking at the 3D model on the computer screen.

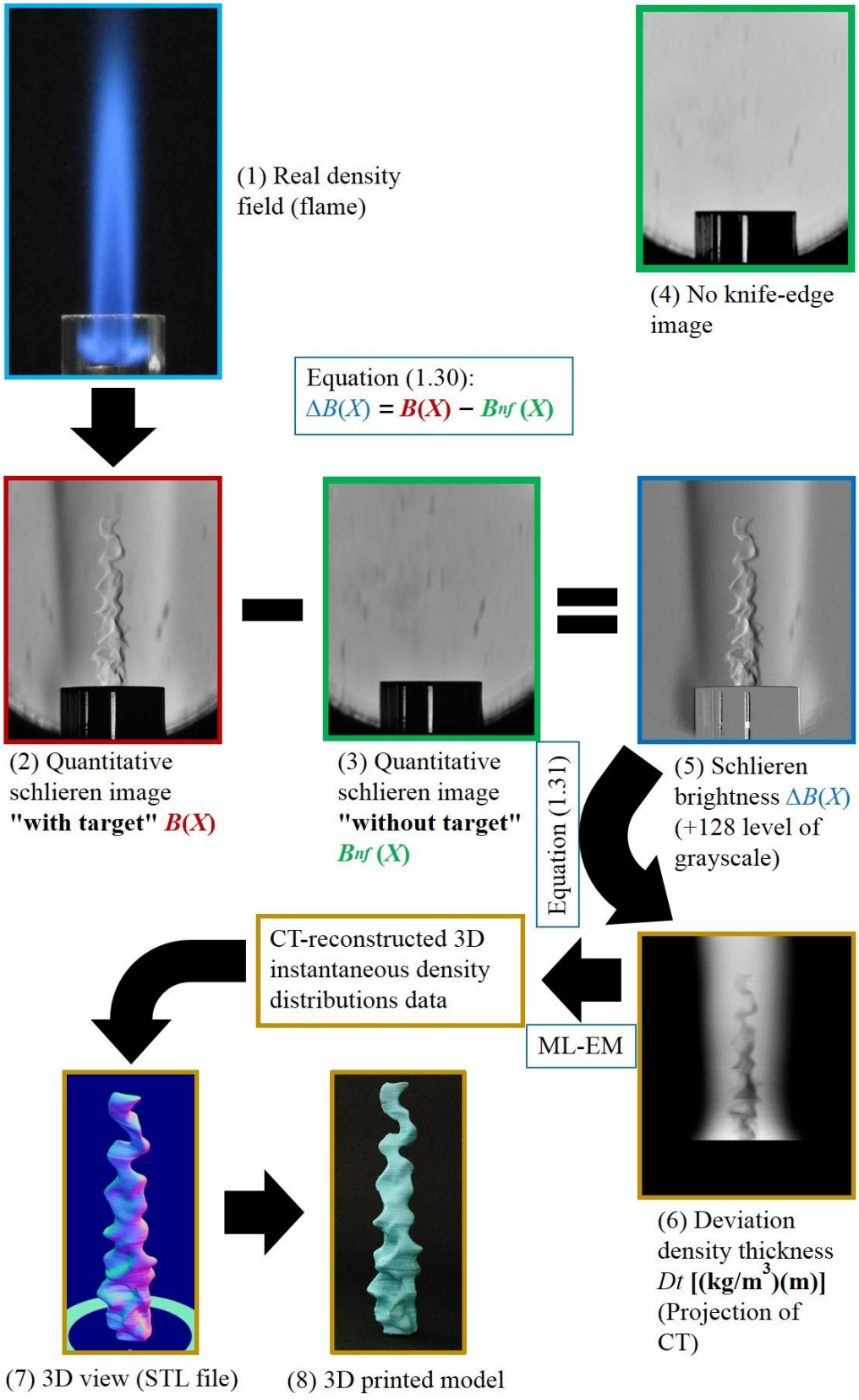

Fig. 1.32 Overview of the images processing in the schlieren 3D-CT technique.

2

CHAPTER 2

Journal of Flow Control, Measurement & Visualization, 8(2), 25-44

Quantitative Schlieren Image-Noise Reduction Using Inverse Process and Multi-path Integration

Published: 2020.04.30

https://doi.org/10.4236/jfcmv.2020.82002

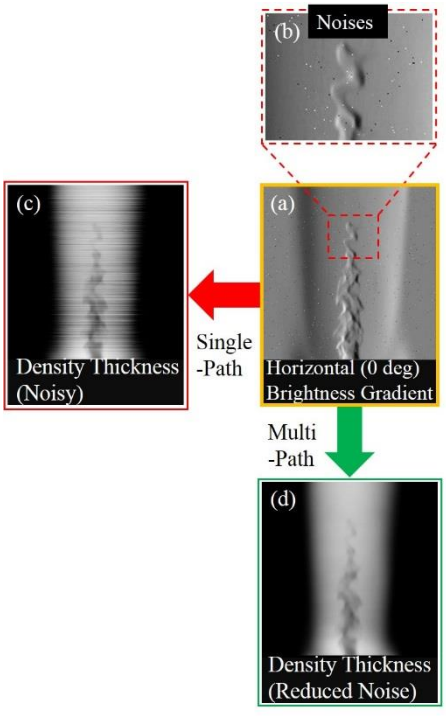

Abstract

This report deals with introducing two new techniques based on a novel concept of complex brightness gradient in quantitative schlieren images, "inverse process" and "multi-path integration" for image-noise reduction. Noise in schlieren images affects the projections (density thickness) images of computerized tomography (CT). One spot noise in the schlieren image appears in a line shape in the density thickness image. Noise effect like an infectious disease spreads from a noisy pixel to the next pixel in the direction of single-path integration. On the one hand, the noise in the schlieren image reduces the quality of the image and quantitative analysis and is undesirable, on the other it is unavoidable. Therefore, the importance of proper noise reduction techniques seems essential and tangible. In the present report, a novel technique "multi-path integration" is proposed for noise reduction in projections images of CT. Multi-path integration is required the schlieren brightness gradient in two orthogonal directions. The 20-directional quantitative schlieren optical system presents only images of schlieren brightness in the horizontal gradient and another 20-directional optical system seems necessary to obtain vertical schlieren brightness gradient, simultaneously. Using the "inverse process" a new technique enables us to obtain vertical schlieren brightness gradient from horizontal experimental data without the necessity of a new optical system and can be used for obtaining any optional directions of schlieren brightness gradient.

CHAPTER 2
IMAGE-NOISE REDUCTION

2.1. Introduction

In the present report, two new techniques are introduced based on a novel concept of complex brightness gradient in quantitative schlieren images, "inverse process" and "multi-path integration" for image-noise reduction. The new techniques partially are presented in international conferences [11][12] which in detail and entirely will be discussed here. Also, it will be shown an important ability of complex schlieren brightness gradient, which is independence on the path and starting point in the integration process.

Some image noise generating sources are as follows; dusty photography surroundings, dusty and dirty lenses, defective lens surface, lenses and digital cameras. If using the same camera and settings, repeatedly photography for the same target, every obtained image contains slightly different gray values. These variation intensity values are called noise, which generated by the camera. Detailed descriptions of the various types of digital camera noises, along with the supporting figures and diagrams, are given in [25] and many other references cited therein.

The schlieren images brightness change gradually (brightness gradient), while image noise is a random variation of brightness and is generally considered undesirable. Noise can deduct the quality of the image and quantitative analysis [26]. Noise in schlieren images can arise from density gradients anywhere between the source slit and the knife-edge in the wind-tunnel research, and that is why a multiple-source schlieren system is introduced for noise reduction in [27]. Quantitative schlieren imaging requires low noise level images accordingly high data accuracy. Noise in schlieren imaging is unavoidable. There are very few noise reduction techniques studies in the works of literature for schlieren imaging. Accordingly, the lack of proper noise reduction techniques is clear. Therefore, a new approach called "multi-path integration" novel technique against former technique "single-path integration" is introduced for noise reduction in projections (density thickness) images of CT (computerized tomography). The new multi-path integration technique is required schlieren brightness gradient in both

horizontal (*x*-directional) and vertical (*z*-directional) directions, or in other words, in two orthogonal directions (e.g. horizontal and vertical or two perpendicular diagonal directions). The 20-directional quantitative schlieren optical system gives only images of schlieren brightness in the horizontal gradient (*x*-directional) and another 20-directional optical system seems necessary to obtain vertical (*z*-directional) schlieren brightness gradient, simultaneously.

The present investigation represents the new "inverse process" novel technique for obtaining vertical and diagonal schlieren brightness gradient from horizontal experimental data (with vertical knife-edge orientation) without the necessity of a new optical system. The main advantages of the new approach employed are its relative simplicity, the ease of application, without extra cost, and the satisfactory accuracy of results and can be used for obtaining any optional direction of schlieren brightness gradient.

Recently [11], we presented the "inverse process" technique but in a different way than this time. In previous work, the "inverse process" is performed after the CT reconstruction, however, now is done before the CT reconstruction procedure (Fig. 2.1). Indeed, in the previous work phantom (virtual) data of schlieren images are obtained by the "inverse process" and used to evaluate noise reduction technique while in the new "inverse process" technique actual experimental data is used for reproducing other directions of schlieren brightness gradient. By using both white-light and monochromatic sources, color schlieren images have been produced from combining horizontal and vertical gradient brightness of common schlieren images by [28], but for this purpose, two independent knife-edges along two different beam paths are employed. About 70 years ago, a more complex arrangement is presented for obtaining two spatially separated images sensitive to orthogonal path deviations [29]. A good example of the same numerical supersonic jet-exit flow field is rendered as shadowgraph, bright-field schlieren (circular

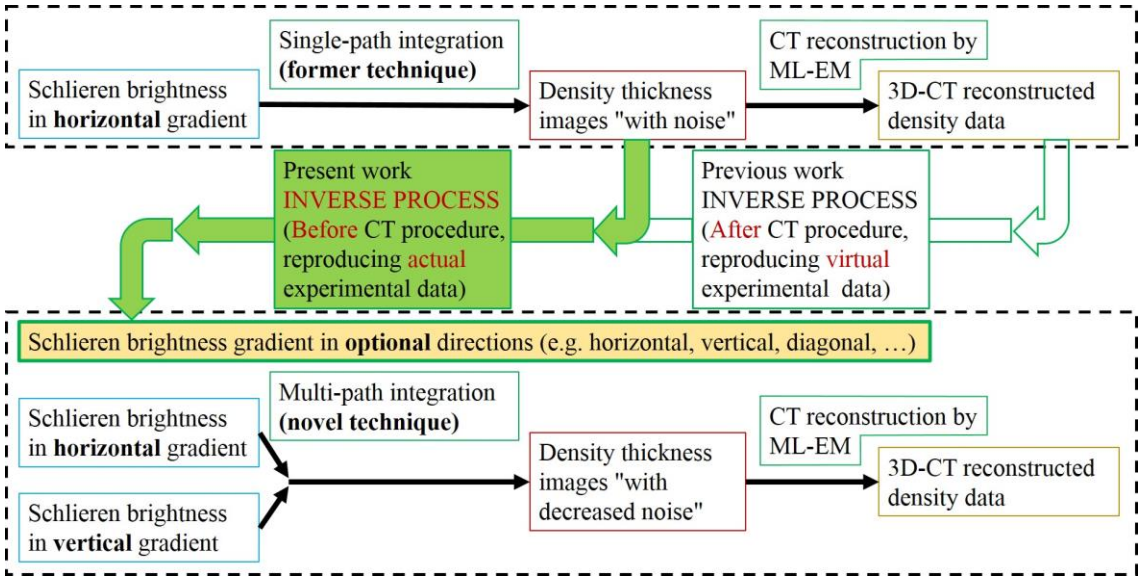

Fig. 2.1 Flow diagram of the "inverse process" new technique for the reproduction of schlieren brightness gradient in horizontal, vertical, diagonal directions and conversion to the new projections (density thickness (*Dt*)) of CT by new "multi-path integration" technique.

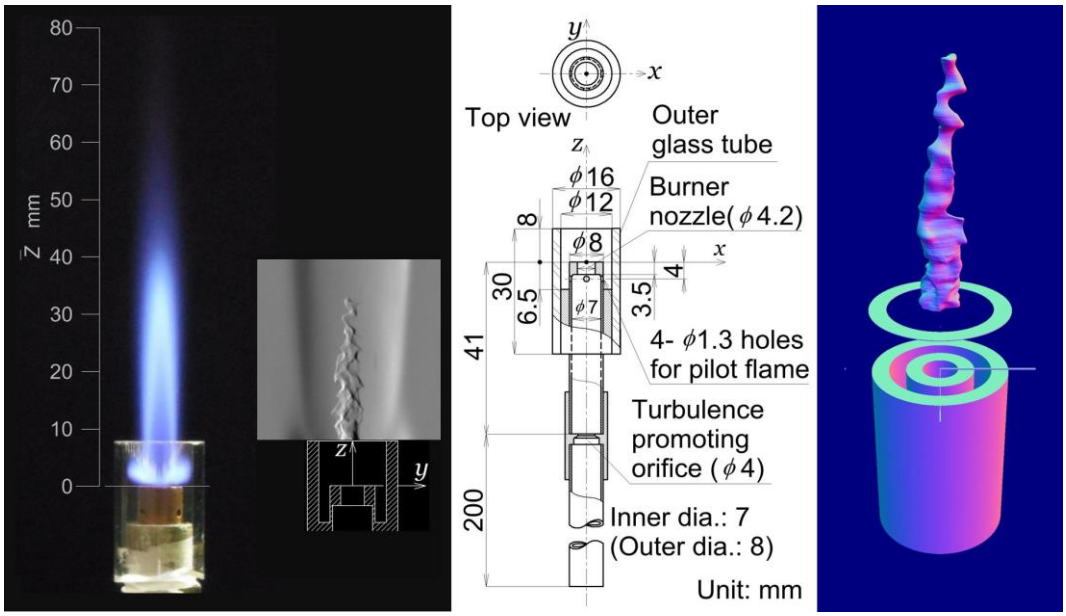

(a) Target flame & schlieren image (b) Burner tip detail (c) 3D model view

Fig. 2.2 High-speed turbulent flame, burner, coordinate system and bird's-eye view of 3D model [6].

cutoff), vertical and horizontal knife-edge schlieren in [30].

In the previous work [6], the target high-speed turbulent burner flames are investigated and reported. Fig. 2.2 depicts target flame, detail dimensions of burner nozzle, coordinate systems and 3D bird's-eye view of the CT reconstructed density data. For more information related to the flow conditions, measured parameters of target flames and burner details refer to the previous work [6]. In the current investigation, the horizontal schlieren brightness gradient data of high-speed turbulent flame [6] with average flow velocity 10 m/s is used for reproducing the 20-directional images of schlieren brightness in horizontal, vertical and diagonal gradient. First, as shown in Fig. 2.1(top), the initial density thickness (*Dt*) images are obtained from images of schlieren brightness in the horizontal gradient (*x*-directional). Next, using the inverse process from density thickness (*Dt*) images, the horizontal (*x*-directional), vertical (*z*-directional) and two diagonals (45 degree and 135 degree) schlieren brightness gradient data of target flame are successfully obtained. Finally, by applying the multi-path integration technique, the new set of projections images of density thickness are successfully obtained (Fig. 2.1 (bottom)). Then, by using the new set of density thickness images "with decreased noise" as projections for CT reconstruction the 3D density distributions of target flame are successfully reconstructed.

2.2. New Techniques and Treatments

2.2.1. Inverse Process

As mentioned before, in the present study, using "inverse process" new approach from density

thickness (*Dt*) images (Fig. 2.1), the horizontal (*x*-directional), vertical (*z*-directional) and two diagonals (45 degree and 135 degree) schlieren brightness gradient data of target flame have been successfully obtained. The relation between deviation brightness ΔB and density thickness *Dt* is expressed by equation (1.31). The equation (1.31) can be rewritten in the following simple forms.

$$d(Dt)/dX \propto \Delta B(X), \tag{2.1}$$

and

$$d(Dt)/dX = \alpha \times \Delta B(X). \tag{2.2}$$

The deviation density thickness can be expressed as,

$$d(Dt(x,z))/dX = Dt(x,z) - Dt(x-1,z). \tag{2.3}$$

Finally, in the inverse process, by combining the equations (2.2) and (2.3), the deviation brightness of the quantitative schlieren image in each direction will be given by:

$$\Delta B(x,z)_{Horizontal,+x} = (1/\alpha) \times \left[Dt(x,z) - Dt(x-1,z) \right], \tag{2.4}$$

$$\Delta B(x,z)_{Vertical,+z} = (1/\alpha) \times \left[Dt(x,z) - Dt(x,z-1) \right], \tag{2.5}$$

$$\Delta B(x,z)_{Diagonal,45^\circ} = (1/\alpha) \times \left[Dt(x,z) - Dt(x-1,z-1) \right], \tag{2.6}$$

$$\Delta B(x,z)_{Diagonal,135^\circ} = (1/\alpha) \times \left[Dt(x,z) - Dt(x+1,z-1) \right]. \tag{2.7}$$

The direction of the schlieren brightness gradient can be changed in the opposite direction only by applying one minus sign in the corresponding equation. Therefore, by using density thickness *Dt* in the inverse process, the schlieren brightness in horizontal, vertical and diagonal directions can be calculated (equations (2.4)-(2.7)) without the necessity of a new optical system. One of the benefits of using this approach is that now we can apply the "multi-path integration" noise reduction technique. The sample results for only camera number 10 are depicted for all mentioned directions in Fig. 2.3. The corresponding result for numerical simulation (refer to section 2.2.4) of the flame is depicted in the top right side and the corresponding knife-edge orientation is shown underneath of each schlieren image in Fig. 2.3.

The knife-edge is a key element in the schlieren setup. Density gradients arising in the test section lead to beam deflection. In common schlieren imaging, the deflected light beams normal to the imaging screen are viewed by focusing onto a knife-edge. The brighter and darker regions of the schlieren images

caused by the deflected light beams above and onto the knife-edge respectively. The knife-edge employs as a cut-off filter for light intensity (brightness). The knife-edge orientation will reveal directional density gradients (brightness gradients). For example, vertical knife-edge orientation present horizontal schlieren brightness gradient data and horizontal knife-edge orientation present vertical schlieren brightness gradient data. In the 20-directional quantitative schlieren optical system, a vertical knife-edge (Fig. 2.3(c1)) is used which for adjusting moves from left to right in the positive *x*-direction.

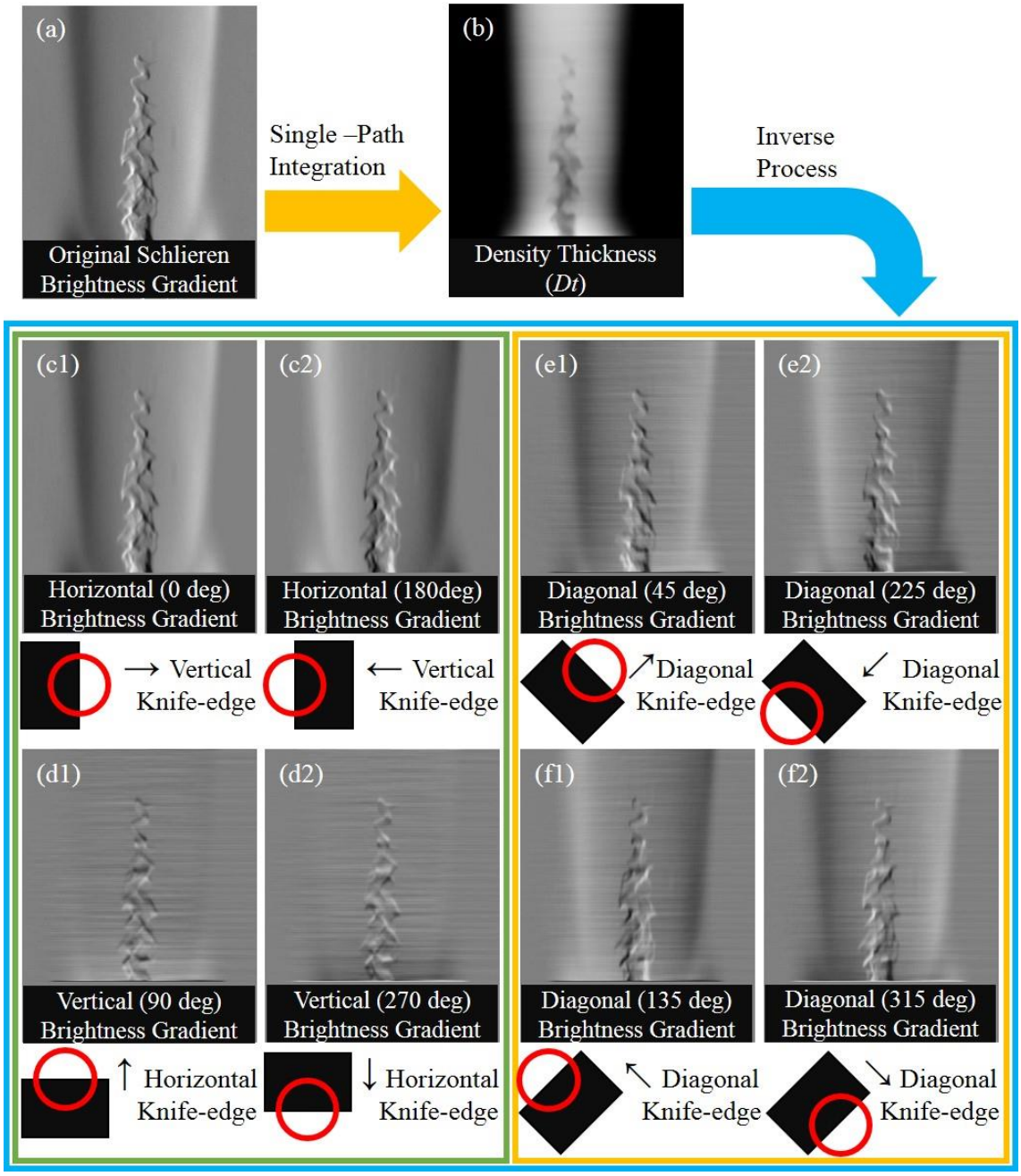

Fig. 2.3 Inverse process for reproduction of schlieren brightness in horizontal, vertical and diagonal gradient.

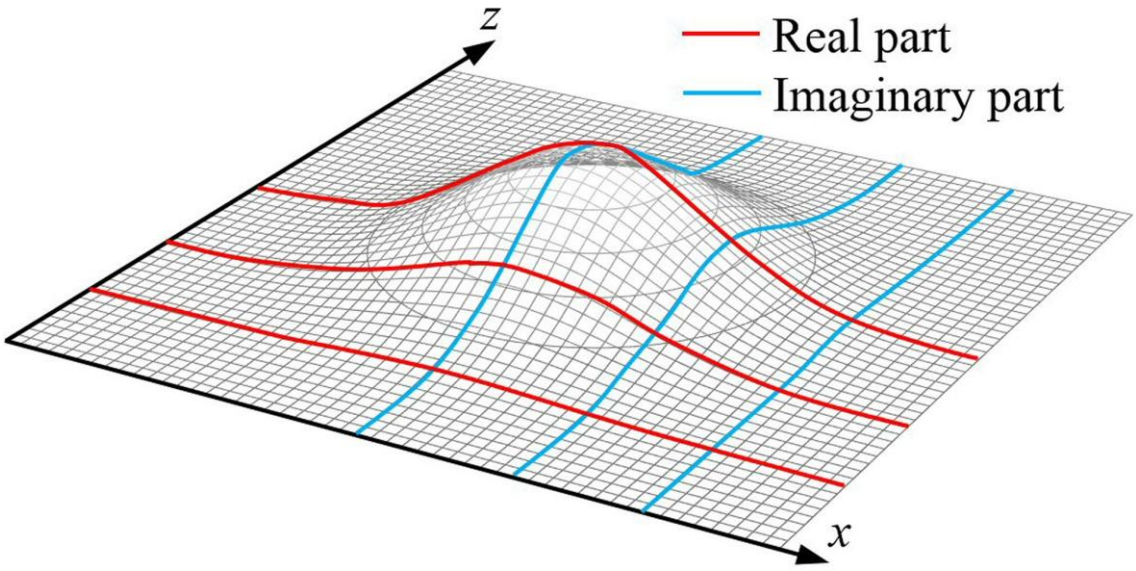

Fig. 2.4 Complex schlieren image explanation.

2.2.2. Complex Schlieren Brightness Gradient

Fig. 2.4 shows an example of contour lines display of density deviation thickness (density thickness). At this figure, the brightness value of the Schlieren image I s given by the gradient (slope) of the curved surface. For example, when a knife-edge parallel to the *z*-axis is used as a schlieren stop (vertical knife-edge) and the light beam is cut in the +*x* direction, the gradient (slope) of the red curve can be obtained by measuring the brightness of the schlieren image. On the other hand, if the knife-edge is inclined 90°, the slope of the blue curve can be obtained.

Therefore, by simultaneously considering the schlieren brightness gradient information in the horizontal direction (red, real part) and vertical direction (blue, imaginary part), the complex gradient of the density thickness distribution at any position can be obtained. The spatial integration to obtain the density thickness distribution can now be performed on any arbitrary path, and noise reduction now becomes possible. In this study, a schlieren image with information on the gradient of density thickness in two orthogonal directions is called a "complex schlieren image".

2.2.3. Cauchy Integration Theorem

The Cauchy integration theorem in complex analysis is an important statement about line integrals for regular functions in the complex plane. Cauchy's integration theorem states that if *f*(z) be a regular function in the simply connected domain *D*, its contour integral on a path does not depend on the integration path and depends only on the beginning and ending points of the path. Therefore, if let *C* be a piecewise continuously differentiable path in *D* with start point *a* and end point *b*, and *F* is a complex antiderivative of *f*, then,

$$\int_C f(z) = \int_a^b f(z) = F(b) - F(a) \quad . \tag{2.8}$$

If $a = b$, then C is a closed curve (loop) within D, accordingly,

$$\oint_C f(z) = 0 \quad . \tag{2.9}$$

We applied the above theorem to develop the noise reduction technique. As shown in Fig. 2.5 and Fig. 2.8, for obtaining density thickness images "with decreased noise" the average of transverse-integration from multi-path is employed. It is remarkable, as a new finding, a new important concept in complex schlieren image could be expressed as follow; The complex schlieren image for obtaining density thickness at an arbitrary position (ending point of the integration path) has one more potential power, which it only depends on the ending point of the path, Therefore, the calculation of density thickness can be performed just by starting integration from any point on any path (Fig. 2.8).

2.2.4. Numerical Simulation

First, as a preliminary investigation and for a deep understanding of complex schlieren brightness, a numerical simulation for schlieren brightness of a flame is performed. The result for numerical simulation is depicted in Fig. 2.5. Schlieren images in horizontal, vertical and diagonal directions of brightness gradients are shown in Fig. 2.5(a1)-(h1). One hundred noises with various brightness in different positions are added to the schlieren images randomly. The noisy density thickness images obtained by single-path integration (former technique) are depicted underneath of corresponding each schlieren images (Fig. 2.5(a2)-(h2)). Fig. 2.5(i) illustrates the density thickness image by employing the "multi-path integration" new technique. Fig. 2.5(i2) depicts the result for the density thickness image in the absence of noise in the schlieren image. As seen in Fig. 2.5(i1) and Fig. 2.7(d) the noise effects are reduced to an acceptable level and slightly present around initial noise spots.

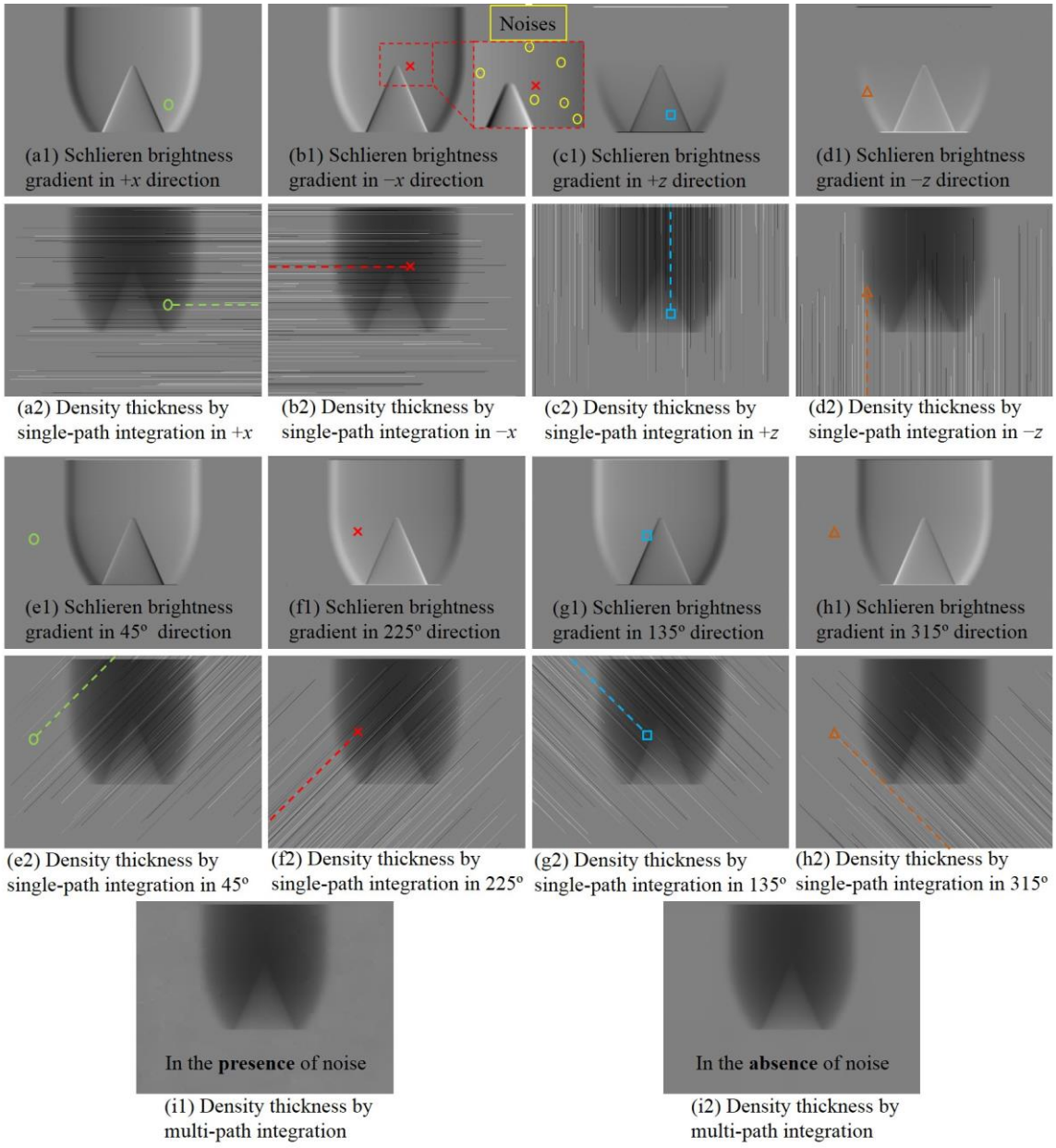

Fig. 2.5 (a1)-(h1) Numerical simulation of schlieren brightness in the horizontal, vertical and diagonal gradient of flame and (a2)-(h2) noisy density thickness (*Dt*) brightness using "single-path integration" underneath of the corresponding each schlieren image, (i) Density thickness brightness using "multi-path integration".

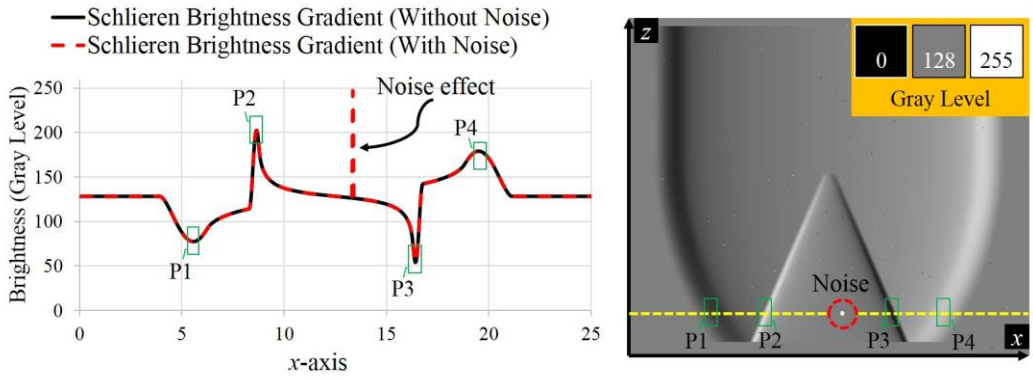

Fig. 2.6 Noise effects on schlieren brightness gradient (simulation result).

2.2.5. Noise Effects

The brightness of schlieren image changes gradually (brightness gradient), while image noise is the variation of brightness suddenly (Fig. 2.6) and is generally considered undesirable. The existence of some noises in the schlieren image affects the density thickness image (Fig. 2.7). Noise effect like an infectious disease spreads from a noisy pixel to the next pixel in the direction of single-path integration former technique (Fig. 2.7(c)). One spot noise in the schlieren image appears in a line shape in the density thickness image, which starts from noise position and continues as a line in the direction of single-path integration (Fig. 2.7(c)). Noise in schlieren imaging is unavoidable and can detract from the quality of the image and subsequent visual and quantitative analysis. Therefore, the need for proper noise reduction techniques is clear. Indeed, using noise reduction technique is not the first option, better than noise reduction is to control the primary generation sources of it, that no noise being produced.

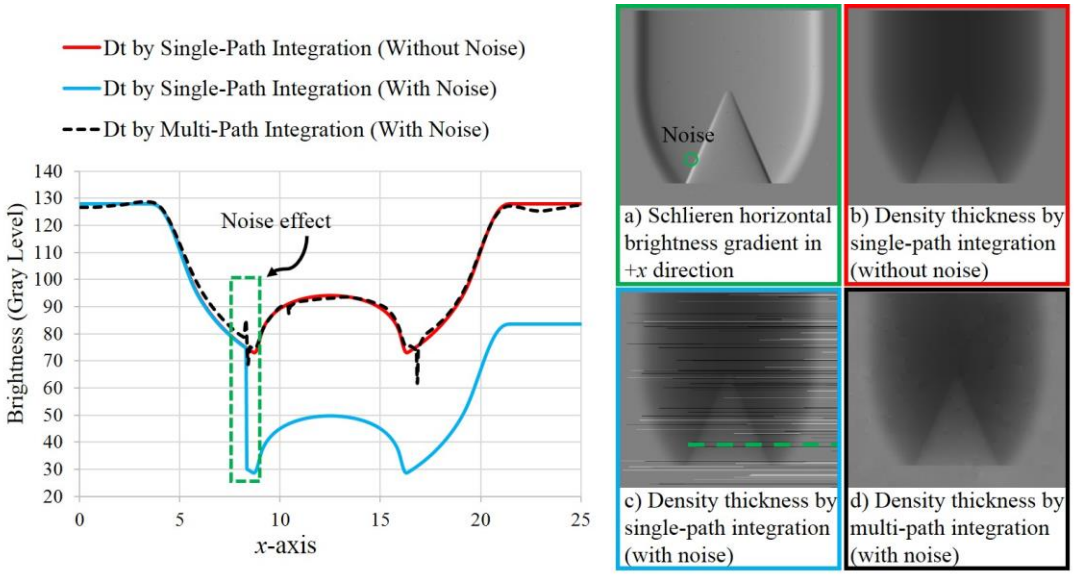

Fig. 2.7 Noise effects on density thickness brightness gradient (simulation result).

2.2.6. Multi-Path Integration Technique

As mentioned before, a new approach called "multi-path integration" novel technique against former technique "single-path integration" is introduced for noise reduction in projections (density thickness) images of CT (computerized tomography). The new multi-path integration technique is required schlieren brightness gradient in both horizontal (*x*-directional) and vertical (*z*-directional) directions, or in other words, in two orthogonal directions (e.g. horizontal and vertical or two perpendicular diagonal directions). In the usual procedure, density thickness image reproduces by transverse-integration of the schlieren image brightness in the single-path along schlieren brightness gradient (path No. 4 in Fig. 2.8(left)). In the present study, for obtaining density thickness images "with decreased noise" the average of transverse-integration from multi-path is employed. These paths are in four main horizontal and vertical directions (totally 28 paths, 7 paths in positive and 7 paths in negative of *x* and *z* directions) (Fig. 2.8), as well as, the paths can be used from two perpendicular diagonal directions. The new procedure "multi-path integration" is one comprehensive technique that including the usual former "single-path integration" technique as well. In the former technique "single-path integration" (path No. 4 Fig. 2.8), the density thickness for pixel (*x* , *z*) can be expressed from equation (2.3) as follow.

$$Dt(x,z) = Dt(x-1,z) + d(Dt(x,z))/dx \quad . \tag{2.10}$$

On the right side of equation (2.10), the first term is density thickness data from prior adjacent pixel (the density thickness for the first-pixel column (1 , *z*) is assumed zero) and the second term comes from schlieren image brightness (equation (1.31)). This second term for *z* (vertical) direction can be obtained

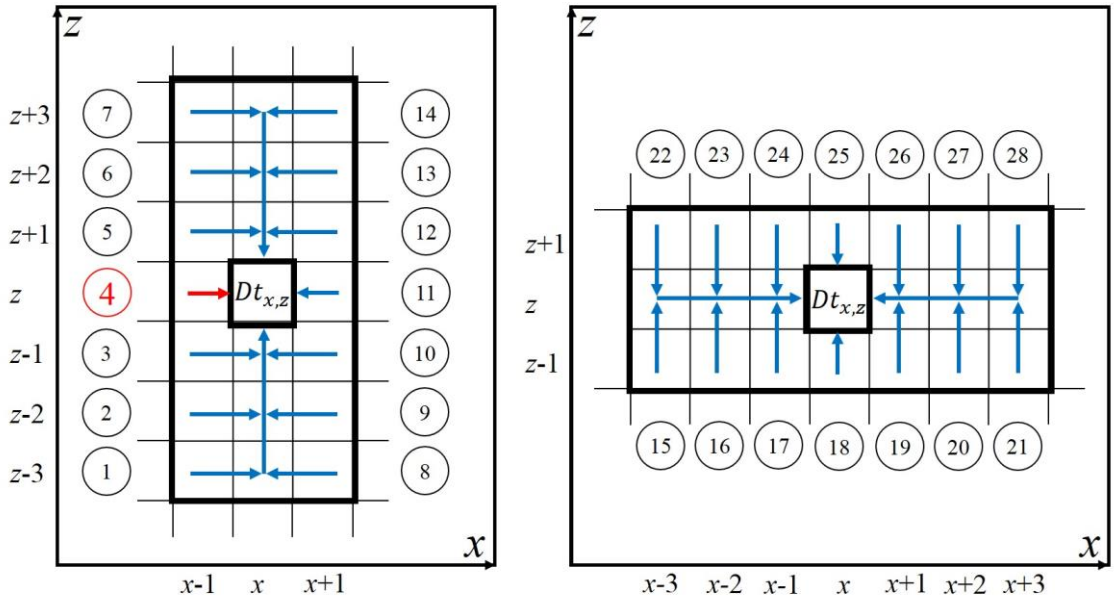

Fig. 2.8 Integration paths (totally 28 paths) for calculating density thickness of pixel (*x* , *z*).

by applying the inverse process technique. Calculation of two sample paths (No. 6 and No. 16) in the new technique "multi-path integration" are shown in the following equations.

$$Dt(x,z) = Dt(x-1,z+2) + \frac{d(Dt(x,z+2))}{dx} - \frac{d(Dt(x,z+1))}{dz} - \frac{d(Dt(x,z))}{dz}, \quad (2.11)$$

and

$$Dt(x,z) = Dt(x-2,z-1) + \frac{d(Dt(x-2,z))}{dz} + \frac{d(Dt(x-1,z))}{dx} + \frac{d(Dt(x,z))}{dx}. \quad (2.12)$$

First, the density thickness for pixel (x , z) is obtained from the multi-path (28 paths). Then, the average of all these paths is considered as the density thickness for the target pixel. In the schlieren imaging system, brightness gradually increases (or decreases) from ambient condition (with constant brightness) to boundary condition and vice versa. This fact is effective whether schlieren photography is containing a complete brightness gradient in the integrating direction or not. Figure 2.9 represents complete (Fig. 2.9(a)) and incomplete (Fig. 2.9(b)) observation of the schlieren brightness gradient for the laminar flame kernel. Hence, if the schlieren photography in one and more directions is not bounded to an ambient condition which means the schlieren photography is not observed complete target flow including the boundary condition, those directions could be omitted (Fig. 2.9(b) (Top direction)), because this treatment will give better results for noise reduction using multi-path integration. In the present study, paths from negative z-direction (7 paths, No. 22 to 28, Fig. 2.8) are not considered in the calculation due to that top area of target flame is not captured by the schlieren photography system, because of the fact that lenses diameters are smaller than target flame height.

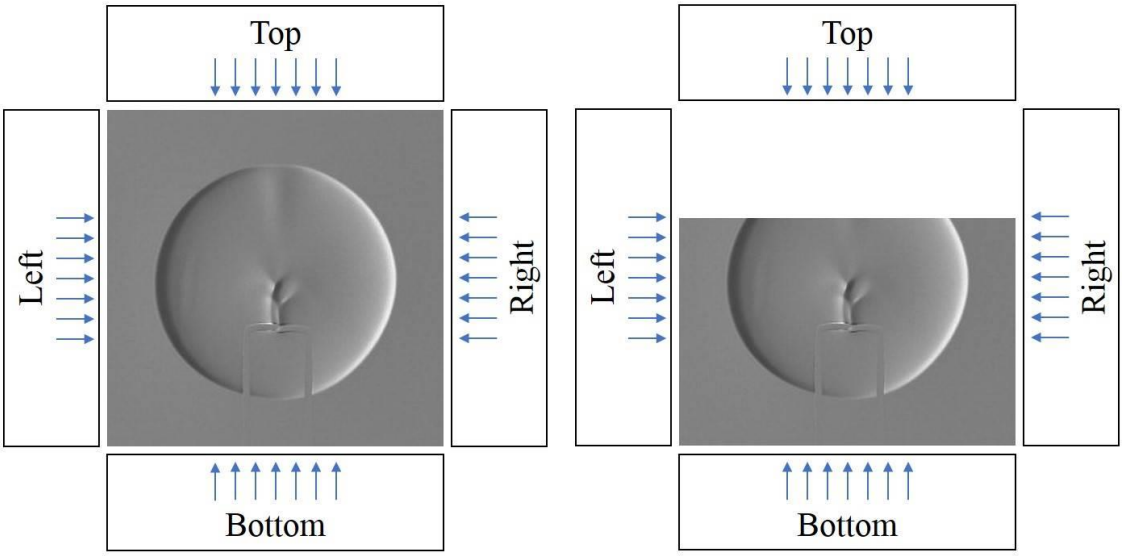

(a) Complete observation (b) Incomplete observation

Fig. 2.9 Sample schlieren images of the laminar flame kernel [9].

2.3. Results and Discussions

2.3.1. Quantitative Schlieren Brightness Images

Figure 2.10 shows quantitative schlieren images of the horizontal brightness deviation from the original experimental data of high-speed turbulent premixed flame [6]. The numbers inserted in each picture express the shooting angles θ. The images of Fig. 2.10 are processed by the above-mentioned "inverse process" to obtain quantitative schlieren images of vertical and diagonal brightness deviation. The results for new horizontal, vertical and diagonal (two directions) deviation brightness of quantitative schlieren images are depicted in Fig. 2.11 to Fig. 2.14, respectively.

2.3.2. Projections (Density Thickness) Images

For better evaluation of the "multi-path integration" noise reduction technique, in the new set of 20-directional schlieren images obtained from the inverse process, one thousand noises are distributed with various brightnesses and in the different positions randomly (Fig. 2.15(e)). Then, by using the former technique "single-path integration", in horizontal, vertical and diagonal directions, the projections images of density thickness with the existence of noise effects obtained (Fig. 2.15(a2)-(d2) and Fig. 2.16 to Fig. 2.19). Finally, the images of Fig. 2.11 (horizontal schlieren brightness gradient) and Fig. 2.12 (vertical schlieren brightness gradient) are processed by the above-mentioned conversion procedure "multi-path integration" to projection images of density thickness "with decreased noise level" (Fig. 2.15(f) and Fig. 2.20).

It is again noteworthy that remember, in which the new set of projections images of density thickness "with decreased noise level" can be obtained by using schlieren brightness gradient in horizontal and vertical or two perpendicular diagonal directions (Fig. 2.15(f)). As seen in Fig. 2.5(i1), Fig. 2.15(f) and Fig. 2.20) the noise effects are reduced to an acceptable level and slightly present around initial noise spots.

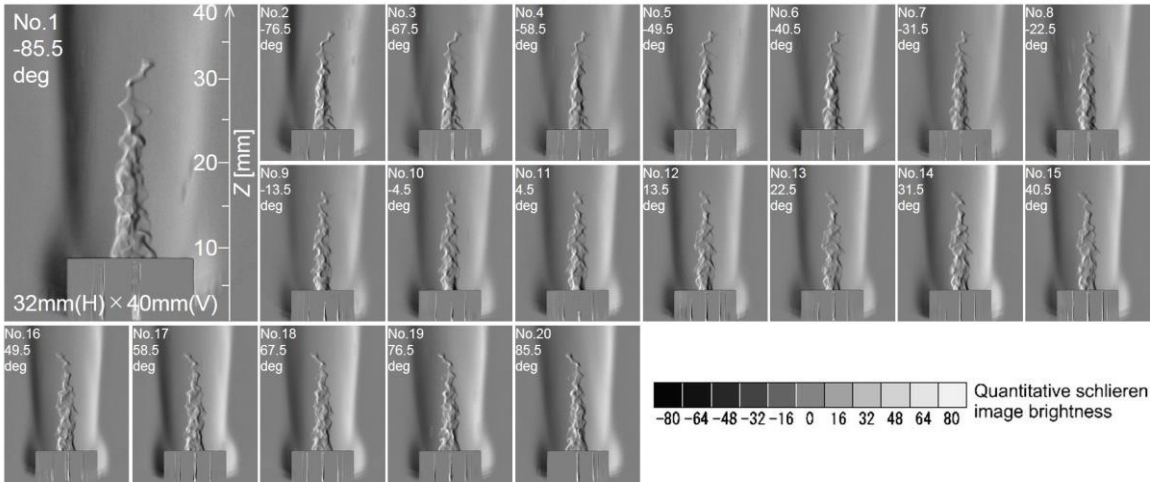

Fig. 2.10 Original quantitative schlieren images of target flame (U = 10 m/s) [6].

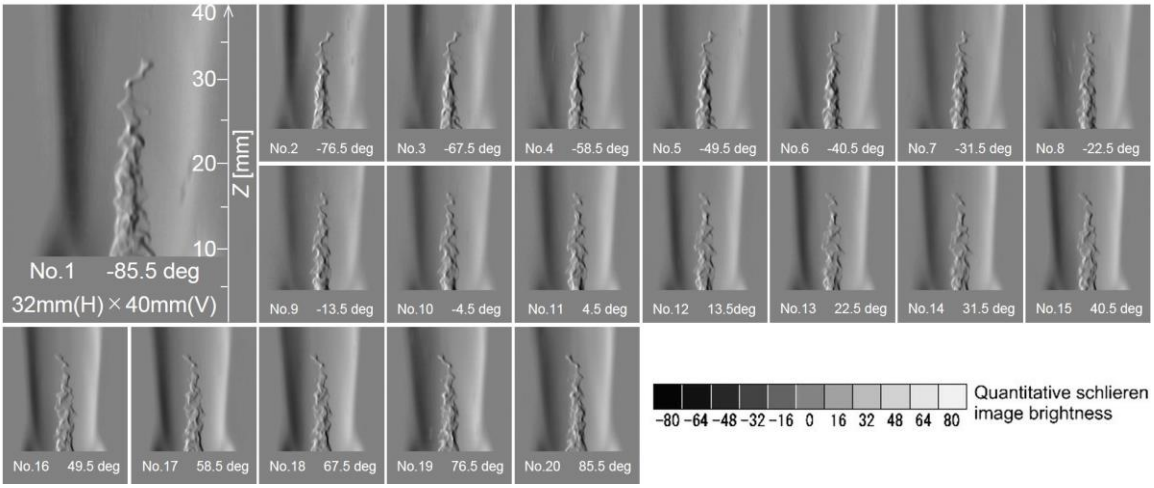

Fig. 2.11 Schlieren images with horizontal (0 degree) brightness gradient from inverse process.

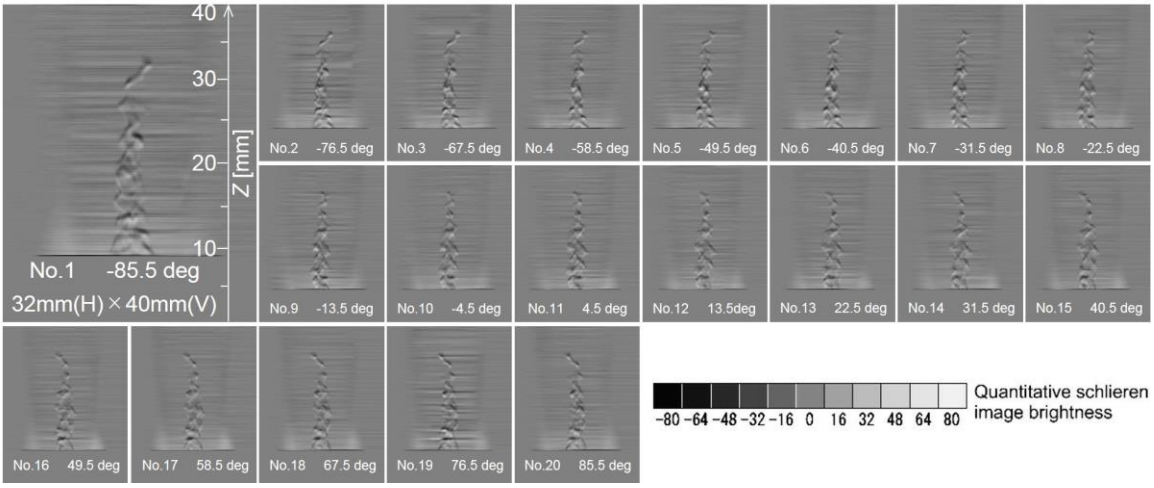

Fig. 2.12 Schlieren images with vertical (90 degree) brightness gradient from inverse process.

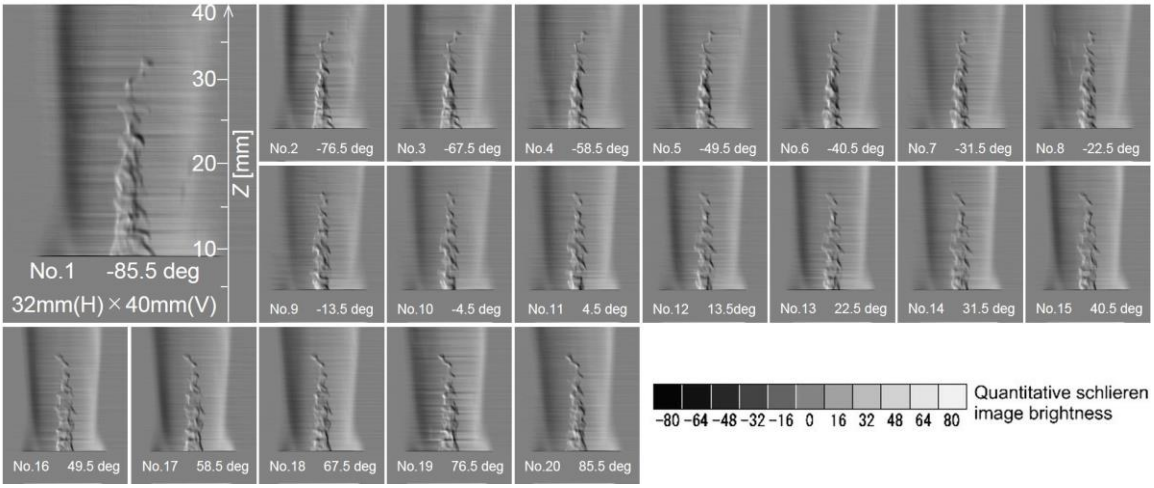

Fig. 2.13 Schlieren images with diagonal (45 degree) brightness gradient from inverse process.

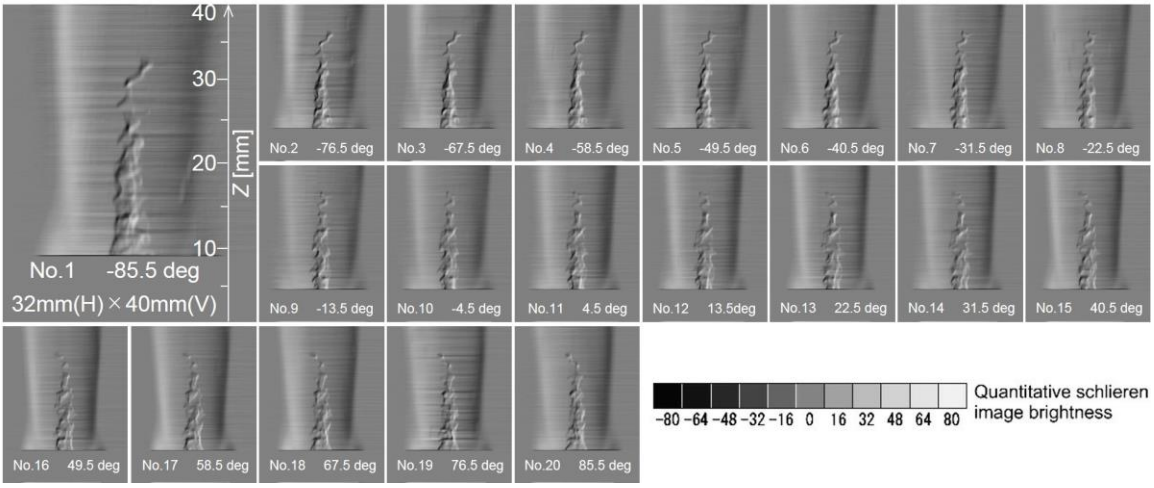

Fig. 2.14 Schlieren images with diagonal (135 degree) brightness gradient from inverse process.

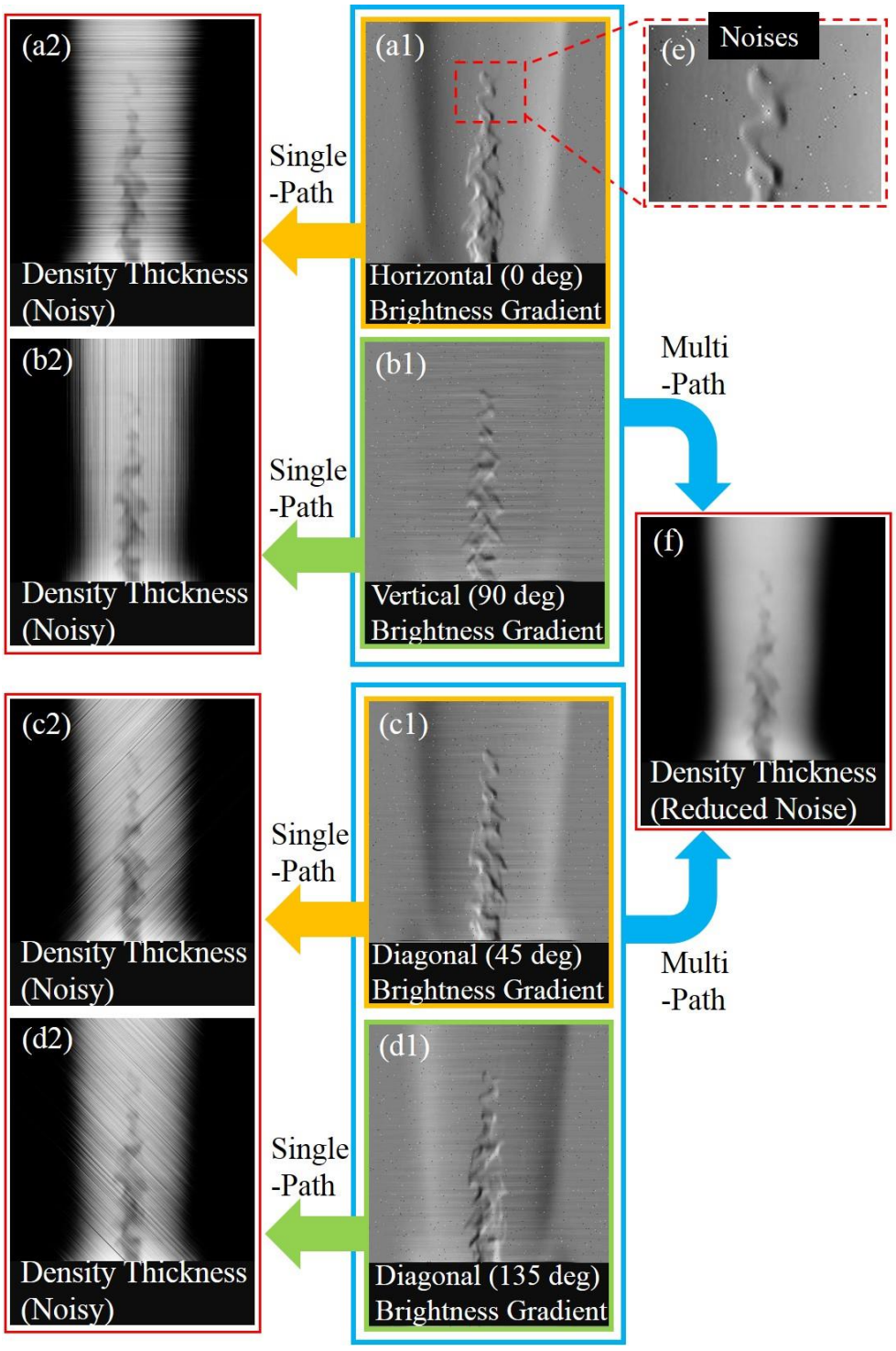

Fig. 2.15 Schlieren brightness in horizontal, vertical and diagonals gradient (a1) to (d1), conversion to the new projection (density thickness (*Dt*)) of CT by new "multi-path integration" technique (f), against noisy density thickness (*Dt*) images by former "single-path integration" technique (a2) to (d2).

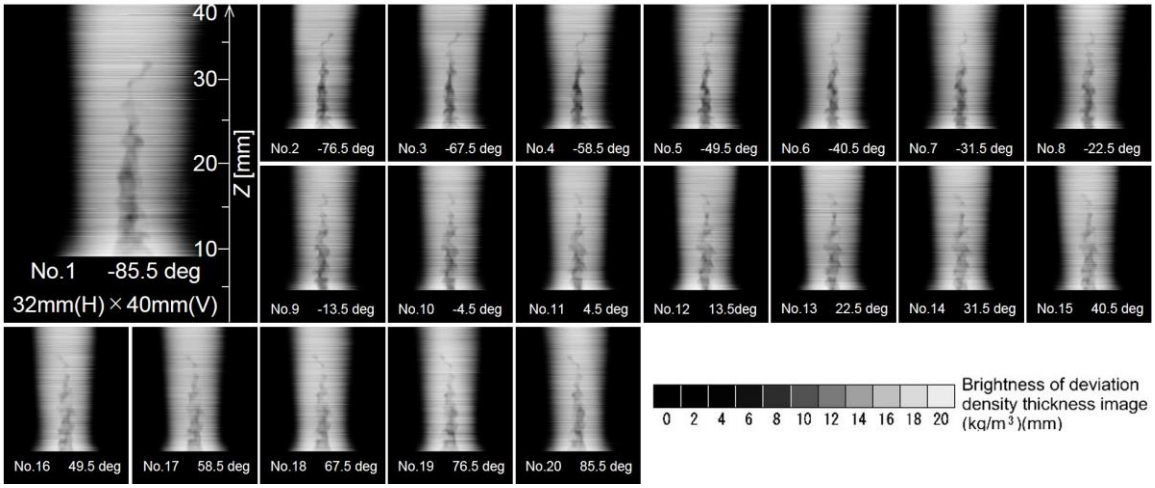

Fig. 2.16 Density thickness (*Dt*) images from "horizontal single-path integration" (noisy).

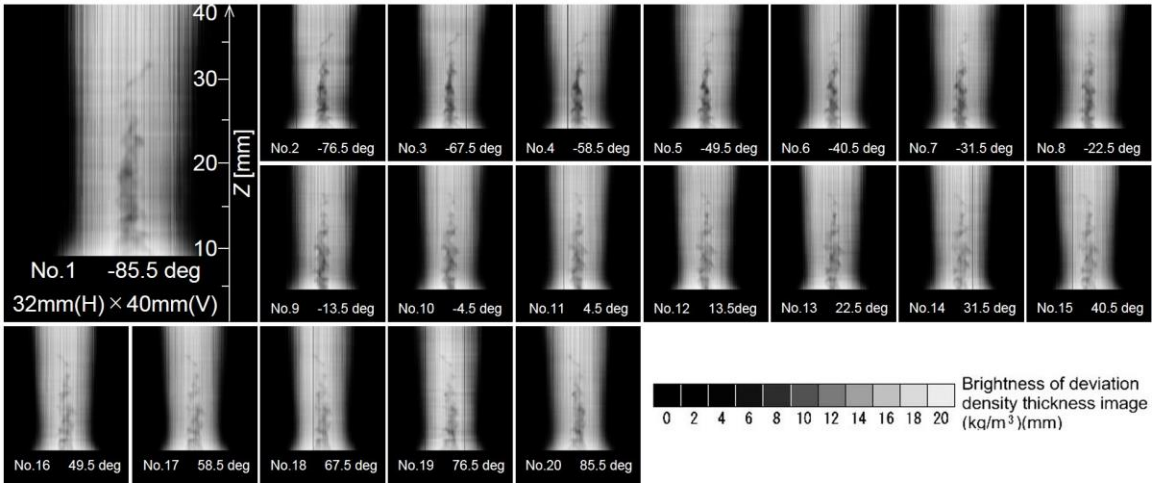

Fig. 2.17 Density thickness (*Dt*) images from "vertical single-path integration" (noisy).

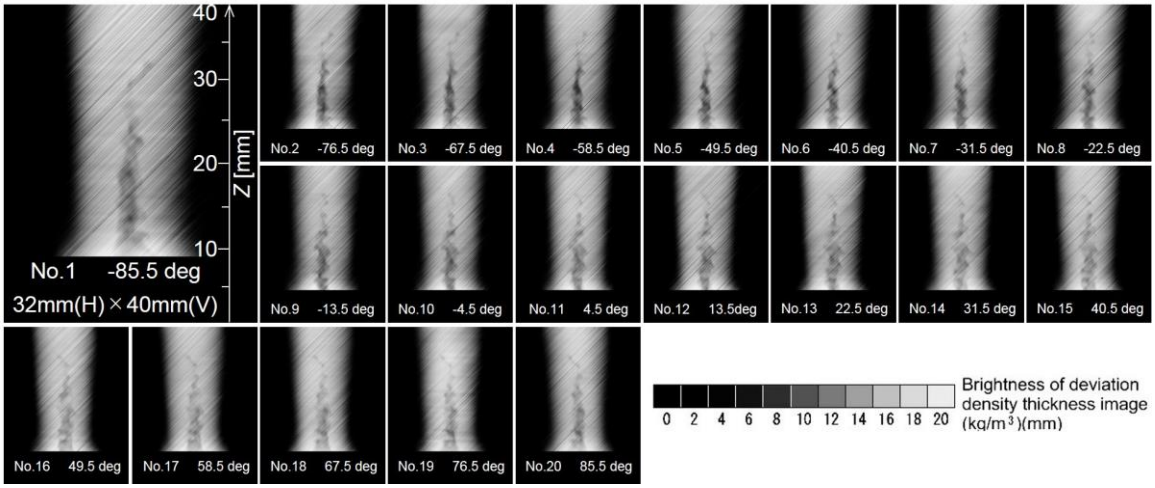

Fig. 2.18 Density thickness (*Dt*) images from "diagonal (45 degree) single-path integration" (noisy).

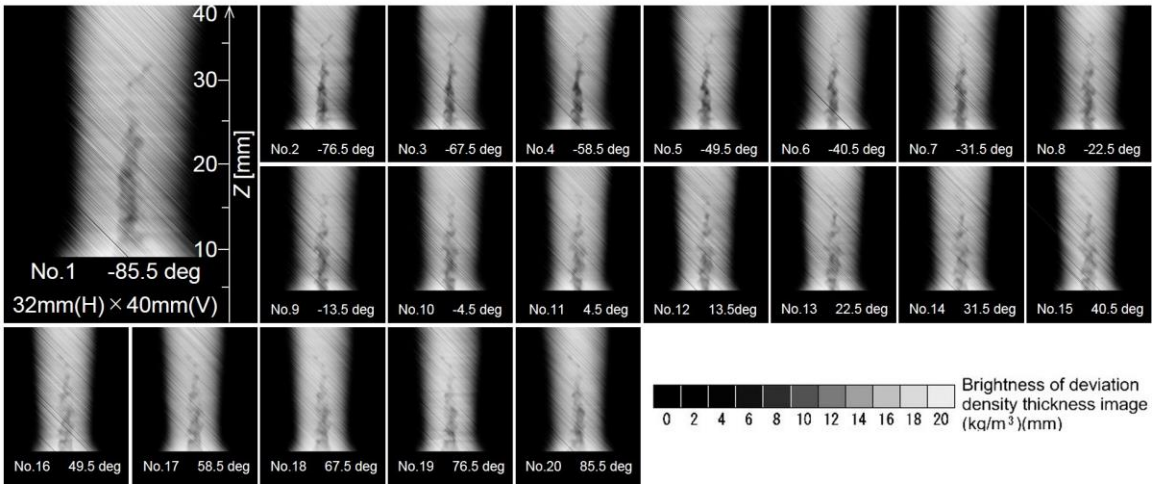

Fig. 2.19 Density thickness (*Dt*) images from "diagonal (135 degree) single-path integration" (noisy).

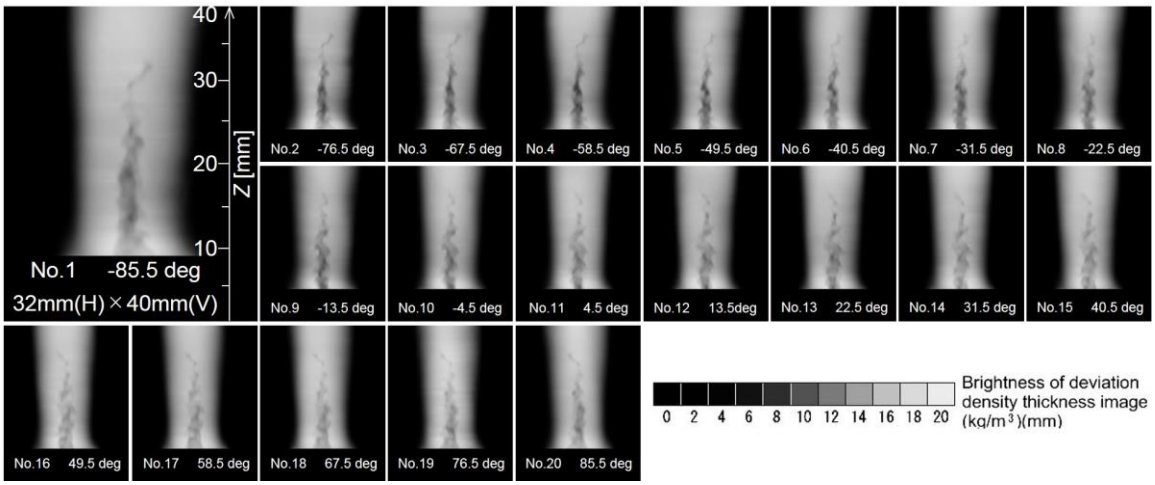

Fig. 2.20 Density thickness (*Dt*) images by "multi-path integration" with "decreased noise level".

2.3.3. CT-Reconstruction Results

By employing the density thickness images, noisy (Fig. 2.16) and with decreased noise level (Fig. 2.20) as projections for CT reconstruction, the 3D instantaneous density distributions of target flame have been successfully obtained for z = 8 mm to 40 mm (Fig. 2.21 and Fig. 2.22).

Figure 2.21 gives a sample set of one horizontal and one vertical cross-section of 3D-CT distributions of density. The values of the densities are displayed in light and dark based on the grayscale level (brightness bar chart) under the images. The darker parts are related to lower density areas with higher temperature and the brighter parts are related to higher density points with lower temperatures. For comparing new and former techniques, the corresponding density contour diagrams of each cross-section are depicted in Fig. 2.22, as well. The density distributions images from multi-path integration in Fig. 2.21(c2) and (c3) are uniform, but the results from single-path integration are streaky Fig. 2.21(c1) and (c4). As shown in Fig. 2.22(c4) the density contour diagrams from single-path integration are zigzagged form in contour lines.

Figure 2.23 provides the quantitative information of CT-reconstructed density distributions on the line of (y, z) = (0 mm, 24 mm). By applying the multi-path integration technique, the density distributions diagrams in the presence of noise have coincided with the absence of noise, but the noise effects clearly visible on the single-path integration results. Results demonstrate the importance of the new technique for noise reduction.

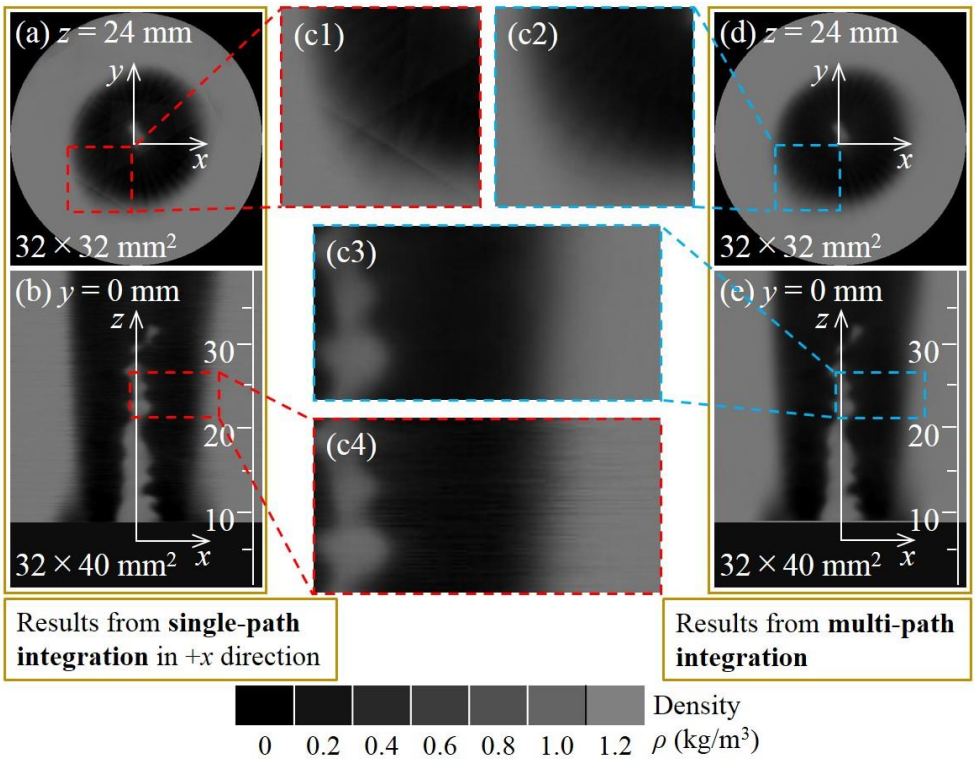

Fig. 2.21 Sample set of horizontal and vertical distributions of CT reconstructed density distribution of target flame.

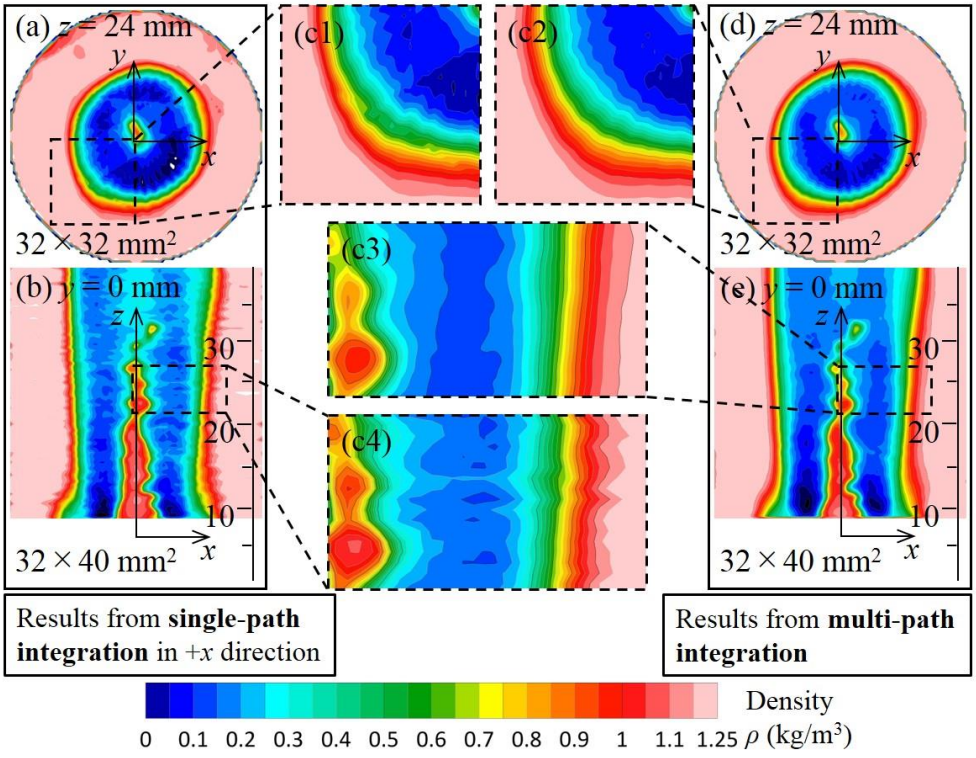

Fig. 2.22 Corresponding density contour diagrams of Fig. 2.21.

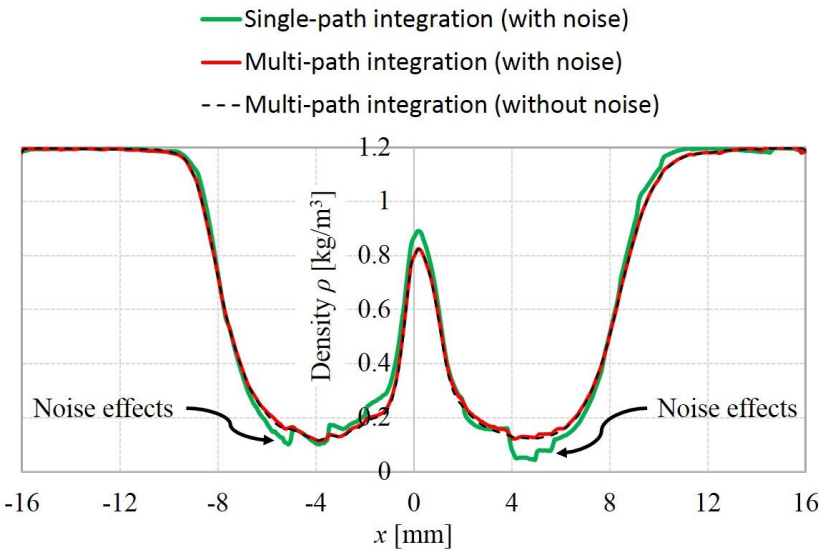

Fig. 2.23 Superposition of radial density distributions of CT-reconstructed density distributions of target flame for $y = 0$ and $z = 24$ mm.

2.4. Summary and Concluding Remarks

We applied the Cauchy integration theorem to develop the noise reduction technique. Based on Cauchy's integration theorem statement contour integral depends only on the beginning and ending points of the paths and does not depend on the integration path. Therefore, the integration procedure in multi-path directions is employed. In the present study, a new technique "multi-path integration" is proposed for "noise reduction" in projections (density thickness *Dt*) images of CT (computerized tomography). The schlieren brightness gradient information in two orthogonal directions (e.g. horizontal and vertical or two perpendicular diagonal directions) is required in the "multi-path integration" technique. The 20-directional quantitative schlieren optical system gives only images of schlieren brightness in the horizontal gradient and another 20-directional optical system seems necessary to obtain vertical schlieren brightness gradient, simultaneously. One suitable solution without the necessity of a new optical system is using the "inverse process". By employing the new "inverse process" technique, the actual experimental data is used for reproducing other directions of the schlieren brightness gradient. This new approach is a simple, efficient and cost-effective solution and can be used for obtaining any optional directions of schlieren brightness gradient. In this study, a schlieren image with information on the brightness gradient in two orthogonal directions is called a "complex schlieren image". It has shown an important ability of complex schlieren brightness gradient, which is independency on the path and starting point in the integration process. The results validate that the "multi-path integration" novel technique has the capability of noise reduction in obtaining projections (*Dt*) images of CT and the 3D density distributions of CT results. However, using noise reduction technique is not the first option, better than noise reduction is to control the primary generation sources of it, that no noise being produced.

3

CHAPTER 3

Journal of Flow Control, Measurement & Visualization, 8(3), 77-101

Multi-Schlieren CT Measurements of Supersonic Microjets from Circular and Square Micro Nozzles

Published: 2020.05.28

https://doi.org/10.4236/jfcmv.2020.83005

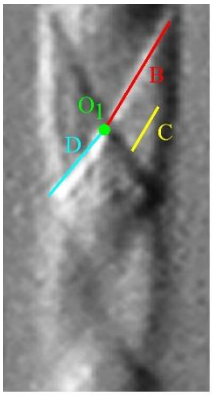

(1) Diagonal view sample from Camera No.5

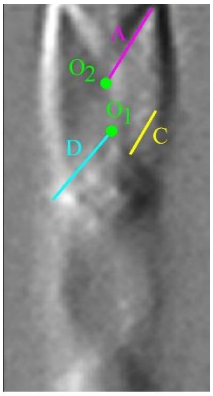

(2) Symetry view sample from Camera No.9

Abstract

Instantaneous three-dimensional (3D) density distributions of a shock-cell structures of perfectly and imperfectly expanded supersonic microjets escaping into an ambient space are measured. For the 3D observation of supersonic microjets, non-scanning 3D computerized tomography (CT) technique using a 20-directional quantitative schlieren optical system with flashlight source is employed for simultaneous schlieren photography. The 3D density distributions data of the microjets are obtained by 3D-CT reconstruction of the projection's images using maximum likelihood-expectation maximization. Axisymmetric convergent–divergent (Laval) circular and square micro nozzles with operating nozzle pressure ratio 5.0, 4.5, 4.0, 3.67, and 3.5 have been studied. This study examines perfectly expanded, overexpanded, and underexpanded supersonic microjets issued from micro nozzles with fully expanded jet Mach numbers M_j ranging from 1.47–1.71, where the design Mach number is M_d = 1.5. A complex phenomenon for free square microjets called axis switching is clearly observed with two types "upright" and "diagonal" of "cross-shaped". The initial axis-switching is 45° within the first shock-cell range. In addition, from the symmetry and diagonal views of square microjets for the first shock-cells, two different patterns of shock waves are viewed. The shock-cell spacing and supersonic core length for all nozzle pressure ratios are investigated and reported.

CHAPTER 3
SUPERSONIC MICROJETS

3.1. Introduction

Visual observation and investigation of fluid flow provide useful and comprehensive insight into a flow field under inspection and help derive quantitative data from the observed flow patterns. Fluids are mostly transparent, and therefore, invisible; there are some good techniques that can visualize flowing fluids with non-uniform density. A schlieren technique is very sensitive to density changes and it can visualize invisible flows in transparent media. This technique has been widely implemented in fluids and combustion. In fluid dynamics, the schlieren imaging technique is a common tool to illustrate detailed descriptions of air flows, shock waves, compressions, and expansion fans in supersonic jet flows for use in aerodynamical studies [1]. In previous works, a non-scanning three-dimensional computerized tomography (3D-CT) technique using a delicate multi(20)-directional quantitative schlieren optical system with a flashlight source was developed and employed to measure instantaneous density distributions of several types of flames in laminar and turbulent flows [6]-[10]; in addition, some new techniques have been introduced [11]-[13].

It is very difficult and unsatisfactory to investigate microjets when using measurement devices because of the very small dimensions of the micro nozzles, especially those close to the micro nozzle exit. In the present study, to provide a suitable technique for the 3D observation of a supersonic microjet (non-uniform density flow), a non-scanning 3D-CT technique using a multi-directional quantitative schlieren technique was employed [6]-[10]. This is the first study wherein the mentioned technique with a non-deviation treatment for projection images (density thickness images) is used to measure instantaneous density distributions on the shock-cell structure of perfectly and imperfectly expanded (overexpanded and underexpanded) supersonic microjets issued from circular and square micro nozzles.

Air microjets are employed to deliver pressure to a workpiece in many industrial activities using simple sonic nozzles [31]. Scroggs and Settles [31] explained that the selection of such sonic nozzles leads to restrictions and undesirable points. They suggested an alternative method: the application of

converging-diverging (Laval) supersonic micro nozzles that have highly uniform and stable properties. A supersonic microjet is a more effective small-scale high-pressure gas delivery device compared to sonic nozzles of comparable scale at equivalent mass flow rates. The main advantage of microjets is their ability to create high-density arrays of microjets without increasing flow rate. To the best of our knowledge, Scroggs and Settles [31] were the first authors to study micro nozzle flow and obtain schlieren images of a shock-cell structure of flow and axial and transverse pitot-pressure distributions. Further, they fabricated converging-diverging micro nozzles by heating and stretching glass capillaries; in these experiments, air was used as the working gas in the experiments. The nozzle exit diameters were 600 μm and 1,200 μm with exit Mach numbers ranging from 1.0-2.8 and Reynolds numbers ranging 20,000-45,000.

Aniskin *et al*. [32] reported a detailed study on the structure of underexpanded mini and microjets with a wide range of diameters ranging from 341-10.4 μm. The working gas in the experiments was nitrogen. The main parameters of supersonic underexpanded microjets are identified, including the size of shock-cells and the supersonic core length of the microjet. Phalnikar *et al*. [33] studied supersonic microjets escaping micro nozzles with diameters ranging between 100-1000 μm and presented the results of only 200 and 400 μm microjets, which include most features of interest; the working gas in their experiment was nitrogen. In addition, Phalnikar *et al.* [33] proposed a correlation for the size of shock-cells in the jet and for the relative supersonic core length. They obtained axial and transverse pressure distributions from a pitot pressure survey.

Supersonic microjets have diverse applications in various fields of engineering and industries; for example, in the cooling of micro-electro mechanical systems (MEMS) components, fine particle deposition and removal, and as actuators to control the ground effect in short take-off and vertical landing (STOVL) aircraft when hovering [33]. Further, microjets have been used in the removal of fine particles from a surface by impinging shock waves [34], microjet engines [35], in active control of gas-dynamic flows, and for significant reduction in the overall sound pressure levels of the aircraft [36] [37] [38], and for jet noise control [39].

Supersonic free jets issued from circular, square, rectangular with different aspect ratios, and regular triangular nozzles are visualized using a laser-induced fluorescence method proposed by Teshima [40]; it is found that these jets expand most prominently in the major and minor axial directions, which results in a cross-shaped cross-section. Tsutsumi *et al*. [41] investigated the structure of underexpanded jets for square nozzles and explained that these types of nozzle are of interest because of their use in clustered combustors of linear aerospike engines. These combustors are designed to minimize intercell gaps using a rectangular exit; the nozzle studied in the report of Tsutsumi *et al*. has a circular throat and a square exit, with the D_{throat} of 6 mm and a nozzle wall thickness of 1.5 mm. Noncircular jets were identified as an efficient technique for passive flow control [42]. Cabaleiro and Aider [43] reported the observation of the axis-switching of a microjet for the first time for free noncircular microjets.

There are very few experimental studies on supersonic microjets, especially for the square

cross-section, in the literature. However, with a few exceptions (e.g. [44][45]), most studies used the schlieren technique from a qualitative point of view and not for quantitative measurements. In most studies, quantitative measurements of the jets spreading as well as shock-cell spacing were obtained using micro-pitot probe surveys. In the present study, quantitative measurements and qualitative investigations are combined, and supersonic microjets from circular and square micro nozzles have been successfully CT-reconstructed with a custom-made 20-directional schlieren optical system. The results show instantaneous 3D density distributions downstream of the micro nozzles exit. Further, shock-cell spacing, supersonic core length, axis switching, and two different shocks patterns of the symmetry and diagonal views of square microjets are clearly observed and investigated.

3.2. Experimental Apparatus Setup and Methods

3.2.1. Image Processing

Figure 3.1 shows a conceptual framework for the formation of a projection image (density thickness) in the proposed schlieren 3D-CT system. Detailed descriptions of the various sections of Fig. 3.1(a)-(k), along with the supporting formula, are provided in the previous reports [6]-[13] and many other references cited therein. Here, for brevity, the main points of Fig. 3.1 are explained as follows. Density, deviation density, and density thickness values with an asterisk sign (*) express actual values, and those without the sign represent derived values from the CT-reconstruction process. Fig. 3.1(a) depicts density distribution $\rho^*(x, y)$ of target flow with an ambient gas (air) region of constant density ρ_a^*(= 1.2 kg/m^3) on the periphery of the observed range of radius R. Fig. 3.1(b)-(k) shows observations in the direction of θ from the x-axis in the inclined coordinates denoted by $X(\theta)$ and $Y(\theta)$.

The first goal is obtaining the density thickness of deviation density ($Dt^*(X(\theta))$), as shown in Fig. 3.1(d) with a unit of (kg/m^3)(m). The density thickness of deviation density $Dt^*(X(\theta))$ is obtained automatically from schlieren observation using spatial integration of deviation density $\Delta\rho^*(X(\theta),Y)$ along the line of sight. In other words, the density distribution of target flow is reconstructed using a 2D distribution (image) of "density thickness" as a projection in the CT-reconstruction process. In practice for obtaining density thickness of deviation density (Fig. 3.1(i)), the image processing activity starts from Fig. 3.1(e) by obtaining two sets of images, "with target" and "without target" (without any disturbance in the test section) with a horizontal brightness gradient in the x-direction. Two sets of images are presented by schlieren observation as $B(X)$ and $B_{nj}(X)$ (brightness of schlieren image in no-jet condition). To obtain the density thickness of deviation density $Dt(X(\theta))$ from $B(X)$ and $B_{nj}(X)$, both as shown in Fig. 3.1(f)-(i). As indicated in Fig. 3.1(f) and Fig. 3.1(g), the deviation brightness in schlieren image $\Delta B(X)$

$$\Delta B = B(X) - B_{nj}(X), \tag{3.1}$$

is scaled to $d(Dt)/dX$ by

$$d(Dt)/dX = (1/K)(\Delta s/f)[\Delta B(X)/B_{nj}(X)], \tag{3.2}$$

where K is the Gladstone-Dale constant for air (K = 2.26 × 10^{-4} m^3/kg), Δs (= 1 mm × 2 mm (Hor. × Ver.)) is the transparent width of the light source image on schlieren stop location and f (= 300 mm) is the focal length of the convergent lens. Deviation density thickness $Dt(X(\theta))$ is, therefore, reproduced by the transverse integration of $d(Dt)/dX$ from schlieren images, as shown in Fig. 3.1(h). Finally, the density thickness $Dt'(X(\theta))$ is obtained by adding the thickness of $(\rho_a^* - \rho_{ref})$ to the deviation density thickness $Dt(X(\theta))$ on the peripheral of the observed range of radius R (Fig. 3.1(i)), as expressed by

$$Dt'(X(\theta)) = Dt(X(\theta)) + 2\left(R^2 - X^2(\theta)\right)^{1/2}(\rho_a^* - \rho_{ref}). \tag{3.3}$$

In the present study, the ρ_{ref} = 0.8 is selected as a reference density, because of the minimum jet density is above this amount. Using non-deviation treatment for projections of CT by employing reference density, guarantee which the CT-reconstructed deviation density $(\Delta\rho(X(\theta),Y)+(\rho_a^*-\rho_{ref}))$ is

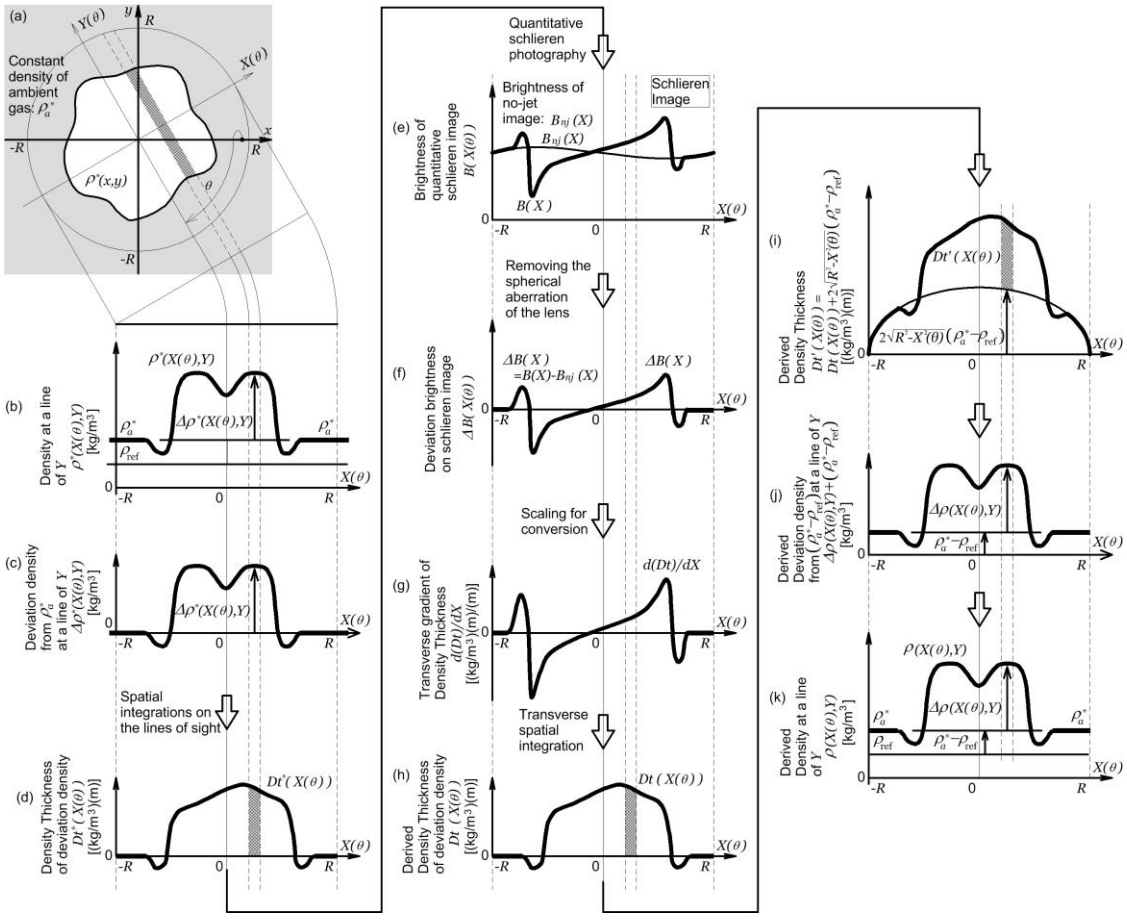

Fig. 3.1 Processes of formation of schlieren brightness and conversion to projections (density thickness (Dt)) of CT.

non-negative and CT-reconstruction is possible.

3.2.2. CT-Reconstruction

Density thickness images are used for CT-reconstruction by maximum likelihood-expectation maximization (ML-EM) [46] as an appropriate CT algorithm to obtain the 3D reconstruction of density distribution; the ML-EM method [6]-[13] is employed for CT-reconstruction. The CT procedure is carried out in each horizontal plane of the *z*-axis for the reconstruction of deviation density distribution $\Delta\rho(x,y)$ from a linear data set of density thickness $Dt'(X(\theta))$ (Fig. 3.1(j)). Finally, 2D density distribution (ρ_{ref}+[$\Delta\rho(X(\theta),Y)$+(ρ_a*−ρ_{ref})]) is obtained as follow, and ρ_{ref}, in which one step (Fig. 3.1(i)) was added, in this step again subtracted and removed (Fig. 3.1(k)),

$$\rho(x,y) = \Delta\rho(x,y) + \rho_a{}^* . \tag{3.4}$$

The reconstruction was performed cross-section by cross-section and then the cross-sections were stacked to form a three-dimensional density distribution. Therefore, a 2D distribution $\rho(x,y)$ is accumulated in layers to form the 3D-CT distribution $\rho(x,y,z)$. In the present study, the density thickness projections images of 50(H) × 375(V) pixel (2 × 15 mm^2) are used for CT-reconstruction to produce 3D data 50 (x) × 50 (y) × 375 (z) pixel (2 × 2 × 15 mm^3). The voxel size is 0.04 mm in each direction.

3.2.3. Micro Nozzles and Coordinate System

A circular [47] and a square [48] cross-section axisymmetric convergent-divergent (Laval) micro nozzles, with design Mach number M_d = 1.5, is studied. Details dimensions of micro nozzles are illustrated in Fig. 3.2. The circular nozzle has a throat diameter of 922 μm, an exit diameter of 1000 μm, and an area ratio A_e/A_{th} = 1.18; the square nozzle has a throat size of 850 × 850 μm^2, an exit size of 1000 × 1000 μm^2, an area ratio A_e/A_{th} = 1.38. The convergent and divergent section lengths are 6000 μm and 1300 μm, respectively. Detailed descriptions of micro nozzles are reported in [47][48]. The micro nozzle wall contour from parts A to B was designed using a sinusoidal curve and from parts B to C was calculated using the axisymmetric method of characteristics [49] to provide uniform and parallel flow at the downstream of the micro nozzle exit. In the camera system, the target supersonic microjet/non-uniform density field is observed from a 180° direction using numerous schlieren optical systems simultaneously. Twenty systems capture multi-directional views in the 20 angle positions from θ = −85.5° to +85.5° at intervals of 9°. The schematic diagram of a 20-directional and a single instance of a quantitative schlieren camera system is provided in Fig. 3.3. The center of the nozzle exit is selected as the origin of the *xyz*-coordinate system; the nozzle exits are then located downward in the negative *z*-axis. The *x*-axis is located between camera No. 10 (θ = −4.5°) and camera No. 11 (θ = +4.5°).

(a) Micro nozzle

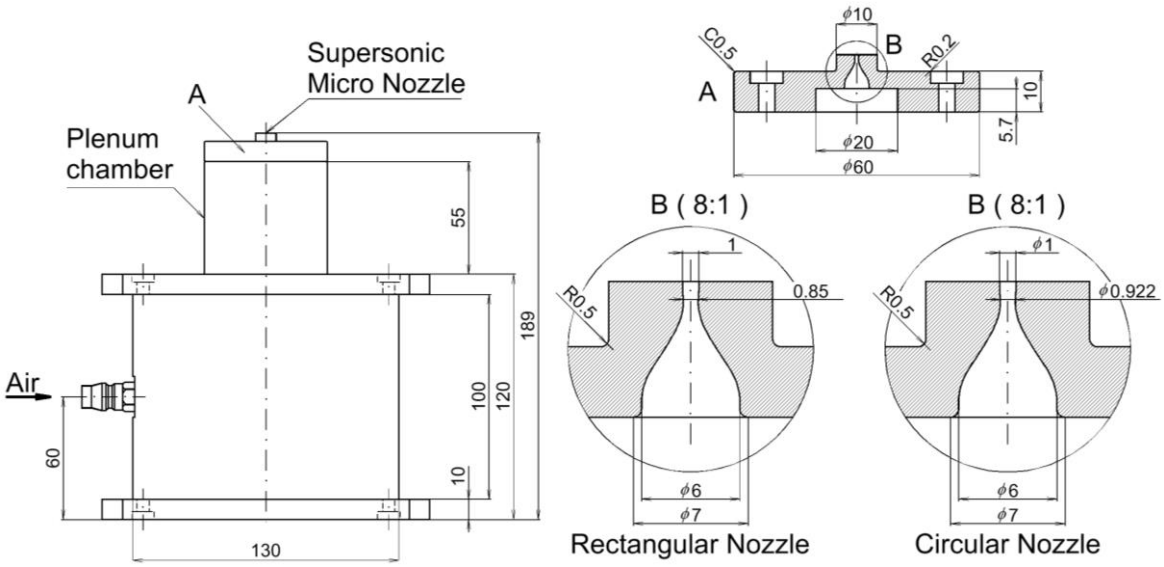

(b) Schematic diagram of the micro nozzles (dimensions in mm)

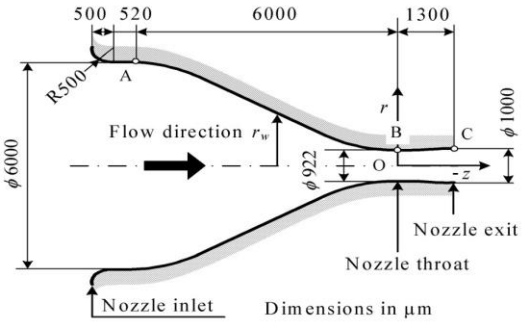

Part A to B: $r_w = 1270 \sin\left[\frac{\pi}{6000}(z-3000)\right] + 1731$

Part B to C: Axisymmetric method of characteristics

(c) Circular nozzle [47] (dimensions in μm)

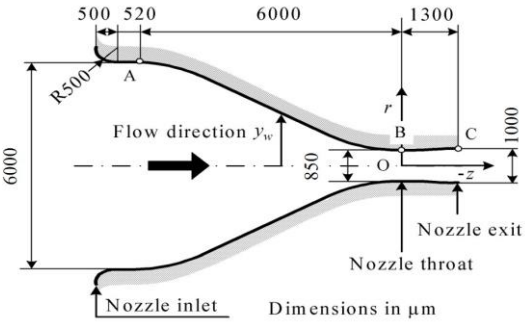

Part A to B: $y_w = 1288 \sin\left[\frac{\pi}{6000}(z-3000)\right] + 1713$

Part B to C: Method of characteristics

(d) Square nozzle [48] (dimensions in μm)

Fig. 3.2 Details dimensions of the micro nozzles.

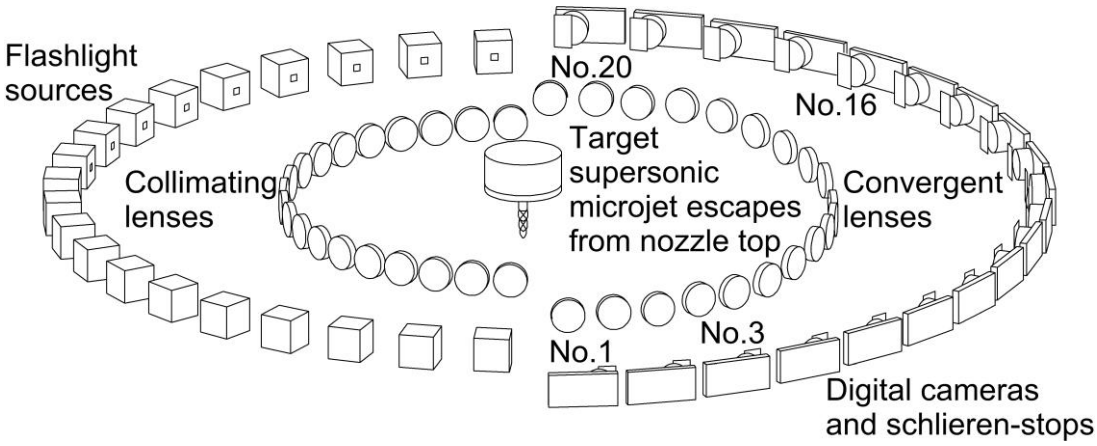

(a) Schematic of 20-direction schlieren camera

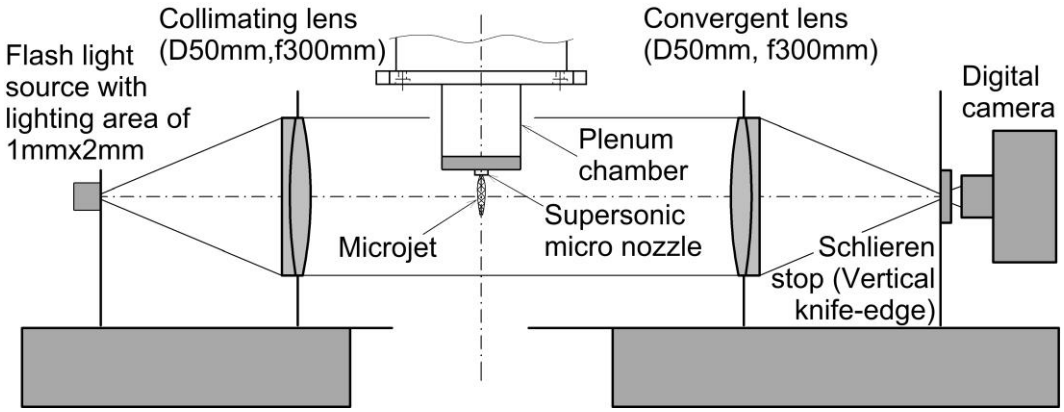

(b) Single unit of quantitative schlieren optical system

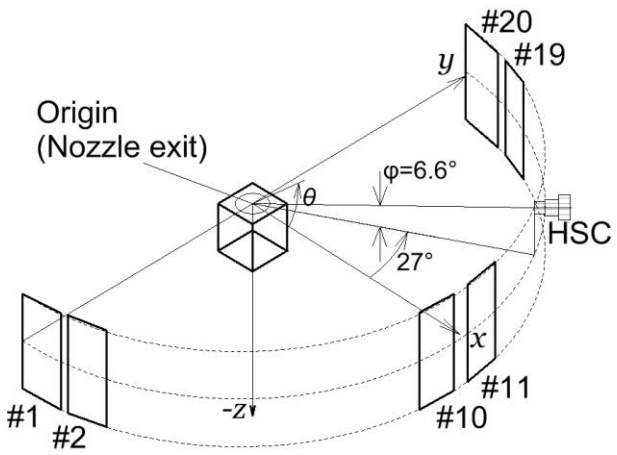

(c) Coordinate system

Fig. 3.3 Multi-direction schlieren optical system and coordinate system.

The schematic of the air delivery system is shown in Fig. 3.4 for both circular and square micro nozzles. A flow meter and a pressure gauge from SMC Co. are used as measuring instruments. The specifications of the flow meter, pressure gauge, and compressor supplying compressed air are shown below.

Pressure gauge specifications

Model:	SMC ISE30A
Rated pressure range:	-0.1 to 1.0 MPa
Withstand pressure:	1.5 MPa
Display/Minimum unit setting:	0.001 MPa
Power supply voltage:	12 to 24 VDC ±10%
Operating temperature range:	Operating: 0 to 50°C, Stored: -10 to 60°C (no freezing or condensation)

Flow meter specifications

Model:	SMC PFM750
Flow rate range:	1 to 50 L/min
Rated pressure range:	-70 to 750 kPa
Minimum unit setting:	0.1 L/min
Power supply voltage:	24 VDC ±10%
Operating fluid temperature:	0 to 50°C (with no freezing and condensation)

Air compressor specifications

Model:	PAOCK UD-1010 II
Maximum working pressure:	0.8 MPa
Tank capacity:	10 L
Flow rate:	90 L/min

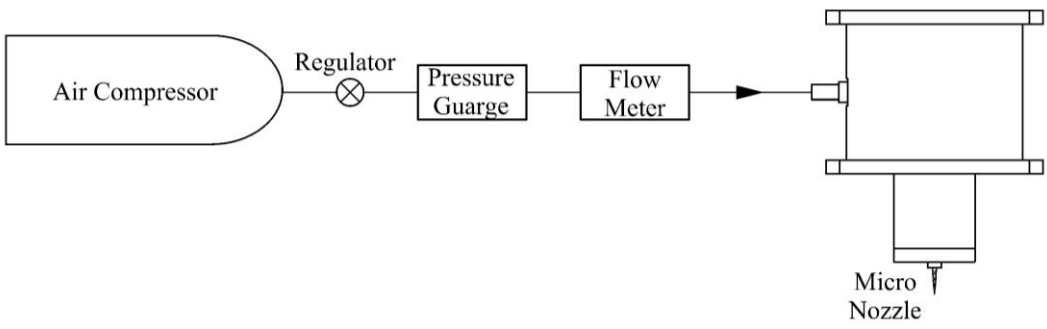

Fig. 3.4 Schematic of air delivery system.

3.2.4. Isentropic Nozzle-Flow Relations [50]

In real life all fluids are compressible - even water - their density will change as pressure changes to some greater or lesser quantity. The following equation (3.5) is frequently used in the analysis of compressible flows and relates pressure, density, and temperature for an isentropic process.

$$\frac{p_2}{p_1} = \left(\frac{\rho_2}{\rho_1}\right)^{\gamma} = \left(\frac{T_2}{T_1}\right)^{\gamma/(\gamma-1)}, \tag{3.5}$$

where γ is the specific heat ratio of air (=1.4).

In the present study, circular and square cross-section axisymmetric convergent-divergent (Laval) micro nozzles are studied. A schematic diagram of the convergent-divergent (Laval) nozzle is shown in Fig. 3.5. Inside the convergent-divergent nozzle in the flow direction, the speed of flow increases while pressure and temperature decrease.

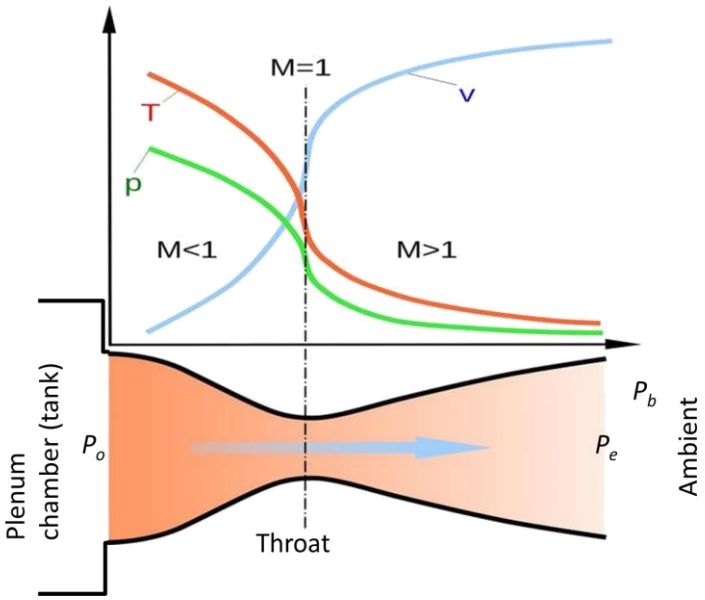

Fig. 3.5 Schematic diagram of convergent-divergent (Laval) nozzle.

A convergent-divergent nozzle can be identified with the design Mach number. Mach number is a dimensionless quantity expressing the ratio of the speed of a flow to the speed of sound in the surrounding medium ($M = V / a$), which classifies the flow regimes to the following classifications:

$M < 1$ (subsonic flow)
$M = 1$ (sonic flow)
$M > 1$ (supersonic flow)

In a convergent-divergent nozzle, the wall contour on the inlet side converges to a minimum area also known as the throat. After that, it diverges from the throat to the nozzle exit. The convergent portion of the nozzle accelerates the subsonic flow to sonic conditions at the throat, and then it is further accelerated to supersonic speeds in the divergent region until it reaches the nozzle exit. The design Mach number (M_d) at the exit depends on the ratio of the nozzle exit area (A_e) and the throat area (A^*), which is expressed in the following equation,

$$\frac{A_e}{A^*} = \frac{1}{M_d}\left(\frac{1+\frac{1}{2}(\gamma-1)M_d^2}{\frac{1}{2}(\gamma+1)}\right)^{\frac{\gamma+1}{2(\gamma-1)}}, \tag{3.6}$$

and, the fully expanded jet Mach number (M_j) depends on the ratio of the fully expanded jet cross-section area (A_j) and the throat area (A^*), which is expressed in the following equation,

$$\frac{A_j}{A^*} = \frac{1}{M_j}\left(\frac{1+\frac{1}{2}(\gamma-1)M_j^2}{\frac{1}{2}(\gamma+1)}\right)^{\frac{\gamma+1}{2(\gamma-1)}}. \tag{3.7}$$

The relation between stagnation (plenum chamber, tank) conditions and a point in the flow as a function of the Mach number at that point are defined in the following equations for pressure, density and temperature, respectively (subscript *o* represents the stagnation condition).

$$\frac{P_o}{P} = \left[1+\frac{1}{2}(\gamma-1)M^2\right]^{\frac{\gamma}{\gamma-1}}, \tag{3.8}$$

$$\frac{\rho_o}{\rho} = \left[1+\frac{1}{2}(\gamma-1)M^2\right]^{\frac{1}{\gamma-1}}, \tag{3.9}$$

$$\frac{T_o}{T} = \left[1+\frac{1}{2}(\gamma-1)M^2\right], \tag{3.10}$$

Each convergent-divergent nozzle is designed for one Mach number when operated at ideal conditions. Whether the nozzle operates at the ideal condition depends on the nozzle pressure ratio (*NPR*) of the flow. The nozzle pressure ratio (*NPR*) is defined as the ratio of the stagnation pressure (P_o) to the ambient pressure (P_b) (equation (3.11)). The design nozzle pressure ratio (*DNPR*) is defined as the ratio of the stagnation pressure (P_o) to the exit pressure (P_e), which the nozzle operates at the ideal, design

condition (equation (3.12)).

$$NPR = \frac{P_o}{P_b} = \left[1 + \frac{1}{2}(\gamma - 1)M_j^2\right]^{\frac{\gamma}{\gamma-1}}, \tag{3.11}$$

$$DNPR = \frac{P_o}{P_e} = \left[1 + \frac{1}{2}(\gamma - 1)M_d^2\right]^{\frac{\gamma}{\gamma-1}}. \tag{3.12}$$

3.2.5. Supersonic Microjets

The jet pressure ratio (*JPR*) is defined as the ratio of the exit pressure (P_e) to the ambient pressure (P_b). It is straightforward to derive an equation for jet pressure ratio (*JPR*) by dividing the last two equations ((3.11) and (3.12)),

$$JPR = \frac{P_e}{P_b} = \left[\frac{1 + \frac{1}{2}(\gamma - 1)M_j^2}{1 + \frac{1}{2}(\gamma - 1)M_d^2}\right]^{\frac{\gamma}{\gamma-1}}. \tag{3.13}$$

Based on the jet pressure ratio (*JPR*), a convergent-divergent nozzle can be operated at two conditions, which referred to as design condition and off-design condition. When the convergent-divergent nozzle operates at the design condition, the supersonic jet is said to be perfectly (ideally, correctly) expanded. When the convergent-divergent nozzle operates at off-design condition, two different shock patterns in the core region are observed, which are referred to as overexpanded and underexpanded supersonic jets. The above descriptions related to the supersonic jets regions are summarized in Table 3.1.

Table 3.1 The supersonic jets regions.

Design condition (Pressure matched)	1	Perfectly-expanded (ideally, correctly)	if $P_e/P_b=1$ or $M_j=M_d$
Off-design condition (Pressure mismatched)	2	Overexpanded	if $P_e/P_b<1$ or $M_j<M_d$
	3	Underexpanded	if $P_e/P_b>1$ or $M_j>M_d$

A jet is referred to as underexpanded if jet pressure ratio (*JPR*), $P_e/P_b > 1$, overexpanded if $P_e/P_b < 1$, and perfectly expanded or pressure matched if $P_e/P_b = 1$. In the present work, axisymmetric convergent-divergent (Laval) circular and square micro nozzles with operating nozzle pressure ratios ($NPR = P_o/P_b$) of 5.0, 4.5, 4.0, 3.67, and 3.5 have been studied. This study examines perfectly-expanded

(ideally, correctly expanded) and imperfectly-expanded (overexpanded and underexpanded) supersonic microjets issued from micro nozzles with fully expanded jet Mach numbers M_j ranging from 1.47 to 1.71. The design Mach number of these micro nozzles is M_d = 1.5. The isentropic nozzle-flow relation [50] is used in the analysis of supersonic flow. The ambient and flow conditions for target supersonic microjets are summarized in Table 3.2 and Table 3.3, respectively.

Table 3.2 Conditions of ambient and micro nozzles.

Quantity	Symbol	Circular Nozzle	Square Nozzle
Ambient temperature	T_b	300.35 K (27.2 °C)	296.55 K (23.4 °C)
Back (ambient) pressure	P_b	0.101 MPa	0.102 MPa
Nozzle design Mach number	M_d	1.5	1.5
Nozzle exit diameter or exit size	D or $h \times b$	1000 μm (1 mm)	1000×1000 μm^2

Table 3.3 Flow conditions of targets supersonic microjets.

Quantity [Unit]	Symbol	Nozzle	Nozzle Pressure Ratio NPR (= P_o/P_b)				
			5.0	4.5	4.0	3.67	3.5
Absolute (Stagnation) pressure [MPa]	P_o	Circular	0.505	0.455	0.404	0.371	0.354
		Square	0.510	0.459	0.408	0.374	0.357
Gauge pressure [MPa]	P_G	Circular	0.404	0.354	0.303	0.270	0.253
		Square	0.408	0.357	0.306	0.272	0.255
Jet pressure ratio (JPR)	P_e/P_b	Circular	1.36	1.23	1.09	1.0	0.95
		Square					
Exit pressure [MPa]	P_e	Circular	0.138	0.124	0.110	0.101	0.096
		Square	0.139	0.125	0.111	0.102	0.097
Fully expanded jet Mach number	M_j	Circular	1.709	1.638	1.559	1.5	1.467
		Square					
Fully expanded jet diameter / height [μm]	D_j	Circular	1070	1044	1018	1000	991
	h_j	Square					
Reynolds number	Re	Circular	29875	29083	28140	27410	26991
		Square	29978	29182	28237	27504	27084
Operating condition	-	Circular / Square	Underexpanded			Full expanded	Over expanded

3.3. Results and Discussions

In this study, the supersonic micro-jets have been successfully CT-reconstructed with the non-scanning 3D-CT technique using a 20-directional quantitative schlieren system. The results show the instantaneous 3D density distributions downstream of the nozzles exit. The 3D-CT reconstruction results for supersonic micro-jets issuing from circular and square micro nozzles are shown in the following subsections.

3.3.1. Quantitative Schlieren and Projections (Density Thickness) Images

The quantitative schlieren images are derived from the schlieren images photographed simultaneously from 20 directions (as shown in Fig. 3.1**(**f)). The brightness of schlieren images (B) are calibrated by grayscale by subtracting the state without target images (B_{nj}). The place where the brightness value becomes 0 is changed to 128. In the quantitative schlieren images, the color of the two sides of jet boundaries is different (dark and bright) because the knife-edge orientation will reveal directional density gradients. In our schlieren optical system the knife-edge located from left to right.

The quantitative schlieren images are processed by the mentioned conversion procedure (Sec. 3.2.1) to projection images of deviation density thickness (density thickness) (as shown in Fig. 3.1**(**i)). The deviation density thickness (density thickness) images are spatially-integration of deviation density in the horizontal direction along the line of sight which automatically obtains from schlieren observation.

Figure 3.6 indicates a sample set of quantitative schlieren images for all *NPR* only for camera No. 12, and the corresponding sample set of projection images of density thickness $Dt'(X(\theta))$ are depicted in Fig. 3.7. The positions of the first "shock-cell spacing (length) L_s" and "supersonic core length L_c" are depicted by the dashed line in Fig. 3.6 and Fig. 3.7, which will be discussed in section 3.3.4.

Figure 3.8(a) to Fig. 3.17(a) indicate 20-directional quantitative schlieren images and corresponding projection images of density thickness (Fig. 3.8(b) to Fig. 3.17(b)) for supersonic microjets issuing from the circular and square micro nozzles with operating nozzle pressure ratios 5.0, 4.5, 4.0, 3.67 and 3.5, respectively.

A grayscale level showing the brightness value of the quantitative schlieren image is displayed below the images, also, the value of the deviation density thickness is displayed in light and dark based on the grayscale level under the images. The brighter parts are related to the more thickness of the deviation density from the surrounding air density. The numbers inserted in each picture express the camera number and the shooting angle θ. Each image is 2 mm × 15 mm in size. The scale of the z coordinate is also shown in image No. 10.

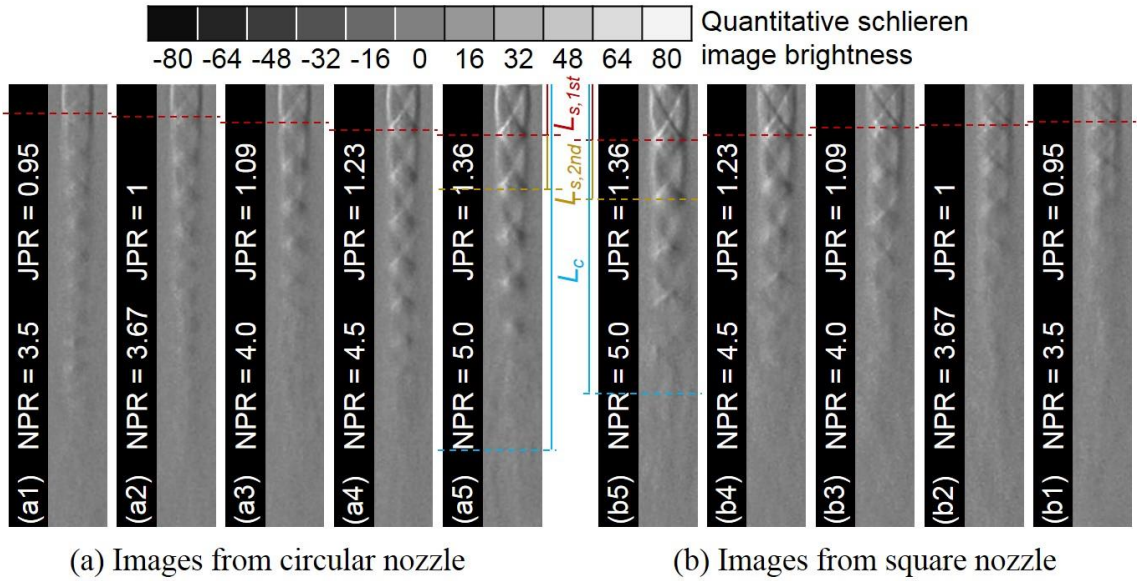

Fig. 3.6 Quantitative schlieren images of overexpanded (a1, b1), perfectly-expanded (a2, b2) and underexpanded (a3-a5, b3-b5) of supersonic microjets (images from camera No.12).

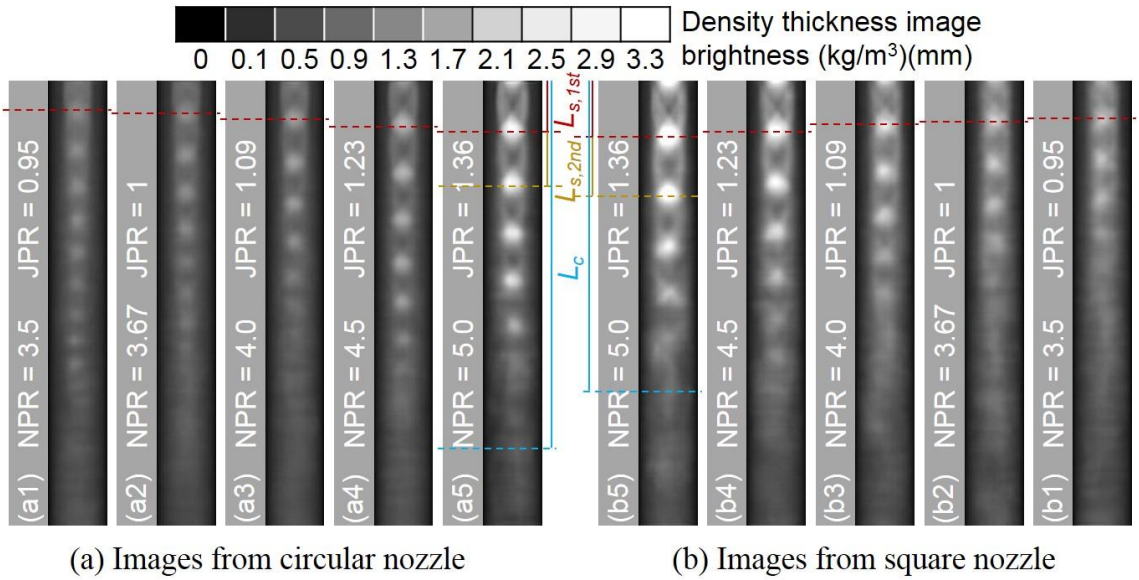

Fig. 3.7 Density thickness images of overexpanded (a1, b1), perfectly-expanded (a2, b2) and underexpanded (a3-a5, b3-b5) of supersonic microjets (images from camera No.12).

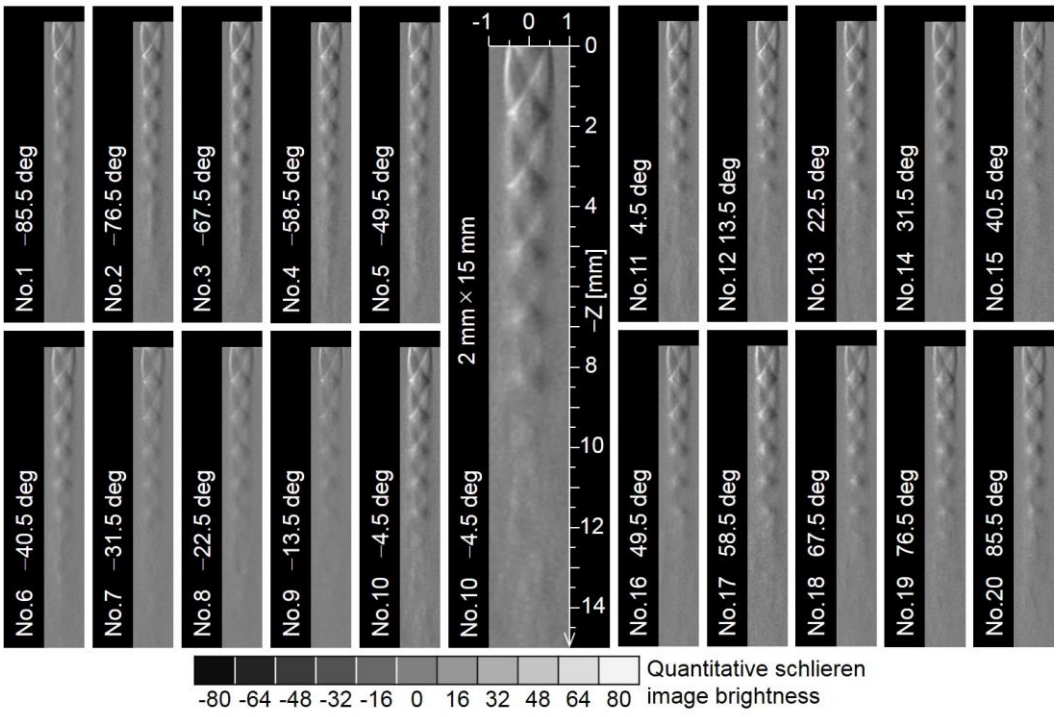

(a) Quantitative schlieren images, circular microjet

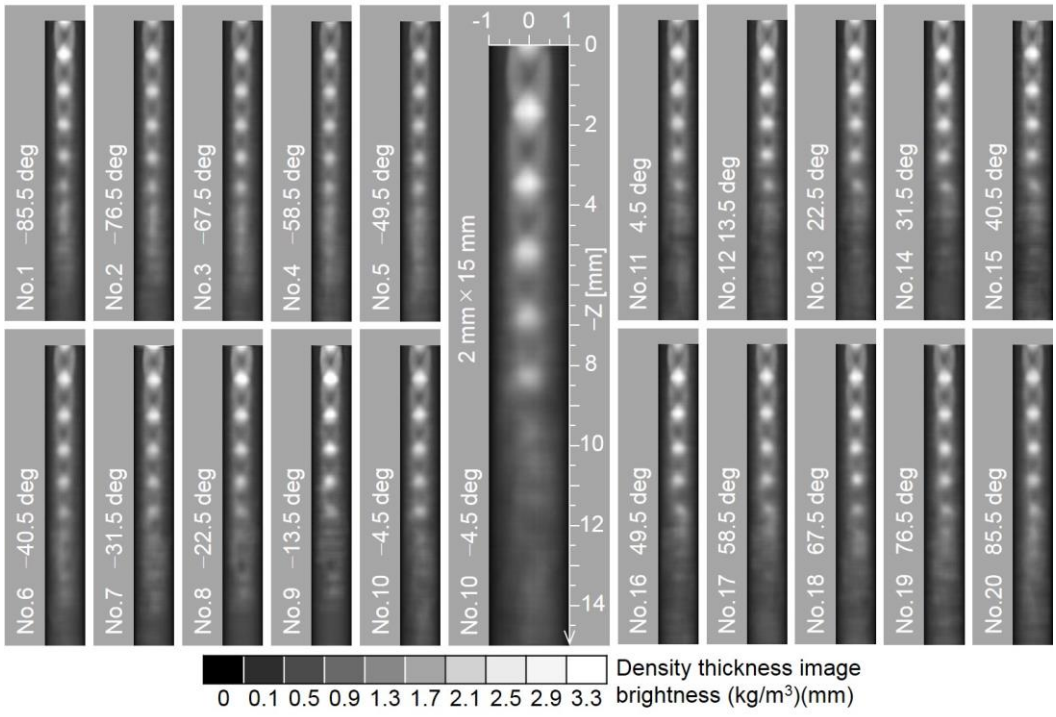

(b) Density thickness images, circular microjet

Fig. 3.8 Quantitative schlieren and density thickness images, circular nozzle, *NPR* = 5.0.

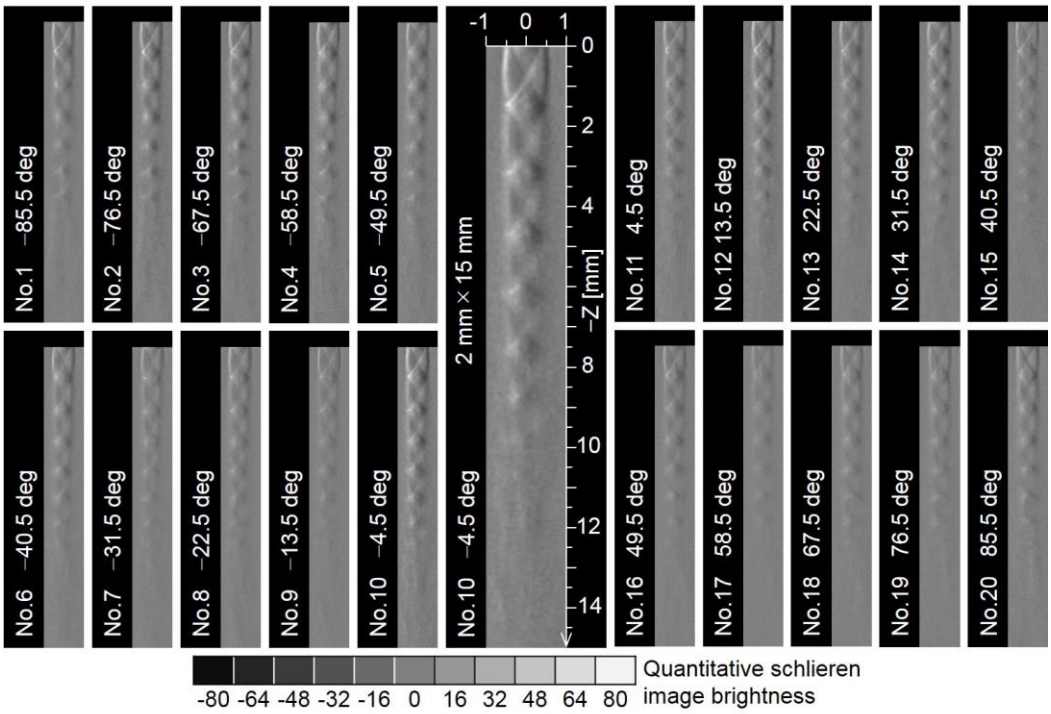

(a) Quantitative schlieren images, circular microjet

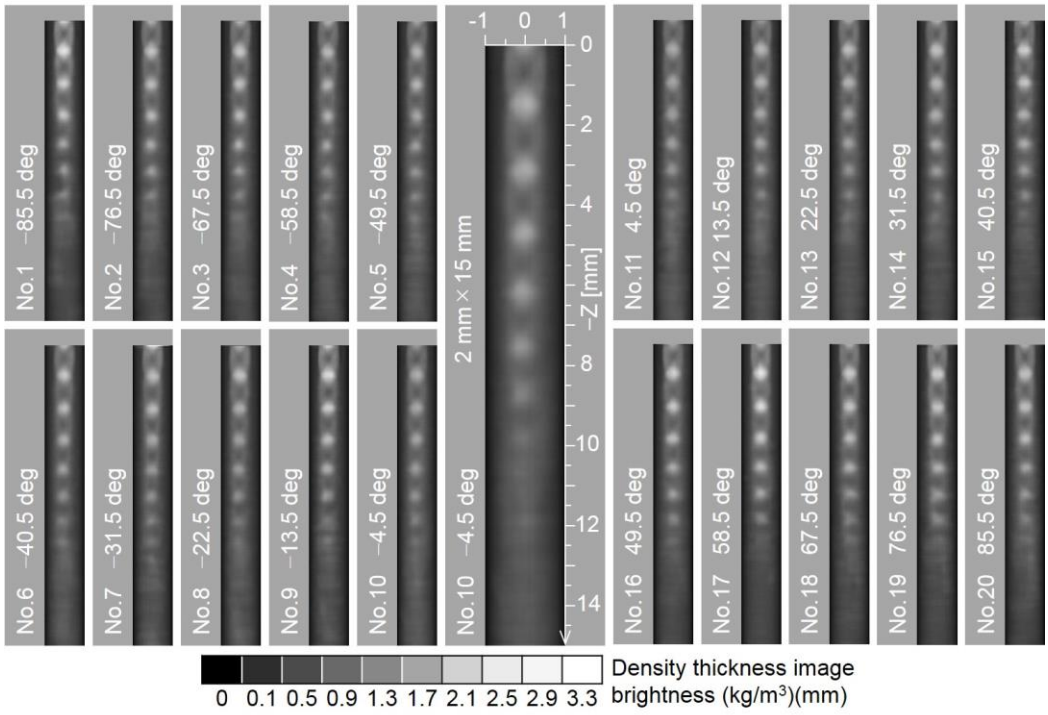

(b) Density thickness images, circular microjet

Fig. 3.9 Quantitative schlieren and density thickness images, circular nozzle, *NPR* = 4.5.

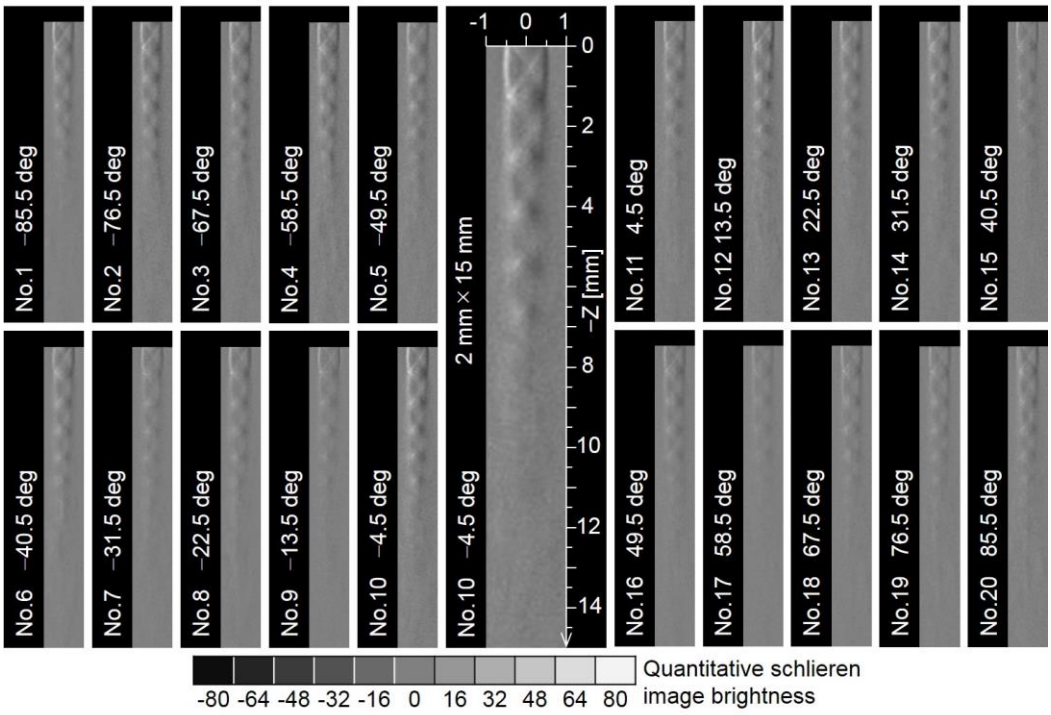

(a) Quantitative schlieren images, circular microjet

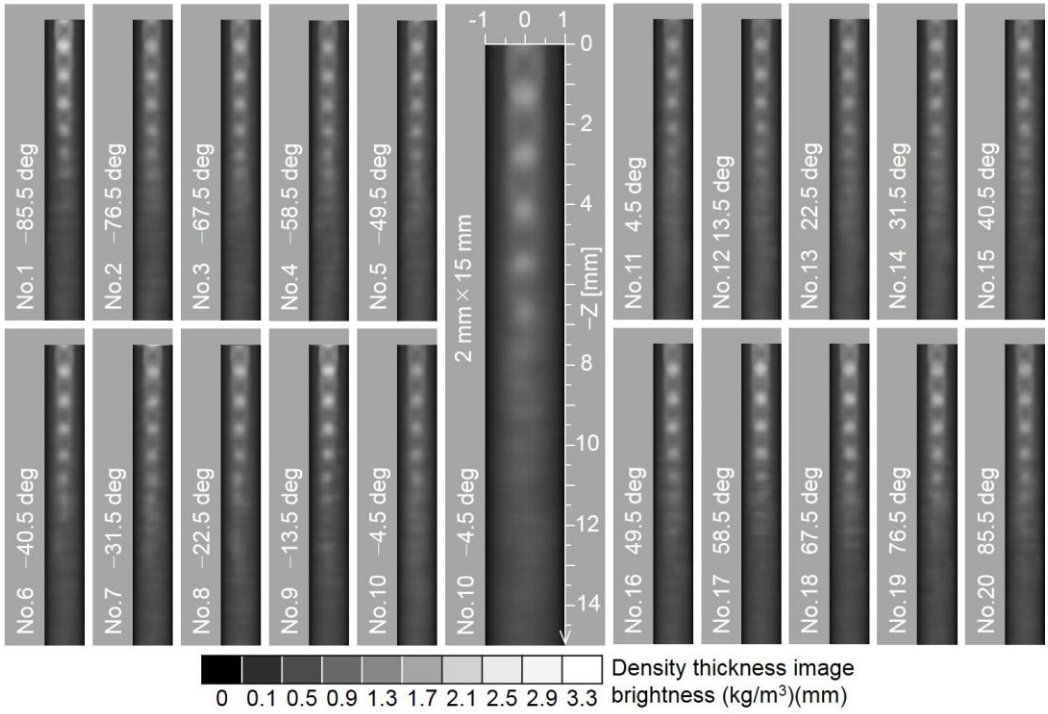

(b) Density thickness images, circular microjet

Fig. 3.10 Quantitative schlieren and density thickness images, circular nozzle, *NPR* = 4.0.

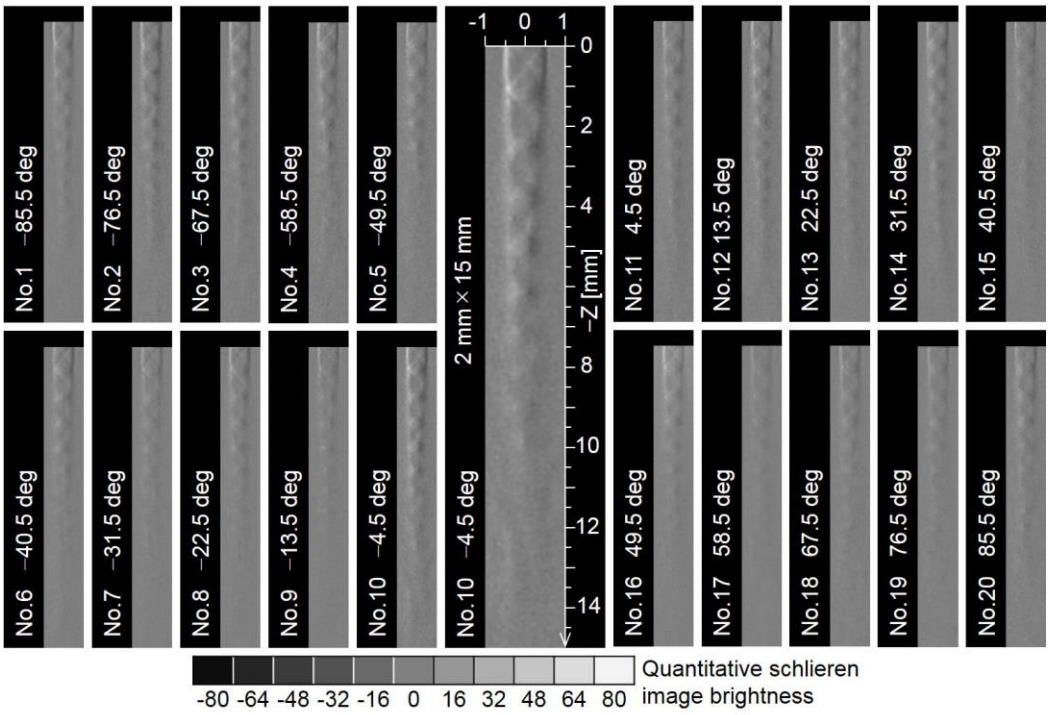

(a) Quantitative schlieren images, circular microjet

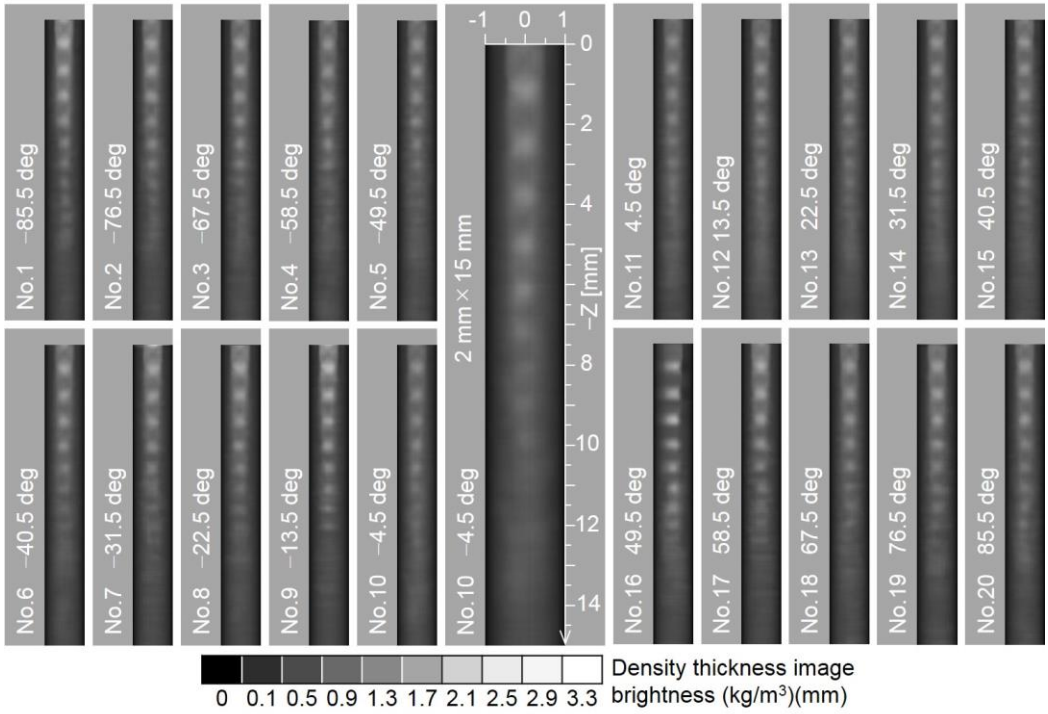

(b) Density thickness images, circular microjet

Fig. 3.11 Quantitative schlieren and density thickness images, circular nozzle, *NPR* = 3.67.

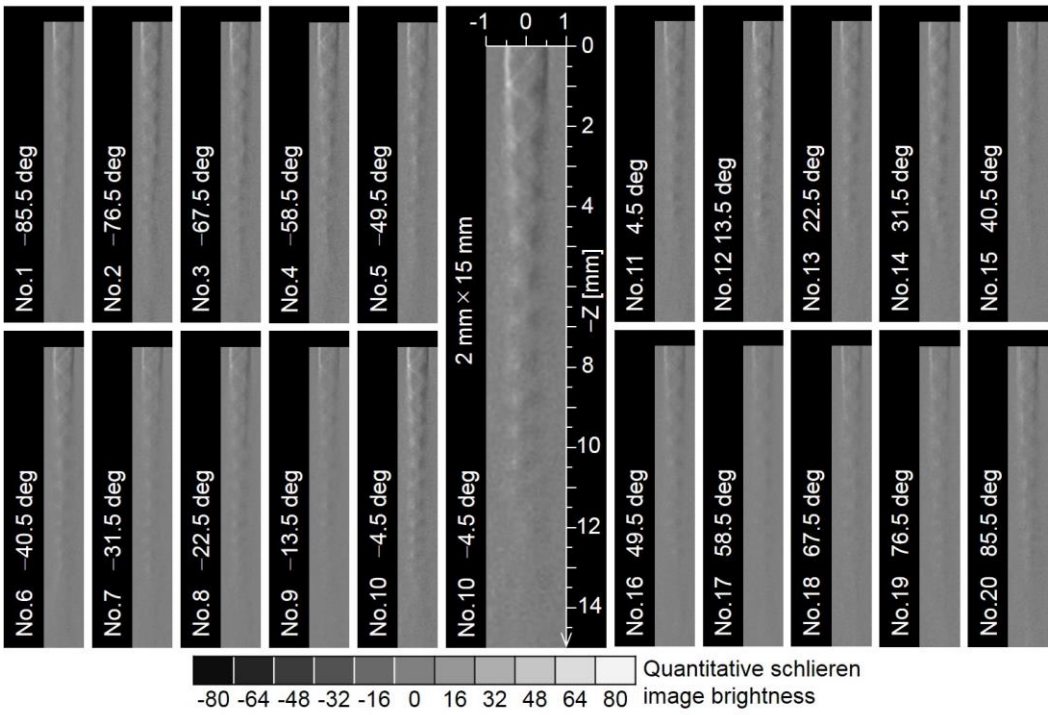

(a) Quantitative schlieren images, circular microjet

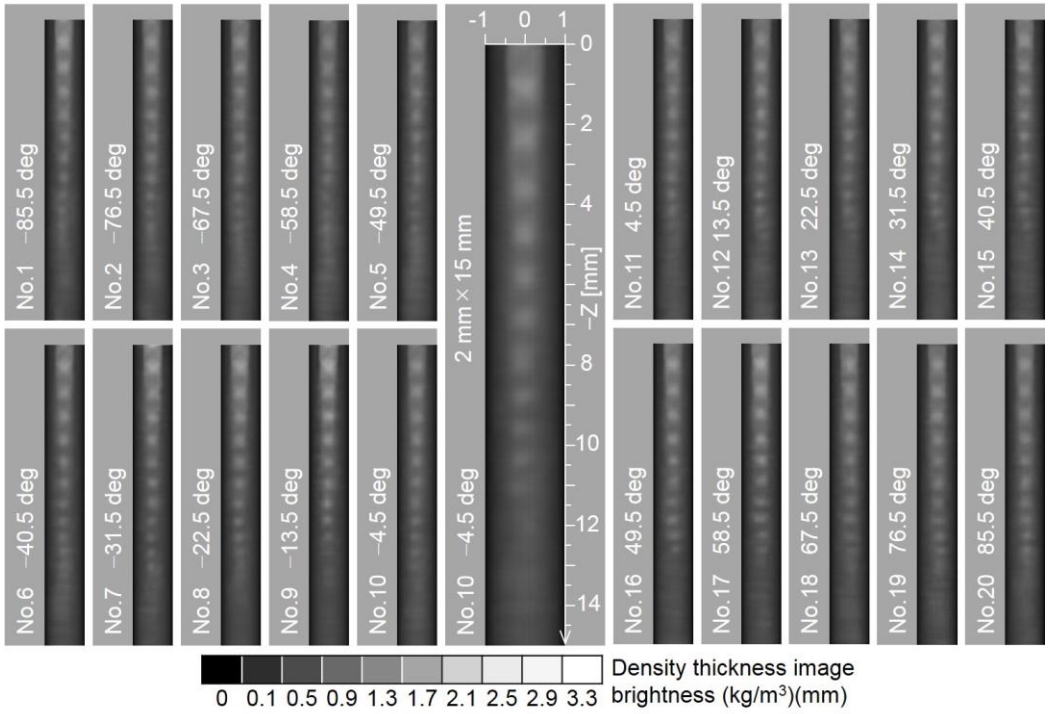

(b) Density thickness images, circular microjet

Fig. 3.12 Quantitative schlieren and density thickness images, circular nozzle, *NPR* = 3.5.

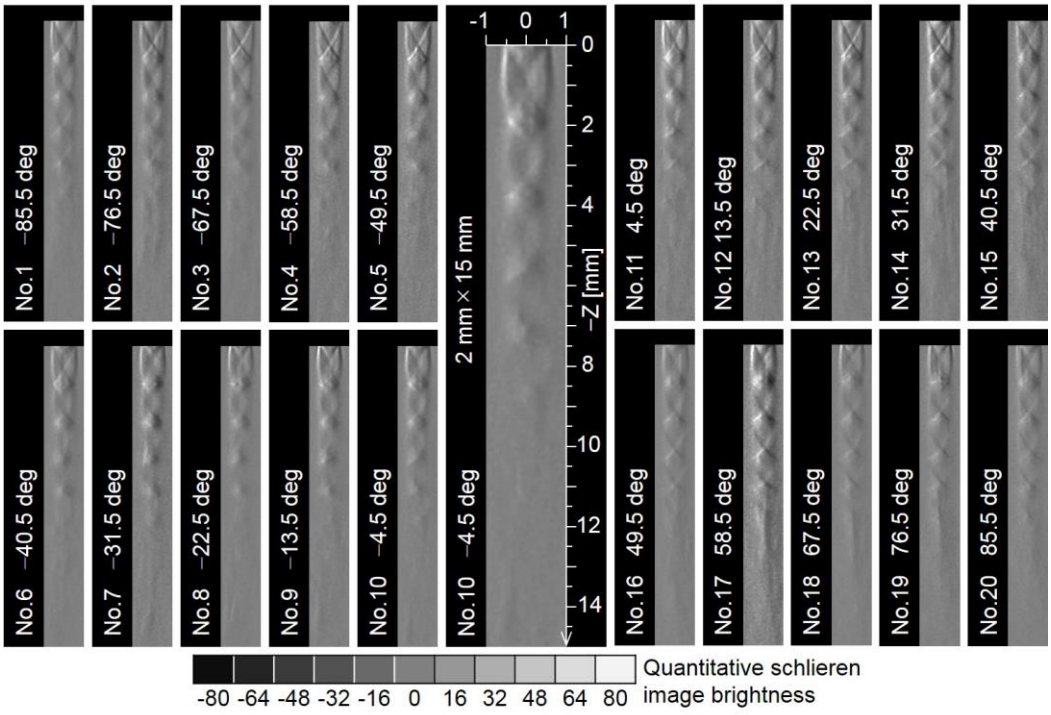

(a) Quantitative schlieren images, square microjet

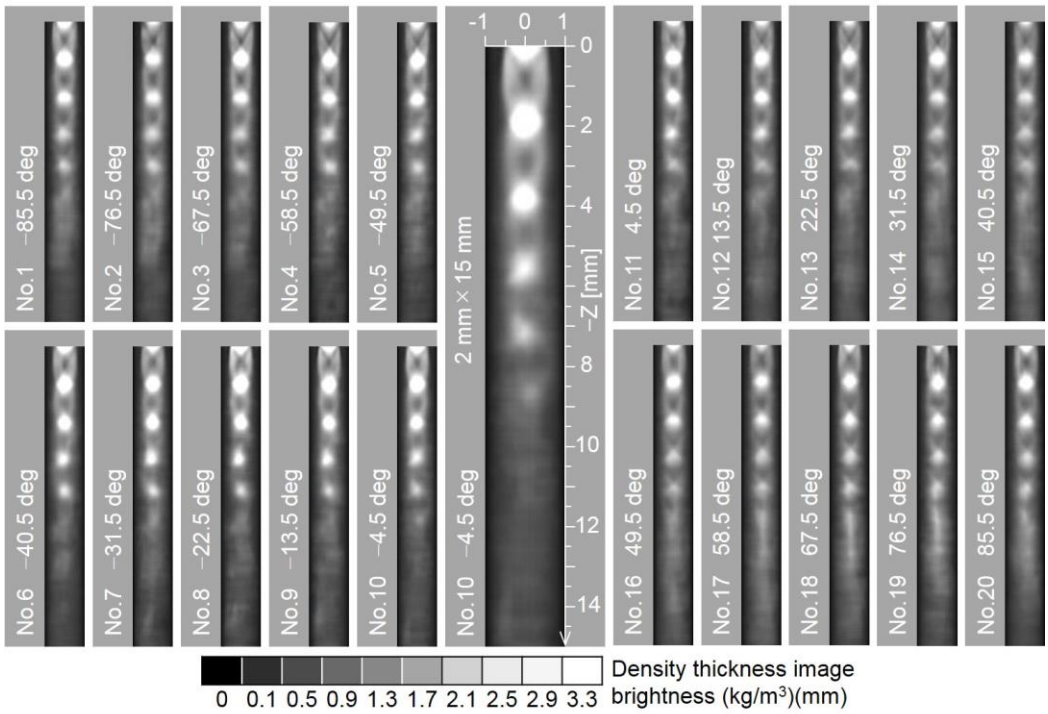

(b) Density thickness images, square microjet

Fig. 3.13 Quantitative schlieren and density thickness images, square nozzle, *NPR* = 5.0.

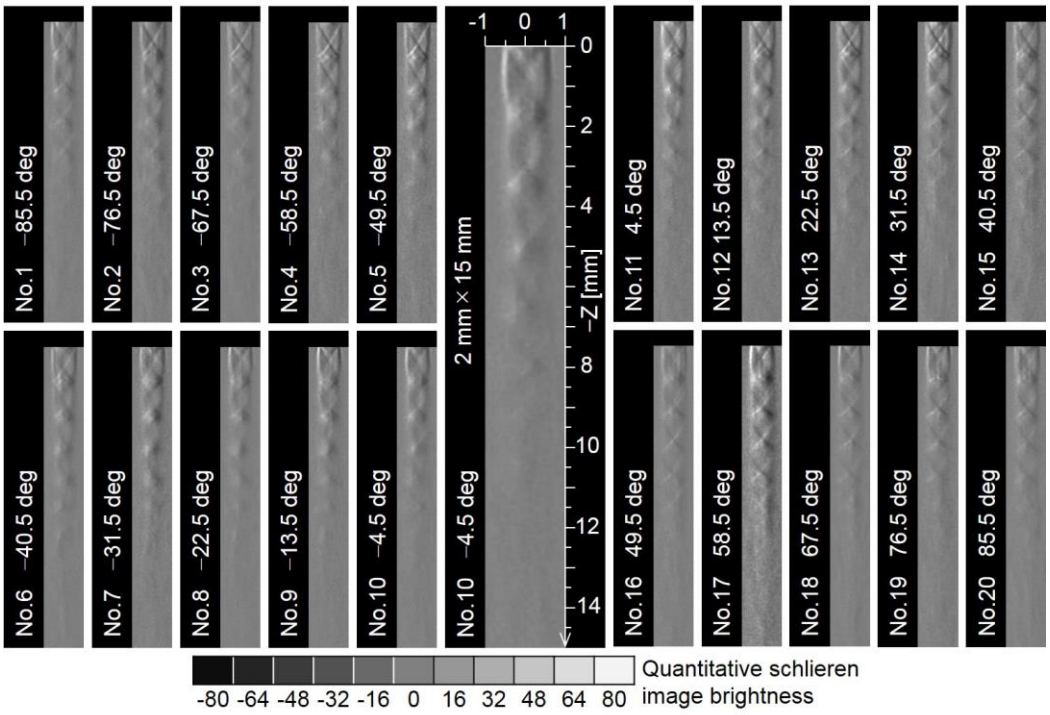

(a) Quantitative schlieren images, square microjet

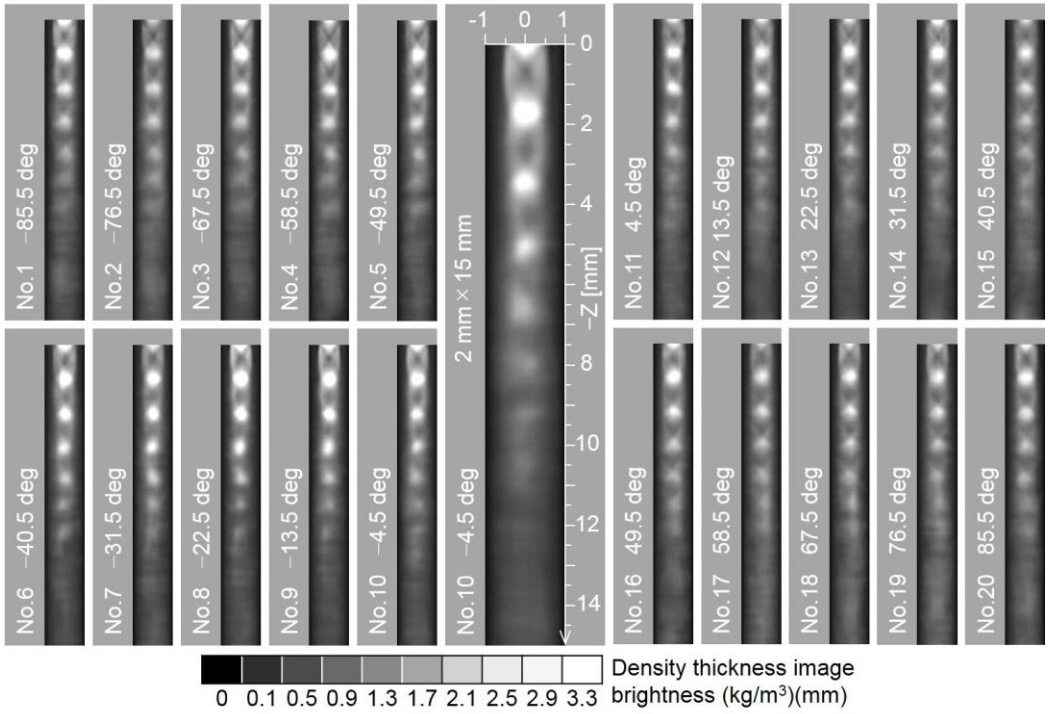

(b) Density thickness images, square microjet

Fig. 3.14 Quantitative schlieren and density thickness images, square nozzle, *NPR* = 4.5.

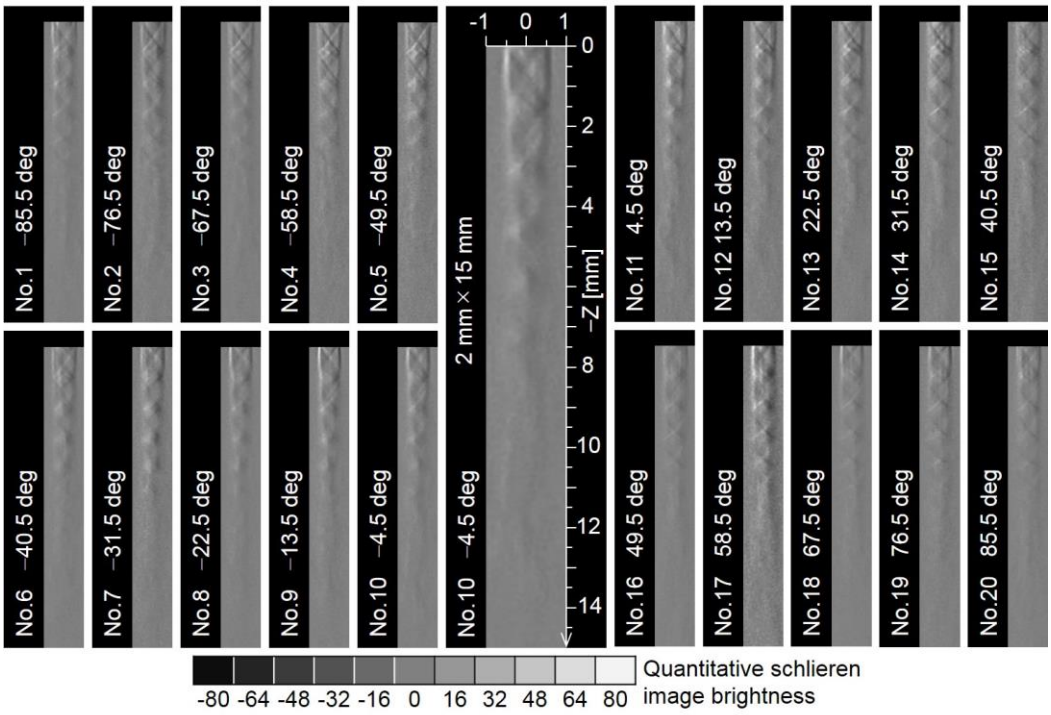

(a) Quantitative schlieren images, square microjet

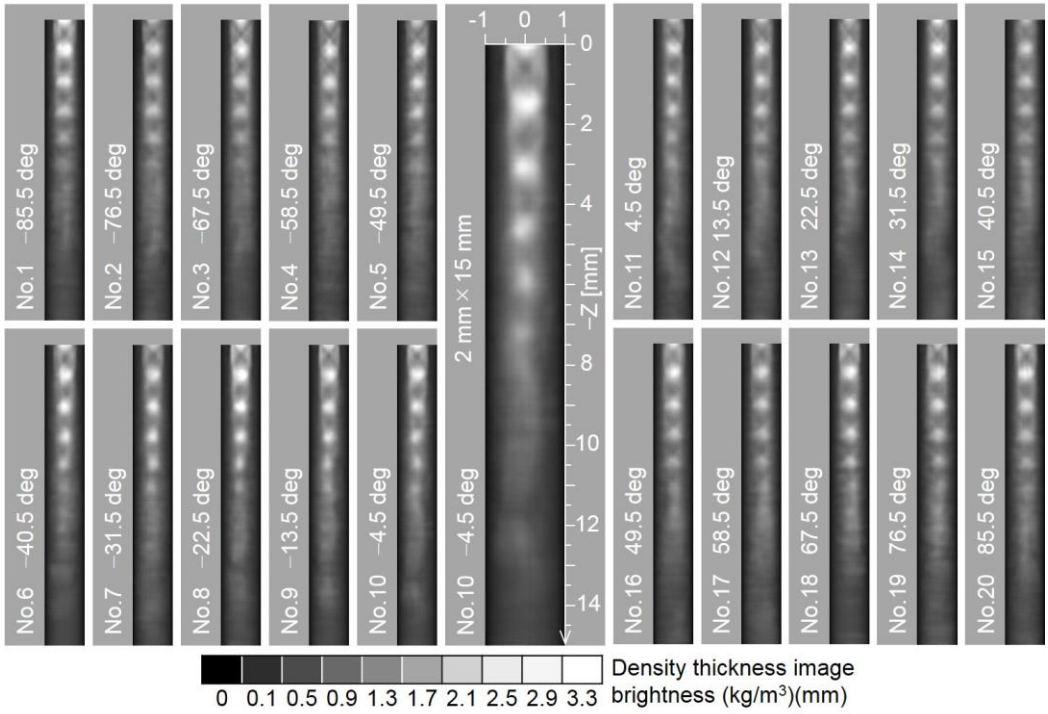

(b) Density thickness images, square microjet

Fig. 3.15 Quantitative schlieren and density thickness images, square nozzle, *NPR* = 4.0.

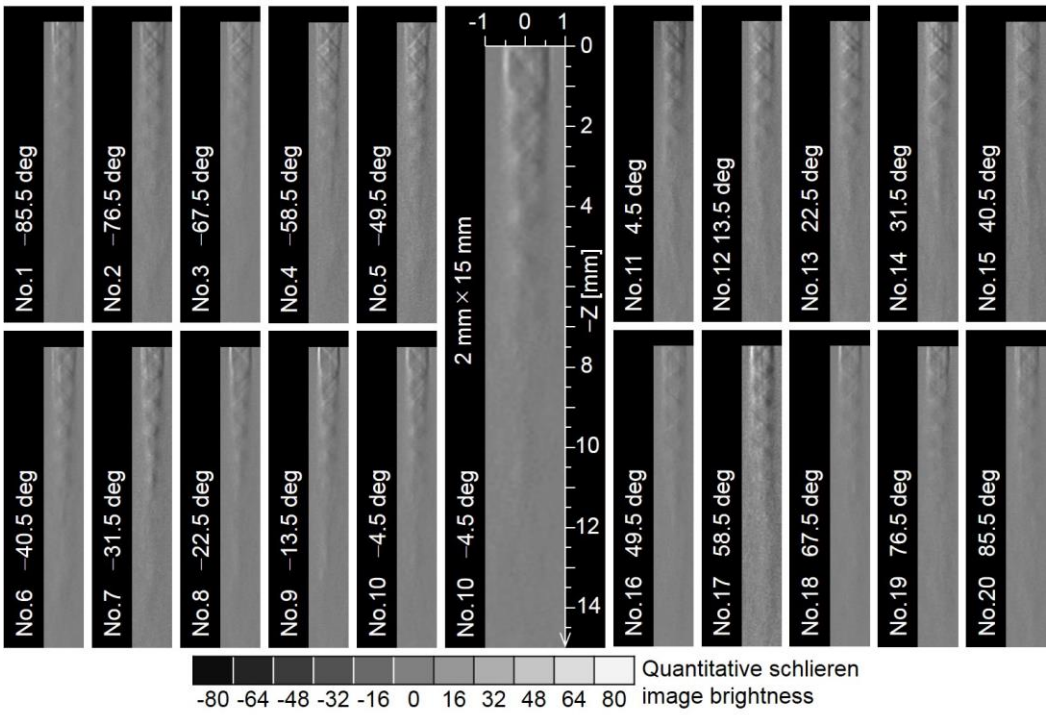

(a) Quantitative schlieren images, square microjet

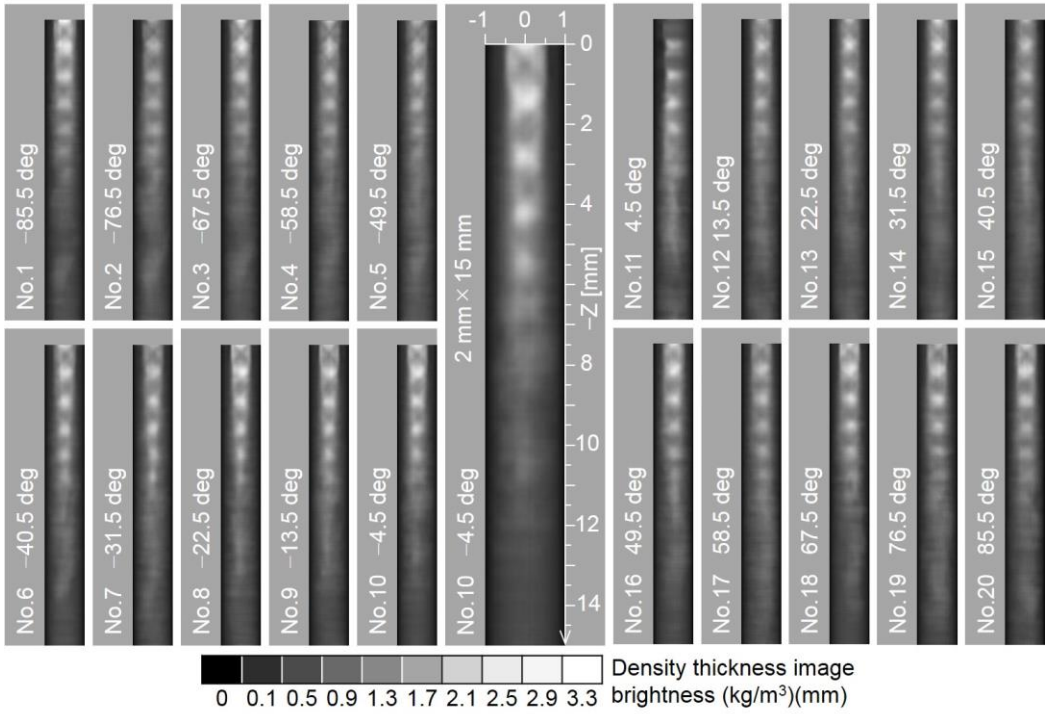

(b) Density thickness images, square microjet

Fig. 3.16 Quantitative schlieren and density thickness images, square nozzle, *NPR* = 3.67.

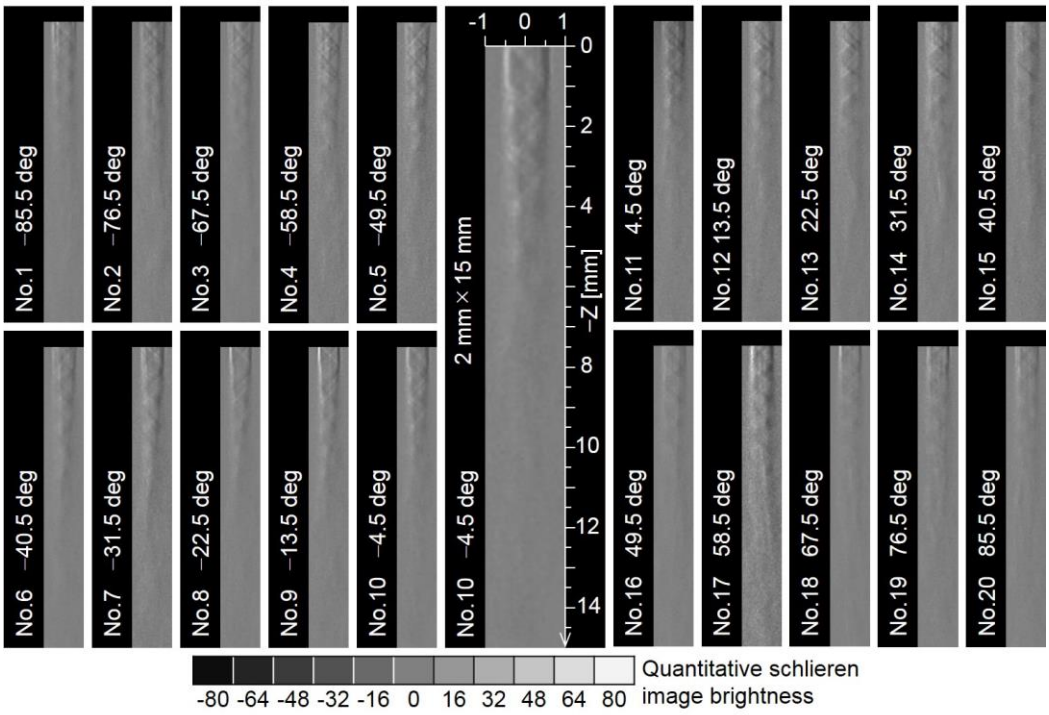

(a) Quantitative schlieren images, square microjet

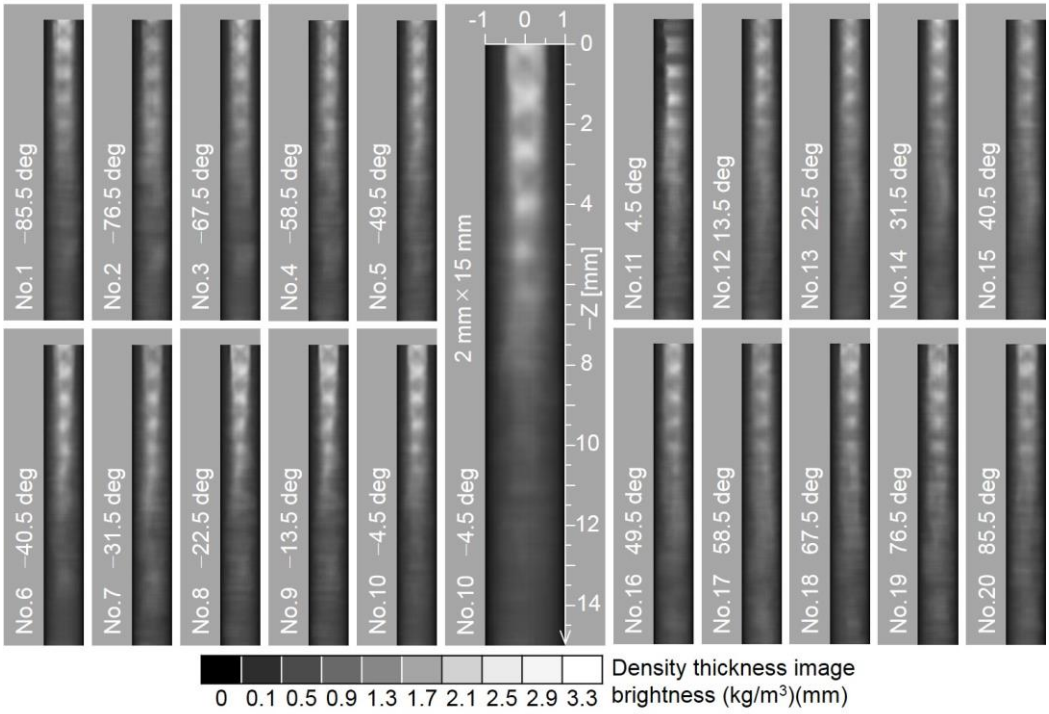

(b) Density thickness images, square microjet

Fig. 3.17 Quantitative schlieren and density thickness images, square nozzle, *NPR* = 3.5.

3.3.2. CT-Reconstruction Results

Using the density thickness images (Fig. 3.8(b) to Fig. 3.17(b)) as projections for CT reconstruction, 3D (three-dimensional) instantaneous density distributions of supersonic microjets have been successfully obtained for z = 0 to 15 mm. Figure 3.18 gives sample vertical and horizontal CT-reconstructed distributions of density for different positions for circular underexpanded microjets, NPR = 5.0.

The values of the densities are displayed in light and dark based on the grayscale level (brightness bar chart) under the images. The darker parts are related to lower density areas and the brighter parts are related to higher density points. The corresponding density contour diagrams of each cross-section are depicted, as well.

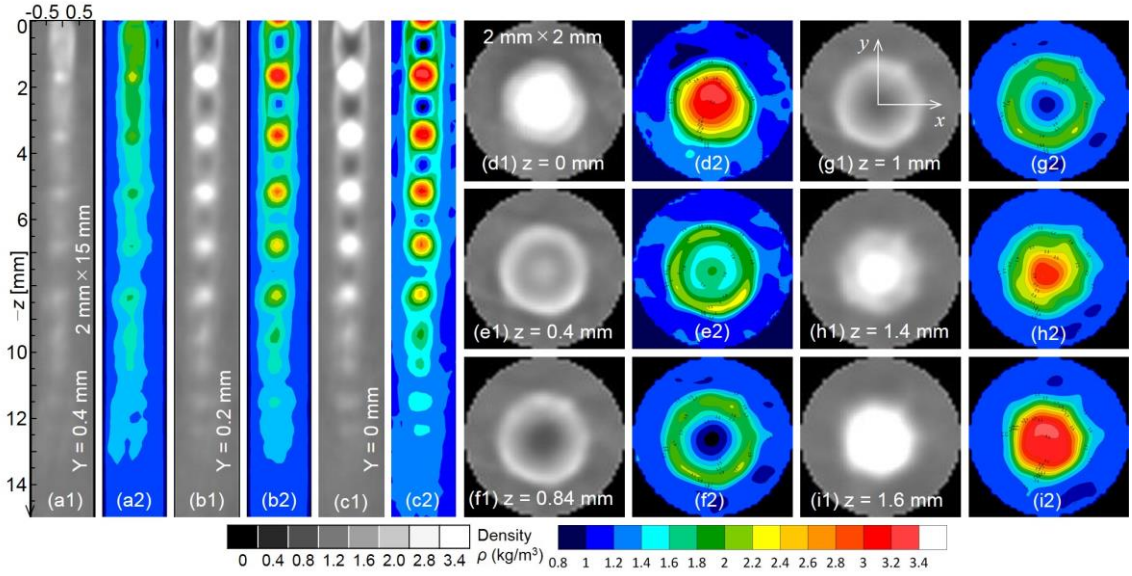

Fig. 3.18 Sample set of vertical (a-c) and horizontal (d-i) of CT-reconstructed density distributions of target supersonic microjet and corresponding contour diagrams, circular micro nozzle, NPR = 5.0.

3.3.3. Square Microjets Structure and Axis-switching

Figure 3.19(a) shows a sketch of underexpanded supersonic jets structure [51][52]. As the jet emerges from the nozzle outlet, it goes through expansion fans and expands to the ambient pressure at the jet boundary. Therefore, in the beginning, the jet size increases, and then, the jet diameter gradually decreases because of the reflection of the expansion fans as compression waves from the jet boundary. The compression waves converge and form intercepting shocks (inception, incident or barrel shocks). Then, the intercepting shocks intersect and reflected shocks are formed; this intersects with the jet boundary and reflects as expansion fans again; however, this process is repeated.

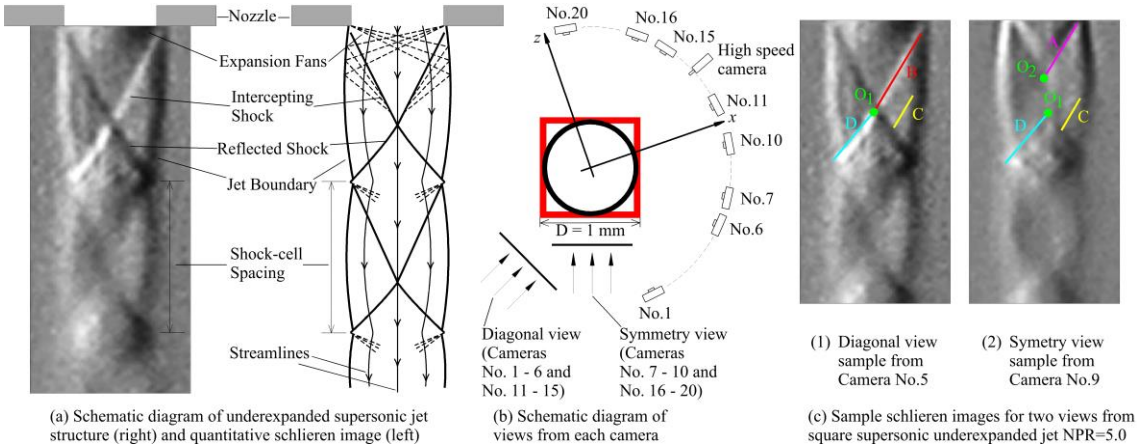

(a) Schematic diagram of underexpanded supersonic jet structure (right) and quantitative schlieren image (left)

(b) Schematic diagram of views from each camera

(c) Sample schlieren images for two views from square supersonic underexpanded jet NPR=5.0

Fig. 3.19 Structure of underexpanded supersonic jets and types of square microjets shock waves based on types of the view angle.

Based on the viewing angle, two types of schlieren images (Figure 3.19(c)) for square supersonic microjets are observed using multi-schlieren optical system photography. Views for the square nozzle outlet, toward the "side" represent the "symmetry view" and toward the "corner" represent the "diagonal view". As depicted in Figure 3.19(b), the corner of the square micro nozzle outlet located toward high-speed camera is used for pre-investigation and for time-series observation. The types of view for each camera are shown in Figure 3.19(b). Sample schlieren images for both types of views are shown in Fig. 3.19(c) for the underexpanded square supersonic microjet, NPR = 5.0, and the schlieren images for all 20 directions are illustrated in Figure 3.13(a). As reported in [40][41][53], the shock waves of the first shock-cell (intercepting and recompression shock waves) can be categorized into four groups, as marked by the letters A, B, C, and D (Figure 3.19(c)). In the symmetry planes, the jet expands, and on the diagonal planes, the expansion recompresses by shock waves. Such expansion and recompression form a cross-shaped jet cross-section (Figure 3.20(d)). The size of the barrel-shaped section for a circular and square supersonic microjet, NPR = 5.0, for two types of view is $D_{circular}$ = 31 pixel = 1.24 mm, $D_{square\_symmetry}$ = 32 pixel = 1.28 mm, and $D_{square\_diagonal}$ = 35 pixel = 1.4 mm. The diagonal of a square is equal to $D_{sq} = (2)^{1/2}S = 1.41S$ = 1.41 mm, where S = 1 mm equals one side length of the square. Therefore, it is straightforward that the diagonal view must be wider than the symmetry view as shown in Fig. 3.19(c) unlike that reported by some research papers.

Figure 3.20(a1) shows a sample vertical (including two shock-cells) and Fig. 3.20(b1)-(h1) show sample horizontal CT-reconstructed distributions of density and corresponding density contour diagrams (Fig. 3.20(a2)-(h2)) for different positions for the square underexpanded microjets, NPR = 5.0. The horizontal cross-sections are seven samples for the first shock-cell among 46 CT-reconstructed cross-sections. The overall horizontal numbers of CT-reconstructed cross-sections are 375 for microjets in this investigation. As shown in Figure 3.20(b) at the nozzle exit, there is almost one bright (higher density points) square-shaped cross-section. This cross-section moves away from the nozzle outlet, a brighter diamond-shaped inside a square is visible (Figure 3.20(c)), and then, the brighter diamond shape gradually becomes smaller and disappears. A side of the brighter diamond-shaped turns inward faster

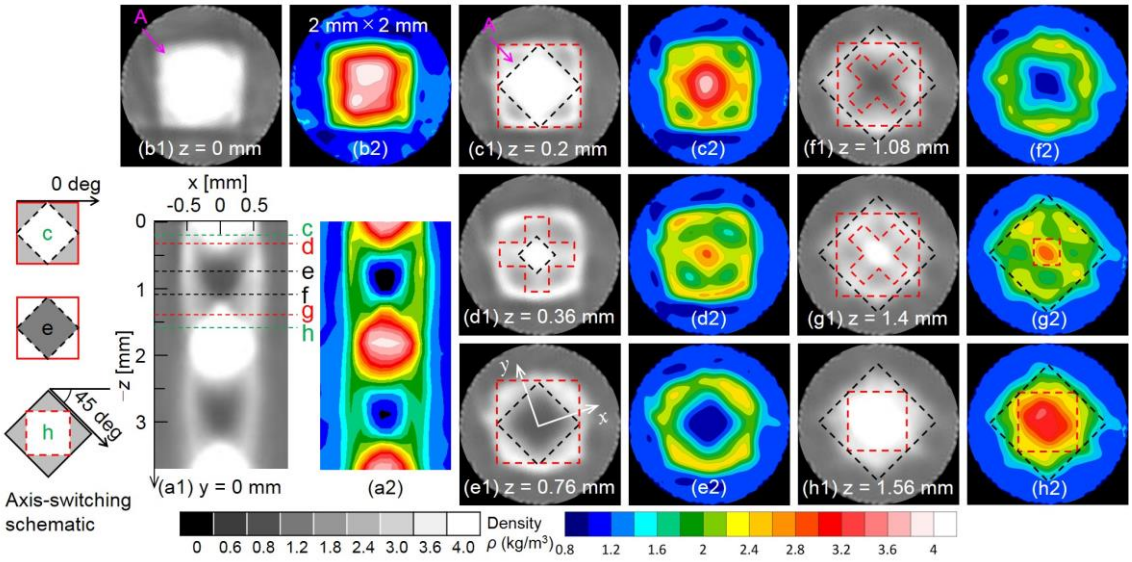

Fig. 3.20 Sample set of vertical and horizontal of CT-reconstructed density distributions of target supersonic microjet, square micro nozzle, *NPR* = 5.0.

than the corner based on shock waves (A) suppression, which results in an upright cross-shaped (Figure 3.20(d)). In Figure 3.20(e) a darker (lower density areas) diamond-shaped form inside a square is visible. Then, a darker diagonal cross-shaped (Figure 3.20(f)) forms are obtained by shock waves suppression in darker diamond-shaped corners. Moving toward the point of shocks intersection the darker diagonal cross-shaped gradually disappears, and brighter diagonal cross-shaped form (Fig. 3.20(g)) appears. The brighter point at the center of the diagonal cross-shaped gradually becomes larger till it forms a brighter square shape surrounded by a diamond-shaped (Figure 3.20(h)), which is located near to the end of first shock-cell.

By comparing cross-sections near the nozzle outlet and the near end of the first shock-cell, we can see microjet axis-switching clearly as sketched on the left side of Figure 3.20. Axis switching is a phenomenon in which the cross-section of an asymmetric jet develops gradually, and in such a manner that, after a certain distance from the nozzle exit, the major and the minor axes are interchanged. Therefore, as observed, the initial axis-switching is 45° inside the first shock-cell with two types "upright" (Figure 3.20(d)) and "diagonal" (Figure 3.20(f) and (g)) of "cross-shaped". In this investigation, the first switchover takes place in the first shock-cell. The second occurs a little farther downstream in the second shock-cell, the subsequent ones are usually weak; however, they may not be easily detectable.

Recently, Cabaleiro and Aider [43] observed the axis-switching of a microjet for the first time, and probably in small-scale, in this investigation is for the second time such delicate, complex and beautiful phenomenon for square microjets is observed more clearly. The deformation of a micro-vortex ring caused by induction because of corner vortices is responsible for axis switching as it occurs in large-scale non-circular jets [43][54][55].

Further, Zaman [54] introduced the second mechanism caused by the induced velocities of two streamwise vortex pairs situated at the ends of the major axis (Fig. 3.21). These two vortex pairs can

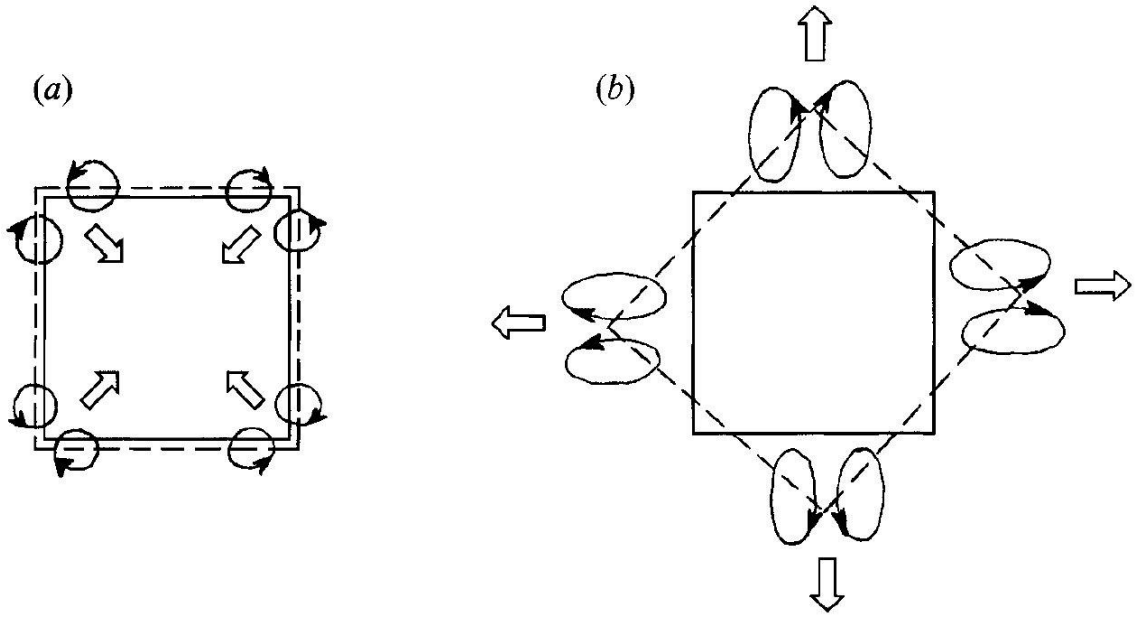

Fig. 3.21 Schematic of mean streamwise vorticity distributions in a square jet [54], (*a*) distribution close to the jet exit (distribution of streamwise vortex pairs promoting axis switching), (*b*) distribution farther downstream (distribution of streamwise vortex pairs resisting axis switching).

effectively enhance (Fig. 3.21(a)) or resist (Fig. 3.21(b)) axis-switching, which depends on their relative distribution at the edge of the nozzle.

Figure 3.22 and Fig. 3.23 give sample vertical and horizontal CT-reconstructed distributions of density for different positions for supersonic microjets issuing from the circular and square micro nozzles with operating nozzle pressure ratios 4.5, 4.0, 3.67 and 3.5, respectively

For better evaluation of the reconstructed density values, radial and axial density distributions diagrams are illustrated in Fig. 3.24 to Fig. 3.29. Amplitude increases and decreases along the jet downstream, which is higher for square microjets compared to circular microjets. Thus, it reaches a peak value near the center of the diamond-like pattern and after these points gets its minimum values periodically.

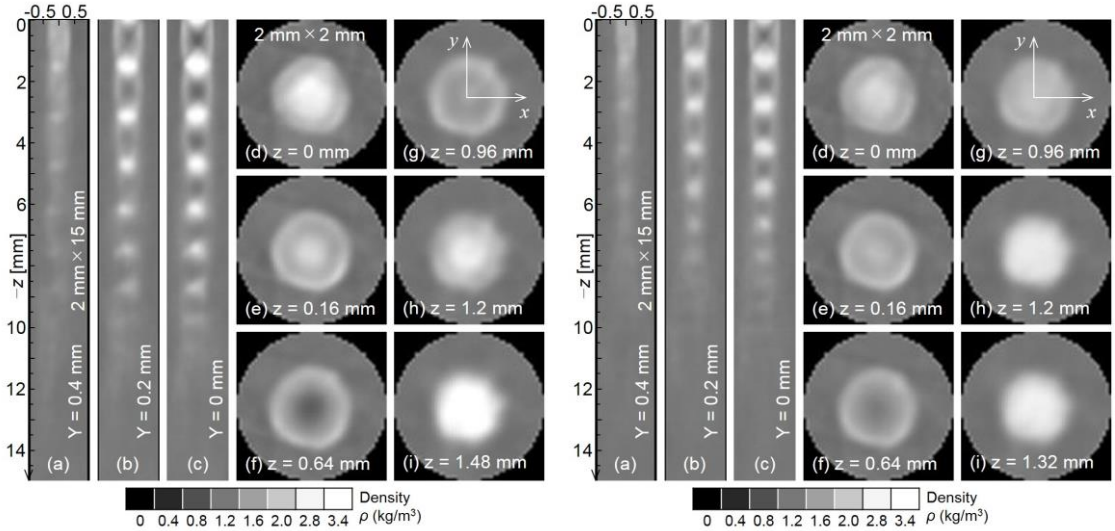

(a) *NPR* = 4.5

(b) *NPR* = 4.0

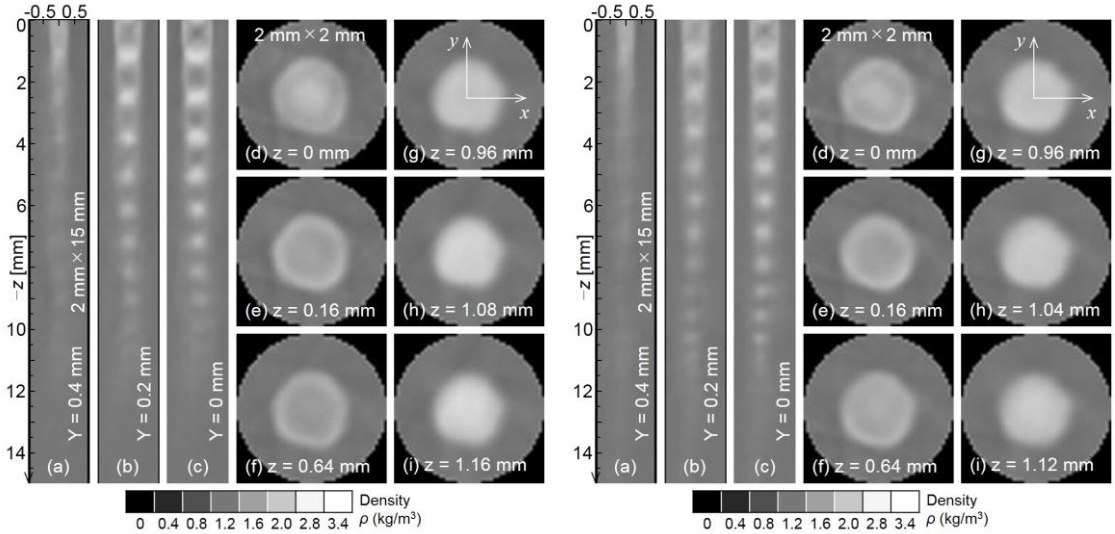

(c) *NPR* = 3.67

(d) *NPR* = 3.5

Fig. 3.22 Sample set of vertical (a-c) and horizontal (d-i) of CT-reconstructed density distributions diagrams of target supersonic microjets, circular micro nozzle.

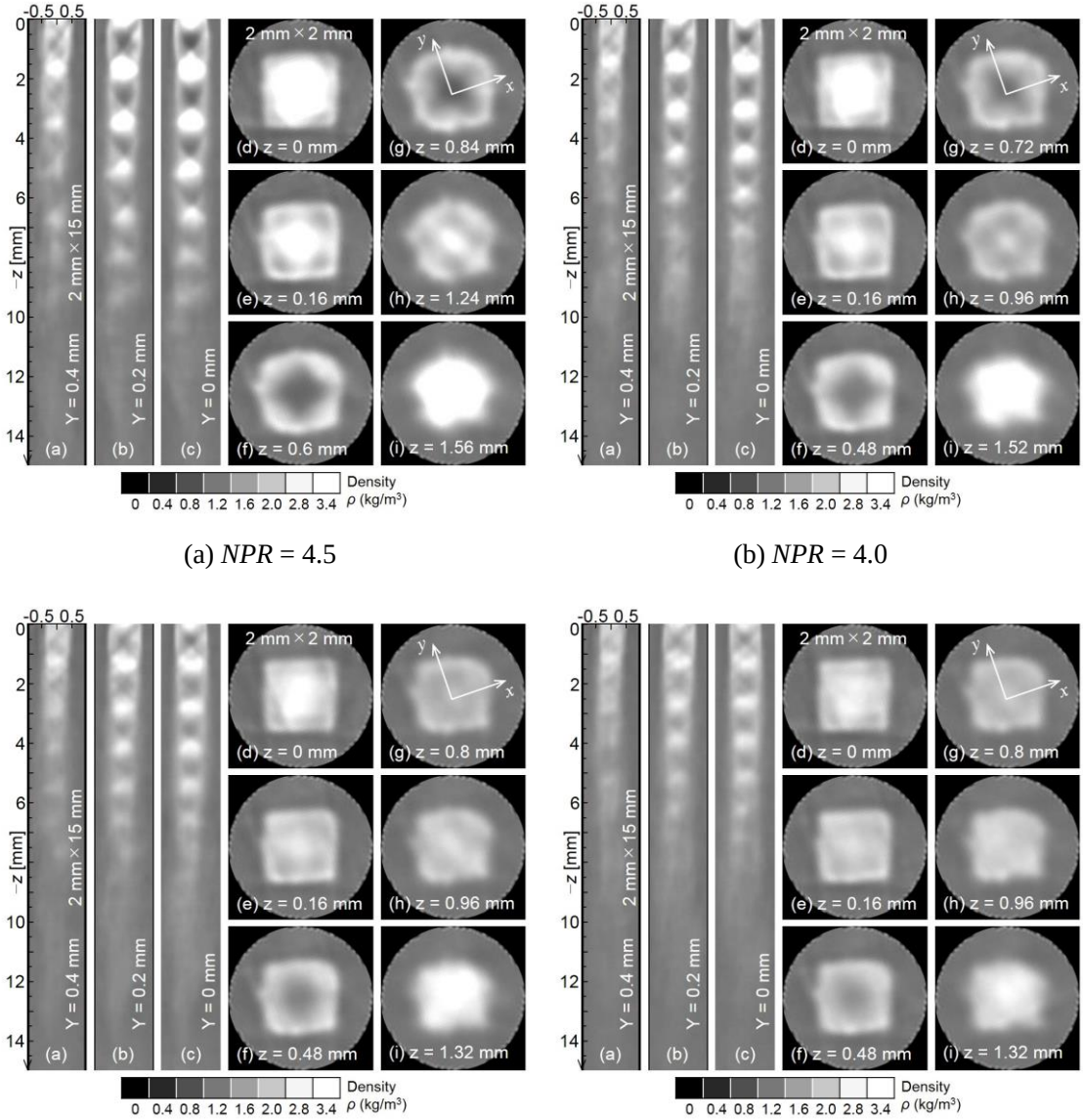

Fig. 3.23 Sample set of vertical (a-c) and horizontal (d-i) of CT-reconstructed density distributions diagrams of target supersonic microjets, square micro nozzle.

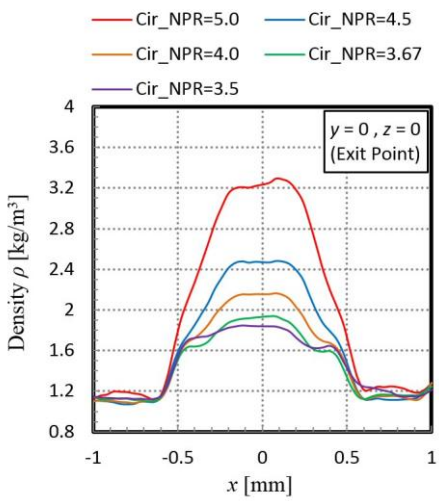

(a) Radial diagrams, circular microjets

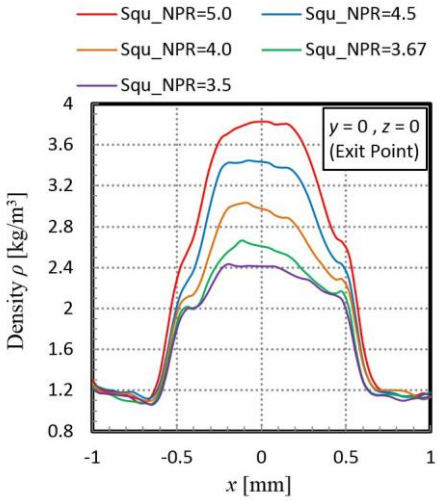

(b) Radial diagrams, square microjets

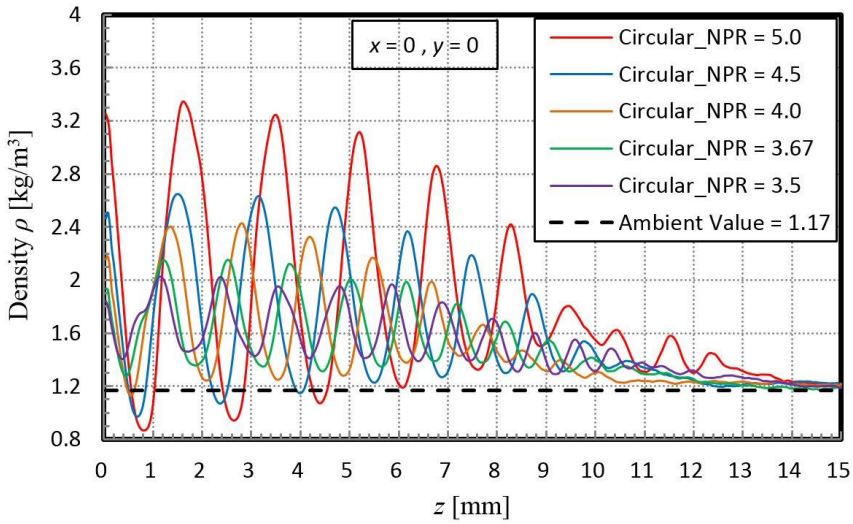

(c) Axial diagrams, circular microjets

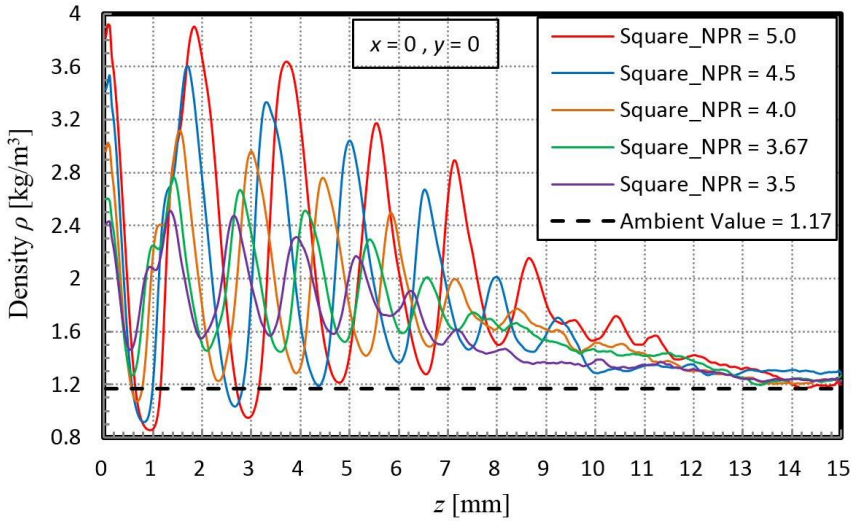

(d) Axial diagrams, square microjets

Fig. 3.24 Radial and axial diagrams for circular and square microjets.

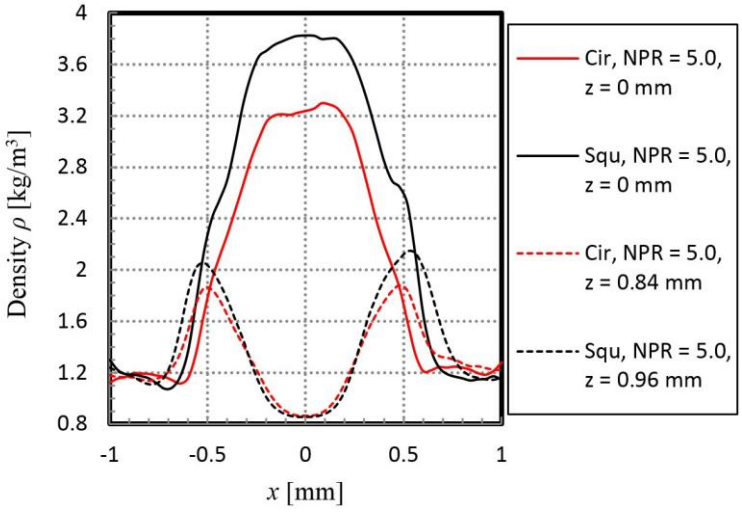

(a) Radial diagram

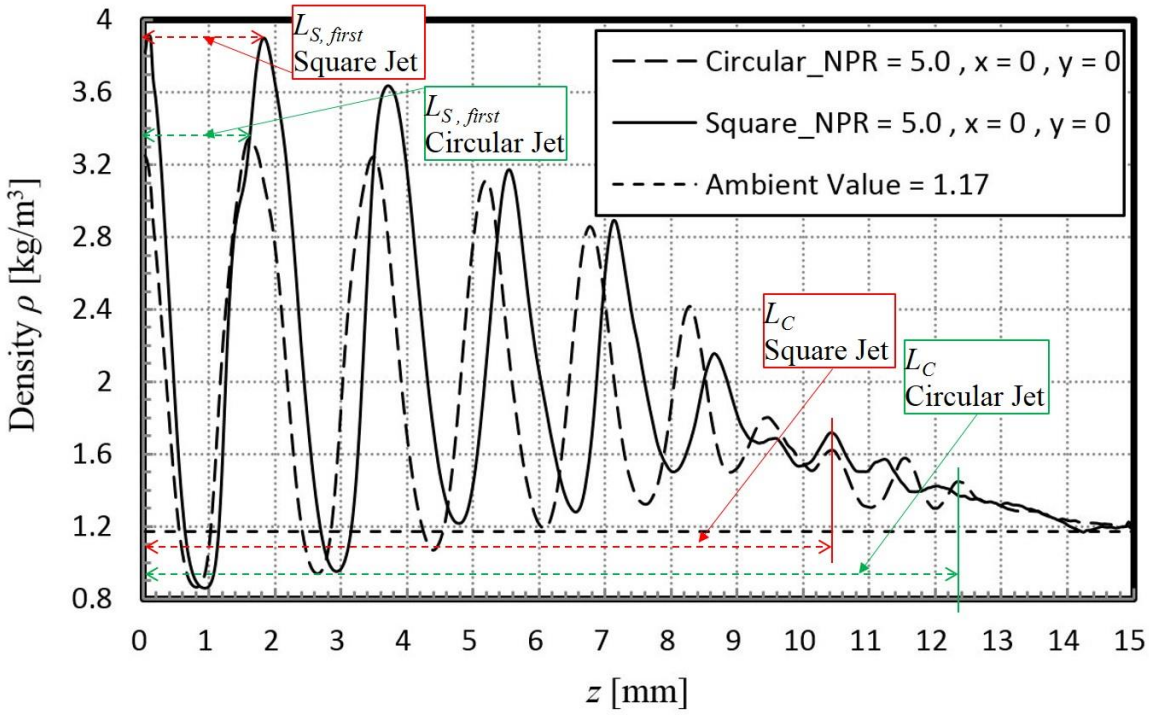

(b) Axial diagram

Fig. 3.25 Radial and axial superposition diagrams for circular and square microjets, *NPR* = 5.0.

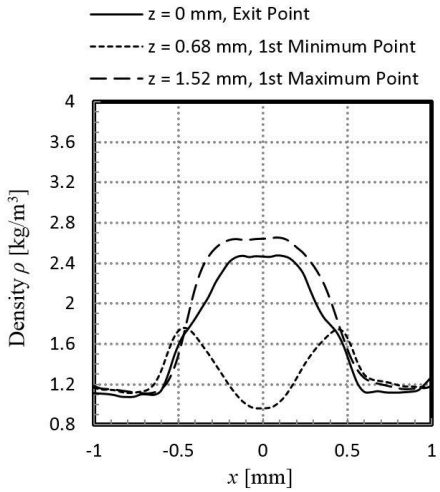

(a) Radial diagram, circular

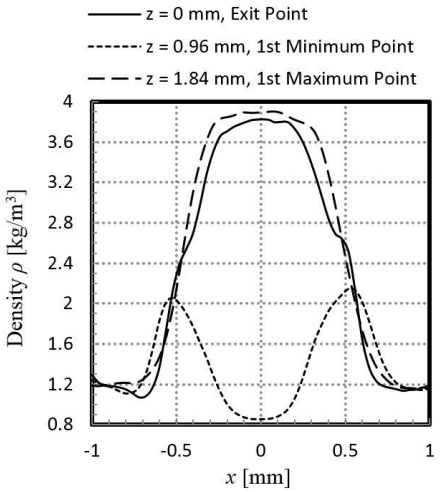

(b) Radial diagram, square

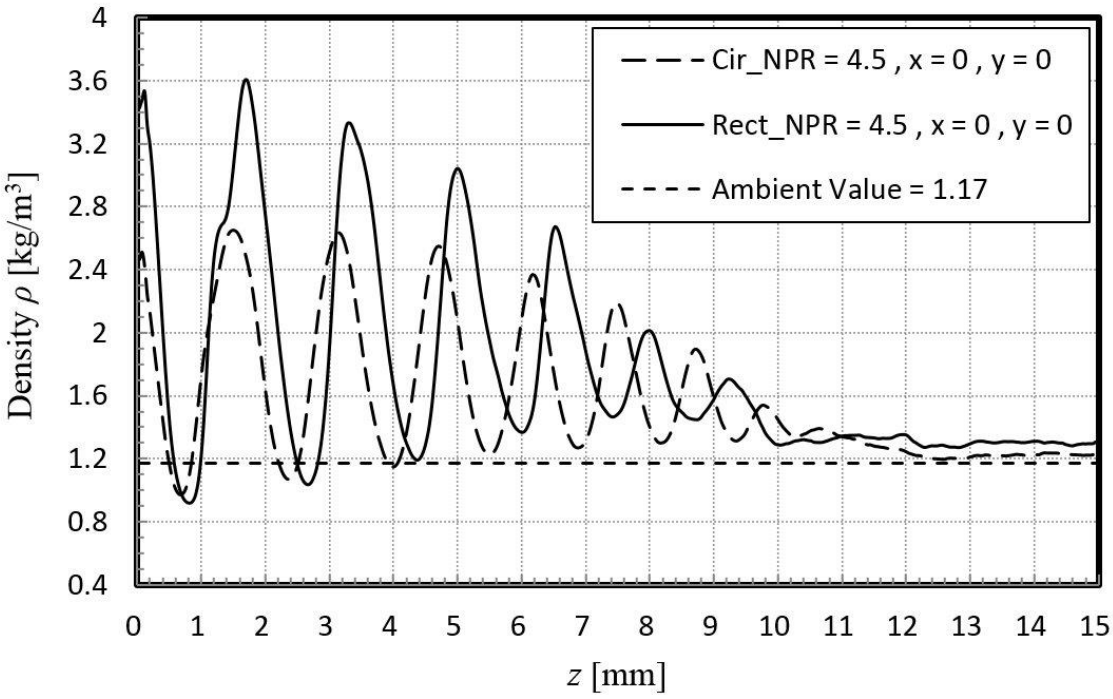

(c) Axial diagram

Fig. 3.26 Radial and axial superposition diagrams for circular and square microjets, *NPR* = 4.5.

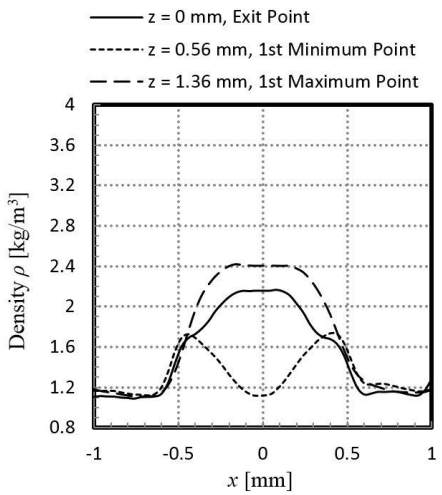

(a) Radial diagram, circular

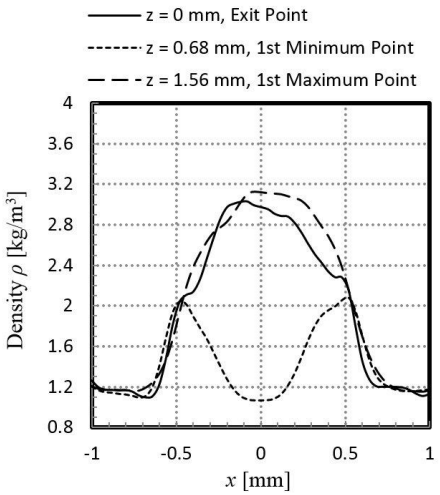

(b) Radial diagram, square

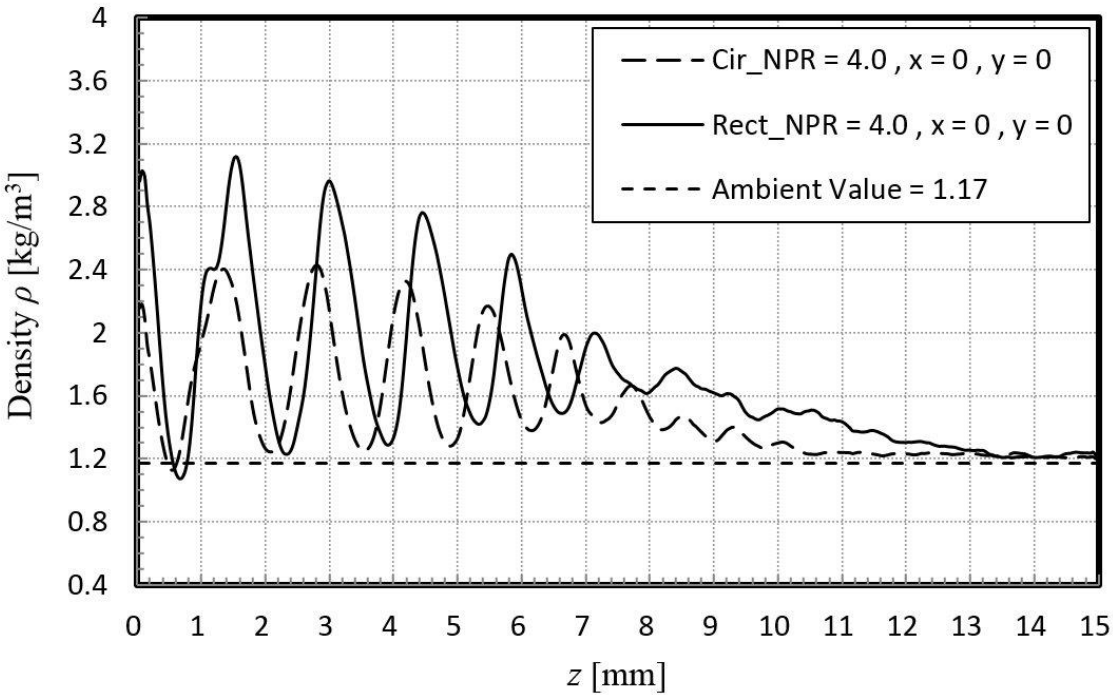

(c) Axial diagram

Fig. 3.27 Radial and axial superposition diagrams for circular and square microjets, *NPR* = 4.0.

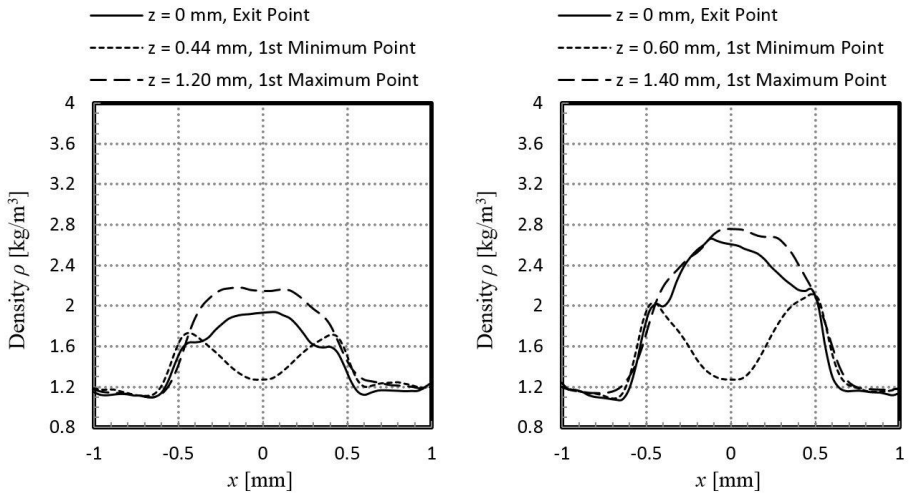

(a) Radial diagram, circular (b) Radial diagram, square

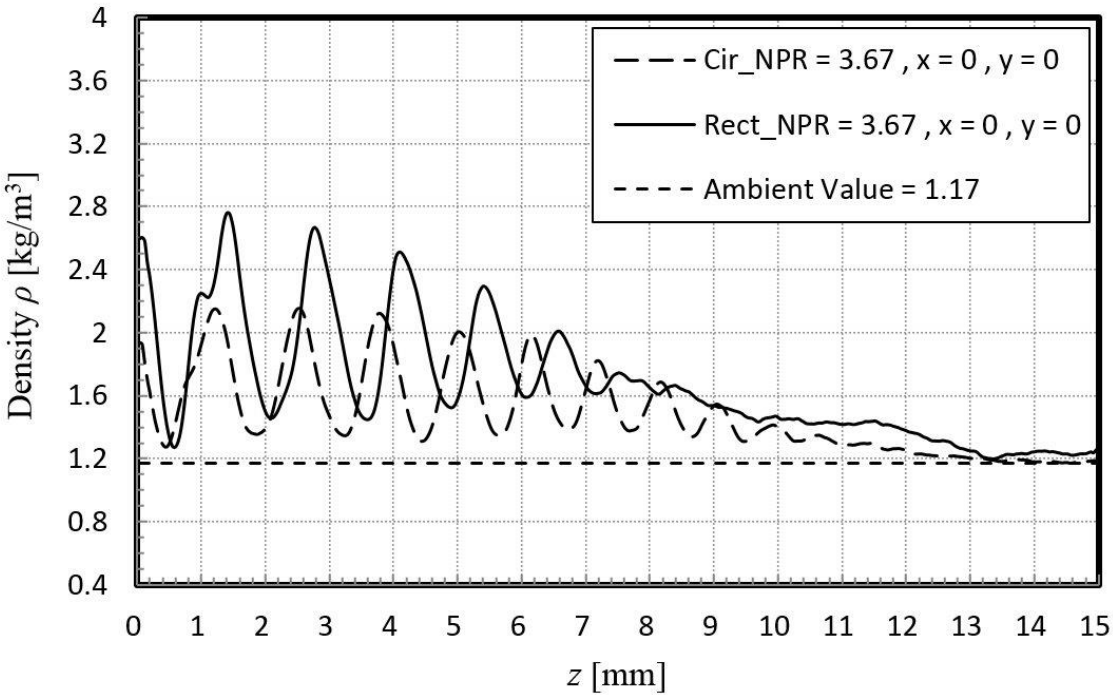

(c) Axial diagram

Fig. 3.28 Radial and axial superposition diagrams for circular and square microjets, *NPR* = 3.67.

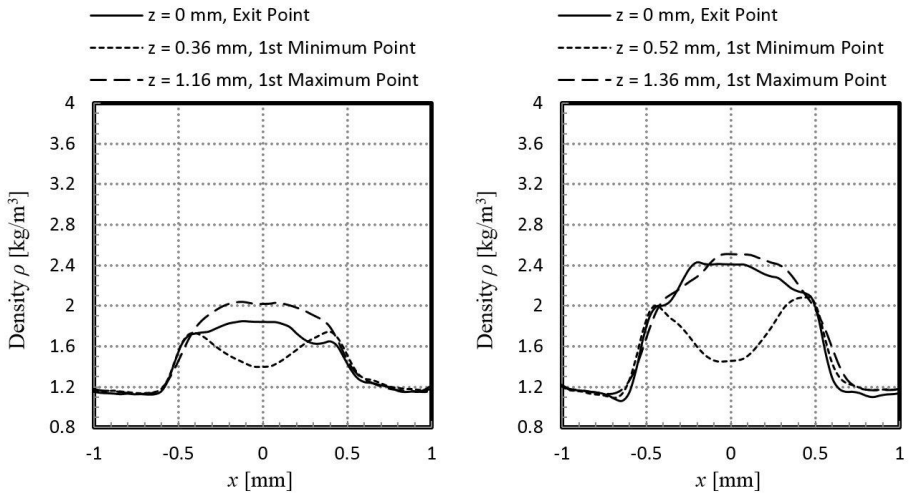

(a) Radial diagram, circular (b) Radial diagram, square

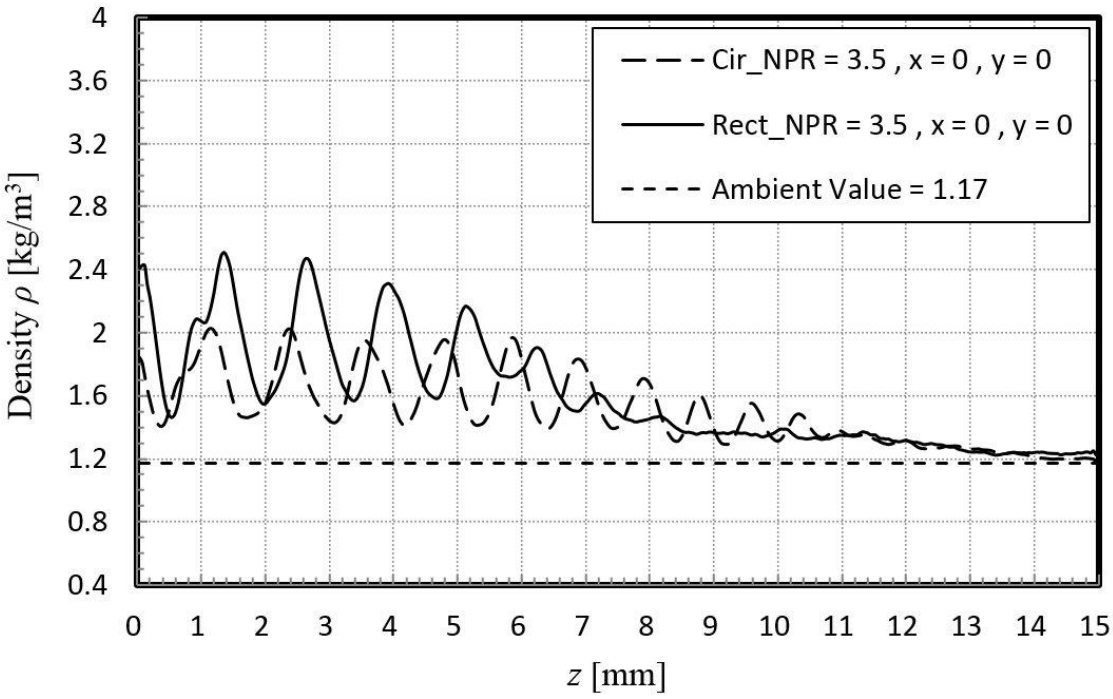

(c) Axial diagram

Fig. 3.29 Radial and axial superposition diagrams for circular and square microjets, *NPR* = 3.5.

3.3.4. Shock-cells Spacing (L_s) and Supersonic Core Length (L_c)

Shock-cell parameters are important to characterize supersonic jets, such as "shock-cell spacing (length) L_s" and "supersonic core length L_c". Note that shock-cell spacing L_s for all shock-cells can be obtained from schlieren images. The shock-cell spacing for the first five shock-cells based on our experimental data and results is depicted in Fig. 3.30(a) and (b) for circular and square supersonic microjets, respectively. The cross-section area of a square is larger than a circle with a diameter equal to the width of the square, and accordingly, square microjets have larger shock-cells lengths and amplitudes than circular microjets. Furthermore, the second shock-cells length is longer than the first shock-cells length for circular microjets in all nozzle pressure ratios except for *NPR* = 3.5 (overexpanded microjet); however, for square microjets, the second shock-cells length is shorter than the first shock-cells length.

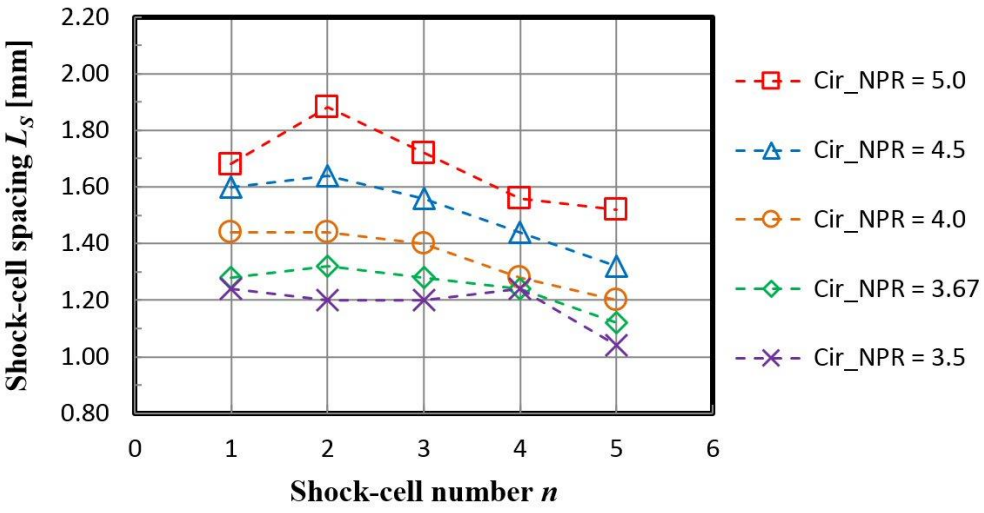

(a) Circular microjets

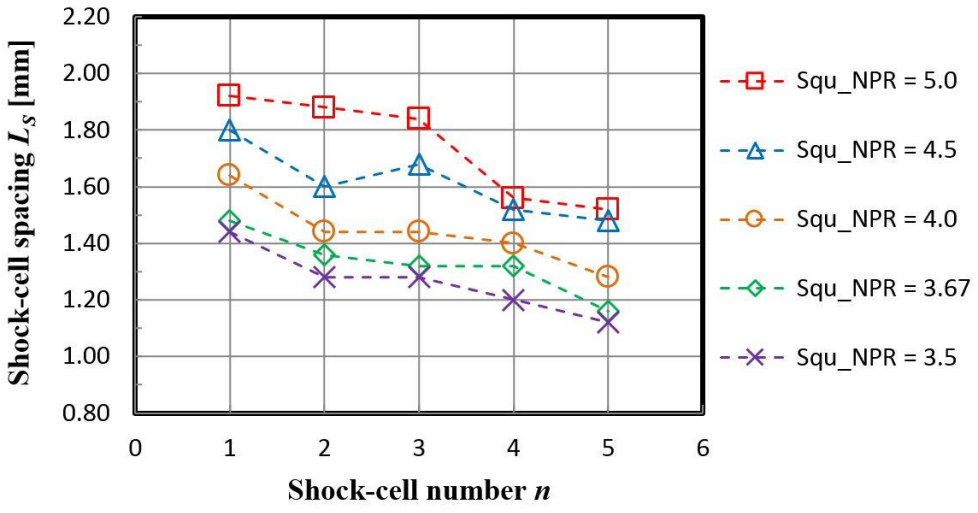

(b) Square microjets

Fig. 3.30 Shock-cell spacing (length) L_s for five shock-cells from present experimental data.

Tam and Tanna [56] and Tam [57] proposed the following relations (equations (3.14) and (3.15)) for estimating the first shock-cell spacing (L_s) in supersonic circular [56] and rectangular [57] jets, respectively,

$$L_s = \pi D_j (M_j^2 - 1)^{1/2} / 2.40483 \quad , \tag{3.14}$$

$$L_s = \frac{2h_j \sqrt{\left(M_j^2 - 1\right)}}{\sqrt{\left(1 + \frac{h_j^2}{b_j^2}\right)}} . \tag{3.15}$$

Where M_j, D_j, b_j, and h_j are the fully expanded jet Mach number, diameter (for circular jets), width, and height (for rectangular jets), respectively. Since for square jets $h_j = b_j$ then, equation (3.15) gives,

$$L_s = h_j [2(M_j^2 - 1)]^{1/2} . \tag{3.16}$$

We can obtain the fully expanded jet diameter D_j (for circular jets) and the fully expanded jet height h_j (for square jets), using the following equation (3.17). The equation (3.17) can be derived by dividing the two equations (3.6) and (3.7),

$$\frac{D_j}{D} = \frac{h_j}{h} = \left[\frac{1 + \frac{1}{2}(\gamma - 1) M_j^2}{1 + \frac{1}{2}(\gamma - 1) M_d^2} \right]^{\frac{\gamma+1}{4(\gamma-1)}} \left(\frac{M_d}{M_j} \right)^{\frac{1}{2}} . \tag{3.17}$$

For the first shock-cell spacing L_s, Mehta and Prasad [58] obtained a linear relation for circular macrojets, and Phalnikar *et al.* [33] proposed the following correlation (equation (3.18)) based on the experimental data for estimating the first shock-cell L_s, no attempt was made to compute the lengths of the second and later cells for microjets.

$$L_s = D(0.57 M_j^2 - 0.15) \tag{3.18}$$

where D is the nozzle diameter.

We compare the shock-cell spacing L_s determined from our experimental results and estimated using Tam, Phalnikar and Mehta's correlations, as shown in Fig. 3.31(a) for circular microjets and Fig. 3.31(b) for square microjets. An overall good agreement is seen between the first shock-cells spacing in this study and Tam's correlation.

However, the measured values of the L_s in our studies a little differ from those estimated by Tam's correlation. The L_s in the present study, about 9-13% for circular and 4-8% for square microjets, are smaller than those predicted by Tam's correlation (equations (3.14) and (3.16)). Similar comparisons were also made by Hu and McLaughlin [59]; their L_s of about 10% was smaller than that predicted by Tam's correlation (equation (3.14)). Further, they mentioned that the difference is attributed to a thicker boundary layer caused by the low Reynolds number for the microjets, as the boundary layer thickness would be inversely proportional to that of Reynolds number, and the Reynolds number directly proportional to the nozzle outlet size [59]. Schlichting [60] for the boundary layer thickness (δ) for turbulent flow obtained one estimated equation, $\delta \approx 0.37x/Re_x^{1/5}$, where x is the distance downstream from the nozzle exit and Re_x is the Reynolds number. For circular and rectangular microjets, NPR = 5.0,

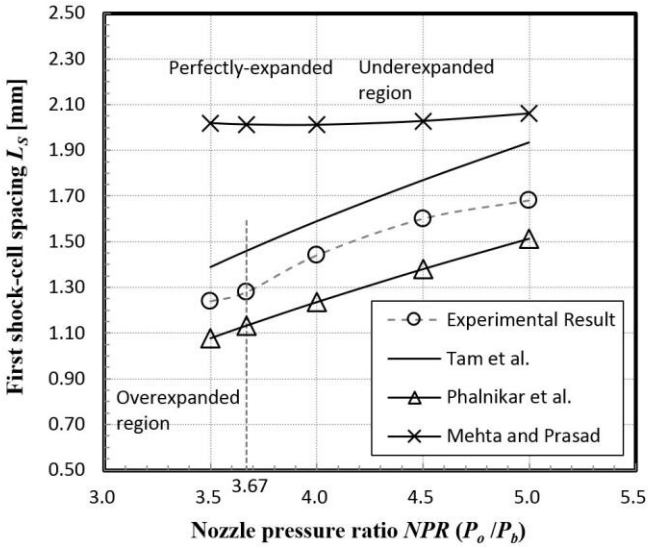

(a) Circular microjets

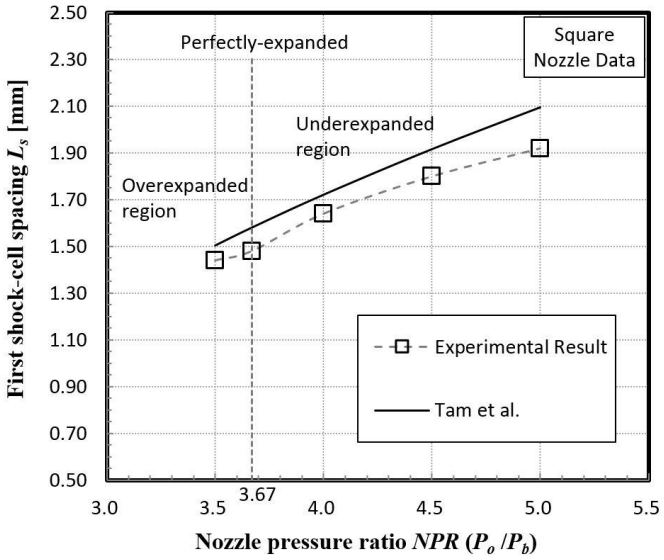

(b) Square microjets

Fig. 3.31 Shock-cell spacing (length) L_s for first shock-cell.

the boundary layer thickness within a distance equal to the nozzle diameter is almost one-pixel (0.04mm) or rarely two-pixel (0.08mm) and based on Schlichting equation [60] the boundary layer thickness is δ = 0.045 mm. This compares very well with the experimental values given the level of approximation. Phalnikar *et al*. [33] conducted experiments using micro nozzles with internal diameters (200 μm and 400 μm) smaller than 1000 μm, and Mehta performed experiments using macro nozzles with internal diameters (23000 and 30000 μm) several times bigger than 1000 μm; accordingly, as shown in Fig. 3.31(a), Phalnikar and Mehta's correlations results are the lowest and the highest, respectively. Since the smaller nozzle exit size and accordingly low Reynolds number resulted in smaller L_s.

Further, "supersonic core length L_c" is usually uses to characterize supersonic jets. It is defined [33] as the distance from the nozzle exit to the axial location along the centerline, where the local flow Mach number drops below 1.0 and reaches a local sonic velocity. Scroggs and Settles [31] estimated L_c as the length of the conical region surrounding shock-cells from schlieren images. Phalnikar *et al*. [33] proposed the following correlation (equation (3.19)) for estimating L_c for circular microjets,

$$L_c = D[(1.8 \times NPR) + 2.9], \tag{3.19}$$

where D is the nozzle diameter and NPR = Nozzle pressure ratio (P_o/P_b). We used CT-reconstructed density data for estimating L_c and compared it with the equation (3.19), as shown in Fig. 3.32. As depicted in Fig. 3.32 the "supersonic core length L_c" for square microjets is less than that for circular microjets (Fig. 3.32(a)), unlike "shock-cell spacing L_s" (Fig. 3.32(b)) for square microjets, which is larger than that for circular microjets. A good agreement is seen between the Phalnikar relation and our circular microjets experimental data, and equation (3.19) is proposed for the circular microjets and not for the square microjets.

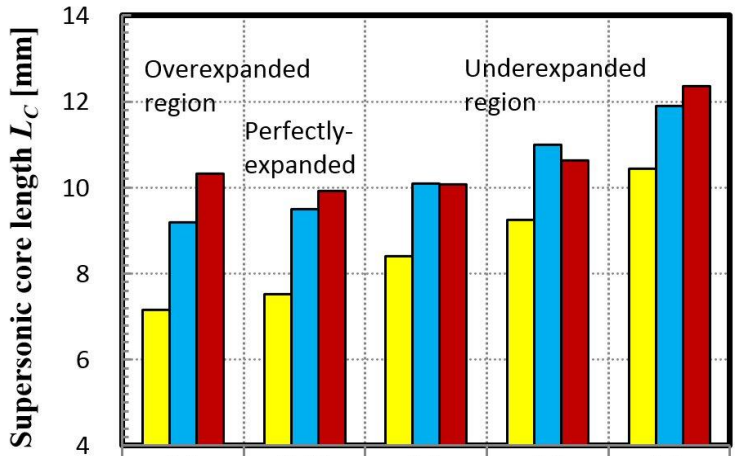

	3.5	3.67	4.0	4.5	5.0
Square Nozzle	7.16	7.52	8.40	9.24	10.44
Phalnikar et al.	9.20	9.51	10.10	11.00	11.90
Circular Nozzle	10.32	9.92	10.08	10.64	12.36

Nozzle pressure ratio NPR (P_o /P_b)

(a) Supersonic core length L_c

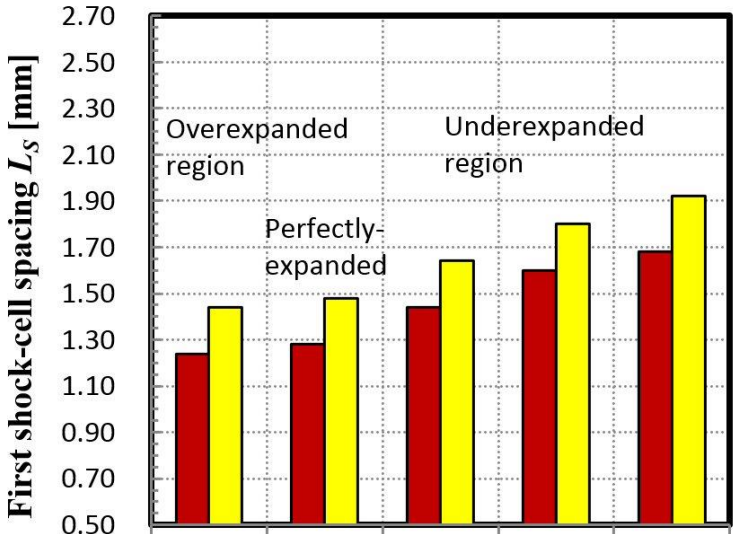

	3.5	3.67	4.0	4.5	5.0
Circular Nozzle	1.24	1.28	1.44	1.60	1.68
Square Nozzle	1.44	1.48	1.64	1.80	1.92

Nozzle pressure ratio NPR (P_o /P_b)

(b) First shock-cell spacing L_s

Fig. 3.32 "Supersonic core length L_c" versus first "shock-cell spacing L_s".

3.4. Summary and Concluding Remarks

By employing the non-scanning 3D-CT technique using a 20-directional quantitative schlieren optical system, 3D-CT reconstructions of instantaneous density distributions of the shock-cells structure of circular and square supersonic microjets were obtained successfully. The results clearly demonstrated the flow pattern downstream of the micro nozzle exit. The multiple reflected waves configuration achieved a diamond-like form throughout the exhaust microjets.

A complex phenomenon for free square microjets, which is called axis-switching, is clearly observed with two types "upright" and "diagonal" of "cross-shaped". In addition, for the first shock-cells from the symmetry and diagonal views of square microjets, two different patterns of shock waves were observed.

The "shock-cell spacing L_s" and "supersonic core length L_c" for all nozzle pressure ratios were investigated and reported. Comparisons with experimental and theoretical computations (particularly those of Tam and Tanna [56] and Tam [57]) showed an overall remarkably good agreement for the first "shock-cells spacing L_s" and "supersonic core lengths L_c" in this study and other correlations. As microjets have low Reynolds number, some acceptable differences exist between the compared results.

4

CHAPTER 4

11th Asia-Pacific Conference on Combustion
Sydney, 10-14 December 2017

Schlieren CT Measurement of 3D Density Distributions of Flame Kernels of Spark-Ignited Direct-Injection of Free, Cavity-Guided and Plane-Guided Fuel Jets

Published: 2017.12.10

http://www.anz-combustioninstitute.org/proceedings.php

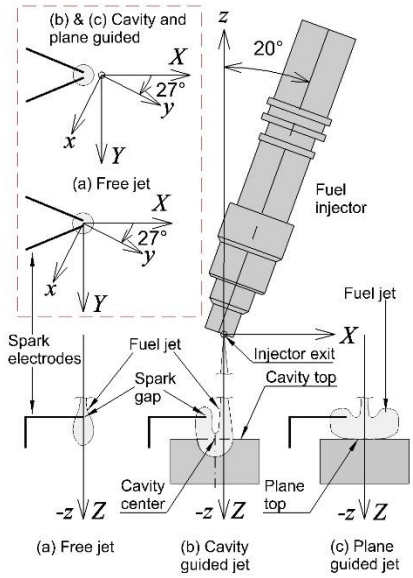

Abstract

Measurement of three-dimensional (3D) density distribution of the initial flame kernels induced by spark-ignition of three type of fuel jets escaping into an ambient space from direct injection nozzle has been conducted. Propane gas is used as a fuel. First, a flame kernel from a spark-ignited free jet is investigated. Next two types of wall-guided (cavity and plane) are used to model fuel jets controlled by a piston bowl shape cavity in a gasoline direct injection(GDI) engine. For 3D observation of flame kernels of fuel jets, non-scanning 3D-CT (three-dimensional computer tomography) technique using a delicate multi-directional quantitative schlieren system with flash light source is employed. By using ML-EM (Maximum Likelihood-Expectation Maximization) an appropriate CT algorithm the 3D density distribution data are successfully reconstructed. The 3D data of initial flame kernel after ignition is of importance to further understanding of the complicated ignition process of the GDI engine.

CHAPTER 4
DIRECT-INJECTION OF FUEL JETS

4.1. Introduction

The "turbulent flame", which is a flame formed in turbulent flow, causes the flame surface to be disturbed by large and small eddies and the area of the flame surface to increase. Many combustion equipment and engines deal with the turbulent flames. It is very difficult to measure the three-dimensional structure of the entire flame, because of the "three-dimensionality" and "unsteadiness" nature of the turbulent flames, time series, the variation of instantaneous structures of the turbulent flames. In addition to turbulent flames, many other fluid phenomena deal with "three-dimensionality" and "unsteadiness", such as spark ignition flames and jets.

In previous works [4]-[10], by employing and developing a non-scanning 3D-CT technique using a multi-directional quantitative schlieren optical system with flashlight source, measurement of the instantaneous density distribution of several types of flame in laminar and turbulent flows have been successfully obtained. In the present study, the mentioned method has been used to investigate the three-type of flame kernels from spark-ignited of free, cavity-guided, and plane-guided fuel jets issuing from a direct injection nozzle. It is the first time, which the mentioned technique with non-deviation treatment for projection images (density thickness images) is used to measure the instantaneous density distributions of flame kernels.

4.2. Direct Injection Nozzle and Ambient Conditions

In the automotive engine, gasoline direct injection(GDI) system is a recent generation of technology to improve engine efficiency [61]. In the present investigation, a direct injection nozzle (injector) is used to measure the "density distributions of flame kernels from spark-ignited direct-injection of fuel jets".

Figure 4.1 indicates the schematic diagrams of the injector and the fuel jets in three configurations. The fuel injector (Mitsubishi Electric Corporation, EAT-317, installed in Suzuki K6A engine) has 4 holes × 2 rows (8 holes) to generate two fuel jets (in 40° interval) for injecting in two intake paths of the K6A

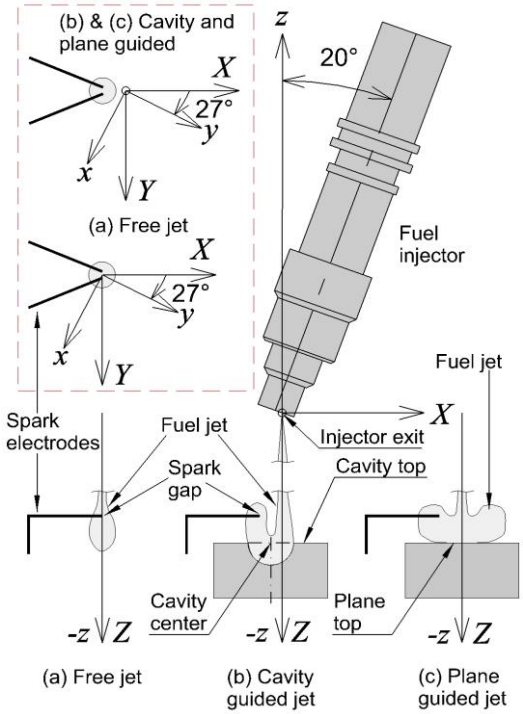

Fig. 4.1 Schematic of fuel jet injection system.

engine. The holes have an exit diameter of 0.15 mm. In this study by blocking 4 holes of the injector, one fuel jet flowing vertically downward is obtained by installing the fuel injector at 20° as shown in Fig. 4.1. Propane gas is used as a fuel. Figure 4.1(a) indicates spark ignition on the free fuel jet to obtain a flame kernel. Two types of wall-guided (cavity and plane) are used to model fuel jets controlled by a piston bowl shape cavity in a GDI engine (Fig. 4.1(b) and (c)). The cavity portion is a hemispherical shape having a diameter of 8 mm, a depth of 4 mm. The position of the spherical center represents the position of the cavity. In the present investigation, the ambient condition is recorded as ambient temperature 25.6°C and ambient (back) pressure 0.101 MPa.

Figure 4.2((a) and (c)) illustrates the concept of 20-directional schlieren camera. In the camera system, the target flame kernel/non-uniform density field is observed from 180º direction by numerous schlieren optical system simultaneously. Twenty systems capture the multi-directional views in the 20 angle positions from θ = −85.5º to 85.5º at an interval of 9º. Here angle θ is defined as the horizontal angle from the *x*-axis. The center of the injector exit has been selected as an origin of the *XYZ*-coordinate system for the injection system. The origin of the multi-directional optical system (*xyz*-coordinate) coincides with the *XYZ*-coordinate system as shown in Fig. 4.2(b). The *x*-axis is located between camera No.10 (θ = −4.5º) and camera No.11 (θ = +4.5º). The single unit of quantitative schlieren system in the multi-directional schlieren camera is diagramed in Fig. 4.2(d). This system is composed of two convex achromatic lenses of 50 mm in diameter and 30 0mm in focal length, a light source unit, a vertical knife-edge (for obtaining horizontal schlieren brightness gradient images), and a digital camera. The neutral density (ND) filter (Fuji 1.5, exposure adjustment multiple 3.16) and stepped ND filter is used for calibrating the cameras. The light unit is a xenon flashtube that emits full-spectrum white light with a

uniform luminance rectangular area of 1 mm × 2 mm and a 35 μs duration.

Between cameras No.13 and No.14, a high-speed camera (HSC) (Photron made FASTCAM-512 PCI

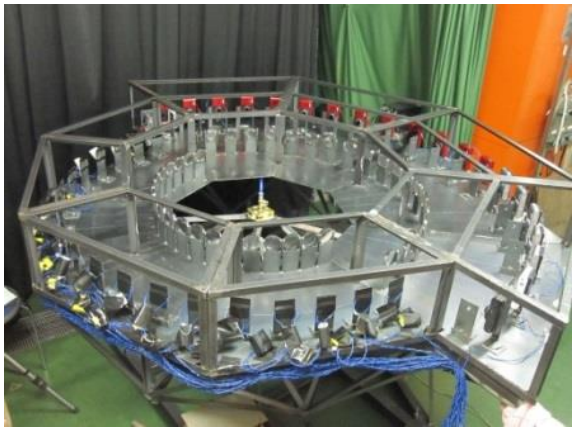

(a) Schlieren camera system

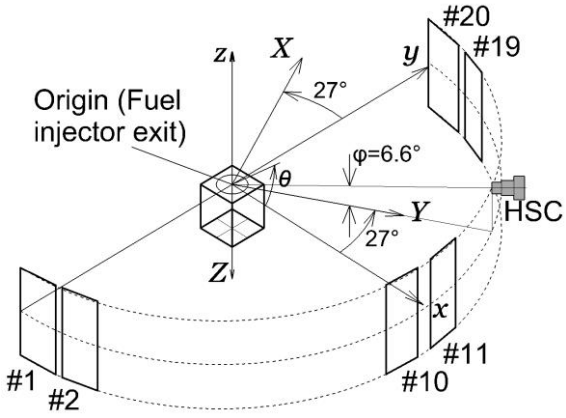

(b) Coordinate system

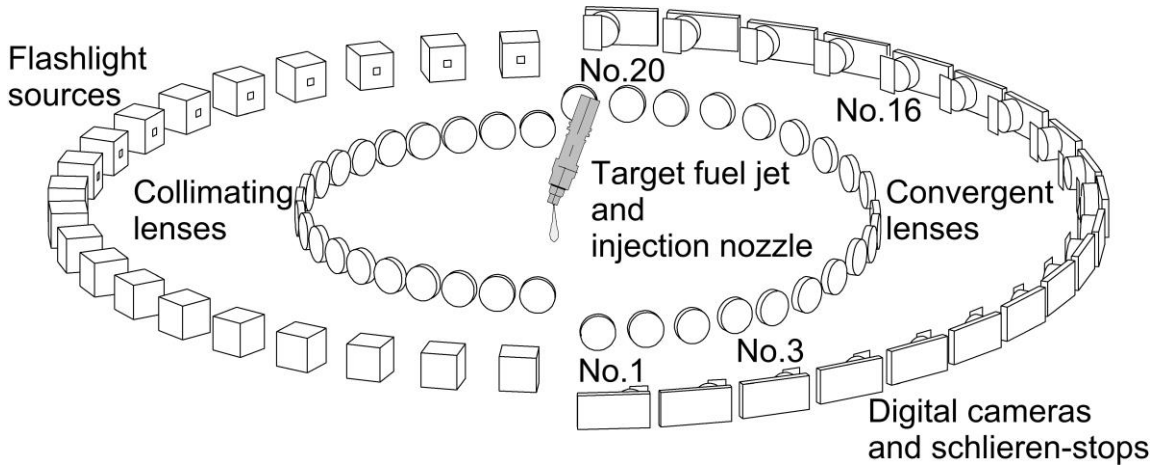

(c) Schematic of 20-direction schlieren camera

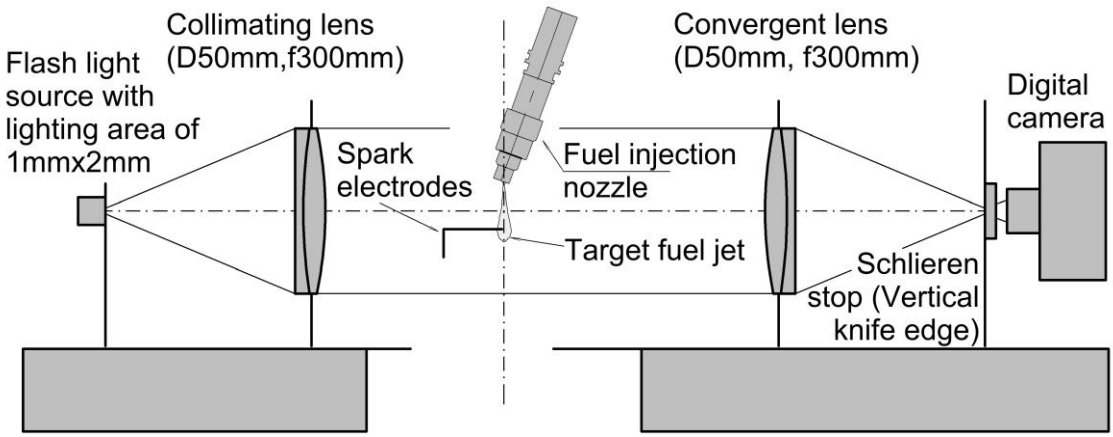

(d) Single unit of quantitative schlieren system

Fig. 4.2 Multi-direction schlieren and coordinate system.

2K) as a single direction schlieren imaging device is installed in the direction of a horizontal angle θ = 27° and a dip angle φ = 6.6° that simultaneously is used with the 20-directional schlieren camera as shown in Fig. 4.2(b). The ignition electrode (nichrome wire, 0.4 mm in diameter and 1 mm gap) centerline is in the direction of the horizontal angle θ = 27° + 90° (Fig. 4.1). The previously mentioned fuel injection coordinates (*XYZ*) are set to this angle. The lag timings of the fuel jet injection, the ignition, the flash of the light source and the shutter operation timing of the shooting camera group for simultaneous schlieren photography are set by an electronic circuit. To avoid malfunction due to noise generated by the high voltage spark circuit, visible light laser diode and optical fiber are used for signal transmission to the fuel injector drive circuit, the spark circuit and the flash circuit.

4.3. Results and Discussion

The time series formation of spark-ignited flame kernels for cavity-guided fuel jet is shown in Fig. 4.3. There is a time lag of 0.5 ms between each stage of fuel injection (a), ignition (b), flame kernel formation (c), and light source flash time (d) for all flame kernels. The position of the ignition electrode for free jet and wall-guided is (X,Y,Z)=(0 mm,0 mm,12 mm) and (X,Y,Z)=(−4 mm,0 mm,12 mm) respectively, and the position of the cavity center and top of the plane are (X,Y,Z)=(−2 mm,0 mm,15 mm). In another word, ignition electrode (a black stripe in the results (see Fig. 4.7 and Fig. 4.8)) and wall-guided top are located below injector at z = −12 mm and z = −15 mm respectively.

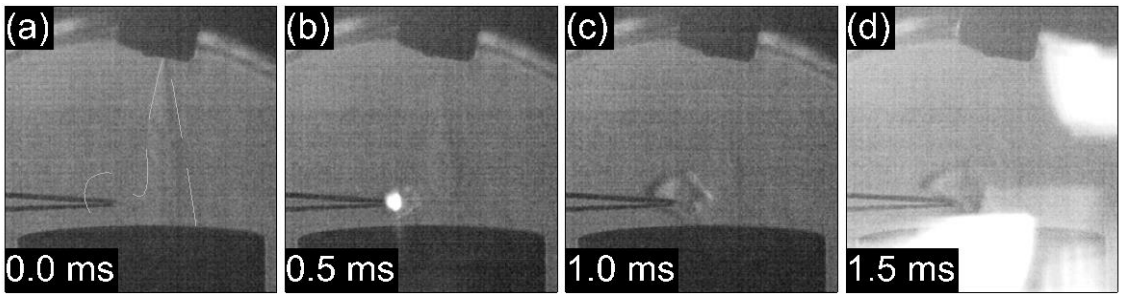

Fig. 4.3 High-speed schlieren images of the formation of the spark-ignited flame kernel of cavity guided fuel jet.

4.3.1. Quantitative Schlieren Brightness Images and Density Thickness Images

Figure 4.4 indicates a sample set of quantitative schlieren images of deviation brightness in schlieren images for the spark-ignited flame kernels of free fuel jet (1st row images), cavity guided fuel jet (2nd row images) and plane guided fuel jet (3rd row images). The numbers inserted in each picture express the shooting angles θ. The images of Fig. 4.4 are processed by the aforementioned conversion procedure to projection images of density thickness $Dt'(X(\theta))$, as shown in Fig. 4.5.

In the present study, the "density thickness" projection images of 500 (H) × 500 (V) pixel (20 mm × 20 mm) are used for CT reconstruction to produce 3D data 500 (x) × 500 (y) × 500 (z) pixel (20 mm × 20 mm × 20 mm). The voxel size is 0.04 mm in each direction.

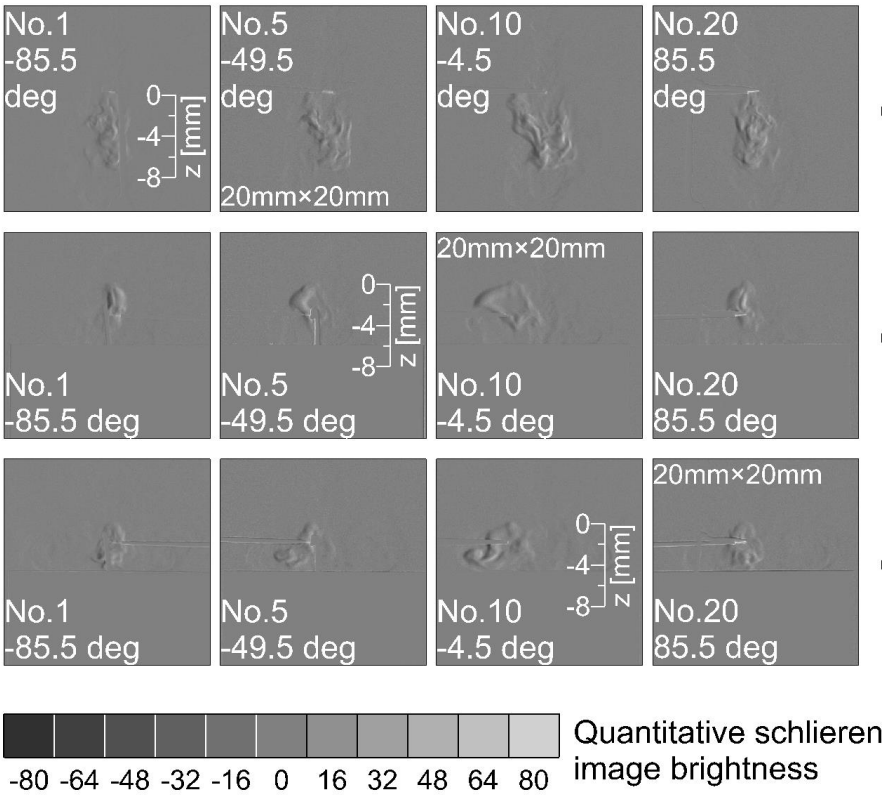

Fig. 4.4 The sample set of quantitative schlieren images of flame kernels for the free fuel jet (1st row images), cavity guided fuel jet (2nd row images) and plane guided fuel jet (3rd row images).

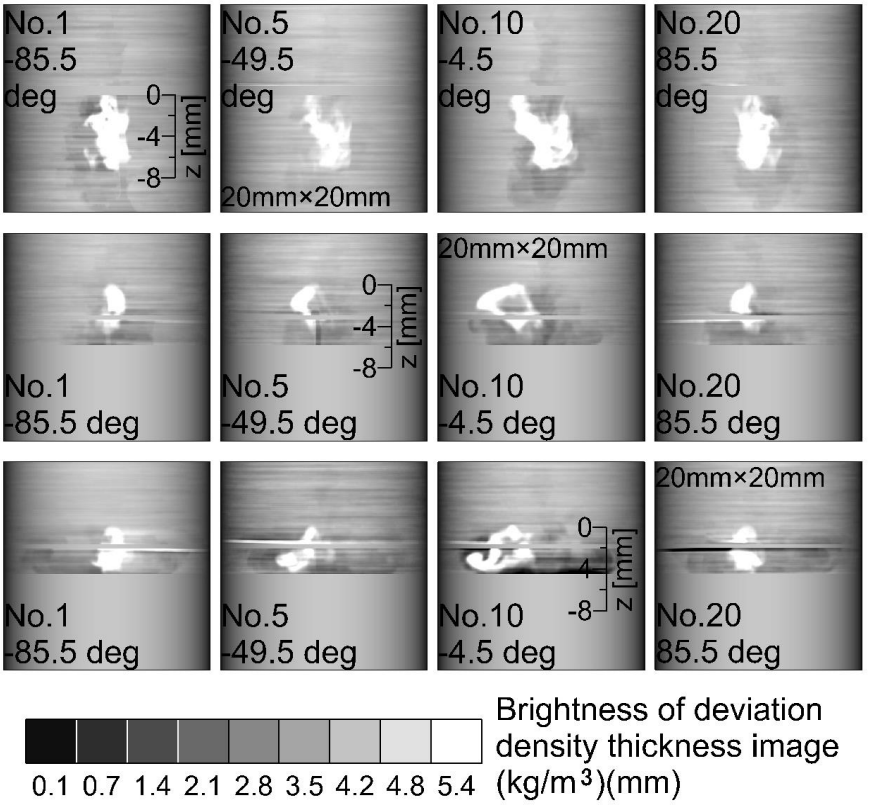

Fig. 4.5 The sample set of density thickness images of flame kernels for the free fuel jet (1st row images), cavity guided fuel jet (2nd row images) and plane guided fuel jet (3rd row images).

4.3.2. 3D-CT Reconstruction of Flame Kernels and Density Distributions Diagrams

Using the density thickness images of Fig. 4.5 as projections for CT reconstruction, the 3D instantaneous density distribution of flame kernels of fuel jets has been successfully obtained. Figure 4.6 (free fuel jet), Fig. 4.7 (cavity guided fuel jet) and Fig. 4.8 (plane guided fuel jet) give one sample of horizontal and one sample of vertical distributions of CT-reconstructed density for different positions for all type of flame kernels. The darker parts are related to the lower density areas with higher temperatures and vice versa. The corresponding density contour diagrams of each cross-section are depicted below them. The ignition electrode depicted as a black stripe in the results (see Fig. 4.7 and Fig. 4.8)). For better evaluation of the reconstructed density values, the superposition of axial density distributions diagrams are illustrated in the Fig. 4.9 and Fig. 4.10 respectively. Generally, results clearly demonstrate the minimum density values are about 0.2 kg/m^3 for burnt gas.

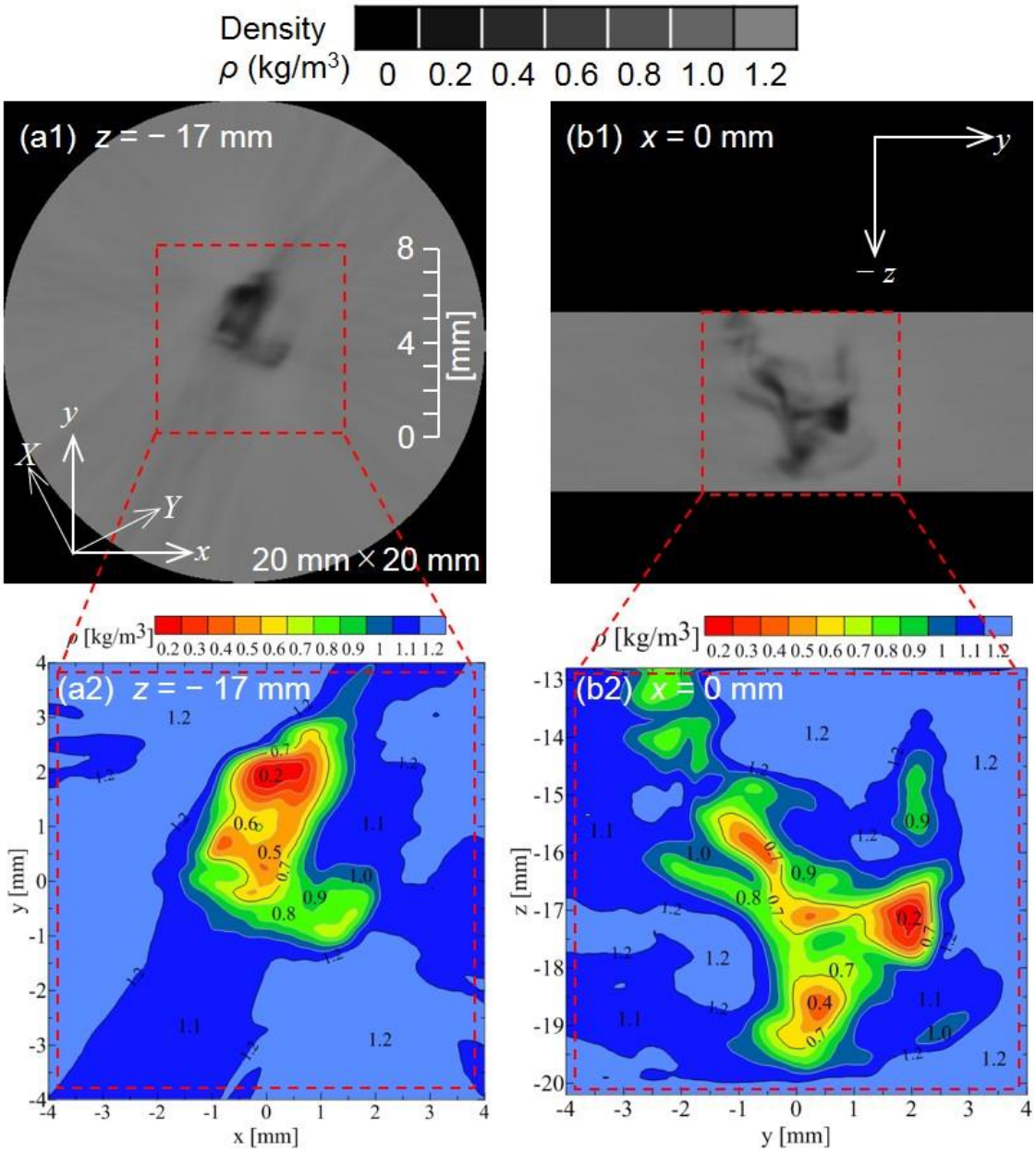

Fig. 4.6 Sample set of horizontal (left (a)) and vertical (right (b)) CT-reconstructed density distributions ((a1) and (b1)) and corresponding density contour diagrams ((a2) and (b2)) of flame kernels for the free fuel jet.

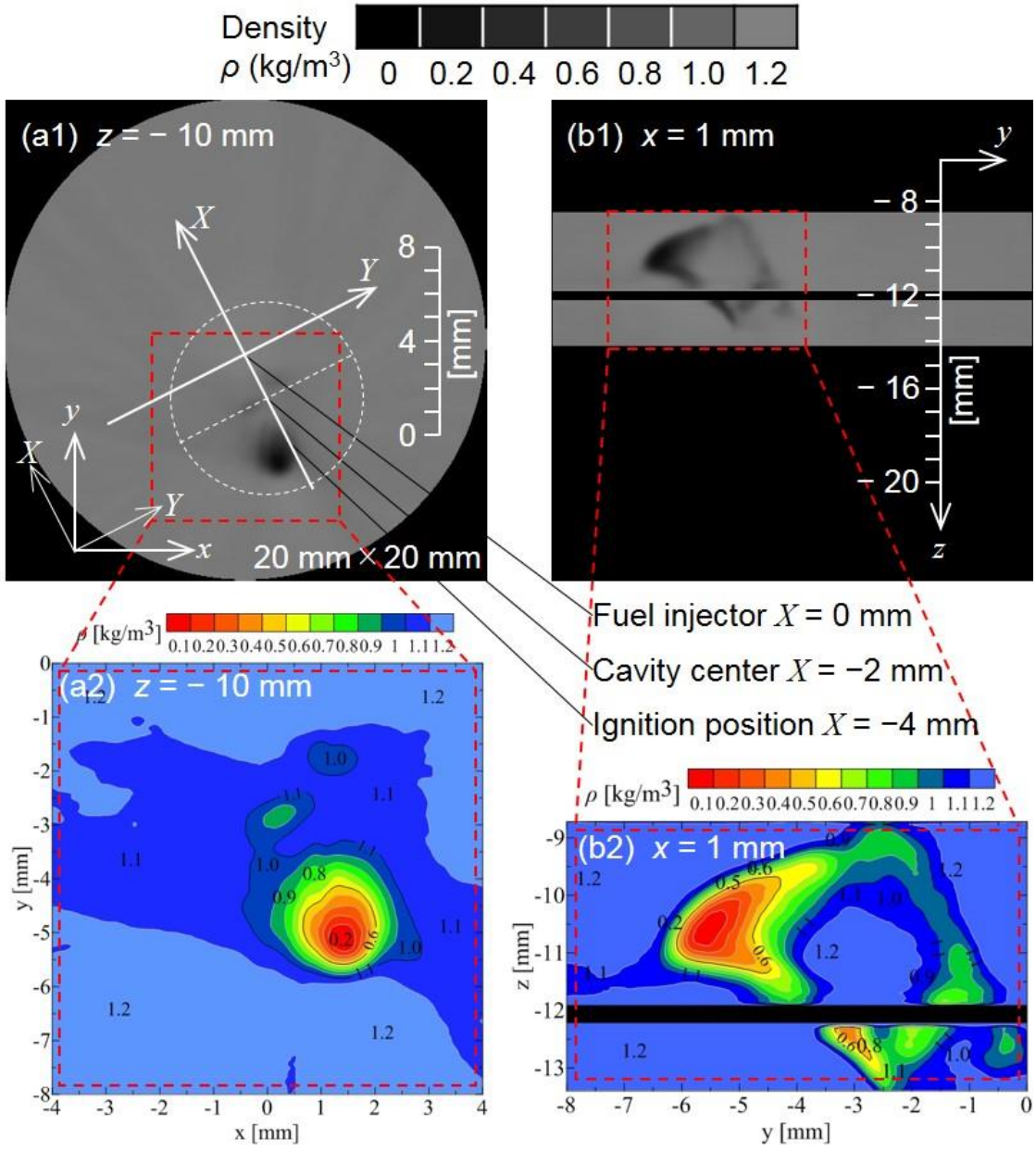

Fig. 4.7 Sample set of horizontal (left (a)) and vertical (right (b)) CT-reconstructed density distributions ((a1) and (b1)) and corresponding density contour diagrams ((a2) and (b2)) of flame kernels for the cavity guided fuel jet.

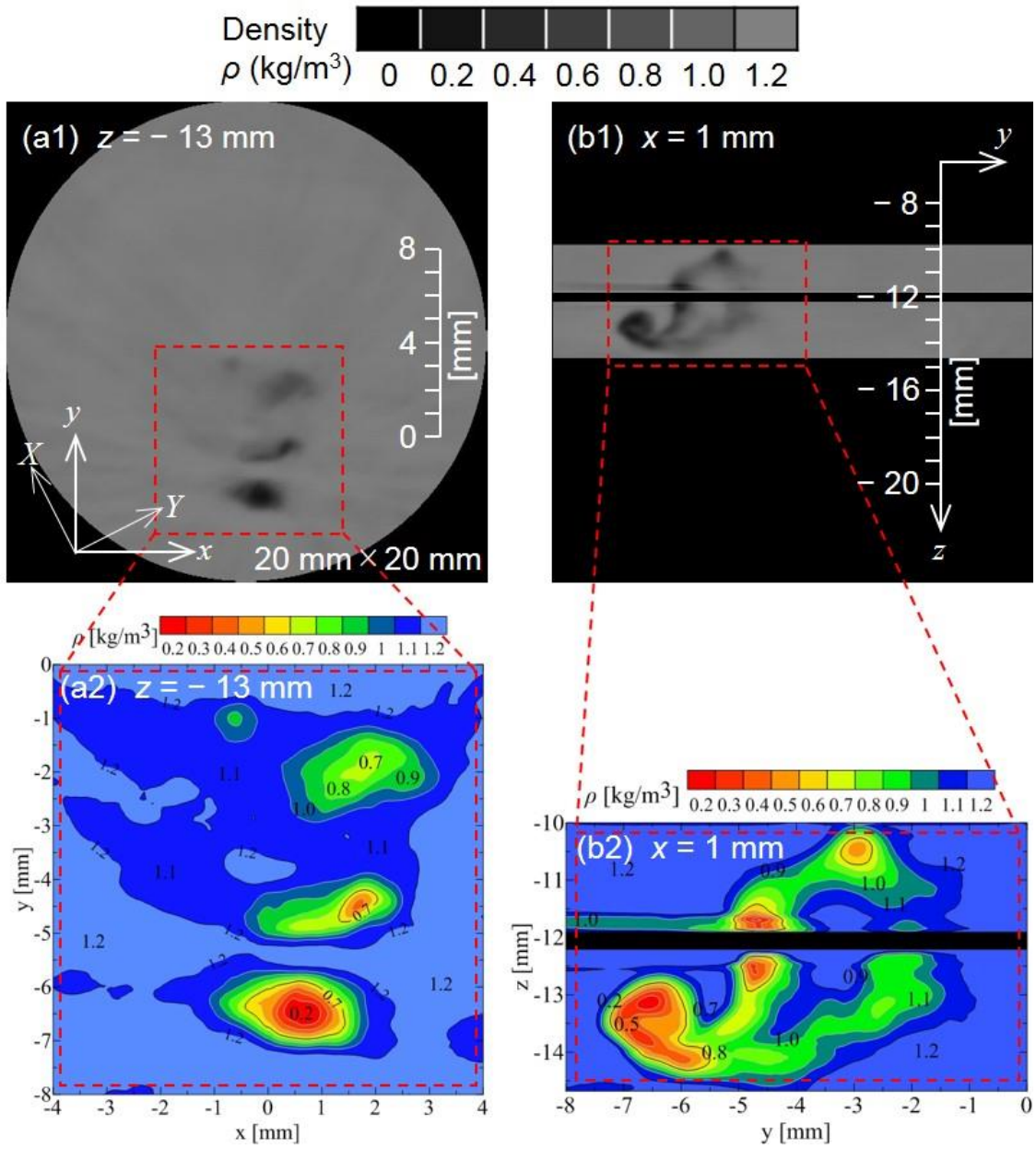

Fig. 4.8 Sample set of horizontal (left (a)) and vertical (right (b)) CT-reconstructed density distributions ((a1) and (b1)) and corresponding density contour diagrams ((a2) and (b2)) of flame kernels for the plane guided fuel jet.

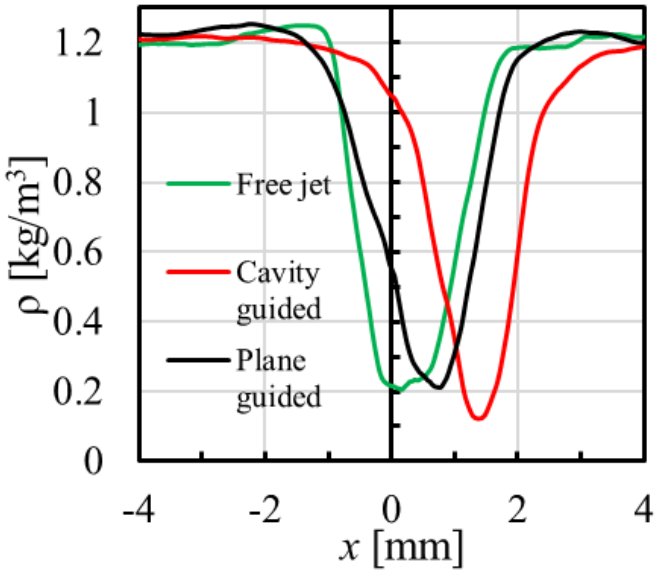

Fig. 4.9 Superposition of axial density distributions of flame kernels, (x-axis): free (y = 2 mm, z = −17 mm), cavity guided (y = −5 mm, z = −10 mm) and plane guided (y = −6.5 mm, z = −13 mm) fuel jets.

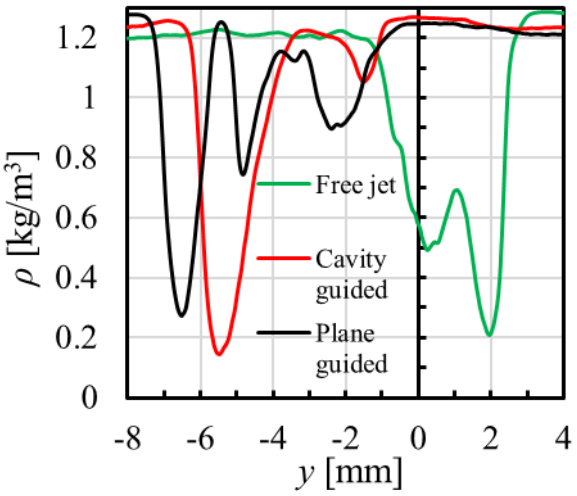

Fig. 4.10 Superposition of axial density distributions of flame kernels, (y-axis): free (x = 0 mm, z = −17 mm), cavity guided (x = 1 mm, z = −10 mm) and plane guided (x = 1 mm, z = −13 mm) fuel jets.

4.4. Summary and Concluding Remarks

By employing the non-scanning 3D-CT technique using a 20-directional quantitative schlieren system, CT reconstruction of the instantaneous 3D density distribution of the spark-ignited flame kernels in propane/air fuel jets from direct injection nozzle have been successfully obtained. The 3D structure of the initial flame kernel after ignition is of great importance in understanding the ignition phenomena and can be served as validation data for numerical simulations.

5

CHAPTER 5

Journal of the Combustion Society of Japan (CSJ), 62(202), 338-346

Multi-Schlieren 3D-CT Measurements of Instantaneous Equivalence Ratio Distributions of a Premixed Gas Field Based on Modified Refractive Index

Published: 2020.11.06

https://doi.org/10.20619/jcombsj.1910

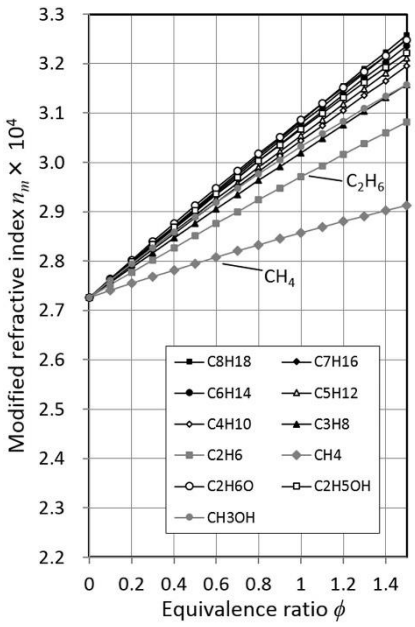

Abstract

In quantitative measurements and investigations, "equivalence ratio" and "refractive index" are the most significant parameters in combustion flow fields. Experimental and analytical studies were performed to understand the relation between equivalence ratio and refractive index in flow fields. A "universal relationship" between the refractive index of a premixed gas of fuel and air and its equivalence ratio has been established in this study. Through this relationship, we can calculate the equivalence ratio of any premixed gas (except those of light fuels) from its refractive index using a unique coefficient. The uniqueness of the relation coefficient enables us to obtain the equivalence ratio of even a multi-fuel premixed gas from its refractive index. In this study, the novel relationship is applied to a non-scanning 3D-CT (computerized tomography) technique using a multi(20)-directional quantitative schlieren optical system with a flashlight source. Instantaneous equivalence ratio distributions of a dual-fuel premixed gas flow with two jets of ethanol/air and propane/air mixtures are measured by CT-reconstruction. Good agreement was observed between the CT-reconstructed data and the proposed comprehensive relation.

CHAPTER 5
REFRACTIVE INDEX AND EQUIVALENCE RATIO

5.1. Introduction

The global community is currently looking for fuel-efficient and environmentally viable alternatives for many traditional energy conversion approaches. One of the efficient ways is to use "dual-fuel vehicles" (vehicles with multifuel engines), which are used in certain regions. For improving life cycle value of the vehicles, Yanmar has developed a reliable "dual-fuel engine" [62] that can use diesel and gas for the marine engine sector. Evaluating air/fuel mixture and calculating the equivalence ratio in these dual-fuel engines requires certain new techniques that can facilitate the complicated treatment of two or more mixed fuels. In this study, a universal relationship between a "modified refractive index n_m" of a premixed gas of fuel and air and its "equivalence ratio φ" is introduced.

The equivalence ratio represents the mixing ratio of various fuels and oxidizers (air), and is an important parameter for expressing conditions such as proper mixing, excess fuel, and excess air for combustion, and particularly, for state-of-the-art premixing fuel-air technology. For calculating the equivalence ratio, it is necessary to know the type of fuel and its concentration ratio. It is complicated to measure the equivalence ratio in a flow field with multiple fuel types using conventional investigation techniques. Hence, the objective of this work is to study the equivalence ratio, which is important for combustion. Further, we propose a measurement method for the equivalence ratio of premixed gas with multiple types of fuels of unknown components, based on the modified refractive index of the premixed gas field. Furthermore, this is applied to the three-dimensional computerized tomography (3D-CT) technique using a multi-directional quantitative schlieren optical system to try to measure the instantaneous 3D equivalence ratio distributions of the flow field where the premixed gas exists. First, the "3D modified refractive index n_m" distributions data of the target flow are obtained using 3D-CT reconstruction of the projection's images. Further, the corresponding "equivalence ratio φ" is calculated using the proposed "universal relationship" between a modified refractive index and its equivalence ratio. In the multi-directional quantitative schlieren optical system, by narrowing the width of the light source, it is possible to measure fields with a small difference in the refractive index. In this study in comparison

to the previous investigations, the width of the light source changed from 1 mm to 0.25 mm. The digital cameras used for this measurement remodified again (refer to section 1.18 and 1.19). The modification point of the cameras is that the previous lenses are replaced by the binocular objective lenses. The binocular objective lens focal length and lens diameter are 80 mm and 21mm, respectively.

Kawahara *et al*. [63] developed a heterodyne interferometry system with a fiber-optic sensor. This system provides a refractive index (consequently, temperature) measurement technique for unburned gas in a commercially produced spark-ignition (SI) engine. Sharma *et al*. [64] experimentally determined the refractive index and density for binary liquid mixtures of eucalyptol with hydrocarbons, and from measured values, refractive index deviations at different temperatures were computed. Nita *et al*. [65] present experimental data of the refractive index for pseudo-binary mixtures of reformate gasoline with ethanol, isopropanol, and *n*-butanol over the entire composition range and for temperature ranging from 293.15 K to 313.15 K. The refractive index mixture rules are discussed by Heller [66].

5.2. Methods and Experimental Setup

5.2.1. Overview of the Proposed Method

In this study, we obtained an instantaneous 3D modified refractive index distributions using the 3D-CT reconstruction method. Using the 20 modified optical path length O_{plm} images derived from the 20 quantitative schlieren images as projection data, the CT-reconstruction procedure has been successfully performed.

We propose a new method for obtaining the equivalence ratio distributions from the modified refractive index distributions. Using this method, it is possible to obtain instantaneous 3D distributions of equivalence ratios in the presence of multiple types of fuels with unknown components for hydrocarbon fuels with three or more carbon atoms.

5.2.2. Derivation of Equivalence Ratio φ based on Modified Refractive Index n_m

The method for obtaining the equivalence ratio from the measured modified refractive index is discussed as follows.

The gas refractive index n is expressed by equation (5.1) using the modified refractive index n_m as,

$$n = 1 + n_m. \tag{5.1}$$

It can be expressed by equation (5.2) using the Gladstone-Dale relation (ρ: density, K: Gladstone-Dale constant) as,

$$n = 1 + \rho K. \tag{5.2}$$

Therefore, the modified refractive index n_m, density, and Gladstone-Dale constant of a gas have the following relationship,

$$n_m = \rho K. \tag{5.3}$$

In the combustion of hydrocarbon-type fuels $C_aH_bO_c$, the formula for the chemical equilibrium of hydrocarbon fuel-air premixes based on the equivalence ratio φ and hydrocarbon components is,

$$C_aH_bO_c + [(a + 0.25b - 0.5c) / (0.21\varphi)] (0.79N_2 + 0.21O_2). \tag{5.4}$$

Therefore, the air fuel ratio (AFR) of the premixed gas is,

$$\text{Air} : C_aH_bO_c \quad = \quad [(a + 0.25b - 0.5c) / (0.21\varphi)] : 1, \tag{5.5}$$

or

$$AFR = (a + 0.25b - 0.5c) / (0.21\varphi). \tag{5.6}$$

The density of the premixed gas ρ_{mix} can be obtained by the following equation using the mass fraction X_i known from the mass ratio obtained by equation (5.6).

$$\rho_{mix} = \Sigma_i \rho_i X_i = \rho_{Air} X_{Air} + \rho_{Fuel} X_{Fuel} + \ldots, \tag{5.7}$$

where,

$$X_{Air} = AFR / (1 + AFR), \tag{5.8}$$

$$X_{Fuel} = 1 / (1 + AFR), \tag{5.9}$$

Therefore, the product of the density of the premixed gas and Gladstone-Dale constant K is obtained by the following equation (5.10).

$$\rho_{mix} K_{mix} = \Sigma_i \rho_i K_i X_i. \tag{5.10}$$

Further, based on equation (5.3) $n_m = \rho K$ (*i.e.* $n_m = \rho_{mix} K_{mix}$), therefore, equation (5.10) shows the relationship between the equivalence ratio φ and modified refractive index n_m (= $n - 1$, n: refractive index) of the premixed gas. The results of this relationship are illustrated in Fig. 5.1 for certain hydrocarbon-type fuels. The Gladstone-Dale constant K [67] in Table 5.1 is used to calculate the modified refractive index. Equation (5.7) shows the relationship between the equivalence ratio φ and the density ρ of the premixed gas, which illustrated in Fig. 5.2 for certain hydrocarbon-type fuels. In Fig. 5.2,

it can be seen that the slope of the line varies greatly depending on the fuel type.

In Fig. 5.1, except for methane and ethane, it can be observed that the relationship between the equivalence ratio and modified refractive index can be represented by a single straight line regardless of the fuel type because they are present in a close range and their differences are very small and negligible. We propose the following correlation (equation (5.11)), which reflects the variation of the results shown in Fig. 5.1.

$$n_m = 0.0000326\,\varphi + 0.0002726. \tag{5.11}$$

Although, the Gladstone-Dale constants in Table 5.1 differ by more than 20%. In Fig. 5.1, the uncertainty is for the upper limit (Octane C8H18) +8.9%, the lower limit (Propane C3H8) -11%, and Ethanol +4.6%. Hence, the equivalence ratio can be obtained using a universal relationship that does not depend on the fuel type, and the equivalence ratio can be measured even when multiple fuels with unknown components are mixed together. This method can be applied to gas alarms, which utilize refractive index sensors [68]-[70].

Table 5.1 Gladstone-Dale constant for some gases [67].

Fuel		Gladstone-Dale Constant K [m^3/kg]
Methane	CH_4	6.150×10^{-4}
Ethane	C_2H_6	5.628×10^{-4}
Propane	C_3H_8	5.458×10^{-4}
Butane	C_4H_{10}	5.324×10^{-4}
Pentane	C_5H_{12}	5.183×10^{-4}
Hexane	C_6H_{14}	5.195×10^{-4}
Heptane	C_7H_{16}	5.165×10^{-4}
Octane	C_8H_{18}	5.131×10^{-4}
Dimethyl ether (DME)	C_2H_6O	4.290×10^{-4}
Ethanol	C_2H_5OH	4.148×10^{-4}
Methanol	CH_3OH	3.912×10^{-4}
Air		2.273×10^{-4}

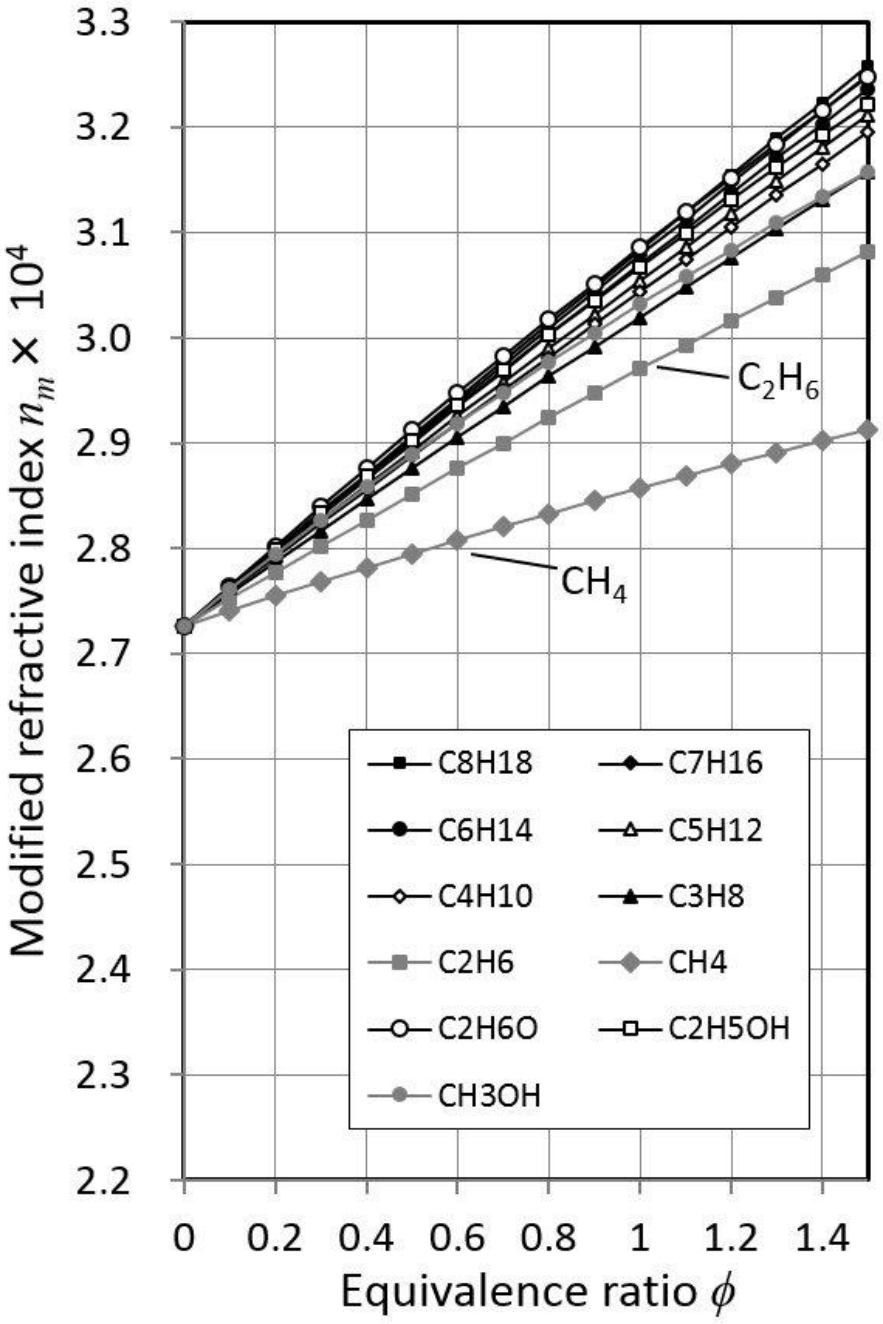

Fig. 5.1 Relationship between φ and n_m.

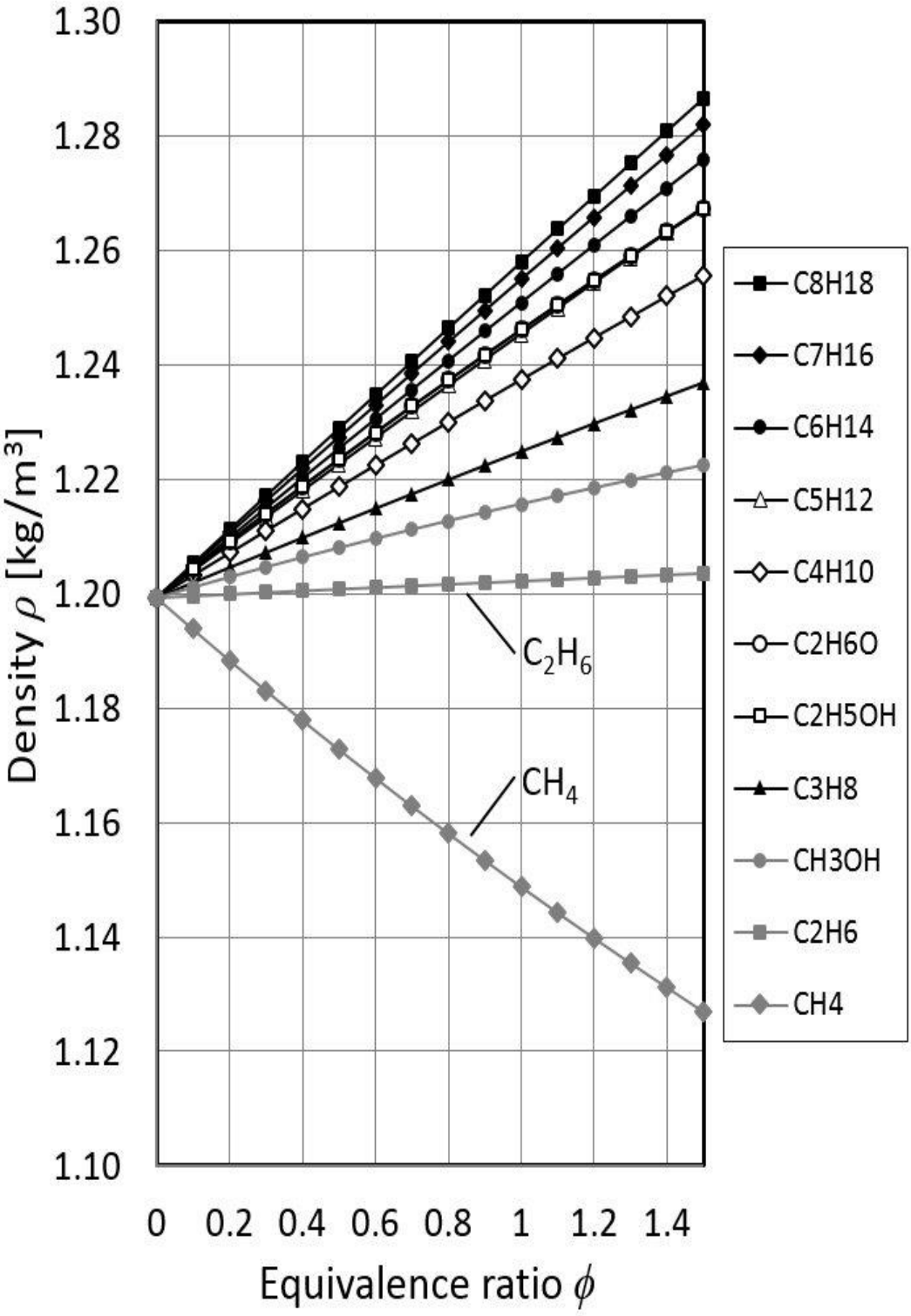

Fig. 5.2 Relationship between φ and ρ.

5.2.3. Image Processing

To obtain the modified refractive index distributions, the 3D-CT measurement requires the distribution of the "modified optical path length O_{plm}" integrated on the ray as projection data. The modified optical path length distribution O_{plm} is obtained based on the diagram in Fig. 5.3. Figures 5.3(b)-(e) show the schlieren observation process from an angle θ for the refractive index profile $n^*(x, y)$ in Fig. 5.3(a). Quantities with an asterisk sign (*) express the actual values and without asterisk represent derived values from the CT-reconstruction process. Fig. 5.3(b)-(h) show observations in the direction of θ from x-axis in the inclined coordinates which are denoted by $X(\theta)$ and $Y(\theta)$. The primary goal is to obtain the modified optical path length O_{plm}^* of deviation modified refractive index (Δn_m^*), which is shown in Fig. 5.3(d) with the unit of length (m). Here, the modified refractive index deviation Δn_m^* is defined as the modified refractive index deviation $\Delta n_m^* = n_m^* - n_{ma}^*$ from the modified refractive index n_{ma}^* of the surrounding gas (air) region of constant modified refractive index $n_{ma}^*(= 2.726\times10^{-4})$ on the periphery of the observed range of radius R, as $n_m^* > n_{ma}^*$, Δn_m^* is non-negative and CT-reconstruction is possible. The modified optical path length of deviation modified refractive index ($O_{plm}^*(X(\theta))$) is called modified optical path length O_{plm}^*. It is automatically obtained from the schlieren observation by spatially-integration of deviation modified refractive index $\Delta n_m^*(X(\theta),Y)$ along the line of sight. The modified refractive index distributions of the target flow field are reconstructed using 2D distributions (image) of modified optical path length O_{plm} as the projection in the CT-reconstruction process.

In practice, for obtaining modified optical path length O_{plm} (Fig. 5.3(h)), the image processing activity starts from Fig. 5.3(e) by obtaining two sets of images, "with target" and "without target" (without any disturbance in the test section) with a horizontal brightness gradient in the x-direction. Two sets of images present by the schlieren observation as $B(X)$ and $B_{nj}(X)$ (brightness of schlieren image in no-jet/no-disturbance condition). $B_{nj}(X)$ is a schlieren brightness distribution when there is no refractive index distribution ($n^*(x, y) = n_a^*$). To obtain the modified optical path length $O_{plm}(X(\theta))$ from $B(X)$ and $B_{nj}(X)$, both are processed as depicted in Fig. 5.3(f)-(h). As indicated in Figs. 3(f) and (g), deviation brightness in schlieren image $\Delta B(X)$

$$\Delta B(X) = B(X) - B_{nf}(X), \tag{5.12}$$

is scaled to $d(O_{plm}(X(\theta)))/dX(\theta)$ by the next expression.

$$d(O_{plm}(X(\theta)))/dX(\theta) = \alpha \times (B(X) - B_{nf}(X)), \tag{5.13}$$

where α depends on transparent width of the light source image on schlieren stop location and focal length of the convergent lens, and will be determined as follow.

Based on the explanation of sections 1.5 to 1.7, combining equation (1.17) and equation (1.26), then,

$$\frac{\Delta B(X)}{B_0(X)} = \frac{f}{a_0}\int_{-\infty}^{+\infty}\left(\frac{\partial n_m}{\partial x}\right)ds\,, \tag{5.14}$$

If the knife-edge is rotated by 90º, the deflection angle on *y*-axis will be measured, then,

$$\frac{\Delta B(X)}{B_0(X)} = \frac{f}{a_0}\int_{-\infty}^{+\infty}\left(\frac{\partial n_m}{\partial y}\right)ds\,. \tag{5.15}$$

In addition, the "modified optical path length O_{plm}" can be expressed as follows.

$$O_{\rho lm}(X(\theta)) = \int_{-\infty}^{+\infty} n_m(x,s)ds\,, \tag{5.16}$$

and

$$O_{\rho lm}(X(\theta)) = \int_{-\infty}^{+\infty}\int_{0}^{x}\frac{dn_m(x,s)}{dx}dxds\,. \tag{5.17}$$

By combining the equation (5.14) and equation (5.17), "modified optical path length O_{plm}" can be expressed as follows.

$$O_{\rho lm}(X(\theta)) = \int_{0}^{x}\frac{a_0}{f}\frac{\Delta B(X)}{B_0(X)}dx\,. \tag{5.18}$$

Accordingly, by using this equation, the "modified optical path length O_{plm}" from schlieren image brightness is calculable. Where a_0 is transparent width of the light source image on schlieren stop location (a_0 = 0.25 mm × 2 mm (width × height)), and f (= 300 mm) is focal length of the convergent lens. The relation between α in the equation (5.13) and transparent width of the light source and focal length of the convergent lens is clear now. Therefore, based on equation (5.13), modified optical path length O_{plm} is reproduced by transverse-integration of $d(O_{plm}(X(\theta)))/dX(\theta)$ from schlieren images, as shown in Fig. 5.3(h). Furthermore, $O_{plm}*(X(\theta) = -R) = O_{plm}*(X(\theta) = +R) = 0$.

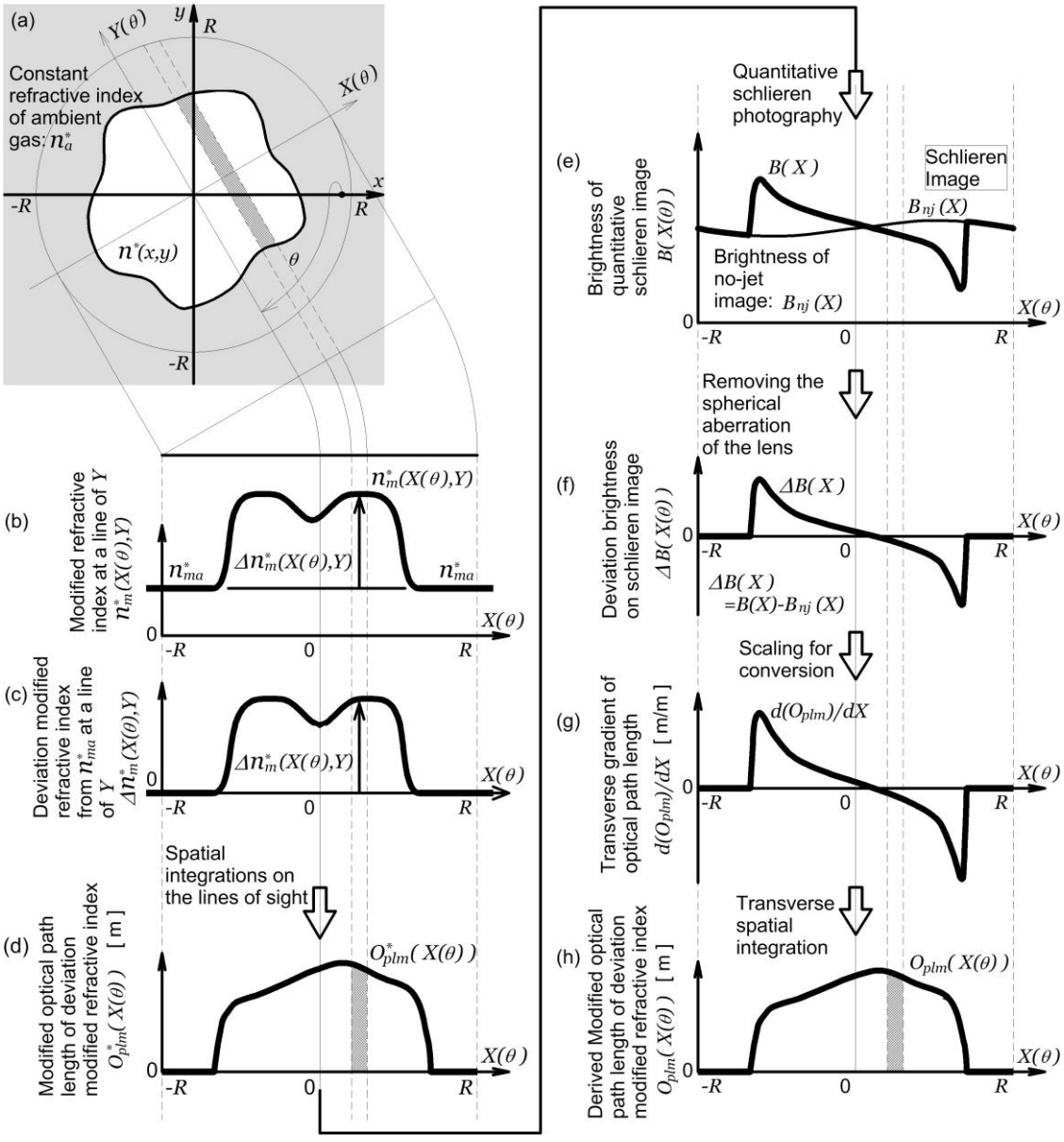

Fig. 5.3 Process of formation of schlieren brightness and conversion to projections O_{plm} of CT.

5.2.4. CT-Reconstruction

The images of modified optical path length O_{plm} are used as projections for CT-reconstruction by maximum likelihood-expectation maximization (ML-EM) an appropriate CT algorithm to obtain the 3D reconstruction of modified refractive index distributions. ML-EM (distributed back-projection) method is employed for CT-reconstruction. The CT-reconstruction procedure is performed in each horizontal plane of z-axis for the reconstruction of deviation modified refractive index distributions $\Delta n_m(x, y)$ from linear data set of modified optical path length $O_{plm}(X(\theta))$ (Fig. 5.3(c)). Further, 2D modified refractive index distribution (Fig. 5.3(b)) is obtained as follows.

$$n_m(x, y) = \Delta n_m(x, y) + n_{ma}^*. \tag{5.19}$$

The reconstruction is performed for each cross-section, and the cross-sections are stacked to form the 3D modified refractive index distribution. Therefore, the 2D distributions $n_m(x, y)$ are accumulated in layers to form 3D-CT distribution $n_m(x, y, z)$. In this study, the modified optical path length $O_{plm}(X(\theta))$ projections images of 900(H) × 100(V) pixel (27 mm × 3 mm) are used for CT-reconstruction to produce 3D data 900(x) × 900(y) × 100(z) pixel (27 mm × 27 mm × 3 mm). The voxel size is 0.03 mm in each direction.

5.2.5. Experimental Injection Nozzle and Flow Conditions

Figures 5.4 shows an overview of the premixed gas injection device used in this experiment and an outline of its nozzles shape and size. This injection device can inject two different fuels simultaneously by filling the parts shown in red in Fig. 5.4 with premixed gas and rotating the lower motor. A stepping motor (manufactured by Plexmotion, SSA-PR-42D2, built-in driver) was used in this experimental setup. When the motor rotates, the plunger of the syringe moves, and the syringe is passed through the acrylic tube connected to the upper part of the syringe, then, the air-fuel mixture is injected. As depicted in Fig. 5.4(top), the convergent nozzle shape is provided with a constricted flow part with an inlet diameter of 12 mm and an outlet diameter of 6 mm to inject the premixed gas in a laminar flow. In the present measurement, laminar flow meters used as shown in Fig. 5.5. These laminar flow meters was designed, which can be used at a flow rate of around 50 l/min for the airflow and 3 l/min for the propane flow to maintain the laminar flow. In addition, the flow rate was calibrated by the soap bubble method. A differential pressure gauge was used to measure the differential pressure between the front and rear chambers of the laminar flow meter. In this investigation, the ambient temperature and pressure are measured 20.1 °C and 1018.3 hPa respectively. In this experiment, ethanol-air and propane-air premixed gases with an equivalence ratio φ = 1 are injected simultaneously, and 20-directional simultaneous quantitative schlieren imaging is performed. The target "two premixed jets/non-uniform density field" is observed from a 180° angle using numerous schlieren optical systems simultaneously (Fig. 5.6(a)). A single instance of the multi-directional quantitative schlieren camera system is illustrated in Fig. 5.6(b).

By narrowing the width of the light source, it is possible to measure fields with a small difference in the refractive index. In this study in comparison to the previous investigations, the width of the light source changed from 1mm to 0.25 mm (Fig. 5.6(b)). The center between two-nozzle exits has been selected as the origin of the *xyz*-coordinate system. The premixed gases outlet center coordinate is (*x*, *y*, *z*) = (0, −8, 0) for ethanol-air and (*x*, *y*, *z*) = (0, +8, 0) for propane-air.

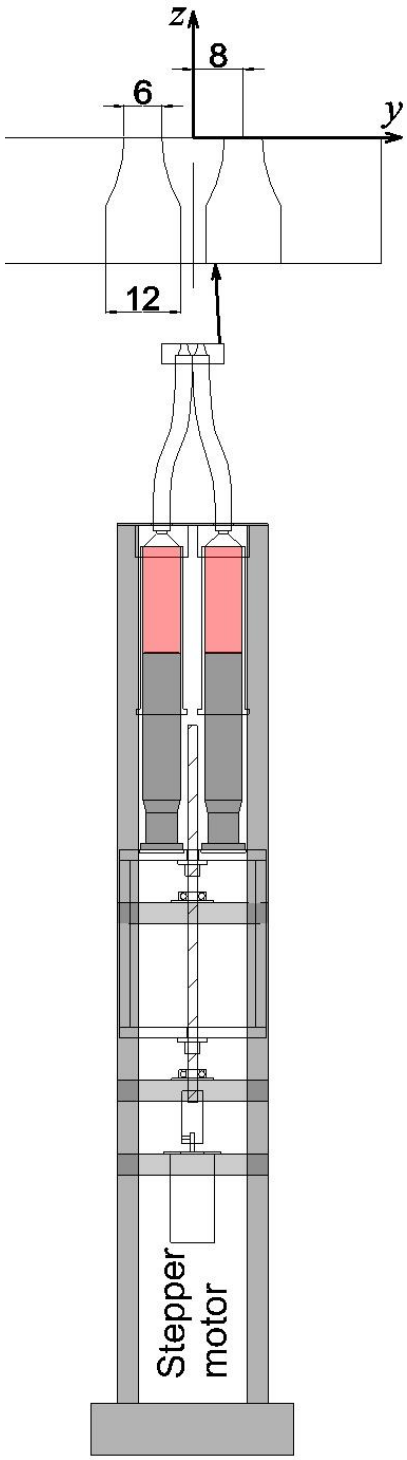

Fig. 5.4 Schematic of injector.

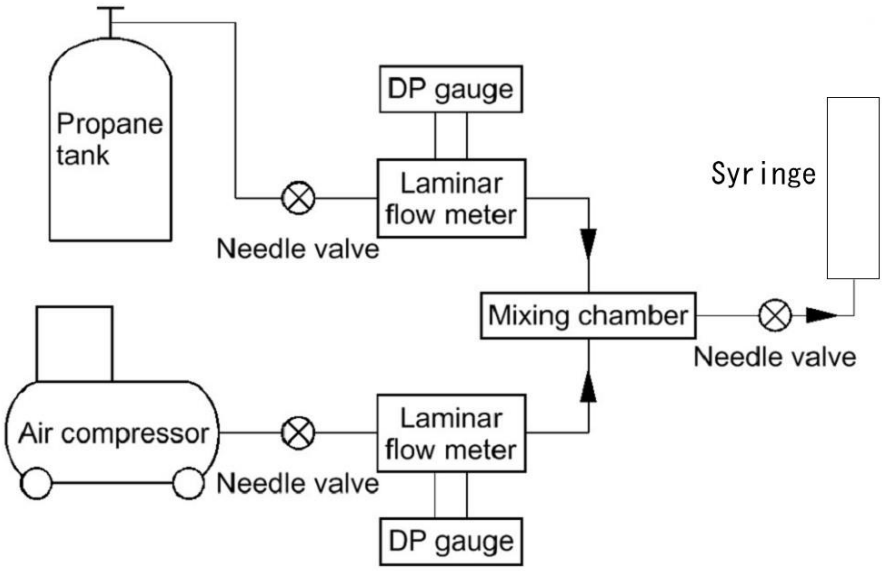

Fig. 5.5 Propane-air premixture delivery system diagram.

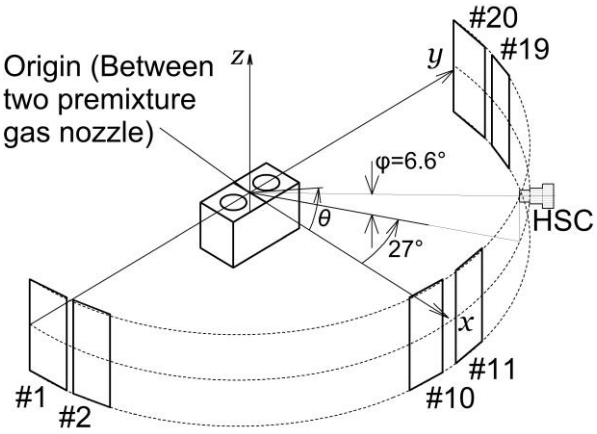

(a) Schematic of 20-direction schlieren camera

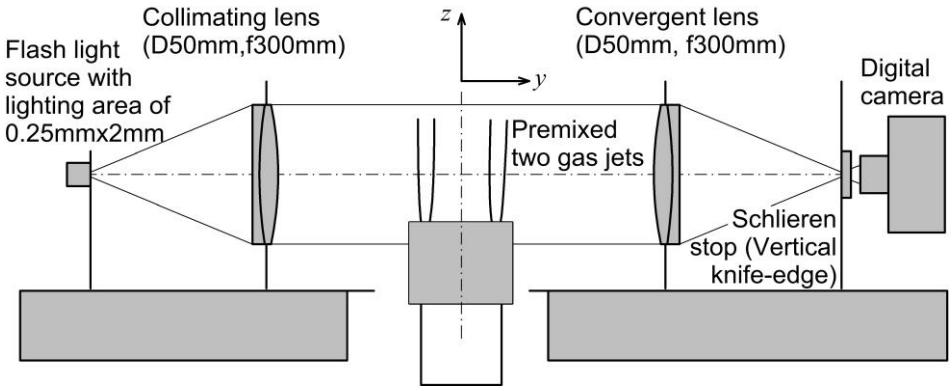

(b) Single unit of the quantitative schlieren optical system

Fig. 5.6 Coordinate systems.

5.3. Results and Discussion

In this study, the injected two premixed gas jets have been successfully CT-reconstructed with the non-scanning 3D-CT technique using a 20-directional quantitative schlieren system. The results show the instantaneous 3D distributions of the modified refractive index n_m of two premixed gas jets downstream of the nozzles exit. Further, from the modified refractive index distributions obtained by CT-reconstruction, the 3D distributions of the equivalence ratio φ for the premixed gas jets obtained as well. The 3D-CT reconstruction results for target flows are shown in the following subsections.

5.3.1. Quantitative Schlieren Brightness Images

Figures 5.7 shows quantitative schlieren images of the two premixed gas jets ethanol-air and propane-air which obtained simultaneously by the multi(20)-directional schlieren camera system.

The brightness of schlieren images (B) are calibrated by grayscale by subtracting the state without target images (B_{nj}). The place where the brightness value becomes 0 is changed to 128. A grayscale level showing the brightness value of the quantitative schlieren image is displayed below the image. In the quantitative schlieren images, the color of the two sides of the jets boundaries is different (dark and bright) because the knife-edge orientation will reveal directional density gradients. In our schlieren optical system the knife-edge located from left to right.

The insets in each image are the values of the shooting angles θ. Each image is 900 (H) × 1000 (V) pixel (27 mm × 30 mm) in size. The scale of the z coordinate is also shown in image No. 6.

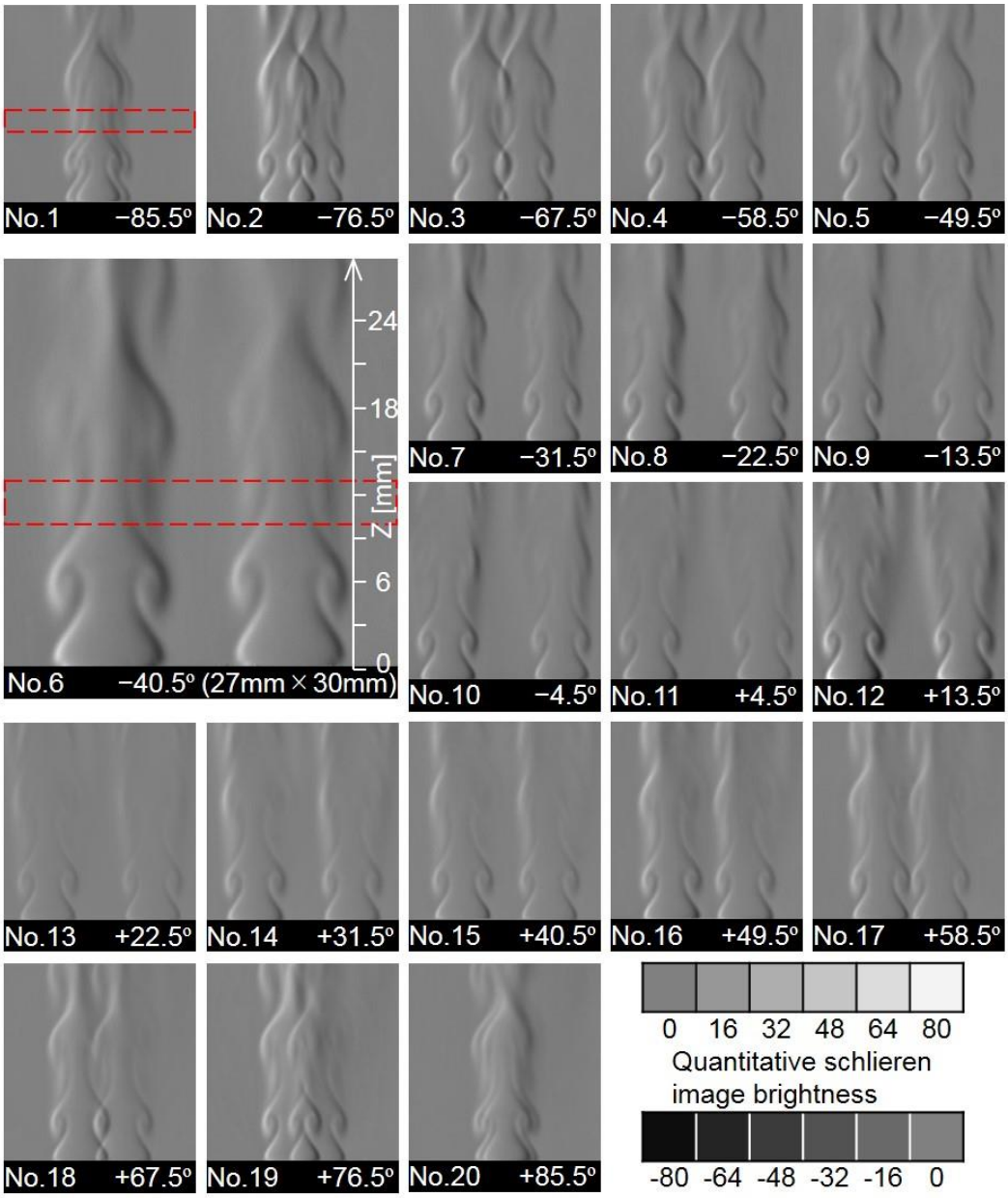

Fig. 5.7 Quantitative multi(20)-schlieren images of stoichiometric (equivalence ratio = 1) two premixed jets in the ambient air (ethanol (almost left) - propane (almost right)).

5.3.2. Projections (Modified Optical Path Length O_{plm}) Images

The images of Fig. 5.7 are processed by the aforementioned conversion procedure to projection images of modified optical path length O_{plm} as shown in Fig. 5.8.

Due to the big size of data (900 (H) × 1000 (V) pixel), our computer has no capacity to process this big amount of data in the CT reconstruction procedure. Therefore the selected area (900 (H) × 100 (V) pixel) is used for obtaining projection images and in the CT reconstruction process as shown by the red dashed line in Fig. 5.7. The detail of the projection images that are used for 3D-CT reconstruction to produce 3D data in this investigation is listed in Table 5.2.

Table 5.2 The obtained images in each experiment.

Quantitative schlieren images size	900 (H) × 1000 (V) pixel (27 mm × 30 mm)
Projection images size	900 (H) × 100 (V) pixel (27 mm × 3 mm)
3D data size	900 (x) × 900 (y) × 100 (z) pixel (27 mm × 27 mm × 3 mm)
Voxel size (in each direction)	0.03 mm

The modified optical path length O_{plm}* is automatically obtained from the schlieren observation by spatially-integration of deviation modified refractive index Δn_m* along the line of sight. The modified refractive index distributions of the target flow field are reconstructed using 2D distributions (image) of modified optical path length O_{plm} as the projection in the CT-reconstruction process.

The value of the modified optical path length is displayed in light and dark based on the grayscale level under the images. The brighter parts are related to the more value of the modified optical path length from the surrounding gas (air) region of constant modified refractive index n_{ma}*(= 2.726×10^{-4}) on the periphery of the observed range.

Three-dimensional reconstruction is performed using these images data as projection images.

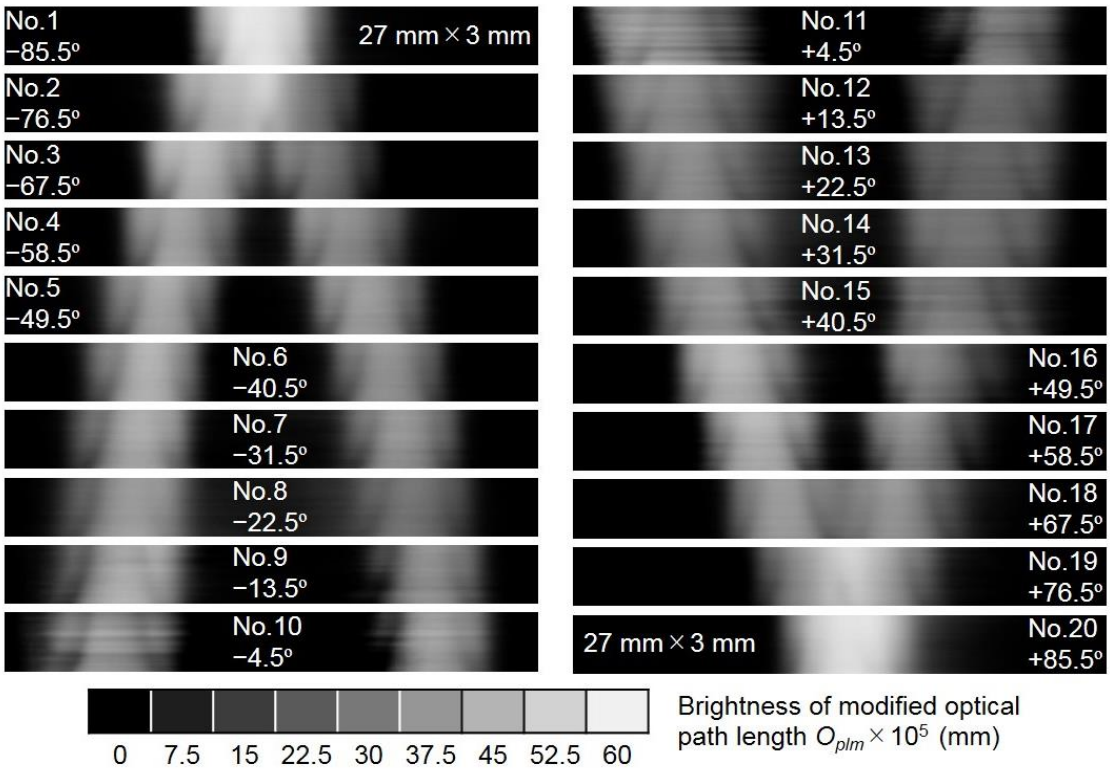

Fig. 5.8 Projection images of modified optical path length O_{plm}.

5.3.3. CT-Reconstruction Results

Using the modified optical path length O_{plm} images (Fig. 5.8) as projections for CT-reconstruction, 3D instantaneous modified refractive index n_m distributions of flow targets of two premixed gas jets were successfully obtained.

Figure 5.9(left) shows a sample of horizontal distribution of modified refractive index n_m for z = 11.1 mm position for stoichiometric (φ = 1) premixed jets. Figure 5.9(right) shows the corresponding contour diagram of Fig. 5.9(left). The values of the modified refractive index is indicated by the brightness level as shown by the brightness bar charts in the inset. Figure 5.10 shows the radial distribution diagram of the modified refractive index n_m and equivalence ratio φ for x = 0 and z = 11.1 mm. In Fig. 5.10, the modified refractive index n_m is obtained from CT-reconstructed data and corresponding equivalence ratio φ is calculated from the universal relationship (equation (5.11)) between a modified refractive index and its equivalence ratio. It is observed that the peak value of the equivalence ratio in the potential core of the premixed gas jets is approaching to φ = 1 on the left and right sides, despite the different fuel types (ethanol, propane). An acceptable agreement is observed between the CT-reconstructed data and proposed universal relationship between a modified refractive index of a premixed gas of fuel and air, and its equivalence ratio.

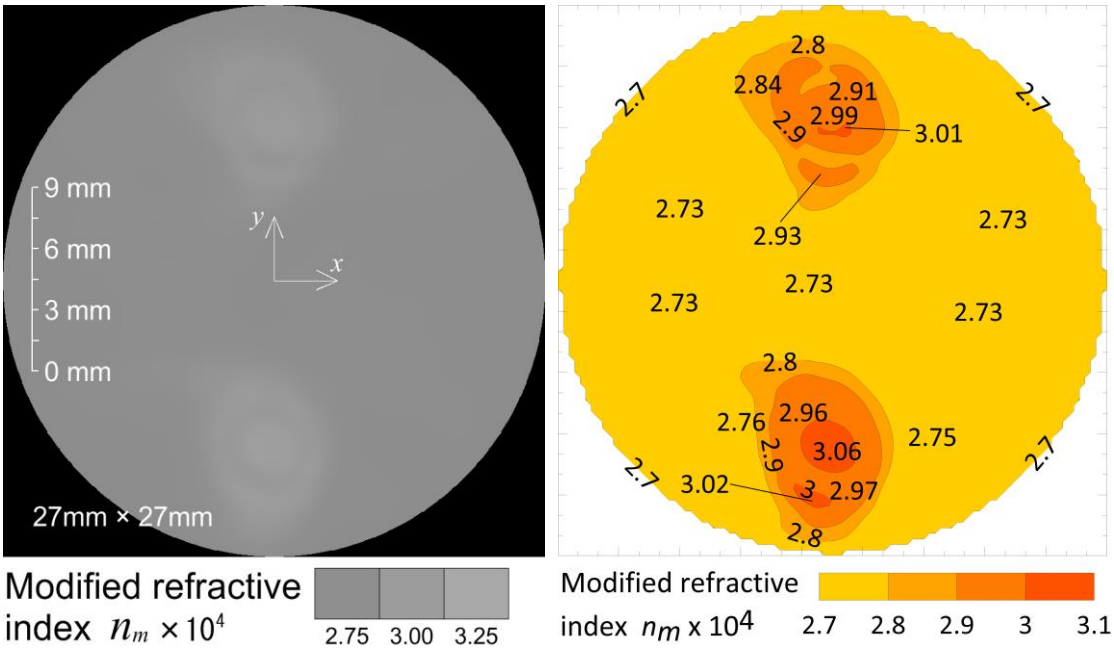

Fig. 5.9 3D-CT reconstructed horizontal distribution result (left) and the corresponding contour diagram (right) of n_m for stoichiometric (φ = 1) premixed jets for propane (top) - ethanol (bottom), z = 11.1 mm.

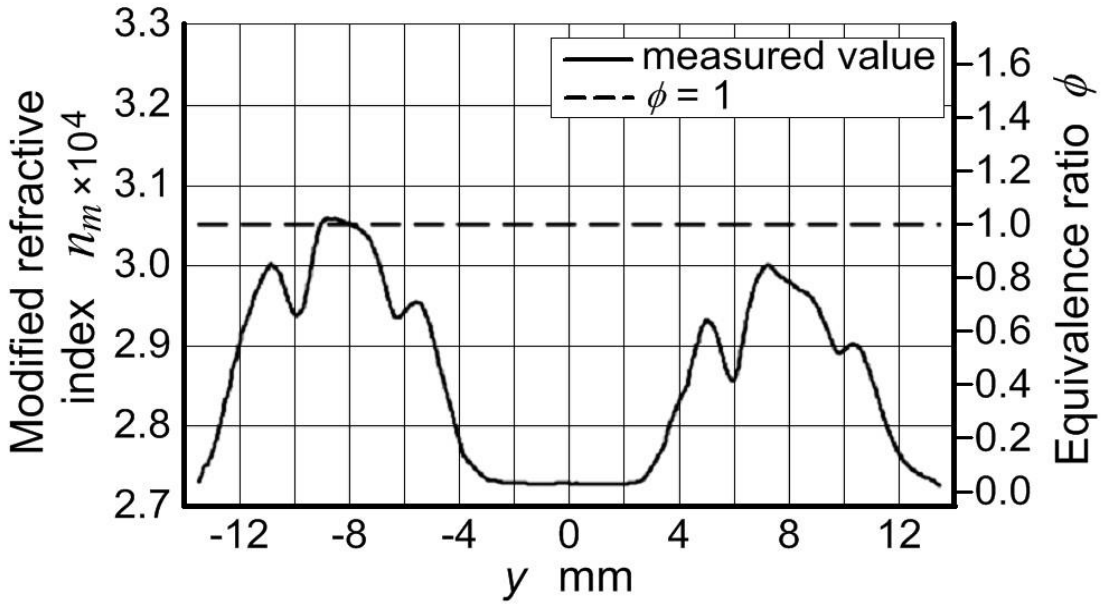

Fig. 5.10 Radial diagram of n_m (from CT-reconstructed result) and equivalence ratio φ (using equation (5.11)) for ethanol (left) - propane (right), x = 0 and z = 11.1 mm.

5.4. Summary and Concluding Remarks

An experimental study was performed to obtain the detailed information required for understanding the relationship between the modified refractive index of a premixed gas of fuel and air and its equivalence ratio. Here, a "universal relationship" between the "modified refractive index n_m" of a premixed gas of fuel and air and its "equivalence ratio φ" was proposed. The results confirm good agreement between the CT-reconstructed data and the proposed universal relationship. Therefore the equivalence ratio can be obtained by a universal coefficient that does not depend on the fuel type and can be measured when multiple fuels with unknown components are combined. This method can be applied to gas alarms technology. Its application in other fields should be investigated.

6

CHAPTER 6

Conclusions

" Smart Are Never Offended, They Come to CONCLUSIONS. " **(*Agatha Christie*)**

In the present study, for measuring density distributions, a measurement method of combining quantitative schlieren and three-dimensional computerized tomography (3D-CT) employed. In addition, in the present work, the results of the conducted research for more improvement and development of the mentioned method reported.

In **CHAPTER 1**, the necessary information about the research method and the experimental apparatus setup is stated.

In **CHAPTER 2**, we have described two new techniques "multi-path integration" and "inverse process" for "noise reduction" in projections (density thickness) images of CT (computerized tomography). We found that the "multi-path integration" novel technique has the capability of noise reduction in obtaining projections (density thickness) images of CT and the 3D density distributions of CT results. By applying the new "inverse process" technique, real experimental data is used to reproduce other directions of the schlieren brightness gradient. This new approach is a simple, efficient, and cost-effective solution that can be used to obtain any optional directions of the schlieren brightness gradient.

In **CHAPTER 3**, by employing the 20-directional quantitative schlieren 3D-CT technique, 3D-CT reconstructions of instantaneous density distributions of the shock-cells structure of circular and square supersonic microjets have obtained successfully. Two different patterns of shock waves were observed from the symmetry and diagonal views of square microjets. In addition, a complex phenomenon for free square microjets, which is called axis-switching, was clearly observed with two types "upright" and "diagonal" of "cross-shaped". Comparisons with experimental and theoretical computations showed an overall remarkably good agreement for the first "shock-cells spacing L_s" and "supersonic core lengths L_c" in this study and other correlations.

In **CHAPTER 4**, by employing the non-scanning 3D-CT technique using a 20-directional quantitative schlieren system, the spark-ignited flame kernels in propane/air fuel jets from direct injection nozzle have successfully CT-reconstructed. The instantaneous 3D density distributions of the initial flame kernel after ignition is very important in understanding the complicated

ignition phenomena of the gasoline direct injection (GDI) engine and can be served as validation data for numerical simulations.

In **CHAPTER 5**, an investigation was performed to obtain the detailed information required for understanding the relationship between the modified refractive index of a premixed gas of fuel and air and its equivalence ratio. Here, a "universal relationship" was proposed between the "modified refractive index n_m" of a premixed gas of fuel and air and its "equivalence ratio φ". The results confirm good agreement between the CT-reconstructed data and the proposed universal relationship. This method can be applied to gas alarms technology. Its application in other fields should be investigated.

REFERENCES

[1] Emrich, R.J. (1981) Methods of Experimental Physics: Fluid Dynamics. *Academic Press*, New York, **18**, Part A, 345-366.

[2] Settles, G.S. and Hargather, M.J. (2017) A Review of Recent Developments in Schlieren and Shadowgraph Techniques. *Measurement Science and Technology*, **28**(4), 1-25. https://doi.org/10.1088/1361-6501/aa5748

[3] Miyazato, Y., Ishida, Y., Yamamoto, H. and Matsuo, K. (2011) Measurements in Overexpanded Supersonic Jets by Rainbow Schlieren Deflectometry. *49th AIAA*, Orlando, USA, 4-7 January 2011.

[4] Saiki, Y., Tomida, Y., Shiga, S., Ishino, Y. and Ohiwa, N. (2010) Measurement of a Local Burning Velocity of a Turbulent Premixed Flame by Simultaneous 3D-CT Reconstruction with 40-Lens Camera and Stereoscopic PTV. *Proceedings of the 8th International ERCOFTAC Symposium on Engineering Turbulence Modelling and Measurements (ETMM)*, Marseille, France, 9-11 June 2010, 1-6.

[5] Ishino, Y., Horimoto, K., Kato, T., Ishiguro, S. and Saiki Y. (2013) 3D-CT Measurement of Premixed Flames Using a Multi-Directional Quantitative Schlieren Optical System (Solo-Measurement of Density and Combined-Measurement of Density and Light-Emission distributions). *Procedia Engineering*, **67**, 303-316. https://doi.org/10.1016/j.proeng.2013.12.030

[6] Ishino, Y., Hayashi, N., Bt Abd Razak, I.F. and Saiki, Y. (2015) 3D-CT Measurement of Instantaneous Density Distributions of High-speed Premixed Turbulent Burner Flames with a Multi-directional Schlieren Camera (Effects of Flow Velocity on 3D Flame Front Shape). *Proceedings of the 1st Thermal and Fluids Engineering Summer Conference*, New York, USA, 9-12 August 2015, 121-131. https://doi.org/10.1615/TFESC1.cbf.012970

[7] Ishino, Y., Hayashi, N., Bt Abd Razak, I.F., Kato, T., Kurimoto, Y. and Saiki, Y. (2015) 3D-CT (Computer Tomography) Measurement of an Instantaneous Density Distribution of Turbulent Flames with a Multi-directional Quantitative Schlieren Camera (Reconstructions of High-speed Premixed Burner Flames with Different Flow Velocities). *Flow, Turbulence and Combustion*, **96**(3), 819-835. https://doi.org/10.1007/s10494-015-9658-5

[8] Abd Razak, I.F., Ishino, Y., Hayashi, N., Saiki, Y., and Yahya, W.J. (2015) Three Dimensional Reconstruction of High-Speed Premixed Flames with Three Dimensional Computer Tomography 20-Directional Quantitative Schlieren Camera by Instantaneous Density Distribution. *Journal of Advanced Research in Fluid Mechanics and Thermal Sciences* **15**(1), 1-16. http://www.akademiabaru.com/arfmtsv15_n1_p1_16.html

[9] Ishino, Y., Hayashi, N., Ishiko, Y., Nazari, A.Z., Nagase, K., Kakimoto, K. and Saiki, Y. (2016) Schlieren 3D-CT Reconstruction of Instantaneous Density Distributions of Spark-ignited Flame

Kernels of Fuel-rich Propane-air Premixture. *Proceedings of ASME Heat Transfer Summer Conference*, Washington DC, USA, 10-14 July 2016, HT2016-7423, 1-10. https://doi.org/10.1115/HT2016-7423

[10] Ishino, Y., Hayashi, N., Ishiko, Y., Nagase, K., Kakimoto, K., Nazari, A.Z. and Saiki, Y. (2017) 3D Printing of Spark-Ignited Flame Kernels, Experimentally Captured by 3D-Computer Tomography and Multi-Directional Schlieren Photography. *Heat Transfer*, **139**(2), HT-16-1726. https://doi.org/10.1115/1.4035583

[11] Nazari, A.Z., Ishino, Y., Yamada, R., Motohiro, T., Ito, F., Kondo, H., Miyazato, Y. and Nakao, S. (2018) CT (Computer Tomography) Measurement of 3D Density Distributions of High-speed Premixed Turbulent Flames (Multi-path Integration Image-noise Reduction Technique Based on Novel Concept of Complex Brightness Gradient in Quantitative Schlieren Images). *Proceedings of the 18th International Symposium on Flow Visualization*, Zurich, 26-29 June 2018, 212a, 1-13. https://doi.org/10.3929/ethz-b-000279202

[12] Nazari, A.Z., Ishino, Y., Yamada, R., Motohiro, T., Ito, F., Kondo, H., Miyazato, Y. and Nakao, S. (2019) CT (Computer Tomography) Measurement of 3D Density Distributions of Flame: Obtaining Vertical Gradient Schlieren Brightness from Horizontal Gradient for Image-noise Reduction. *Proceedings of the 4th Thermal and Fluids Engineering Conference*, Las Vegas, 14-17 April 2019, TFEC-2019-27746, 185-194. http://doi.org/10.1615/TFEC2019.cbf.027746

[13] Nazari, A.Z., Ishino, Y., Ito, F., Kondo, H., Yamada, R., Motohiro, T., Saiki, Y., Miyazato, Y., and Nakao, S. (2020) Quantitative Schlieren Image-Noise Reduction Using Inverse Process and Multi-Path Integration. *Journal of Flow Control, Measurement & Visualization* **8**(2), 25-44. https://doi.org/10.4236/jfcmv.2020.82002

[14] Nazari, A.Z., Ishino, Y., Ishiko, Y., Ito, F., Kondo, H., Yamada, R., Motohiro, T., Miyazato, Y., and Nakao, S. (2020) Multi-Schlieren CT Measurements of Supersonic Microjets from Circular and Square Micro Nozzles. *Journal of Flow Control, Measurement & Visualization* **8**(3), 77-101. https://doi.org/10.4236/jfcmv.2020.83005

[15] Nazari, A.Z., Ishino, Y., Motohiro, T., Yamada, R., Ishiko, Y. and Saiki, Y. (2017) Schlieren CT Measurement of 3D Density Distributions of Flame Kernels of Spark-ignited Direct-injection of Free, Cavity-guided and Plane-guided Fuel Jets. *Proceedings of the 11th Asia-Pacific Conference on Combustion*, Sydney, 10-14 December 2017, 297, 1-4. http://www.anz-combustioninstitute.org/proceedings.php

[16] Nazari, A.Z., Ishino, Y., Kondo, H., Motohiro, T., Yamada, R. and Ito, F. (2020) Multi-Schlieren 3D-CT Measurements of Instantaneous Equivalence Ratio Distributions of a Premixed Gas Field Based on Modified Refractive Index. *Journal of the Combustion Society of Japan* **62**(202), 338-346. https://doi.org/10.20619/jcombsj.1910

[17] Merzkirch, W. (1987) Techniques of Flow Visualization. Loughton, SPS, 54-60. https://apps.dtic.mil/dtic/tr/fulltext/u2/a194291.pdf

[18] Zeng, G.L. (2001) Image Reconstruction - a Tutorial. *Computerized Medical Imaging and Graphics*, **25**(2), 97-103. https://doi.org/10.1016/S0895-6111(00)00059-8

[19] Herman, G.T. (2009) Fundamentals of Computerized Tomography: Image Reconstruction from Projections. Springer, London, 125-135.

[20] Yokoi, T., Shinohara, H., Hashimoto, T., Yamamoto, T., and Niio, Y. (2000) Implementation and Performance Evaluation of Iterative Reconstruction Algorithms in SPECT: A Simulation Study Using EGS4. *Proceedings of the Second International Workshop on EGS, KEK Proceedings* 200-20, 224-234. http://rcwww.kek.jp/egsconf/proceedings/2iwoegs/yokoi.pdf

[21] Gonzalez, R.C. and Woods, R. E. (2008) Digital Image Processing. Third Edition, New Jersey, Pearson Education, Inc., 1-60.

[22] https://www.projectorcentral.com/All-About-Bit-Depth.htm (2021.01.09)
[23] https://en.wikipedia.org/wiki/Photoreceptor_cell (2020.12.25)
[24] Hecht, S., Shlaer, S., and Pirenne, M.H. (1942) Energy, Quanta, and Vision. *Journal of General Physiology*, **25**(6), 819-840. https://doi.org/10.1085/jgp.25.6.819
[25] Lambert, T.J. and Waters, J.C. (2014) Quantitative Imaging in Cell Biology: Chapter 3 - Assessing Camera Performance for Quantitative Microscopy. *Methods in Cell Biology*, **123**, 35-53. https://doi.org/10.1016/B978-0-12-420138-5.00003-3
[26] Huang, C., Gregory, J.W. and Sullivan, J.P. (2007) A Modified Schlieren Technique for Micro Flow Visualization. *Measurement Science and Technology*, **18**(5), N32-N34. http://doi.org/10.1088/0957-0233/18/5/N04
[27] Collicott, S.H. and Salyer, T.R. (1994). Noise Reduction Properties of a Multiple-Source Schlieren System. *AIAA Journal*, **32**(8), 1683-1688. https://doi.org/10.2514/3.12160
[28] Chaloupka, J.L., Woods, M., Aas, J., Hutchins, J. and Thistle, J.D. (2014) Color Schlieren Imaging with a Two-path, Double Knife Edge System. *Optics Express*, **22**(7), 8041-8046. https://doi.org/10.1364/OE.22.008041
[29] Barry, F.W. and Edelman, G.M. (1948) An Improved Schlieren Apparatus. *Journal of the Aeronautical Sciences*, **15**(6), 364-365. https://doi.org/10.2514/8.11588
[30] Hadjadj, A. and Kudryavtsev, A. (2005) Computation and Flow Visualization in High-speed Aerodynamics. *Journal of Turbulence*, **6**, N16. https://doi.org/10.1080/14685240500209775
[31] Scroggs, S.D. and Settles, G.S. (1996) An Experimental Study of Supersonic Microjets. *Experiments in Fluids*, **21**(6), 401-409. https://doi.org/10.1007/BF00189042
[32] Aniskin, V., Mironov, S. and Maslov, A. (2013) Investigation of the Structure of Supersonic Nitrogen Microjets. *Microfluid Nanofluid*, **14**(3-4), 605-614. http://doi.org/10.1007/s10404-012-1079-3
[33] Phalnikar, K.A., Kumar, R. and Alvi, F.S. (2008) Experiments on Free and Impinging Supersonic Microjets. *Experiments in Fluids*, **44**(5), 819-830. https://doi.org/10.1007/s00348-007-0438-4
[34] Smedley G.T., Phares, D.J. and Flagan, R.C. (1999) Entrainment of Fine Particles from Surfaces by Impinging Shock Waves. *Experiments in Fluids*, **26**, 116-125. https://doi.org/10.1007/s003480050270
[35] Bayt, R.L. and Breuer, K.S. (2001) Design and Performance of Hot and Cold Supersonic Microjets. *AIAA Journal*, 0721. https://doi.org/10.2514/6.2001-721
[36] Alvi, F.S., Shin. C., Elavaeasan, R., Garg, G. and Krotopalli, A. (2003) Control of Supersonic Impinging Jet Flows Using Microjets. *AIAA Journal*, **41**(7), 1347-1355. https://doi.org/10.2514/2.2080
[37] Kumar, V. and Alvi, F.S. (2006) Use of High-speed Microjets for Active Separation Control in Diffusers. *AIAA Journal*, **44**(2), 273-281. https://doi.org/10.2514/1.8552
[38] Zhuang, N., Alvi, F.S., Alkislar, M.B. and Shih, C. (2006) Supersonic Cavity Flows and Their Control. *AIAA Journal*, **44**(9), 2118-2128. https://doi.org/10.2514/1.14879
[39] Arakeri, V.H., Krothapalli, A., Siddavaram, V., Alkislar, M.B. and Lourenco, L.M. (2003) On the

Use of Microjets to Suppress Turbulence in a Mach 0.9 Axisymmetric Jet. *Journal of Fluid Mech*anics, **490**, 75-98.
https://doi.org/10.1017/S0022112003005202

[40] Teshima, K. (1990) Three-Dimensional Characteristics of Supersonic Jets. *Proceedings of the 17th International Symposium on Rarefied Gas Dynamics*, Aachen, 8-14 July 1990, edited by A. E. Beylich, VCH Verlagsgesellschaft mbH, Weinheim, Germany, 1042-1048.
1991rgd..proc.1042T

[41] Tsutsumi, S. Teramoto, S., Yamaguchi, K. and Nagashima, T. (2006) Structure of Underexpanded Jets from Square Nozzles. *AIAA Journal*, **44**(6), 1287-1291.
https://doi.org/10.2514/1.12946

[42] Gutmark, E.J. and Grinstein, F.F. (1999) Flow Control with Noncircular Jets. *Annual Review of Fluid Mechanics*, **31**, 239-272.
https://doi.org/10.1146/annurev.fluid.31.1.239

[43] Cabaleiro, J.M. and Aider, J.L. (2014) Axis-switching of a Micro-jet. *Physics of Fluids*, **26**, 031702.
http://dx.doi.org/10.1063/1.4868256

[44] Kolhe, P.S. and Agrawal, A.K. (2009) Density Measurements in a Supersonic Microjet Using Miniature Rainbow Schlieren Deflectometry. *AIAA Journal*, **47**(4), 830-838.
https://doi.org/10.2514/1.37332

[45] Ezoe, M., Nakao, S. and Miyazato, Y. (2019) Quantitative Flow Visualization by Rainbow Schlieren Deflectometry and Pitot Pressure Measurements for Leek Peeler Nozzle Jets. *Journal of Flow Control , Measurement & Visualization*, **7**(1), 44-60.
https://doi.org/10.4236/jfcmv.2019.71004

[46] Yokoi, T., Shinohara, H., Hashimoto, T., Yamamoto, T., and Niio, Y. (2000) Implementation and Performance Evaluation of Iterative Reconstruction Algorithms in SPECT: A Simulation Study Using EGS4. *Proceedings of the Second International Workshop on EGS, KEK Proceedings* 200-20, 224-234.
http://rcwww.kek.jp/egsconf/proceedings/2iwoegs/yokoi.pdf

[47] Fukuda, H., Maeda, H., Ono, D., Nakao, S., Miyazato, Y. and Ishino, Y. (2016) Rainbow Schlieren Measurements in Underexpanded Jets from Axisymmetric Supersonic Micro Nozzles. *Proceedings of the 27th International Symposium on Transport Phenomena*, Honolulu, 20-23 September 2016, ISTP27-158, 1-7.

[48] Maeda, H., Fukuda, H., Nakao, S., Miyazato, Y. and Ishino, Y. (2018) Rainbow Schlieren Measurements in Underexpanded Jets from Square Supersonic Micro Nozzles. *EPJ Web Conferences*, **180**, 02058, 1-6.
https://doi.org/10.1051/epjconf/201818002058

[49] Foelsch, K. (1949) The Analytical Design of an Axially Symmetric Laval Nozzle for a Parallel and Uniform Jet. *Journal of the Aeronautical Sciences*, **16**(3), 161-166 and 188.
https://doi.org/10.2514/8.11758

[50] Anderson, J.D. (1982) Modern Compressible Flow with Historical Perspective. McGraw-Hill Book Company, New York.

[51] Zhao, J. (2019) Investigation on Wall Shear Stress Measurement in Supersonic Flows with Shock Waves Using Shear-Sensitive Liquid Crystal Coating. *Aerospace Science and Technology*, **85**, 453-463.
https://doi.org/10.1016/j.ast.2018.12.034

[52] Chapman, C.J. (2000) High Speed Flow. Cambridge University Press, New York.

[53] He, M.S., Qin, L.Z. and Liu, Y. (2015) Oscillation Flow Induced by Underwater Supersonic Gas

Jets from a Rectangular Laval Nozzle. *Procedia Engineering*, **99**, 1531-1542. https://doi.org/10.1016/j.proeng.2014.12.705

[54] Zaman, K.B.M.Q. (1996) Axis Switching and Spreading of an Asymmetric Jet: the Role of Coherent Structure Dynamics. *Journal of Fluid Mech*anics, **316**, 1-27. https://doi.org/10.1017/S0022112096000420

[55] Chen, N. and Yu, H. (2014) Mechanism of Axis-switching in Low Aspect-ratio Rectangular Jets. *Computers & Mathematics with Applications*, **67**(2), 437-444. https://doi.org/10.1016/j.camwa.2013.03.018

[56] Tam, C.K.W. and Tanna, H.K. (1982) Shock Associated Noise of Supersonic Jets from Convergent-Divergent Nozzles. *Journal of Sound and Vibration*, **81**(3), 337-358. https://doi.org/10.1016/0022-460X(82)90244-9

[57] Tam, C.K.W. (1988) The Shock-Cell Structures and Screech Tone Frequencies of Rectangular and Non-Axisymmetric Supersonic Jets. *Journal of Sound and Vibration*, **121**(1), 135-147. https://doi.org/10.1016/S0022-460X(88)80066-X

[58] Mehta, R.C. and Prasad, J.K. (1996) Estimation of Shock-cell Structure of Axisymmetric Supersonic Free Jets. *Indian Journal of Engineering and Materials Sciences*, **3**(4), 141-147. http://nopr.niscair.res.in/handle/123456789/29795

[59] Hu, T.F. and McLaughlin, D.K. (1990) Flow and Acoustic Properties of Low Reynolds Number Underexpanded Supersonic Jets. *J. of Sound and Vibration*, **141**(3), 485-505. https://doi.org/10.1016/0022-460X(90)90640-L

[60] Schlichting, H. (1979) Boundary-Layer Theory. 7th Edition, McGraw Hill, New York. https://en.wikipedia.org/wiki/Boundary_layer_thickness#cite_note-3

[61] Zhao, F., Lai, M.-C. and Harrington, D.L. (1999) Automotive Spark-Ignited Direct-Injection Gasoline Engines, *Progress in Energy and Combustion Science*, **25**, 437-562. https://www.sciencedirect.com/journal/progress-in-energy-and-combustion-science/vol/25/issue/5

[62] https://www.yanmar.com/global/marinecommercial/products/dual_fuel_engine/ (2019.11.19)

[63] Kawahara, N., Tomita, E., Ichimiya, M., Takasu, K., Tsuchida, N., and Goto, K. (2003) Transient Temperature Measurement of Unburned Gas in an Engine Cylinder Using Laser Interferometry with a Fiber-Optic Sensor. *SAE Technical Paper* 2003-01-1799, *Journal of Fuel & Lubricants*, **112**(4), 1044-1051. https://doi.org/10.4271/2003-01-1799

[64] Sharma, S., Patel, P.B., Patel, R.S., and Vora, J.J. (2007) Density and Comparative Refractive Index Study on Mixing Properties of Binary Liquid Mixtures of Eucalyptol with Hydrocarbons at 303.15, 308.15 and 313.15 K. *Journal of Chemistry* **4**(3), 343-349. https://doi.org/10.1155/2007/485378

[65] Nita, I., Geacai, E., Iulian, O., and Osman, S. (2017) Study of the Refractive Index of Gasoline+Alcohol Pseudo-Binary Mixtures. *Ovidius University Annals of Chemistry* **28**(1), 18-24. https://doi.org/10.1515/auoc-2017-0004

[66] Heller, W. (1965) Remarks on Refractive Index Mixture Rules. *The Journal of Physical Chemistry* **69**(4), 1123-1129. https://doi.org/10.1021/j100888a006

[67] Gardiner, JR., W.C., Hidaka, Y., and Tanzawa, T. (1981) Refractivity of combustion gases. *Combustion and Flame* **40**, 213-219. https://doi.org/10.1016/0010-2180(81)90124-3

[68] Zhang, Z., He, J., Du, B., Guo, K., and Wang, Y. (2019) Highly Sensitive Gas Refractive Index Sensor Based on Hollow-Core Photonic Bandgap Fiber. *Optics Express* **27**(21), 29649-29658. https://doi.org/10.1364/OE.27.029649

[69] Xu, Z., Sun, Q., Li, B., Luo, Y., Lu, W., Liu, D., Shum, P.P., and Zhang, L. (2015) Highly Sensitive Refractive Index Sensor Based on Cascaded Microfiber Knots with Vernier Effect. *Optics Express* **23**(5), 6662-6672. https://doi.org/10.1364/OE.23.006662

[70] Wo, J., Wang, G., Cui, Y., Sun, Q., Liang, R., Shum, P.P., and Liu, D. (2012) Refractive Index Sensor Using Microfiber-Based Mach–Zehnder Interferometer. O*ptics Letters* **37**(1), 67-69. https://doi.org/10.1364/OL.37.000067

[71] Zhang, Y., Lin, B., Tjin, S. C., Zhang, H., Wang, G., Shum, P., and Zhang, X. (2010) Refractive Index Sensing Based on Higher-Order Mode Reflection of A Microfiber Bragg Grating. *Optics Express* **18**(25), 26345-26350. https://doi.org/10.1364/OE.18.026345